545

# A STUDY OF THE WAKE STRUCTURE

# BEHIND BLUFF RINGS

by

MASAKI TAKAMOTO

Thesis submitted for the degree of Doctor of Philosophy in the Faculty of Engineering, University of London and for the Diploma of Imperial College.

## SUMMARY

The structure of the wakes of the ring models with various cross-sections has been studied. They are compared with the wakes of a solid circular disk and two flat plates arranged side-by-side. Measurements were carried out in the wind tunnel at Reynolds numbers of the order of $10^4$. Periodic components were extracted from the turbulent velocity fluctuations measured by hot-wires in the wake by employing a conditional averaging technique. Also, surface pressure distributions together with correlation and coherence of the velocity fluctuations in the wake were measured.

The wake structure of the ring model was found to be highly dependent on the geometry of model. A regular and coherent axisymmetric vortex ring shedding alternately from the inside and outside of ring models with $d/w \geq 5.0$ was observed, where $d$ is the mean diameter and $w$ is the width of the ring model. There exists a sudden change of the correlation curves for the ring model between $d/w = 4.5$ and $d/w = 5.0$ and the base pressure coefficient rapidly decreases with increasing $d/w$ between $d/w = 4.0$ and $d/w = 6.0$. Velocity fluctuations in the wake of the ring model with $d/w \leq 4.0$ have a fairly weak predominate frequency and the velocity fluctuation components at the peak frequency are about $180^{\circ}$ out of phase about the axis of symmetry.

The counterrotating inside and outside vortex rings shed from the thin sharp-edged cross-section ring model with $d/w = 6.0$ are nearly $180^{o}$ out of phase with each other at 3.4 w downstream from the ring model. However at further distances downstream they get closer to each other because of the opposite signed self-induced velocities of both sets of vortex rings. A remarkable regular periodic velocity fluctuation was recognised on the axis of symmetry in the wake of a rectangular cross-section ring model. It was also observed that vortex shedding from two flat plates arranged side-by-side with fairly wide spacing is symmetric about the axis of the gap and the arrangement of vortices is almost constant along the wake.

The vortex wakes of a ring and two flat plates were numerically modelled by using infinite rows of circular line vortices and two-dimensional point vortices respectively. The arrangements of vortices and their variation with downstream distance observed in the wind tunnel experiment were well predicted in spite of the simple numerical simulations used.

The streaklines and particle paths in the wakes of ring models and two flat plates were visualized in a water tank at Reynolds numbers just below $10^{2}$. The results from flow visualization agree with the results of the wind tunnel experiments.

## ACKNOWLEDGEMENTS

I have been fortunate to have an enjoyable and rewarding experience at Imperial College and I am very grateful to many people who have made it possible. I would like to express my sincere gratitude to Professor P.W. Bearman for his ideal supervision and his thoughtfulness.

I am also indebted to: Mr. John Coles, Mr. K. Sage, and the technical staff of the Department of Aeronautics; Mr. J. O'Leary the photographer and Mr. A. Mayston, the Librarian, for their friendly and cooperative assistance during the course of this work.

My thanks also to Professor P. Bradshaw, Dr. C.S. Subramanian and Dr. S.C. Luo for their valuable advise on the experiments and to Mrs. R. Fairhurst for proof reading and the typing of this thesis.

I also wish to acknowledge the Japan International Cooperation Agency and the National Research Laboratory of Metrology, Japan for allowing me the opportunity to study abroad.

Finally, I would like to thank my family for their warm support and encouragement.

## CONTENTS


| | | Page |
|---|---|---|
| | SUMMARY | 2 |
| | ACKNOWLEDGEMENTS | 4 |
| | CONTENTS | 5 |
| | LIST OF SYMBOLS | 8 |
| Chapter 1. | **INTRODUCTION** | 13 |
| Chapter 2. | **EXPERIMENTAL ARRANGEMENTS** | |
| 2.1 | Bluff body models | 26 |
| 2.2 | Wind tunnel and range of experimental condition | 32 |
| 2.3 | Hot-wire data acquisition and reduction | 32 |
| 2.4 | Data processing on a mainframe computer | 37 |
| 2.5 | Conditional averaging | 38 |
| 2.6 | Vorticity calculation | 42 |
| 2.7 | Spectral density function and coherence function | 51 |
| Chapter 3. | **EXPERIMENTAL RESULTS** | |
| 3.1 | Wake structure of rings | 54 |
| 3.1.1 | Measurements of base pressure and drag | 55 |
| 3.1.2 | Measurements of correlation and vortex shedding frequency | 60 |

| | | Page |
|---|---|---|
| 3.1.3 | Results of conditional averaging | 82 |
| 3.1.4 | Effects of afterbody shapes | 101 |
| 3.2 | Wake structure of a circular disk | 126 |
| 3.3 | Wake structure of two flat plates arranged side-by-side. | 142 |

Chapter 4. **VORTEX WAKE MODEL**

| | | |
|---|---|---|
| 4.1 | Modelling of the vortex wake of a ring | 169 |
| 4.1.1 | Isolated vortex ring | 170 |
| 4.1.2 | Self induced velocity of a vortex ring | 175 |
| 4.1.3 | Double rows of vortex rings of infinite extent | 180 |
| 4.1.4 | Numerical simulation | 184 |
| 4.2 | Modelling of the vortex wake of two flat plates in a side-by-side arrangement | 194 |

Chapter 5. **FLOW VISUALIZATION**

| | | |
|---|---|---|
| 5.1 | Experimental apparatus and flow visualization techniques | 200 |
| 5.2 | Flow visualization of wakes behind ring models | 203 |
| 5.3 | Flow visualization of wakes behind two flat plates arranged side-by-side | 206 |
| | Figures and Photographs for Chapter 5. | 207 |

Page

Chapter 6. **CONCLUSIONS** 220

**REFERENCES** 226

**APPENDIX A** Maskell's formulae for correction of the blockage effects 236

**APPENDIX B** Induced velocity by an isolated vortex ring 238

**APPENDIX C** Induced velocity of the two-dimensional double vortex street in antiphase 241

# LIST OF SYMBOLS

$A$ : vector, $A_i = \alpha_i$

$A_o$ : constant in King's law

$B$ : vector, $B_i = \beta_i$

$B_o$ : constant in King's law

$\vec{B}$ : vector potential of u

$C_D$ : drag coefficient

$C_p$ : pressure coefficient

$C_{pb}$ : base pressure coefficient

$D$ : diameter of a solid circular disk

$D_o$ : diameter of a wire

$E$ : hot-wire output voltage

$E_o$ : hot-wire output voltage at 0 m/s

$E_R$ : hot-wire output voltage at U

$E(k)$ : complete elliptic integral of the first kind

$G(k)$ : function, $G(k) = k \left\{ \frac{2-k^2}{1-k^2} E(k) - 2K(k) \right\}$

$H(a)$ : function, $H(a) = \frac{\sinh \frac{2\pi a}{\ell}}{\cosh \frac{2\pi a}{\ell} - \cos \frac{2\pi h}{\ell}}$

$I(a)$ : function, $I(a) = \frac{\sin \frac{2\pi h}{\ell}}{\cosh \frac{2\pi a}{\ell} - \cos \frac{2\pi h}{\ell}}$

$J(k)$ : function, $J(k) = \left( \frac{2}{k} - k \right) K(k) - \frac{2}{k} E(k)$

$K(k)$ : complete elliptic integral of the second kind

$L$ : length of a vortex core

$P_{xy}$ : coincident spectal density function

$Q_{xy}$ : quadrature spectral density function

$R_e$ : Reynolds number, $R_e = \frac{Uw}{\nu}$

$R_o$ : radial distance from the vortex core centre to maximum $u_\theta$

$S_t$ : Strouhal number, $St = \frac{fw}{U}$

$S_{xx}$ : power spectral density function

$S_{xy}$ : cross-spatial density function

$U$ : velocity of a free stream

$V$ : volume of a vortex core

$T^*$ : time from a start of the recording, non-dimensionalized by the period of one vortex shedding cycle.

$X$ : matrix

$Z_u$ : vector

$Z_v$ : vector

$a$ : radius of an inside vortex ring

$b$ : radius of an outside vortex ring

$\Delta c$ : rate of change of conditionally averaged values

$d$ : average diameter of a ring model

$d_i$ : inside diameter of a ring model

$d_o$ : outside diameter of a ring model

$e_u^2$ : square error

$e_v^2$ : square error

$f$ : vortex shedding frequency

$f(z)$ : complex potential function

$h$ : spacing between adjacent inside and outside vortices

$k$ : parameter, $k^2 = \dfrac{4ar}{x^2 + (r+a)^2}$

$\ell$ : longitudinal spacing of both vortices

$n$ : constant in King's law, usually $n = 0.45$.

$s$ : distance between $\vec{x}$ and $\vec{x}'$

$t$ : time

$t^*$ : non-dimensional time $t^* = \dfrac{tU}{w}$

$u$ : velocity component in the free stream direction

$u^*$ : non-dimensional velocity, $u^* = \dfrac{u}{U}$

$\vec{u}$ : velocity vector

$u_a$, $v_a$ : induced velocities of inside vortices

$u_b$, $v_b$ : induced velocities of outside vortices

$u_c$ : convection velocity of vortices

$u_\theta$ : circumferencial velocity

| | | |
|---|---|---|
| $u_{xs}$ | : | self-induced velocity |
| $u_x$, $u_y$ | : | velocity fluctuations measured by two single hot-wires |
| $v$ | : | velocity component normal to $u$ |
| $v^*$ | : | non-dimensional velocity, $v^* = \frac{v}{U}$ |
| $x$ | : | distance from a bluff body in the free stream direction |
| $\vec{x}, \vec{x}'$ | : | position vectors |
| $(x,y)$ | : | two-dimensional co-ordinate system |
| $(x,y,z)$ | : | three-dimensional co-ordinate system |
| $(x,r,\theta)$ | : | cylinderical co-ordinate system |
| $y^*$ | : | non-dimensional distance from the axis of symmetry, $y^* = \frac{y}{w}$ |
| $w$ | : | width of a bluff body model |
| $z$ | : | complex number |
| $\Gamma_a$ | : | strength of an inside vortex |
| $\Gamma_b$ | : | strength of an outside vortex |
| $\Gamma^*$ | : | non-dimensional circulation, $\Gamma^* = \frac{\Gamma}{Uw}$ |
| $\alpha_i$ | : | constants in a second-order polynomial equation |
| $\beta_i$ | : | constants in a second-order polynomial equation |
| $\gamma_{xy}$ | : | coherence function |
| $\delta$ | : | thickness of a bluff body model |
| $\varepsilon$ | : | radius of a vortex core |

$\varepsilon_{xy}$ : cross correlation coefficient

$(\eta, \theta)$ : radial co-ordinate system

$\theta$ : angular separation

$\theta_{xy}$ : phase difference function

$\nu$ : kinematic viscosity

$\psi$ : stream function

$\xi$ : non-dimensionalized distance in the radial direction from the inside edge of the ring model

$\omega$ : vorticity, $\omega = \frac{\partial v}{\partial x} - \frac{\partial u}{\partial y}$

$\vec{\omega}$ : vorticity vector

$\omega^*$ : non-dimensional vorticity, $\omega^* = \frac{\omega W}{U}$

Subscripts

(a) : denotes inside vortices

(b) : denotes outside vortices

(') : denotes two-dimensional case

(*) : non-dimensionalized values

# CHAPTER ONE

## INTRODUCTION

The flow around bluff bodies is one of the oldest subjects in fluid dynamics and numerous studies have been carried out because of its increasing importance for practical applications as well as its fundamental interest.

The frequency and configuration of vortices which are formed in the wake of bluff bodies has been one of the main objects of interest in these studies for a long time. The first experimental investigation were made by Strouhal (1878), who discovered the relationship that a frequency, f, of sound generated by a wire vibrating in an air stream is proportional to the flow velocity, U, and inversely proportional to the wire diameter, $D_o$. Today, the ratio $fD_o/U$ is called "Strouhal number". The first theoretical treatment was made by von Karman (1911) who found the stability condition for a staggered array of point vortices which is now famous as the "Karman vortex street". Tyler (1931) measured frequencies of vortex formation behind various shapes of bluff body at low Reynolds numbers. He obtained empirical formulae for the relation between the Strouhal number and the Reynolds number for these bluff bodies. Fail et al. (1957)

measured vortex shedding frequencies from bluff bodies of various aspect ratios and noticed that vortices shed more regularly from the bluff body of a larger aspect ratio, i.e. a longer span comparing to the width of the bluff body. The most intensive sets of experimental observations of this relation are those of Roshko (1954a), Berger (1964) and Gerrard (1978). Based on the concept that all vortex street wakes are similar, Roshko (1955) extended further our understanding of this relation and introduced a universal Strouhal number in conjunction with a modified Kirchhoff method to estimate the wake width. Although the universal Strouhal number is almost constant over a wide Reynolds number range for various cylinders, Bearman (1967) has devised a new universal Strouhal number by using Kronauer's stability condition to determine the lateral spacing of vortices, which can be applied to a wider variety of bluff body shapes, including a bluff body with a splitter plate or with base bleed.

On the other hand, the relationship between Strouhal number and Reynolds number has been utilized practically for a long time. Rayleigh (1945) pointed out that the Strouhal number should be a function of the Reynolds number and that the vortex shedding frequency can be linarly related to the flow velocity in a certain Reynolds number range. This linear relation provides one of the main advantages in practical applications. Kovasznay (1949) observed that vortex shedding behind a circular cylinder is regular and stable in the Reynolds number range 40 to 160. The remarkable regularity makes it possible to measure the vortex

shedding frequency accurately. Roshko (1954b) suggested for the first time a method to determine flow velocities from frequency measurements in the wake of a circular cylinder immersed in a flow. He observed that the method is more accurate than a conventional Pitot-static tube and a manometer at velocities below 4 m/s. The method was demonstrated experimentally by Webster (1964) who confirmed that it is a useful and practical means of measuring low air stream velocities down to a few tenths of a metre per second. Kohan and Schwarz (1973) examined the experimental reproducibility of the linear relation in the Reynolds number range of 40 to 160, and presented precise calibration formulae in three separate Reynolds number ranges. An early attempt to apply this principle for industrial meters was made by Shiba (1960) who developed a ship speed meter which detects fluctuating force on a bluff body caused by vortex shedding. The intensive development of flowmeters applying this principle in the Reynolds number range from $10^{3.5}$ to $10^{5.5}$ was started a couple of decades ago by Yamasaki et al. (1967), Tsuchiya et al (1967) and White et al. (1974). Today, the vortex shedding flowmeter is one of the most popular industrial flowmeters because of its many advantages such as having no moving parts, a wide rangeability and a frequency output which is suitable for digital signal processing.

Nakaguchi et al. (1968) and Bearman and Trueman (1972) investigated the flow around rectangular cross-section cylinders and found that the effect of the body downstream of separation is extremely sensitive to the ratio of the thickness to the width of the section. They showed the drag coefficient increases to a maximum value of about 3 at a ratio of 0.6, whereas the drag coefficient of a thin flat plate or a square cylinder is known as about 2. In general, vortex shedding from a bluff body with a higher drag coefficient is expected to be stronger, which gives improved SN ratio in the detecting signal of the vortex shedding. A great number of investigations into vortex shedding flowmeters have been carried out, most of which concentrated on the afterbody shape of the bluff body to improve regularity of the vortex shedding signal and linearity of the vortex shedding frequency.

Slaouti and Gerrard (1981) investigated the end effects on the wake of a circular cylinder by using flow visualization and found that the three-dimensional structure of the wake depends strongly on the flow configuration at the end of the cylinder. Gerich and Eckelman (1982) also investigated the influence of end plates and free ends on the vortex shedding from a cylinder and found that the end effect causes considerable spanwise non-uniformity of the shedding frequency. These results apparently suggest that the end effect has a detrimental influence on the characteristic of the flowmeter, because the flowmeter is usually used to measure flow rates in a pipe and a two-dimensional

bluff body without a end plate is installed in a pipe. Maull and Young (1973), Stansby (1976) and Rooney and Peltzer (1982) demonstrated experimentally that the vortex shedding from a bluff body in a shear flow breaks down into a number of spanwise cells in each of which the frequency is constant. The breakdown of the shedding increases the uncertainty of the relation between the velocity and the frequency. In order to avoid the end effect problem and also the influence of the axisymmetric velocity profile in a pipe, Takamoto and Komiya (1979, 1982) and Karkhof (1983) used a ring as a bluff body for a vortex shedding flowmeter. However, their investigations were not focussed on the wake structure of a ring, but on the characteristics of the bluff body as a vortex shedding flowmeter.

Axisymmetric bluff bodies such as a disk, a sphere and a ring have received attention from many investigators because of their simple geometrical description and wide variety of practical applications. One of the early investigations on the wake of a disk were performed by Stanton and Marshall (1930), who visualized periodic three-dimensional vortex loops shedding from a disk in a water channel in a low Reynolds number range. Later, Willmarth et al. (1964) also observed horseshoe-shaped vortex loops in the wake of a freely falling disk. Fail et al (1957) measured drag, base pressure and the mean flow pattern of the wake of a disk. Carmody (1964) measured distributions of turbulence intensity and turbulence shear stress, and Hwang and Baldwin (1966) measured the decay of turbulent energy in the wake of a disk. Calvert (1967a)

investigated the flow past an inclined disk and found that the periodic vortex shedding is usually rather weak and the orientation of the plane of the vortex shedding is not fixed and varies from time to time at zero incidence measured from the normal, but the prominence of vortex shedding increases as the angle of incidence increases up to at least $50^{o}$ and a chain of irregular vortex rings sheds regularly from the trailing edge. Roberts (1973), Fuchs et al. (1979) and Scholz (1986) investigated the coherent structure in the wake of a disk by employing cross-spectral analysis of signals from two hot wires or microphones placed in the wake. A peak was observed in the power spectrum of the velocity or pressure fluctuation in the wake and the Strouhal number based on the diameter of the disk was found to be 0.135. They observed a high negative correlation of the fluctuation components at this peak frequency between two positions located at the same downstream distance from the disk, the same radial distance from the axis of symmetry and at an angular separation of $180^{o}$. On the other hand they found almost no correlation at an angular separation of $90^{o}$.

Measurements of the drag of a sphere, the turbulence and the vortex system in the wake of a sphere have been the subjects of a large number of investigations. Fage (1936), Maxwarthy (1969) and Achenbach (1972) measured the drag and the surface pressure distribution of a sphere over various Reynolds number ranges. Gibson et al. (1968), Uberoi and Freymuth (1970) and Riddhagni et al.(1971) measured turbulent energy decay in the wake of a sphere.

Winny (1932) investigated the helical disturbance due to vortex shedding in the wake of a sphere by using two hot wires. Magarvey and MacLatchy (1965) visualized the wake of a sphere in the Reynolds number range 200 to 500. They observed distorted three-dimensional vortex loops in the wake. Calvert (1972) measured frequencies of vortex shedding from a sphere and obtained a Strouhal number of 0.188 in the Reynolds number range $2 \times 10^4$ to $6 \times 10^4$. Achenbach (1974) measured the Strouhal number at higher Reynolds numbers up to $3 \times 10^5$. He found that the flow separation line rotates around the sphere. Pao and Kao (1977) visualized vortex shedding from a sphere in a stratified fluid and Taneda (1978) visualized the wake in the high Reynolds number range $10^4$ to $10^6$. The latter found that the wake performs a progressive wave motion at Reynolds numbers between $10^4$ and $3.8 \times 10^5$, and that it forms a pair of streamwise line vortices which rotate slowly and randomly about the streamwise axis through the centre of the sphere at Reynolds numbers between $3.8 \times 10^5$ and $10^6$.

One of the early investigations into the flow around a ring was performed by Relton (1931) who calculated the stream function for a ring moving with constant velocity in an infinite viscous fluid. Tchen (1954) and Johnson and Wu (1979) obtained approximate solutions and Goren and O'Neil (1980) obtained the exact solution for the drag of a ring at a very low Reynolds number. The drag of a ring falling freely in a fluid has been measured by Amarakoon et al. (1982) and Monson (1983). On the other hand, little seems to be known about the wake structure of a

ring. Roshko (1954b) investigated briefly the wake of a ring made up of a wire with a circular cross-section in the low Reynolds number range 50 to 500, and found that there exists an annular vortex street with a Strouhal number lower than that of a straight wire. Although he has not come to a definite conclusion, he has suggested that there exists a strong interaction of the vortex wake of a ring, which can be similarly observed in the case of a pair of cylinders arranged side by side. Takamoto and Izumi (1981) visualized stable vortex ring shedding alternately from inside and outside of a ring at low Reynolds numbers in a water tank. Monson (1983) observed vortex shedding from rings of various solidity, projected area ratio of the ring to the solid disk with the same diameter, by visualizing the wake of a ring falling freely in fluid. However this may give rise to some difference compared to the wake of a fixed ring in a stream because of oscillations of the ring. He found that there is a critical Reynolds number at which the flow pattern suddenly shifts from the oblique loop wake structure to a counter-rotating vortex ring pair in the high solidity range of around 0.6. Also he observed two annular vortex patterns, either a counter-rotating vortex ring pair or a counter-rotating helical vortex pair, in the solidity range from 0.15 to 0.45. Kamemoto et al. (1986) numerically simulated the wake of a ring by a discrete vortex method. They could recognize the formation of a vortex ring street in the near wake only when the solidity of the ring is very low. In spite of these investigations, the characteristics of a ring, such as base pressure, vorticity and arrangement of vortices in the wake, still

remain to be clarified.

As for other axisymmetrical bluff bodies, Calvert (1967b) measured vortex shedding frequencies from cones of various vortex angles. Maull (1980) investigated the effect of slant base angle on the drag of an axisymmetric body. Xia and Bearman (1983) also examined the wake of an axisymmetric body with a slanted base and found that vortices are formed from the top and bottom of the base and shed out of phase for the majority of the time when the slant angle is greater than about $45^{o}$.

If we consider the cross-sectional view of vortex shedding from a ring containing the axis of symmetry, we can think of its two-dimensional analogue of vortex shedding from two flat plates placed normal to a stream in a side-by-side arrangement. Several investigations on the interaction between two flat plates or circular cylinders, which involve measurements of force, pressure distribution and vortex shedding frequencies and also flow visualization of vortex wakes, have been carried out and they have been reviewed by Zdravkovich (1977). Biermann and Herrnstein (1933) measured the interference drag which is defined as the difference between the drag measured on one of the circular cylinders in a side-by-side arrangement and the drag of the circular cylinder in isolation. They found that the interference drag can be either positive or negative for spacings less than four diameters, although there is practically no interference for

spacings greater than that. Landweber (1942) visualized the wake of two circular cylinders and found that the vortex shedding is mainly in phase, i.e. the vortex shedding is $180^{o}$ out of phase about the axis of the gap, except for a narrow range in the vicinity of the spacing of 2.5 diameters where the vortex shedding is in antiphase, i.e. the vortex shedding is symmetric about the axis of the gap. But his results were corrected by many people later. Spivack (1946) measured the vortex shedding frequency behind two circular cylinders in a side-by-side arrangement and found that there are two different frequencies, one associated with the two cylinders as single bodies and the other related to a double body for gaps of half to one diameter. Hori (1959) measured the surface pressure distribution around one of the two circular cylinders in various arrangements. Bradshaw (1965) visualized the asymmetric flow behind a row of circular cylinders. Ishigai et al. (1971) visualized the wake of two circular cylinders by using the Schlieren method and observed markedly symmetric vortex formation for spacings of 3 and 2.5 diameters. They found that the gap flow is biased to one of the two cylinders bistably and the bias direction intermittently changes for spacings between 2 to 1.25 diameters. Andreopoulos (1972) and Bearman and Wadcock (1973) measured base pressures for two flat plates and two circular cylinders in a side-by-side arrangement respectively, and found that the flat plates experience asymmetric flow over a larger range of gap sizes and the difference in base pressure of the two flat plates is larger compared with circular cylinders. They deduced that the asymmetric flow is due to a near

wake phenomenon rather than being related to the position of boundary layer separation. They also confirmed that the vortex shedding is mainly antiphase at wider gaps. Kamemoto and Bearman (1980) and Stansby (1981) numerically simulated the vortex wakes of two flat plates and two circular cylinders, respectively, in a side-by-side arrangement by using the discrete vortex method. Shida et al. (1984) also numerically calculated the flow around two circular cylinders but he used the finite difference method. Williamson (1985) visualized the wakes of two flat plates and two circular cylinders, and showed that synchronization of vortex shedding occurs either in phase or in antiphase. Hayashi et al. (1986) visualized the biased flow behind groups of flat plates consisting of two, three or four plates in a side-by-side arrangement. However, more investigation is required, especially measurements of vorticity and the arrangement of vortices in the wake.

The basic characteristics of an isolated vortex ring are well known and described in Lamb (1945) and Batchelor (1967) for example. Fraenkel (1970) and Saffman (1970) extended the theory for the motion of vortex rings by taking the effects of viscosity into account. Maxworthy (1972, 1977) investigated experimentally the core structure and stability of a vortex ring which was formed when a short pulse of fluid was ejected from an orifice. Also, a famous and amusing game played by two similar vortex rings moving along a common axis of symmetry, where the former passes through the latter and they repeat the slip through (Batchelor 1967), was

clearly visualized by Yamada and Matsui (1978). But studies on the interference of the vortex street which consists of pairs of coaxial counter-rotating vortex rings can not be found.

In this thesis the structure of the wakes of rings has been investigated and compared with the wake of a disk and the wake of two flat plates in a side-by-side arrangement. These bluff bodies had thin and sharp-edged cross-sections to avoid the Reynolds number dependent effect, except for the rings with a rectangular or triangle cross-sections which were used for the examination of the effect of the afterbody shape. Most of the work involved experiments in a wind tunnel at Reynolds numbers of the order of $10^4$. The circulation, lateral and longitudinal spacings and the vorticity distribution of vortices were measured by employing a conditional averaging technique to the velocity fluctuations measured by hot-wire anemometers. The technique was first developed by Kovasznay (1970) to investigate an intermittent turbulent flow. Davies (1975, 1976), Cantwell (1976), Okude and Matsui (1982), and Steiner (1984) used the technique to investigate vortex wakes, which can remove random velocity fluctuations caused by the turbulent shear layer and extract mean and periodic characteristics of the fluctuations. Then, the vortex wakes of a ring and two flat plates are simulated numerically by simple vortex street models based on the experimental data obtained by the conditional averaging. Also, the wakes of rings and two flat plates in a side-by-side arrangement are visualized in a water tank in a low Reynolds number range and compared with

the results of wind tunnel experiments and the numerical simulations. The study is a basic investigation aimed at improving our knowledge of vortex shedding flowmeters as well as understanding the coherent structures in the wakes of rings, a solid disk and two flat plates in a side-by-side arrangement.

# CHAPTER TWO

## EXPERIMENTAL ARRANGEMENTS

The wake structures of rings, a solid disk and two flat plates in a side-by-side arrangement have been investigated. The experiments were carried out in a wind tunnel and this chapter describes the apparatus used and the processing of the data.

### 2.1 Bluff body models

The dimensions of the rings, the solid disk and the two flat plates used are shown in Table 2.1, and their cross-sections are illustrated in Figure 2.1(a). All the bluff body models, except for the special models, were sharp edged to fix flow separation points. This minimizes any Reynolds number effects and also helps to provide good spanwise coherence of the wake structure. The thickness, $\delta$ , of the model was fixed at 4 mm, regardless of their widths, w, although it would be better to have compared different models with the same ratio of $\delta/w$. However, Davies (1975) and Donoso (1980) measured the base pressure coefficient, $C_{pb}$, of sharp-edged flat plates with $\delta/w$ = 0.25 and 0.125, respectively, and obtained the same value of $C_{pb}$= -1.24 at the Reynolds number order of $10^4$. Also, Bearman and Trueman (1972) obtained $C_{pb}$= -1.3 for the rectangular cylinder of $\delta/w$ = 0.2. Therefore, the effect is thought to be small for all the models, of which $\delta/w$ were less

## TABLE 2.1

| | d/w | w (mm) | d (mm) | $d_o$ (mm) | $d_i$ (mm) | $R_e$ at 10 m/s ($\times 10^4$) |
|---|---|---|---|---|---|---|
| Disk | 1.0 | 100.0 | 100.0 | 200.0 | 0 | 6.8 |
| Ring | 1.2 | 90.9 | 109.1 | " | 18.2 | 6.2 |
| " | 1.5 | 80.0 | 120.0 | " | 40.0 | 5.4 |
| " | 2.0 | 66.7 | 133.4 | " | 66.6 | 4.8 |
| " | 3.0 | 50.0 | 150.0 | " | 100.0 | 3.4 |
| " | 4.0 | 40.0 | 160.0 | " | 120.0 | 2.9 |
| " | 4.5 | 36.4 | 163.6 | " | 127.2 | 2.5 |
| " | 5.0 | 33.3 | 166.7 | " | 133.4 | 2.3 |
| " | 5.5 | 30.8 | 169.2 | " | 138.4 | 2.1 |
| " | 6.0 | 28.6 | 171.4 | " | 142.8 | 2.0 |
| " | 8.0 | 22.2 | 177.8 | " | 155.6 | 1.6 |
| " | 10.0 | 18.2 | 181.8 | " | 163.6 | 1.3 |
| Two flat plates | 4.0 | 28.6 | 114.4 | - | - | 2.0 |
| " | 6.0 | 28.6 | 171.4 | - | - | 2.0 |

* see Figure 2.1 for symbols

** $R_e$: Reynolds number based on w at U = 10 m/s.

than 0.22, except for the special models. The two special ring models, shown in Figure 2.2, were used to examine the effect of the after-body shape on the wake structure of the ring. The one had the rectangular cross-section of $\delta/w = 0.6$, at which ratio the drag of a two-dimensional rectangular cylinder has been shown to be a maximum by Nakaguch et al. (1968) and Bearman and Trueman (1972). Also, the ring with the triangular cross-section was chosen for the other, as some commercial vortex shedding flowmeters install a triangular cylinder as a bluff body.

The rings and the disk were suspended normal to a free stream in the centre of a wind tunnel by piano wires of diameter 0.33 mm. In order to minimize any flow induced vibration six wires were used. The two flat plates spanned the wind tunnel horizontally at mid-height and were placed normal to a free stream in a side-by-side arrangement. Three-dimensional effects caused by interaction with the tunnel wall boundary layers were reduced by using the end plates, shown in Figure 2.1(b). The dimensions of the end plates were found by Donoso (1980) to have an influence on the flow. He found that there were considerable effects if the end plates were not large enough on the wake structure. The end plates for the two flat plates were fixed at about 70 mm from the tunnel wall, so that they were well enough outside the tunnel wall boundary layer. The instrumentation and a ring installed in the wind tunnel are shown in Photo 2.1.

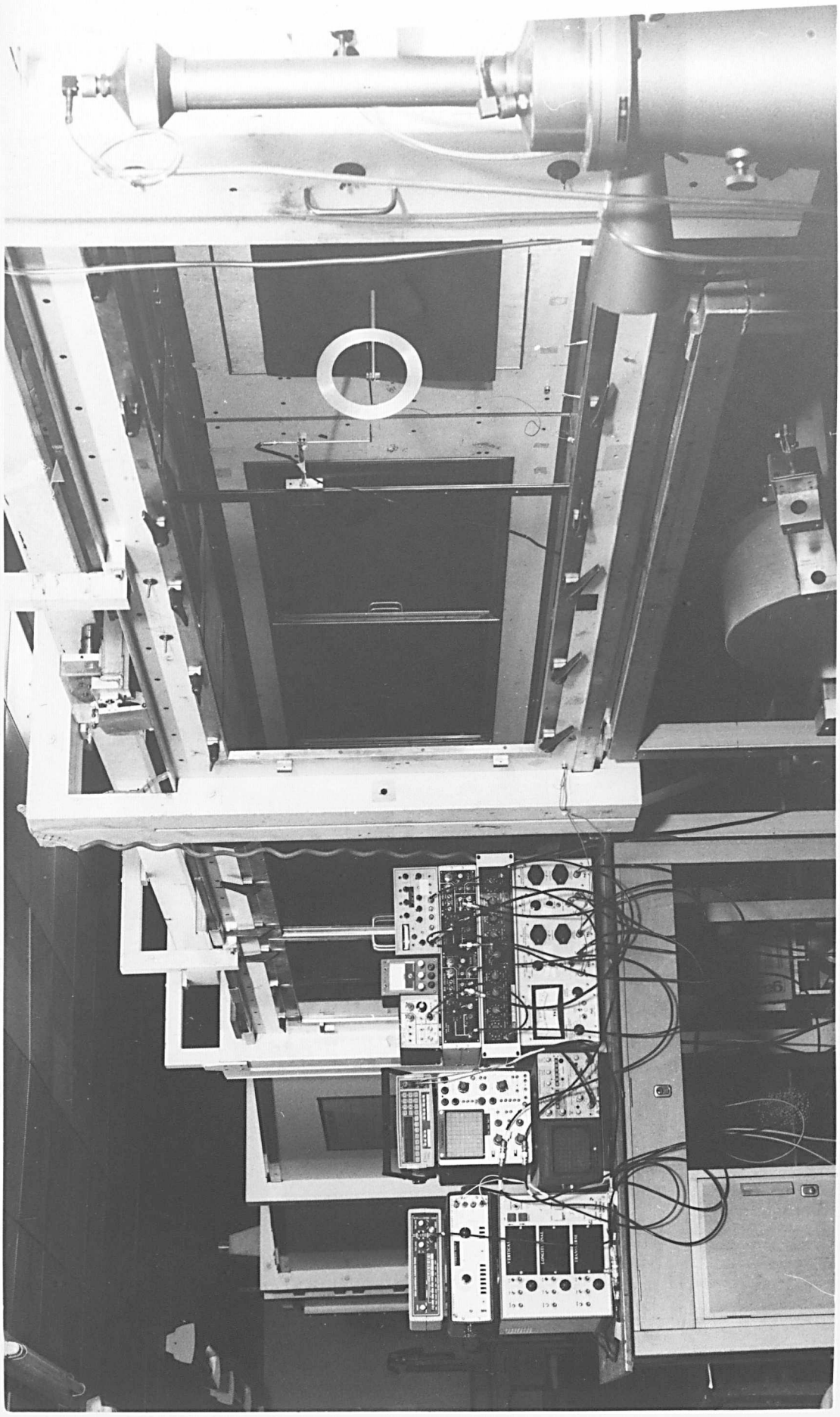


Photo 2.1 A ring suspended in a wind tunnel and an experimental apparatus

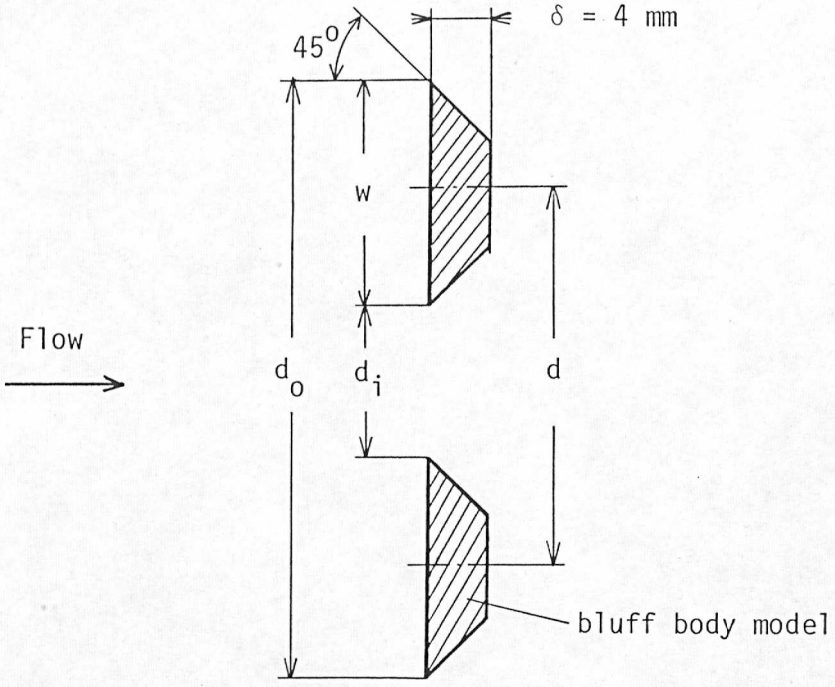



Figure 2.1(a) Cross-sectional view of a ring or two flat plates.

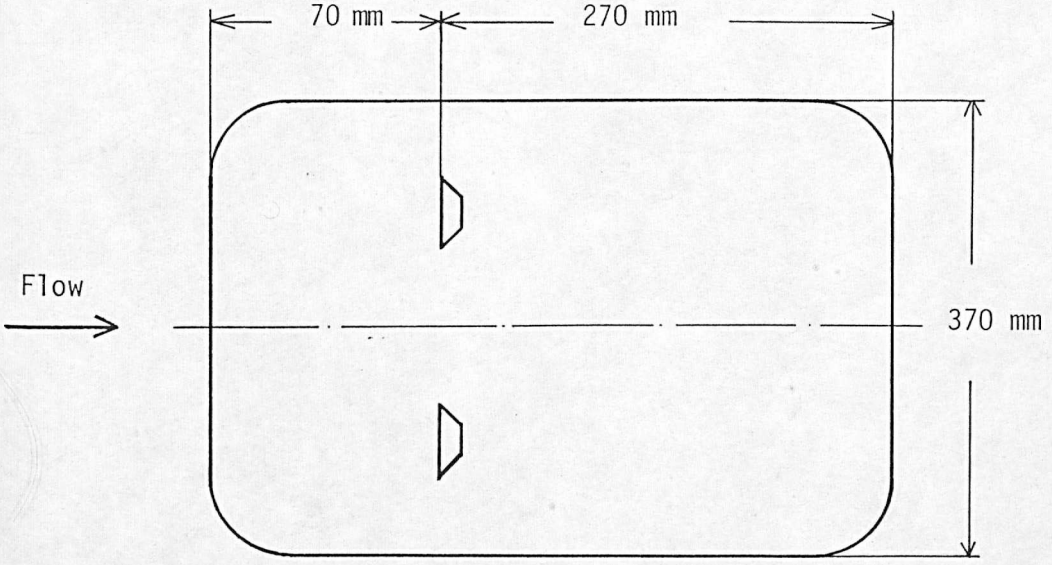



Figure 2.1(b) End plate for two flat plates

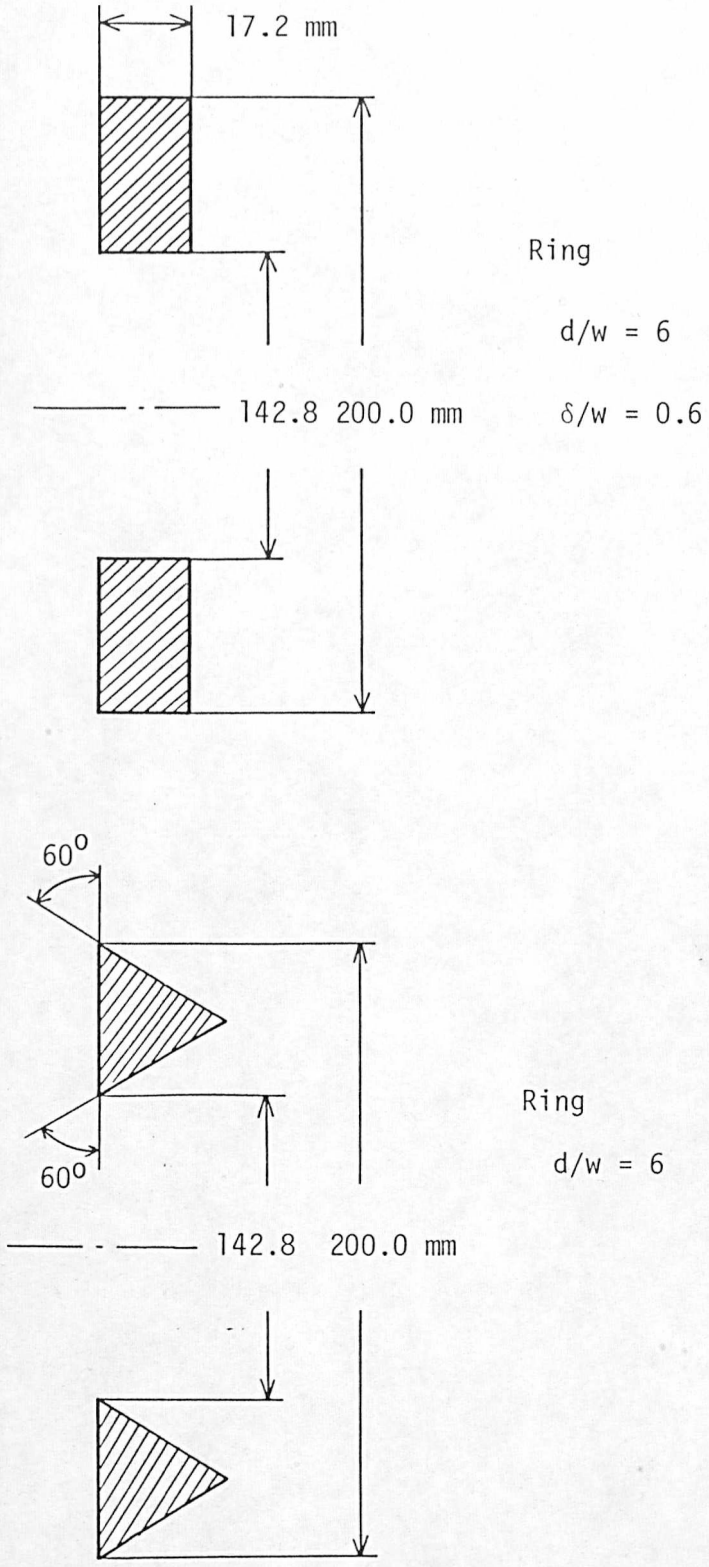



Figure 2.2 Special ring models with a rectangular and a triangle cross-section.

## 2.2 Wind tunnel and range of experimental conditions

Experiments were conducted in a low speed and low turbulence closed-return type wind tunnel, with a high quality stream in the 0.91 m x 0.91 m square test section. The root-mean-square turbulence intensity in the tunnel is about 0.03% and the variations in the velocity profile in the test section is about $\pm$0.5% (Clements and Unwin 1973). The velocity of the free stream, U, was measured by use of a Pitot-static tube and a Betz manometer. Two supports were used for hot-wire probes, one was fixed to the tunnel wall and the other mounted on the tunnel traverse gear, which is capable of describing a cube of side about 0.7 m.

All the measurements in the wind tunnel were carried out at U = 10 m/s, and this gave Reynolds numbers, $R_e$, based on w, between $1.3 \times 10^4$ and $6.8 \times 10^4$ for all the different sized bluff body models tested. Although it is preferable to make measurements at the same Reynolds number, the wakes of the models were highly turbulent and it is thought that the effects of $R_e$ were negligibly small in the above range.

## 2.3 Hot-wire data acquisition and reduction

The experimental work in the wind tunnel mostly involved the measurement of velocities by use of hot-wire anemometers. Two

single-wires were used for measurements of cross-correlations, one single-wire and one cross-wire were used for the conditional averaging of fluctuating velocities. DISA type 55D01 series and TSI model 1053B series constant temperature hot-wire anemometers were used. The single-sensor, DISA type 55P11, and the cross-sensors, PSI 6525 WO 5, had 5 micron platinum wire.

King's law was applied to analyse the hot-wire data (Bradshaw 1975).

$$E^2 = A_o + B_o u^n \tag{2.1}$$

where

$A_o, B_o$ : constant obtained by calibration

E : hot-wire output voltage when the probe wire is in the stream of velocity u

n : constant, usually 0.45

The single-wire was calibrated in a free stream of velocity U by using a Pitot-static tube. The probe wire was placed normal to a free stream and supposed to respond only to the velocity component normal to the probe wire. Then, the following relationship for velocity is found from eqn (2.1).

$$u^* = \frac{u}{U} = \left( \frac{E^2 - E_o^2}{E_R^2 - E_o^2} \right)^{\frac{1}{0.45}} \tag{2.2}$$

where

$u^*$ : non-dimensionalized velocity of u by U

$E_o$ : hot-wire output voltage at velocity 0 m/s

$E_R$ : hot-wire output voltage at velocity U

The calibration of cross-wires, which were placed at angle of about $\pm 45^o$ to a free stream was performed the same way. The following formulae for u, the velocity component in the free stream direction, and v, the normal component, are given by equations (2.3) and (2.4) when each wire is at $\pm 45^o$ to the stream.

$$u^* = \frac{1}{2}\left\{\left(\frac{E_1^2 - E_{01}^2}{E_{R1}^2 - E_{01}^2}\right)^{\frac{1}{0.45}} + \left(\frac{E_2^2 - E_{02}^2}{E_{R2}^2 - E_{02}^2}\right)^{\frac{1}{0.45}}\right\} \qquad (2.3)$$

$$v^* = \frac{1}{2}\left\{\left(\frac{E_1^2 - E_{01}^2}{E_{R1}^2 - E_{01}^2}\right)^{\frac{1}{0.45}} - \left(\frac{E_2^2 - E_{02}^2}{E_{R2}^2 - E_{02}^2}\right)^{\frac{1}{0.45}}\right\} \qquad (2.4)$$

where

$u^*$, $v^*$ : non-dimensional velocity of u,v

suffix 1,2 : wire No. of the cross-wires.

The fluctuating parts of the signals from the hot-wire anemometer outputs were fed to a magnetic tape recorder or a microcomputer. The time mean part of the signal was removed by adjusting the offsets of amplifiers. An EMI SELabs 3000 analogue tape recorder was used to record outputs simultaneously and later large scale data processing was performed on a mainframe computer. The linearity and zero drift of the recorder are within $\pm$0.3% and 0.5% respectively, and a flat frequency response up to $20/2^N$ KHz at a tape speed of $60/2^N$ inches per second (N=0,1,2, ...5). Therefore, recording and playback speeds were decided by considering vortex shedding frequencies and the Nyguist frequency of the digitizer. The microcomputer, a Commodore PET 2001-8, was used for on-line computation of the experimental data, such as cross-correlations, root-mean-square of fluctuating velocities. The microcomputer had an 8-bit MCS 6502 microprocessor, 14K ROM and 24K RAM. Machine language programs were developed which were capable of acquiring 3000 points simultaneously on 2-channels at the maximum sampling speed of about 6 KHz. A/D converters were used in conjunction with sample-and-hold amplifiers. The outline of this system is shown in Figure 2.3.

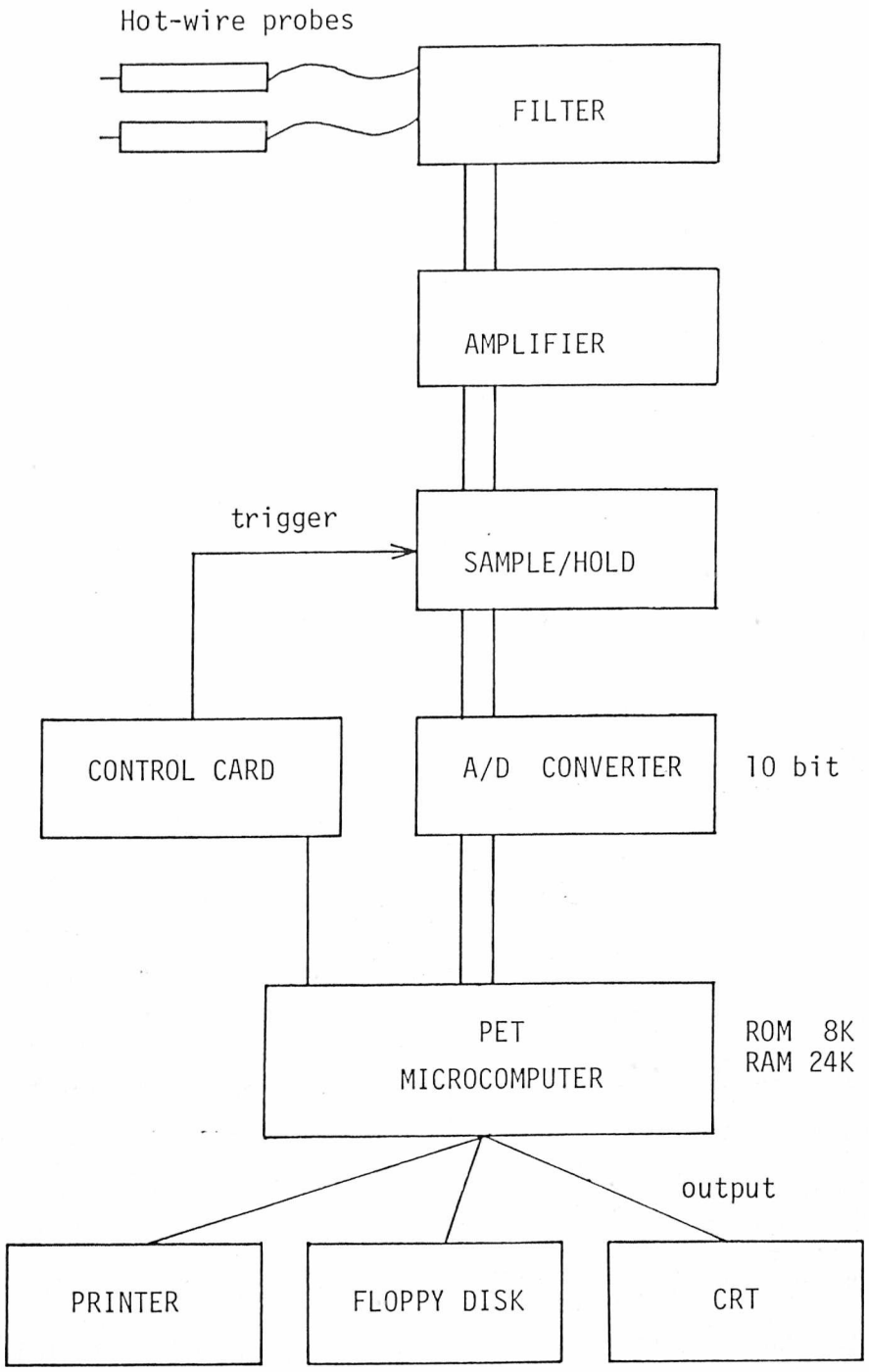



Figure 2.3 On-line data processing by microcomputer.

## 2.4 Data processing on a mainframe computer

Large quantities of hot-wire data recorded on analogue tapes were converted to digital tapes and analysed by a large computer CDC Cyber 855 or Cyber 170 in the Imperial College Computer Centre.

The high speed analogue-to-digital conversion system, developed in the Department of Aeronautics, (Bradshaw, 1984, Subramanian and Bradshaw, 1984), was one of the most powerful tools used in the experiments. The system can convert simultaneously up to 16 channels of ±5 volt range analogue data to 12-bit digital data, with an accuracy of 0.25% of full scale. The total sampling rate is up to 1175 samples per second, and the system writes on to a 9-track half-inch digital tape at the density of 1600 bpi. An Acorn/BBC Model B microcomputer used in the system, controlled the number of channels, the sampling rate and file marks. The output of the 12-bit Datel A/D converter went via the 8-bit parallel IEEE-488 bus to the Cipher 900X digital tape recorder in the system. The 12-bit A/D converter output was delivered to the tape recorder in two consecutive bytes, first the 8 most significant bits and second the 4 least significant bits with 4 null trailings. The data were written in blocks on the digital tape, so that the CDC machine could read a block of data at a time and the maximum block length allowed was 2048 bytes, i.e. 1024 samples.

Once a block of data was read into the core locations of the CDC machine, retrieval and analysis of the data were carried out by Fortran programs. Since the CDC machine's 60-bit word length contained 3 and 3/4 16-bit data samples, 4 words were unpacked at a time, i.e. 15 data samples, by use of a software masking. Unpacked data were recovered to voltage values and then velocity data were reduced using the calibration formulae together, the amplitude and the offsets of the recorded data. An example of the processing for 3-channels of hot-wire data is shown schematically in Figure 2.4 and Figure 2.5.

## 2.5 Conditional averaging

It is known that vortices shed from a bluff body fairly regularly even at high Reynolds numbers. However, the instantaneous velocity field within the wake is highly turbulent because of the superposition of the random velocity fluctuations generated in strong shear layers. Statistic characteristics of the turbulence can be extracted by processing a large quantity of data if a certain periodical phenomenon is buried in the random noise. The conditional averaging technique was used in the present experiments to recover vortex shedding velocities from fluctuating velocities measured in a bluff body wake by hot-wire anemometers. Note that the same result cannot be obtained by using a band-pass filter set at the vortex shedding frequency, because random noise at the vortex shedding frequency band cannot be removed. Also the

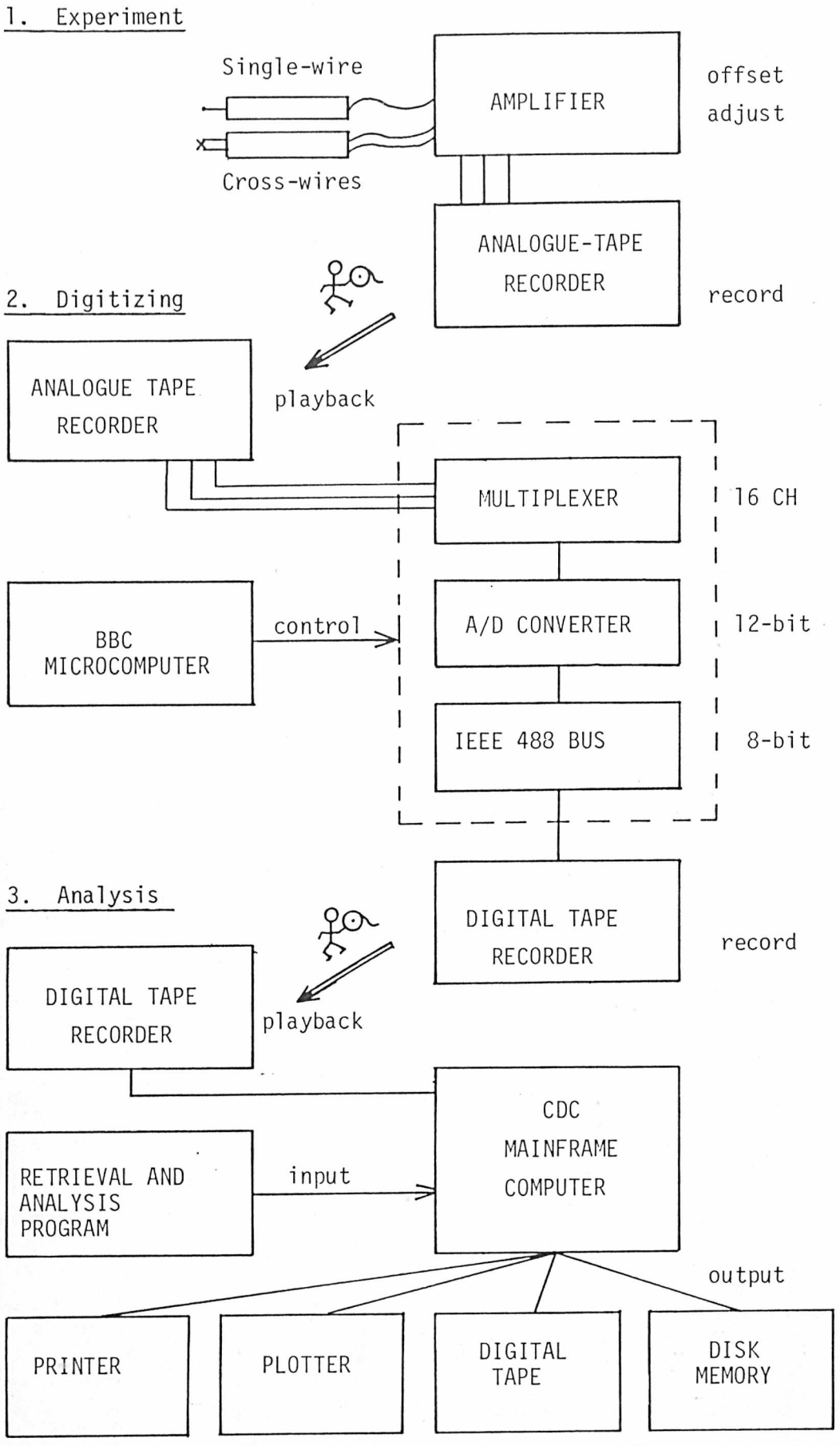



Figure 2.4 Schematic diagram of data processing

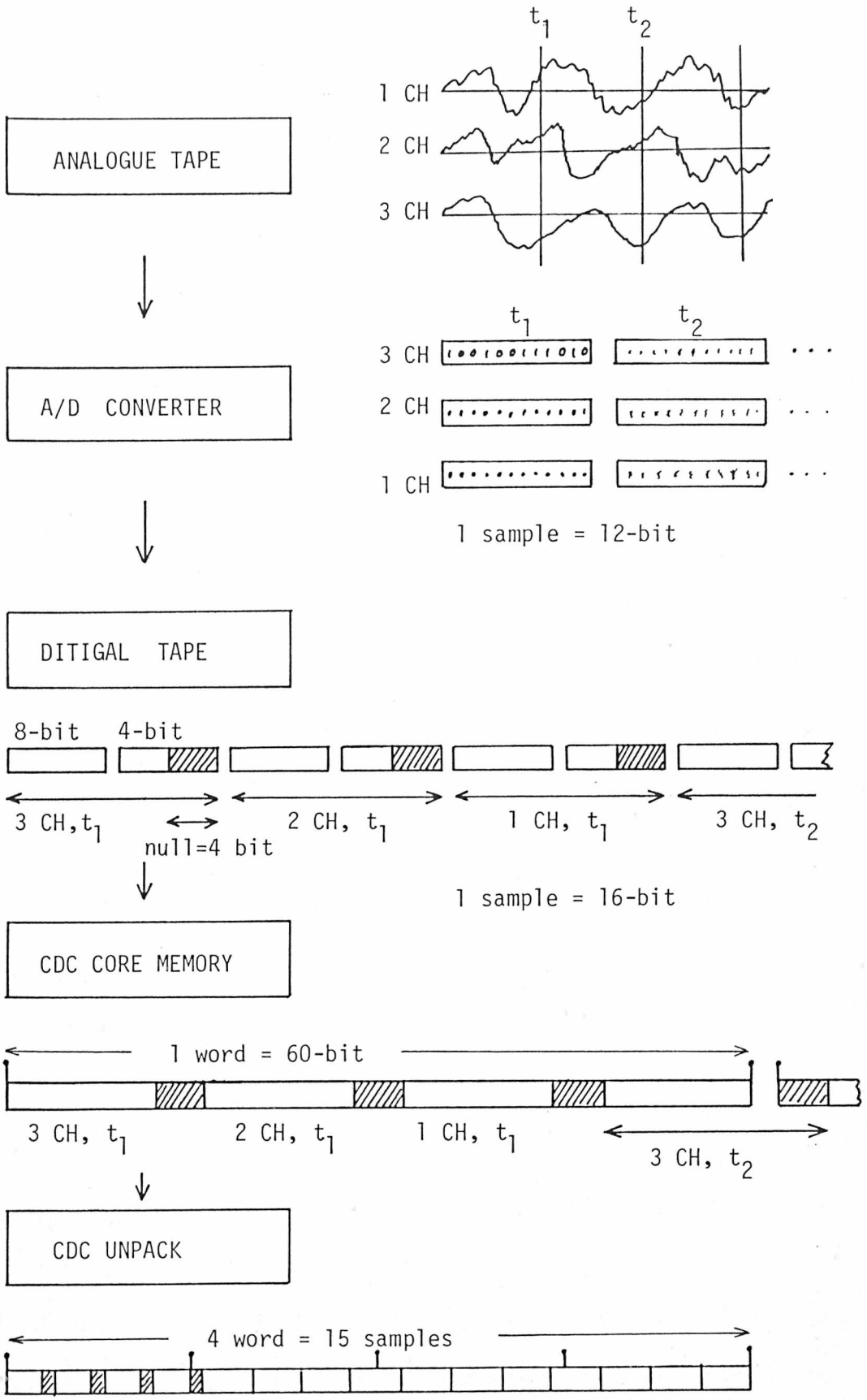



Figure 2.5 Schematic diagram of data length

first harmonic of the vortex shedding frequency, which is detected around the centre of the wake will be excluded.

Three channels of velocity fluctuations were simultaneously sampled; two channels, u and v , measured by the cross-wires were conditionally averaged and the third channel, reference velocity fluctuation measured by the single-wire, was used for control of conditioning. Since the mean of random fluctuations is expected to be zero, a large number of u and v samples, corresponding to the same phase within the vortex shedding cycle, were averaged so that the effect of random fluctuations was eliminated from the averaged velocity fluctuations of the vortex shedding cycle. The single-wire probe was placed in a turbulence-free area outside the wake to sense the phase of the vortex shedding cycle, and the maxima of the reference signal were used as trigger points for each vortex shedding cycle. The exact maximum points were estimated by fitting a second order polynomial equation to the samples around the maximum point to achieve the least-square-error, because small random fluctuations were sometimes contained in the reference signal. The u and v fluctuations were excluded from the conditional averaging when the period between two consecutive trigger points did not coincide with the expected vortex shedding cycle. This occurred because the single-wire probe sometimes encountered a large scale turbulent eddy which gave rise to false trigger points of the vortex shedding cycle. Although velocity fluctuations were stored and

conditionally averaged over three consecutive vortex shedding cycles, only the middle two-thirds were actually used for the calculation of vorticity profile, as the ends of the averaged records were less accurate because of slight variations in the period of the vortex shedding cycle. The structure of the conditional averaging program is shown in Figure 2.6. About $5 \times 10^7$ data samples, which were obtained in one series of measurements at a plane behind a bluff body, were processed in several computer runs.

## 2.6 Vorticity calculation

The cross-wires were traversed through the wake at a fixed downstream position. The distribution of conditionally averaged u, v velocity fluctuations of 3 vortex shedding cycles were calculated in the (t,y) plane at a given x position downstream of the bluff body, where y is a distance in the direction normal to the x-direction and t is time. The vorticity, $\omega$, in the (x,y) plane is defined as

$$\omega(x,y,t) = \frac{\partial v}{\partial x} - \frac{\partial u}{\partial y} \tag{2.5}$$

and it is assumed that $\frac{\partial v}{\partial x}$ can be calculated from the flow in the (t,y) plane by using the relation

$$\frac{\partial v}{\partial x} = -\frac{\partial v}{\partial t} \cdot \frac{\partial t}{\partial x} = -\frac{\partial v}{\partial t} \cdot \frac{1}{u} \tag{2.6}$$

The validity of this relation is discussed in Appendix D.

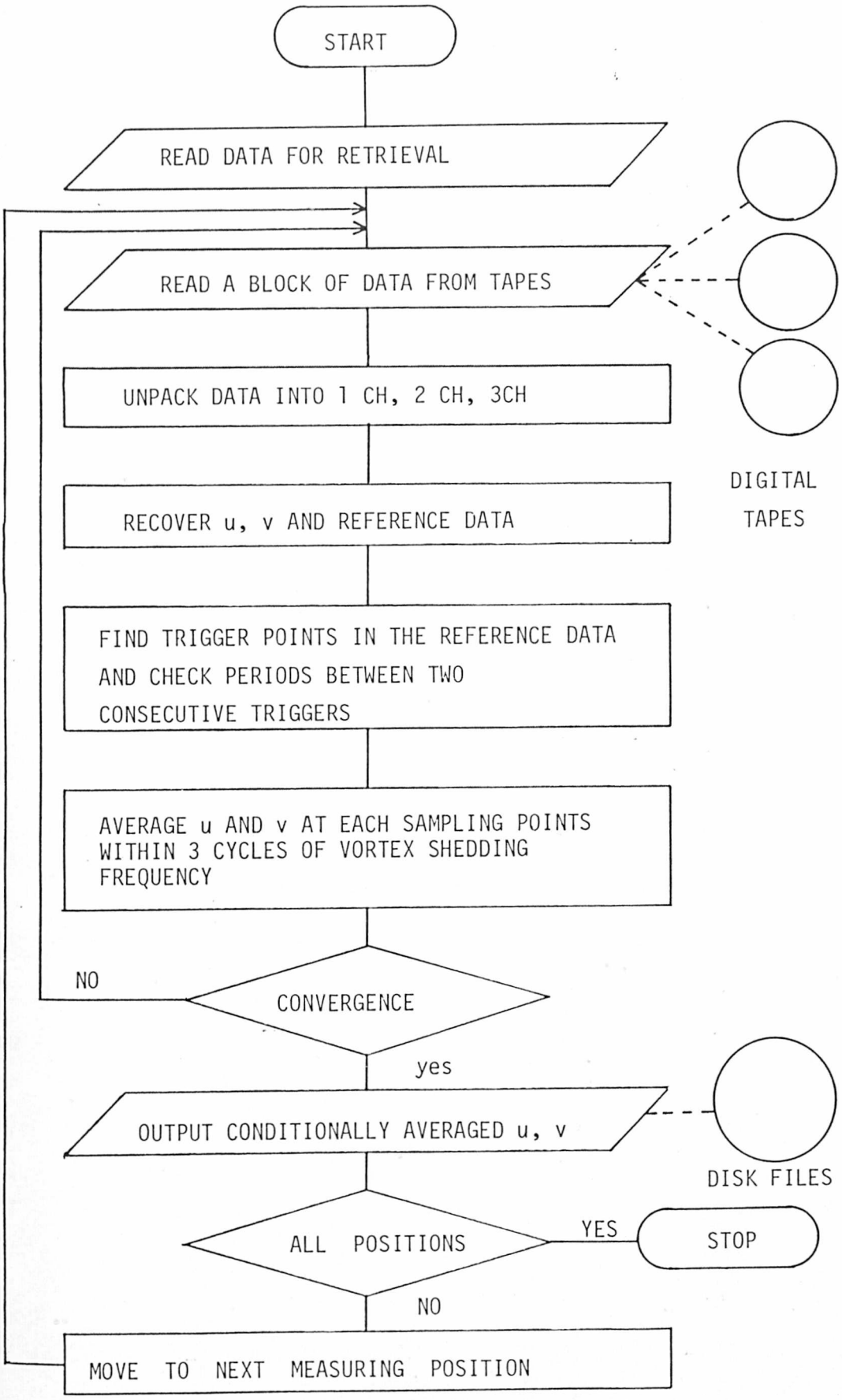



Figure 2.6 Flow chart of conditional averaging program

Let $\omega_{ij}$, $u_{ij}$ and $v_{ij}$ represent $\omega$ and samples of conditionally averaged $u$, $v$ velocities at $(t,y) = (t_i, y_j)$ respectively, as shown in Figure 2.7, then equation (2.5) becomes

$$\omega_{ij} = -\frac{v_{ij} - v_{i-1j}}{\Delta t\, u_{ij}} - \frac{u_{ij} - u_{ij-1}}{\Delta y} \tag{2.7}$$

where $\Delta t$ and $\Delta y$ are the sampling intervals of $t$ and $y$ respectively. The conditionally averaged $u$, $v$ velocities still contained a small random fluctuationand this could give rise to a considerable fluctuation in the differencing calculation of equation (2.7) because of the small sampling steps, hence $\omega_{ij}$ was calculated indirectly.

First, $u$, $v$ in the $(t,y)$ plane were regionally approximated by the following second order polynomial equations.

$$u(t,y) = \alpha_1 t^2 + \alpha_2 ty + \alpha_3 y^2 + \alpha_4 t + \alpha_5 y + \alpha_6 \tag{2.8}$$

$$v(t,y) = \beta_1 t^2 + \beta_2 ty + \beta_3 y^2 + \beta_4 t + \beta_5 y + \beta_6 \tag{2.9}$$

Then, the vorticity is given from equations (2.5), (2.6), (2.8) and (2.9) as follows

$$\omega = -\frac{1}{u}\ (2\beta_1 t + \beta_2 y + \beta_4) - (\alpha_2 t + 2\alpha_3 y + \alpha_5) \qquad (2.10)$$

Here, the parameters $\alpha_i$, $\beta_i$ were determined from the approximations of the equations (2.8) and (2.9) by the least-square-error method. The region of the approximations consisted of 25 samples each of $u_{ij}$, $v_{ij}$ (i:i-2$\sim$i+2, j:j-2$\sim$j+2), i.e. the centre and the surrounding 24 samples as shown in Figure 2.7. The region was swept through all the samples in turn.

The square errors were given by

$$\begin{aligned} e_u^2 = &\left(\alpha_1 t_{i-2}^2 + \alpha_2 t_{i-2} y_{j-2}^2 + \alpha_3 t_{j-2}^2 + \alpha_4 t_{i-2}\right. \\ &\left. + \alpha_5 y_{j-2} + \alpha_6 - u_{i-2,j-2}\right)^2 \\ &+ \cdots \\ &+ \left(\alpha_1 t_{i+2}^2 + \alpha_2 t_{i+2} y_{j+2} + \alpha_3 y_{y+2}^2 + \alpha_4 t_{i+2}\right. \\ &\left. + \alpha_5 y_{j+2} + \alpha_6 - u_{i+2,j+2}\right)^2 \end{aligned} \qquad (2.11)$$

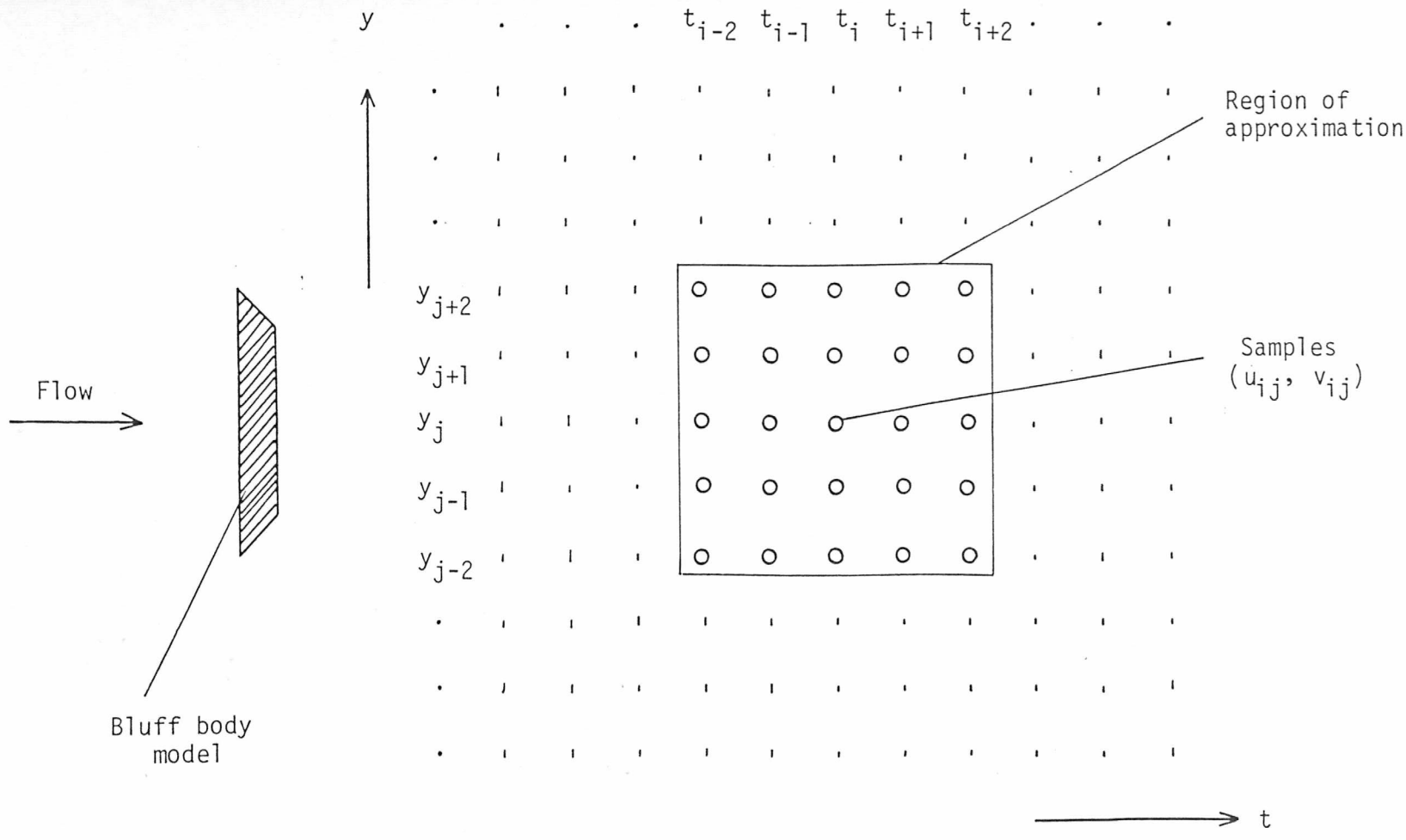



Figure 2.7 Samples of conditionally averaged u, v in the (t, y) plane and region of approximation

$$e_v^2 = \left(\beta_1 t_{i-2}^2 + \beta_2 t_{i-2} y_{j-2} + \beta_3 y_{j-2}^2 + \beta_4 t_{i-2} + \beta_5 y_{j-2} + \beta_6 - v_{i-2,j-2}\right)^2$$

$$+ \ \ldots$$

$$+ \left(\beta_1 t_{i+2}^2 + \beta_2 t_{i+2} y_{j+2} + \beta_3 y_{j+2}^2 + \beta_4 t_{i+2} + \beta_5 y_{j+2} + \beta_6 - v_{i+2,j+2}\right)^2 \qquad (2.12)$$

and from

$$\frac{\partial e_u^2}{\partial \alpha_i} = 0, \quad \frac{\partial e_v^2}{\partial \beta_j} = 0 \ (i,j = 1 \sim 6) \qquad (2.13)$$

next equations (2.14) and (2.15) were obtained.

$$X \cdot A = Zu \quad , \quad X \cdot B = Zv \qquad (2.14)$$

$$\therefore \ A = X^{-1} \ Zu \quad , \quad B = X^{-1} \ Zv \qquad (2.15)$$

where

$$A = \begin{pmatrix} \alpha_1 \\ \alpha_2 \\ \cdot \\ \cdot \\ \cdot \\ \alpha_6 \end{pmatrix} \qquad B = \begin{pmatrix} \beta_1 \\ \beta_2 \\ \cdot \\ \cdot \\ \cdot \\ \beta_6 \end{pmatrix} \tag{2.16}$$

$$Z_u = \begin{pmatrix} \sum\sum t^2u \\ \sum\sum t\ y\ u \\ \sum\sum y^2u \\ \sum\sum t\ u \\ \sum\sum y\ u \\ \sum\sum\ u \end{pmatrix} \qquad Z_v = \begin{pmatrix} \sum\sum t^2v \\ \sum\sum t\ y\ v \\ \sum\sum y^2v \\ \sum\sum t\ v \\ \sum\sum y\ v \\ \sum\sum\ u \end{pmatrix} \tag{2.17}$$

$$X = \begin{pmatrix} \sum\sum t^4 & \sum\sum t^3y & \sum\sum t^2y^2 & \sum\sum t^3 & \sum\sum t^2y & \sum\sum t^2 \\ \sum\sum t^3y & \sum\sum t^2y^2 & \sum\sum ty^3 & \sum\sum t^2y & \sum\sum ty^2 & \sum\sum ty \\ \sum\sum t^2y^2 & \sum\sum ty^3 & \sum\sum y^4 & \sum\sum ty^2 & \sum\sum y^3 & \sum\sum y^2 \\ \sum\sum t^3 & \sum\sum t^2y & \sum\sum ty^2 & \sum\sum t^2 & \sum\sum ty & \sum\sum t \\ \sum\sum t^2y & \sum\sum ty^2 & \sum\sum y^3 & \sum\sum ty & \sum\sum y^2 & \sum\sum y \\ \sum\sum t^2 & \sum\sum ty & \sum\sum y^2 & \sum\sum t & \sum\sum y & \sum\sum 1 \end{pmatrix} \tag{2.18}$$

and the symbol $\sum\sum$ in the equations (2.17) and (2.18) denote that

$$\sum\sum t^k y^\ell u^m = \sum_{h=j-2}^{j+2} \sum_{n=i-2}^{i+2} t_n^k \, y_h^\ell \, u_{nh}^m \tag{2.19}$$

Finally, the approximated vorticity at the centre of the region was given from equations (2.10) and (2.15) as follows

$$\alpha_{ij} = \left( \frac{2\beta_1}{u_{ij}} - \alpha_2 \right) t_i + \left( \frac{\beta_2}{u_{ij}} - 2\alpha_3 \right) y_j$$

$$+ \frac{\beta_4}{u_{ij}} - \alpha_5 \tag{2.20}$$

The flow chart of the vorticity calculation program is shown in Figure 2.8.

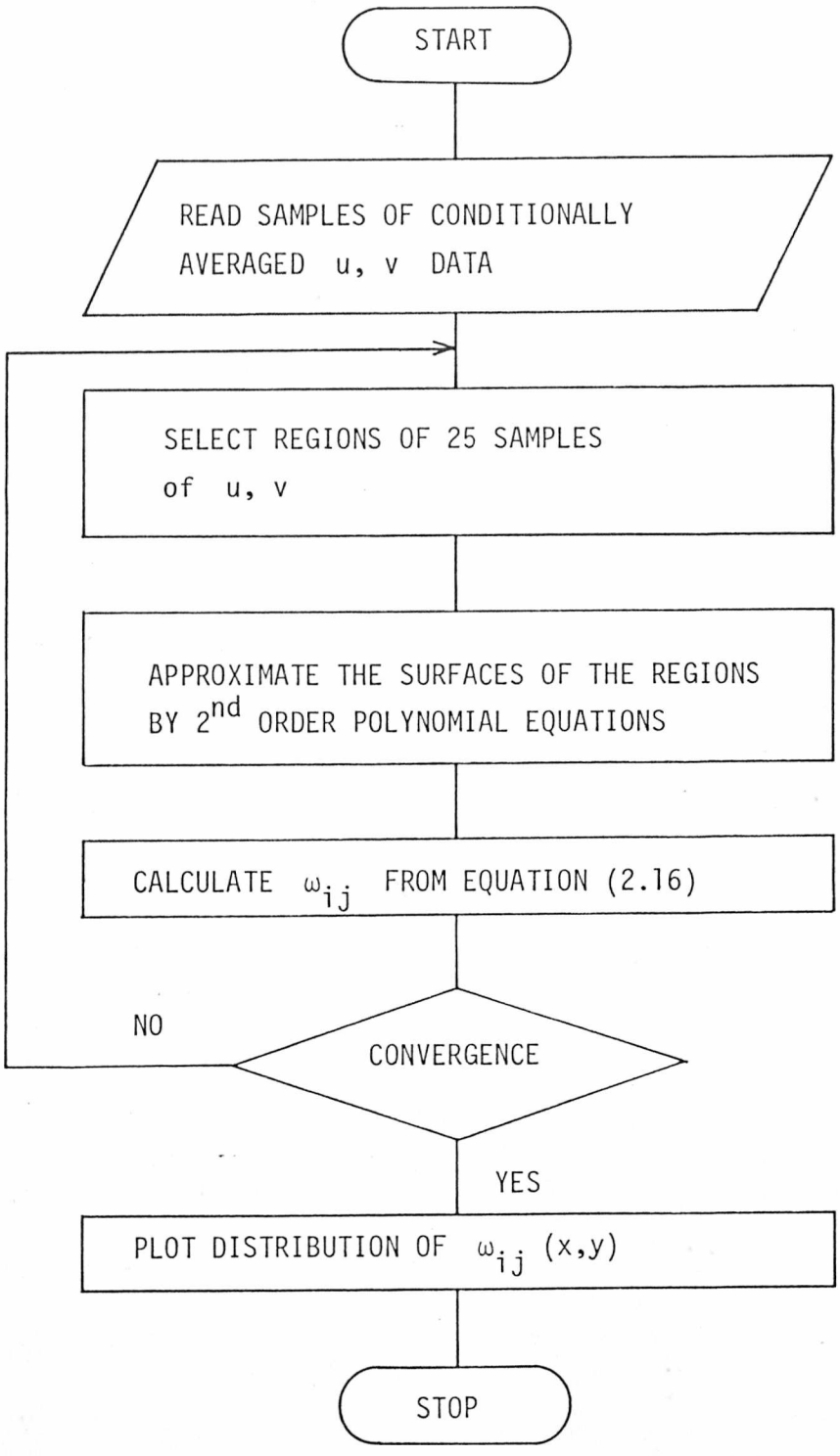



Figure 2.8 Flow chart of vorticity calculation program

## 2.7 Spectral density function and coherence function

The complex cross-spectral functions were calculated from $U_x(t)$ and $U_y(t)$, velocity fluctuations measured by two single-wires in the wake of a bluff body model. The power spectral density function, $S_{xx}(f)$, is defined (Bendat and Piersol 1971) such that

$$S_{xx}(f) = \frac{1}{\sigma_x^2} \lim_{\Delta f \to 0} \left(\frac{1}{\Delta f}\right) \left[ \lim_{T\to\infty} \frac{1}{T} \int_0^T U_x^2(t,f,\Delta f)\, dt \right] \tag{2.21}$$

where $U_x(t,f,\Delta f)$ is the portion of $U_x(t)$ in the frequency range from $f$ to $f+\Delta f$, and

$$\sigma_x^2 = \lim_{T\to\infty} \frac{1}{T} \int_0^T U_x^2(t)\, dt \tag{2.22}$$

It is also given via the Fourier transform of $U_x(t)$.

$$S_{xx}(f) = \frac{1}{\sigma_x^2} \lim_{T\to\infty} \left[ \frac{1}{T} \int_0^T U_x(t)\exp(2\pi i f t)dt \int_0^T U_x(t)\exp(-2\pi i f t)dt \right] \tag{2.23}$$

The cross-spectral density function, $S_{xy}(f)$, is given in the same way.

$$S_{xy}(f)= \frac{1}{\sigma_x \sigma_y} \left( \lim_{T\to\infty} \frac{1}{T_o} \int_o^T U_x(t)\exp(2\pi i f t)dt \int_o^T U_y(t)\exp(-2\pi i f t)dt \right) \tag{2.24}$$

The cross-spectral density function is generally complex such that

$$S_{xy}(f) = P_{xy}(f) - iQ_{xy}(f) \tag{2.25}$$

where the real part, $P_{xy}(f)$, is called the coincident spectral density function and imaginary part, $Q_{xy}(f)$, is called the quadrature spectral density function. The coherence function, $\gamma_{xy}(f)$, and phase angle $\theta_{xy}(f)$, between $U_x(t)$ and $U_y(t)$ at f are defined by

$$\gamma^2_{xy}(f) = \frac{|S_{xy}(f)|^2}{S_{xx}(f).S_{yy}(f)} \tag{2.26}$$

$$\theta_{xy}(f) = \tan^{-1}\left[\frac{Q_{xy}(f)}{P_{xy}(f)}\right] \qquad (2.27)$$

These functions were calculated by the mainframe computer, but exact calculation was not possible, since samples of $U_x(t)$ and $U_y(t)$ existed only in a finite interval of T. However, practical approximations could be obtained by FFT and the main part of the program used for this calculation in the present study was developed by Davies (1975).

# CHAPTER THREE

## EXPERIMENTAL RESULTS

The main objective of the experiments was to study the structure of the vortex wakes of rings and to compare them with those of a circular disk and two flat plates in side-by-side arrangements. Measurements were carried out in the wind tunnel at Reynolds numbers of the order of $10^4$ which are large enough to ensure a fully turbulent wake. The conditional averaging technique is employed to obtain vorticity profiles in the wakes from 3.4 w to 16.0 w downstream of the bluff bodies. The measurements are not corrected for the effect of wind tunnel blockage unless otherwise stated. This chapter describes the experimental results together with some discussion.

### 3.1 Wake structure of rings

Ring models of various shapes were tested. The ratio d/w is chosen as the non-dimensional parameter to specify the shapes of the ring models instead of solidity. This parameter is also applied to denote the spacing of the two flat plates model in side-by-side arrangements. Surface pressures on the models and the correlations of velocity fluctuations in the wakes were measured.

Considerable effort was concentrated on making measurements of vorticity profiles in the wakes. First, thin sharp-edged cross-section ring models and then special ring models are examined in this section. The coordinate system (x,y) used here has its origin at the centre of the models.

### 3.1.1 Measurements of base pressure and drag

The ring models were carefully aligned normal to the free stream direction by adjusting the piano wires supporting the models. Three tappings of 0.5 mm diameter were placed on the base of the model at equal angular separation. The pressure readings at the tappings, which were almost equal, were averaged. Several tappings of the same diameter were also placed on the front face of the models to measure pressure distributions in the radial direction. The pressure measurements were made for the thin sharp-edged cross-section ring models with d/w = 4 to 10 and the geometric blockage of the models varied from 1.2% to 2.4%. These blockage area ratios are not large, but Maskell (1963) has pointed out the effect of wind tunnel blockage is generally greater for a three-dimensional body than for a two-dimensional one. Therefore, the pressure measurements were corrected for the effect of blockage, and Maskell's formulae used for correction are shown in Appendix A. For the pressure measurements the rings were supported by wires from three 80 cm long tubes of 3 mm diameter which projected from the rear of the ring. These tubes transmitted the pressures to a manometer.

Figure 3.1.1 shows measurements of the base pressure coefficient, $C_{pb}$ and corrected $C_{pb}$ plotted against the ratio d/w for $R_e = 1.3 \times 10^4 - 2.9 \times 10^4$. Measurements for a solid circular disk, i.e. d/w = 1, at $R_e = 6 \times 10^5$ by Fail et al. (1957) is also shown in the figure. The variation of $C_{pb}$ with d/w can be broadly divided into three regions: (i) region where $C_{pb}$ gradually decreases with d/w from the $C_{pb}$ of a solid circular disk at the lower end of the d/w range, (ii) region where $C_{pb}$ rapidly decreases with increasing d/w and (iii) region at the high end of the d/w range investigated, where $C_{pb}$ is a little greater than that of a two-dimensional flat plate, which is -1.24 according to Davies (1975) and Donoso (1980). Presumably $C_{pb}$ must return to the two-dimensional value as $d/w \to \infty$.

Figure 3.1.2 shows measurements of pressure coefficient, $C_p$, distributions across the front surface, where $\xi$ denotes non-dimensionalised distance in the radial direction from the inside edge of the ring model, i.e. $\xi = 0$ at the inside edge and $\xi = 1$ at the outside edge. The stagnation line is seen to move towards the inside edge as the ratio d/w decreases. Figure 3.1.3 shows the $C_p$ distribution across the front surface, at centre span, of one of two flat plates arranged side-by-side normal to a free stream, reproduced from Andreopoulos (1972). The stagnation line on the ring model is located more towards the inside edge compared with the two flat plates model.

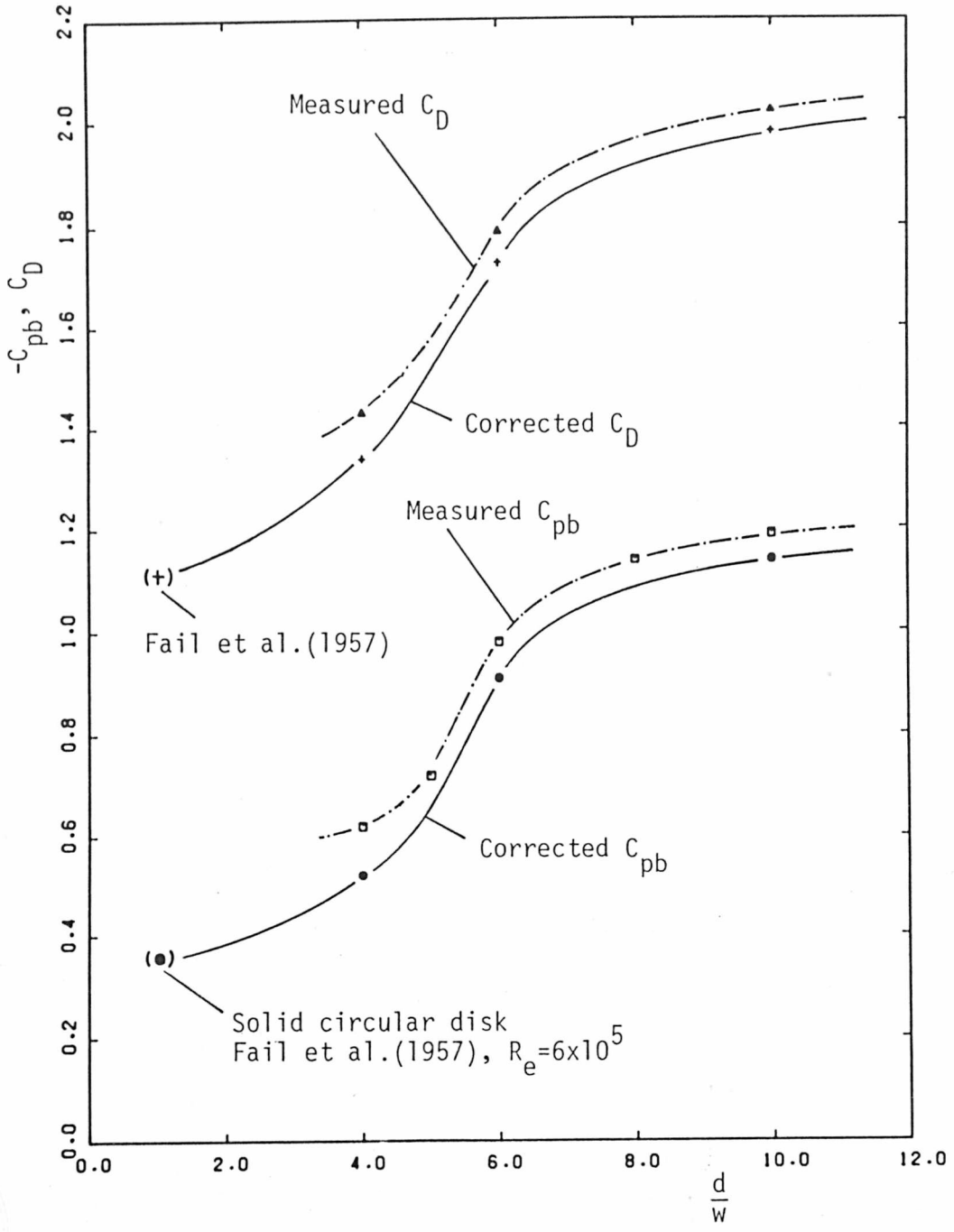



Figure 3.1.1 Base pressure coefficients and drag coefficient of thin sharp-edged cross-section ring models, $R_e = 1.3 \times 10^4 - 2.9 \times 10^4$.

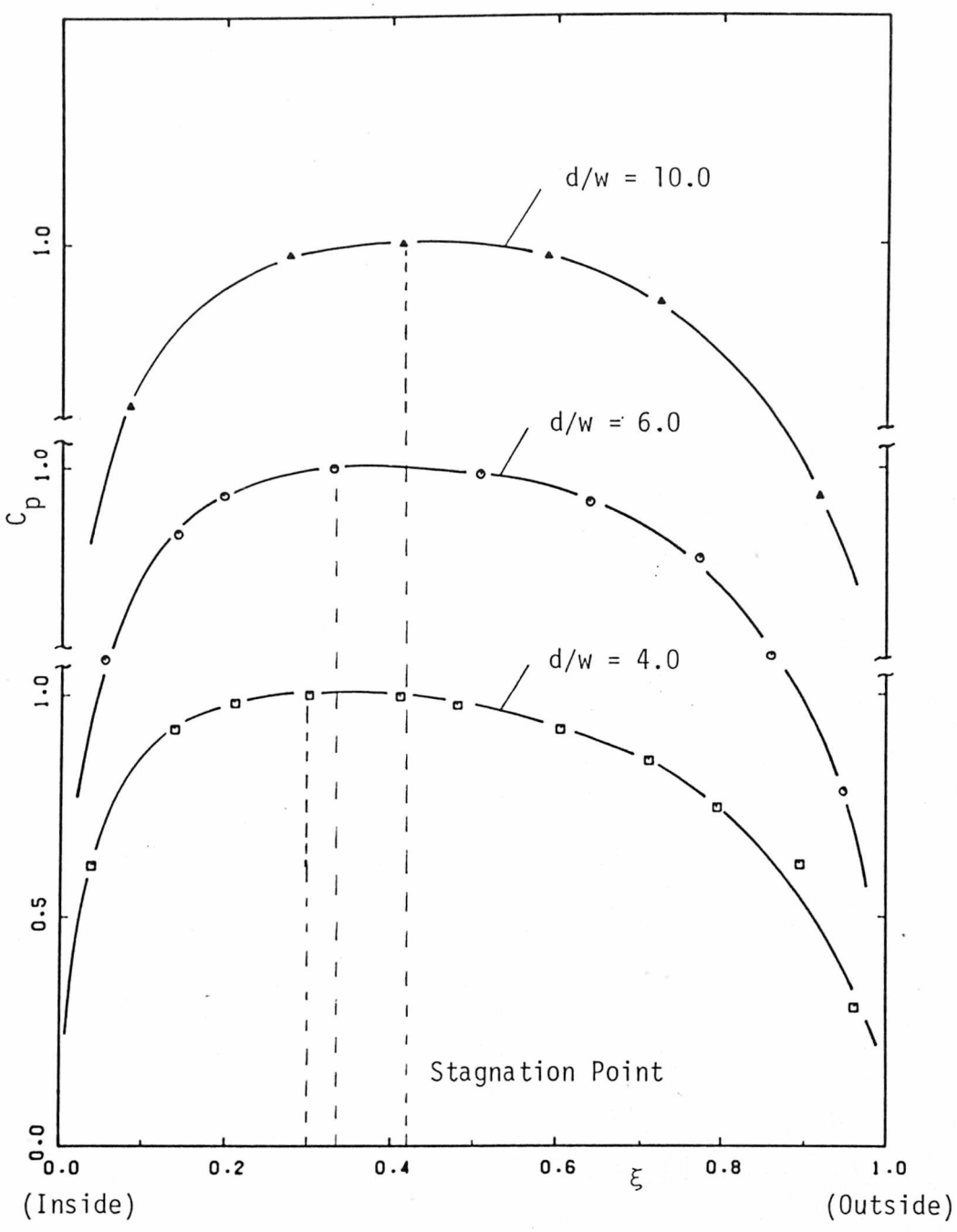
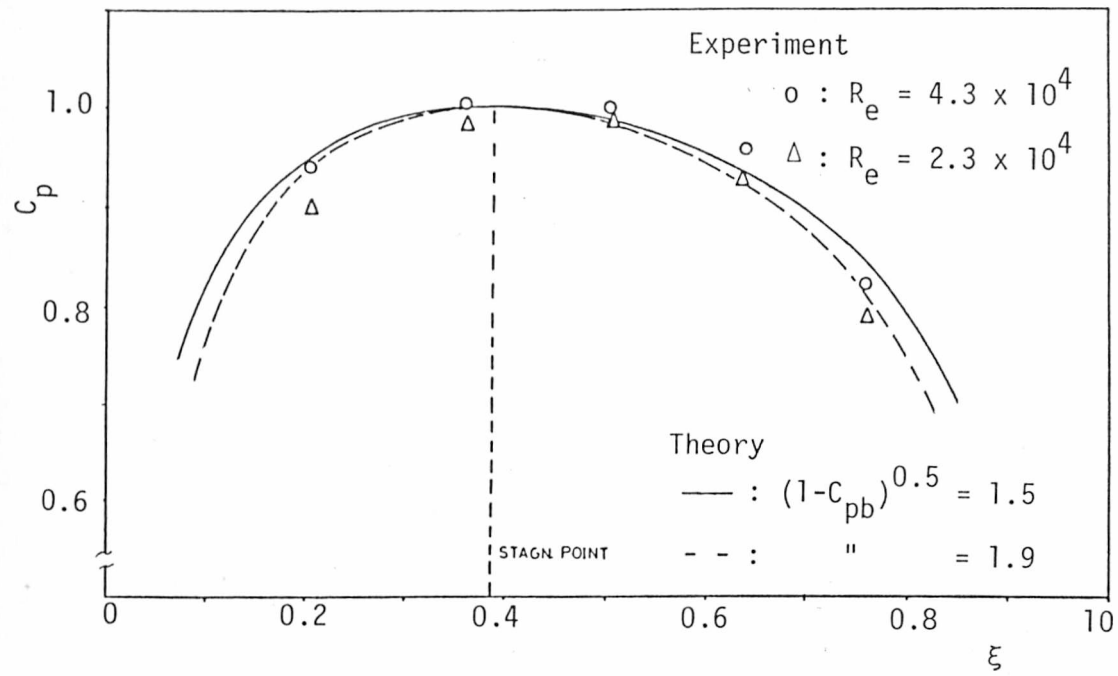
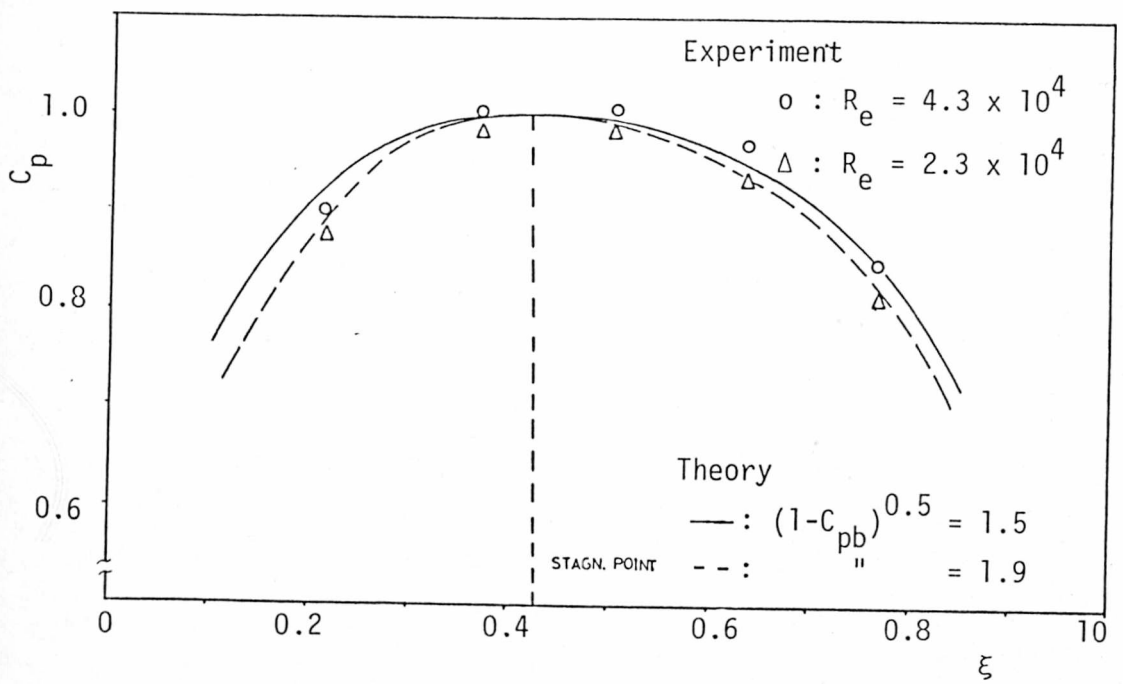



Figure 3.1.2 Pressure coefficient profiles of a front surface of thin sharp-edged cross-section ring models, $R_e = 1.3 \times 10^4 - 2.9 \times 10^4$.




(a) d/w = 3.5




(b) d/w = 7.1

Figure 3.1.3 Pressure coefficient profiles of a front surface of two flat plates in side-by-side arrangements, reproduced from Andreopoulos (1972). Theory; calculated by using the elliptic hodograph method.

The drag coefficients for the rings, $C_D$, are roughly estimated from the $C_p$ distributions, though the number of tappings are not sufficient to make a very accurate integration. The measured $C_D$ and the corrected $C_D$ are shown in Figure 3.1.1. It is found that the higher drag is a direct result of the lower suction on the base as usual, and the drag on only the front face part, i.e. $C_D + C_{pb}$, is independent of the ratio d/w. The front face drag coefficient contribution is about 0.8 for all the models, and is similar to the equivalent two-dimensional case.

### 3.1.2 Measurements of correlation and vortex shedding frequency

The axisymmetry of the shed vortex structures was investigated by measuring the degree of correlation of velocity fluctuations behind the ring models. The correlation measurements were made between the unfiltered outputs of two single hot-wires located outside the wake at angular separation, $\theta$, and at the same radial displacement, on a plane normal to the axis of symmetry. The hot-wires had to be positioned close to the edge of the wake where the turbulent shear layer does not convect over the probes. Therefore, it was decided to measure the correlation at the radial and axial position where maximum correlation can be obtained. The position found by trial and error was around $x = 3.4\ w$ and $y = d_o + 2.6\ w$, i.e. 3.4 w downstream of the model and 2.6 w outside the outside edge of the ring model.

The results of measurements for the thin sharp-edged cross-section ring models with d/w = 4.0 to 10.0 are shown plotted in Figure 3.1.4 as correlation coefficients, $\varepsilon_{xy}$, against $\theta$. All the models show a steady decrease of correlation with increasing separation up to around $\theta = 80^{o}$, and then a gradual decrease up to $\theta = 180^{o}$. It is generally understood that an unsteady cell-like vortex shedding structure can have a positive contribution to the correlation at small separations, which may then decrease rapidly with increasing separation. However, the correlation at large separations, $\theta \approx 180^{o}$, is mainly due to coherent vortex ring structures. There exists a marked sudden change of the correlation curves between d/w = 4.5 and d/w = 5.0, which suggests a structural change of the wakes of the models. The correlations for d/w = 5.0 and d/w = 6.0 are highest for all the models at the maximum separation, i.e. $\theta = 180^{o}$. The correlation for d/w = 4.0 is very low at large separations, but is still positive.

The average value of $\varepsilon_{xy}$ over the range $\theta = 0^{o}$ to $\theta = 180^{o}$ is shown in Figure 3.1.5. Figure 3.1.6 shows the $\varepsilon_{xy}$ replotted along a spanwise separation distance, i.e. a circumferential distance measured as if along the mean circumference of the ring model and non-dimensionalised by w. Although the correlation versus $\theta$ of d/w = 5.0 is highest in Figure 3.1.5, it is found that the replotted $\varepsilon_{xy}$ versus spanwise separation of d/w = 5.0 and d/w = 6.0 lie on the same curve. The correlation

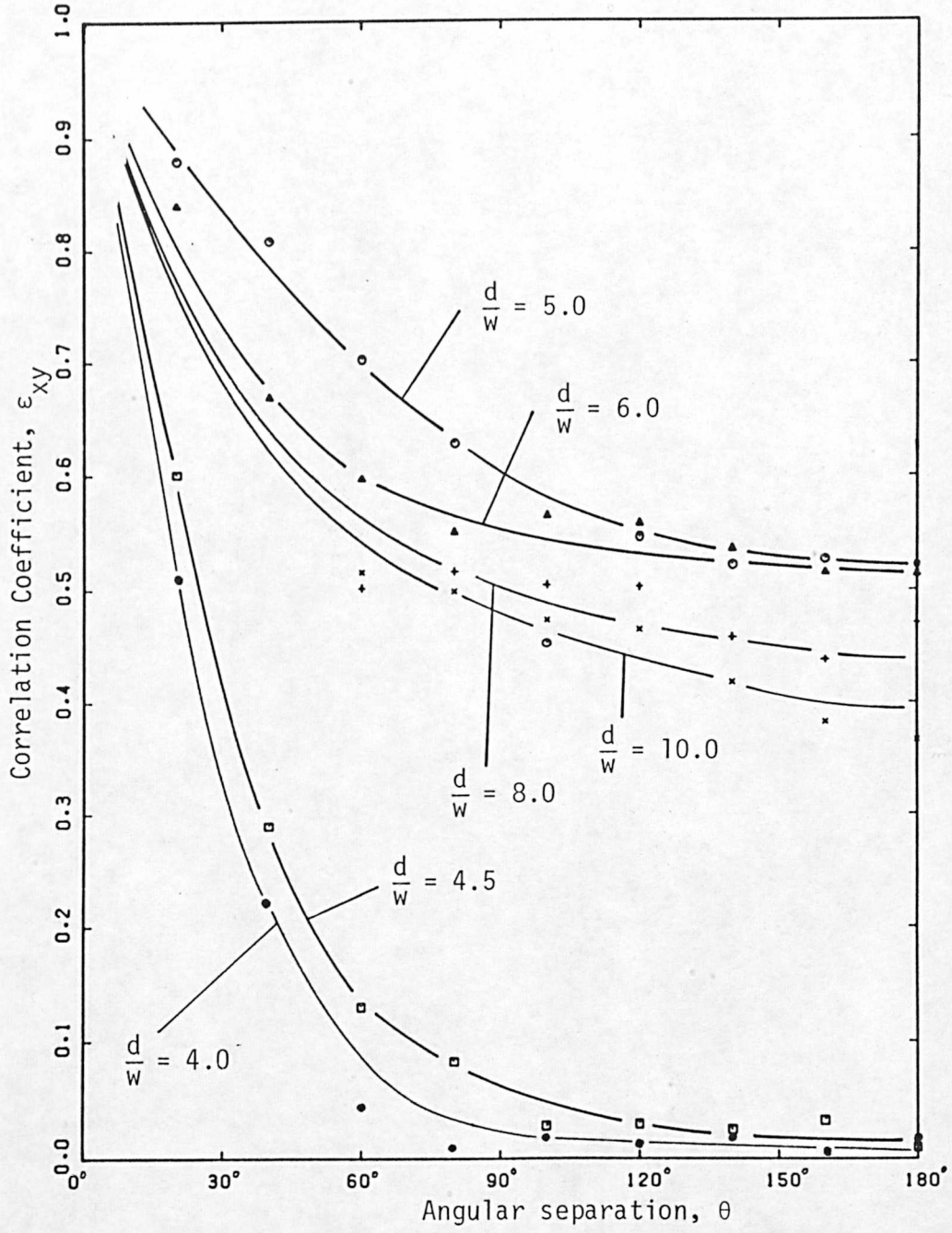



Figure 3.1.4 Variations of the correlation coefficient of velocity fluctuations behind the thin sharp-edged cross-section ring models versus angular separation, $R_e = 1.3 \times 10^4 - 2.9 \times 10^4$.

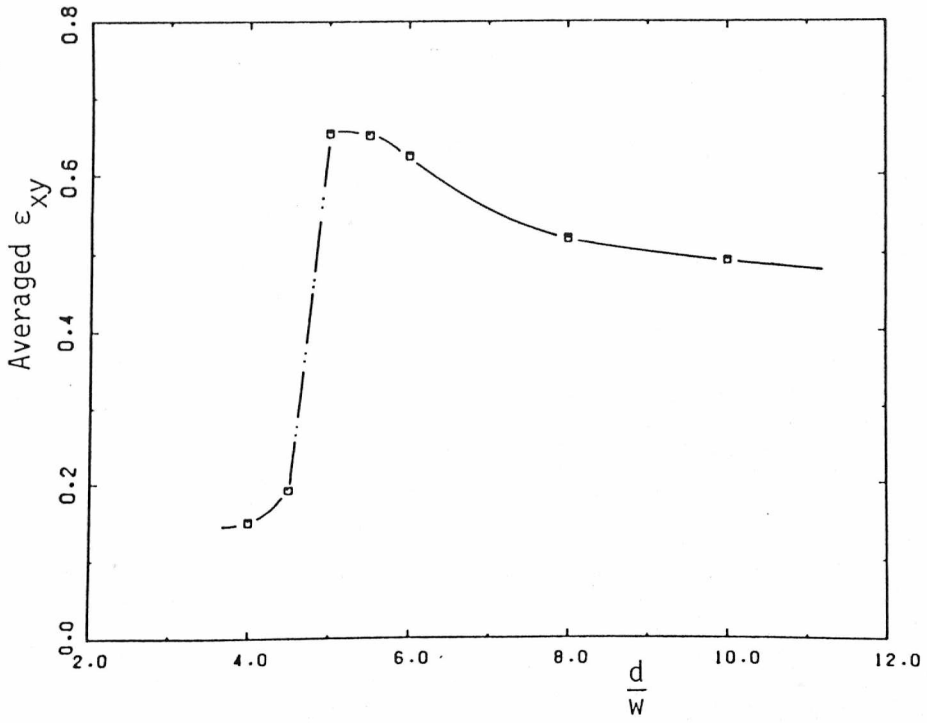



Figure 3.1.5 Averaged correlation coefficients versus $\frac{d}{w}$

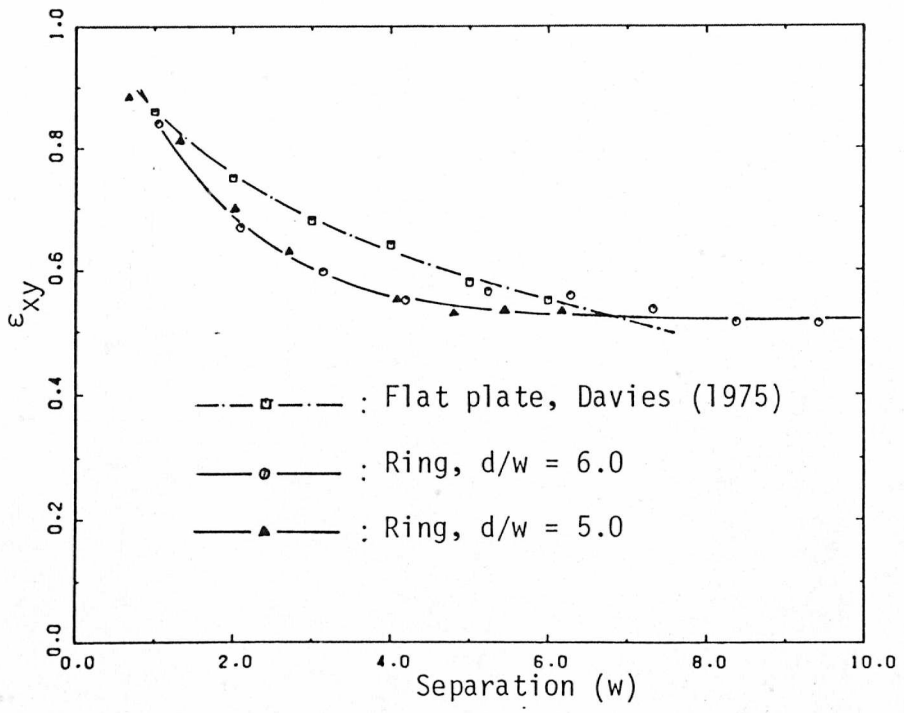


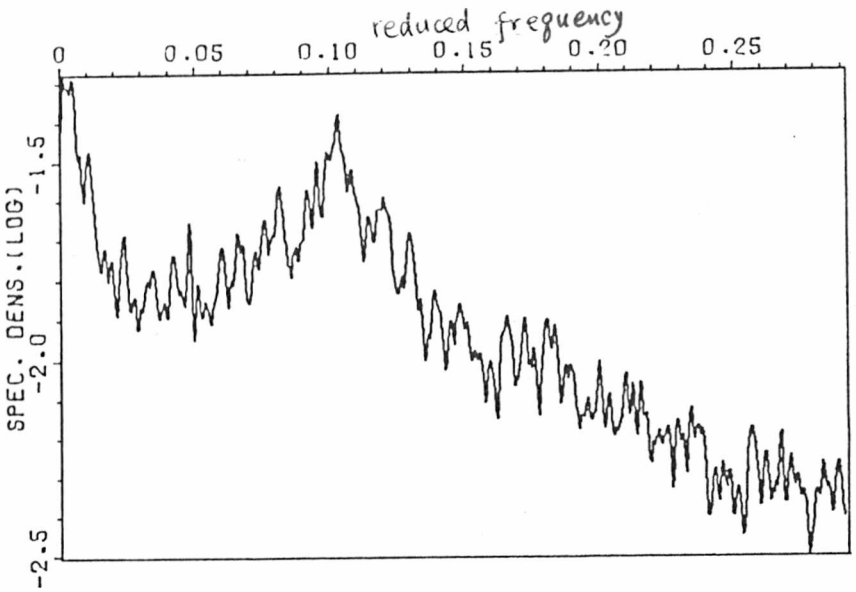

Figure 3.1.6 Correlation along the span

for a sharp-edged flat plate measured by Davies (1975) is also shown in the same figure for comparison. Although the correlation for the flat plate is slightly higher than that of the ring models for small separations, they both decrease to the same degree of correlation at a separation of about 7 w. Data for the flat plate is not available beyond this separation. However, the correlation of a rectangular cylinder of $\delta/w = 0.2$, which may not be very different to the sharp-edged flat plate because of the small $\delta/w$, measured by Bearman and Trueman (1972) shows a steady decrease of the correlation with increasing separation up to 20 w. This is in marked contrast to the ring models which show a nearly constant value of $\varepsilon_{xy}$ beyond a separation of about 5w.

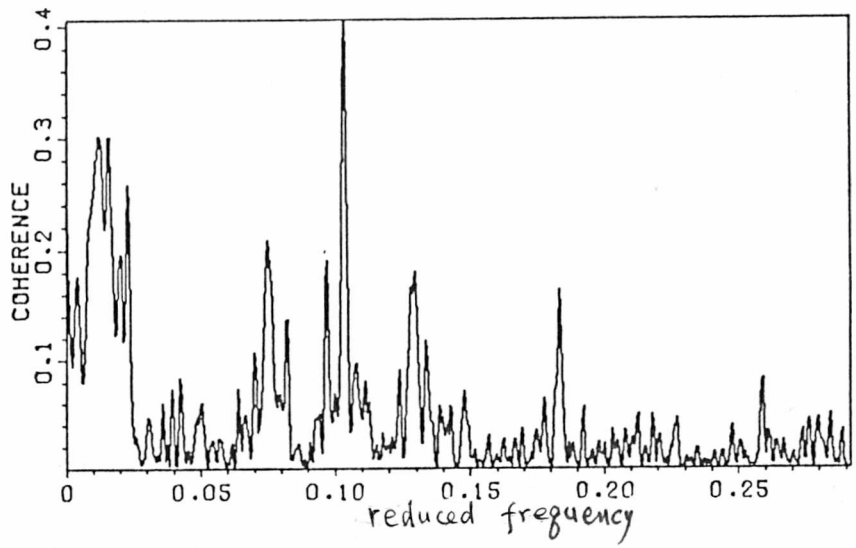
Further analyses of velocity fluctuations measured by two single hot-wires behind the thin sharp-edged cross-section of the ring models with $d/w = 4.0$ to $d/w = 6.0$, the region where $C_{pb}$ rapidly changes with $d/w$ as shown in Figure 3.1.1, were carried out. The two hot-wires were located in the same positions as for the correlation measurements with $\theta = 180^{o}$. Power spectral density, $S_{xx}$, coherence, $\gamma_{xy}$, and phase difference, $\theta_{xy}$, between the two signals for $d/w = 4.0$, 4.5, 5.0 and 6.0 are shown in Figures 3.1.7 to 3.1.10 as functions of the Strouhal number, $S_t$, defined by $fw/U$, where $f$ is a vortex shedding frequency.

Figure 3.1.7 (a) shows $S_{xx}$ for $d/w = 4.0$ and there exists a small broad peak around $S_t = 0.10$ in a high level background

(a) Power spectral density function $S_{xx}$ $(S_t)$




(b) Coherence function $\gamma_{xy}$ $(S_t)$




(c) Phase difference $\theta_{xy}$ $(S_t)$

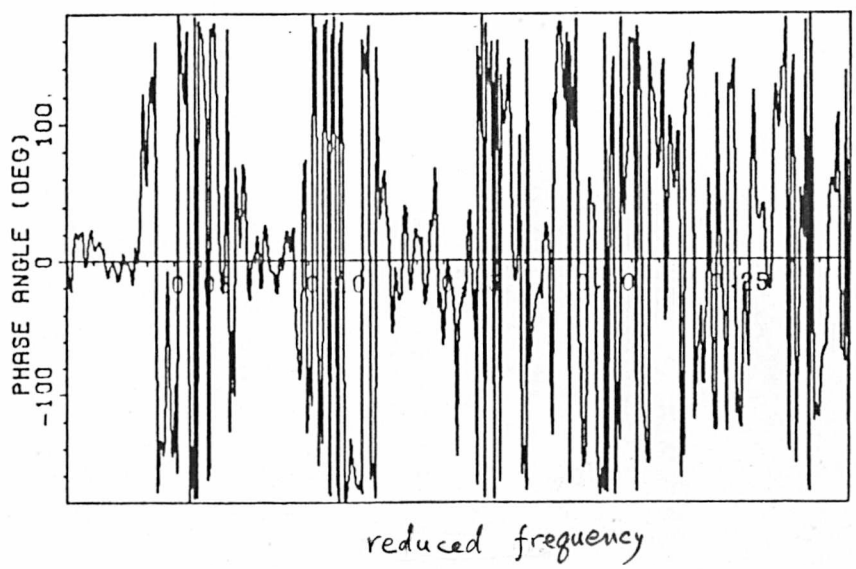
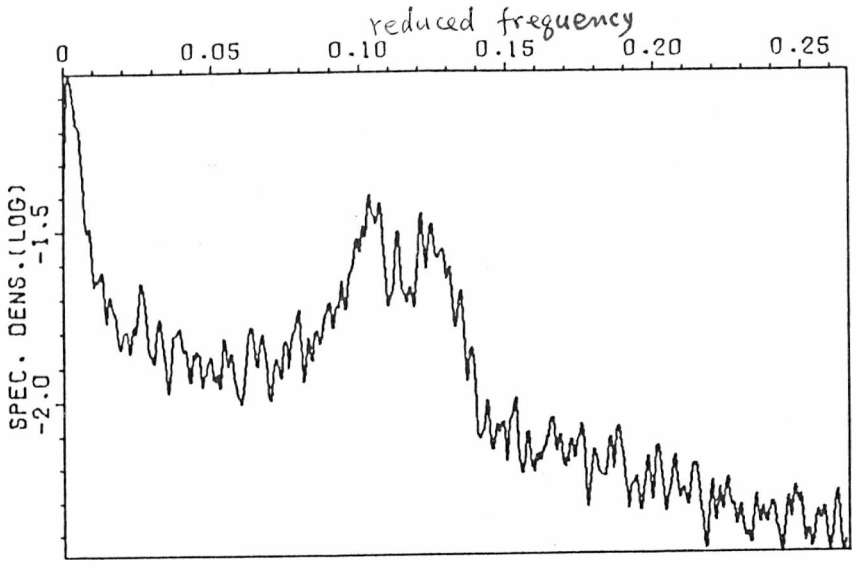
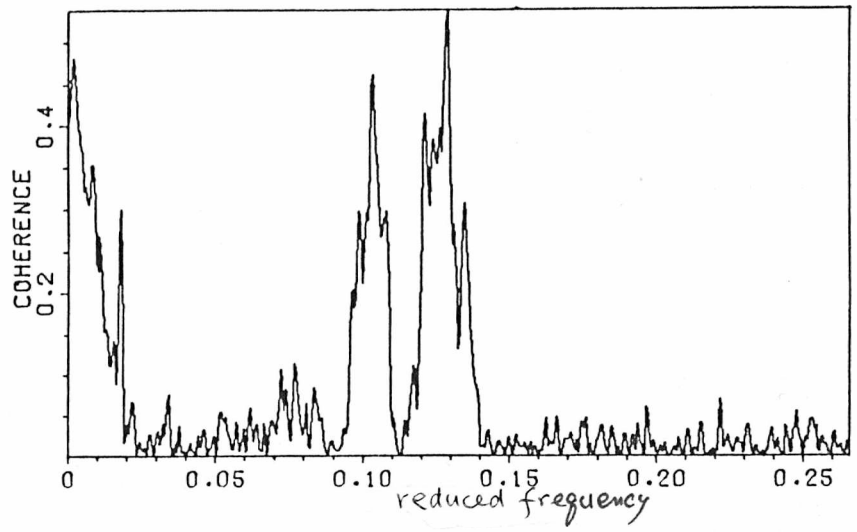



Figure 3.1.7 Analysis of velocity fluctuations behind the ring model of d/w = 4.0

(a) $S_{xx}$ $(S_t)$




(b) $\gamma_{xy}$ $(S_t)$




(c) $\theta_{xy}$ $(S_t)$

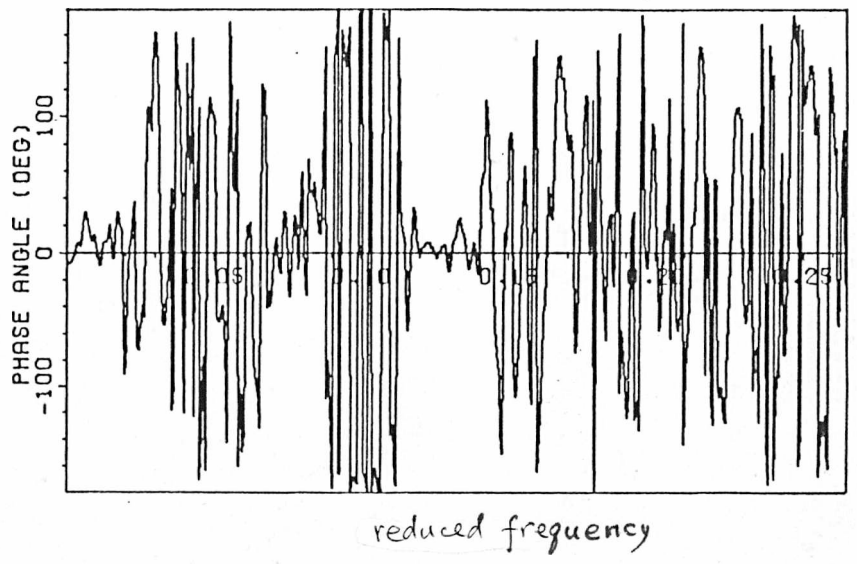
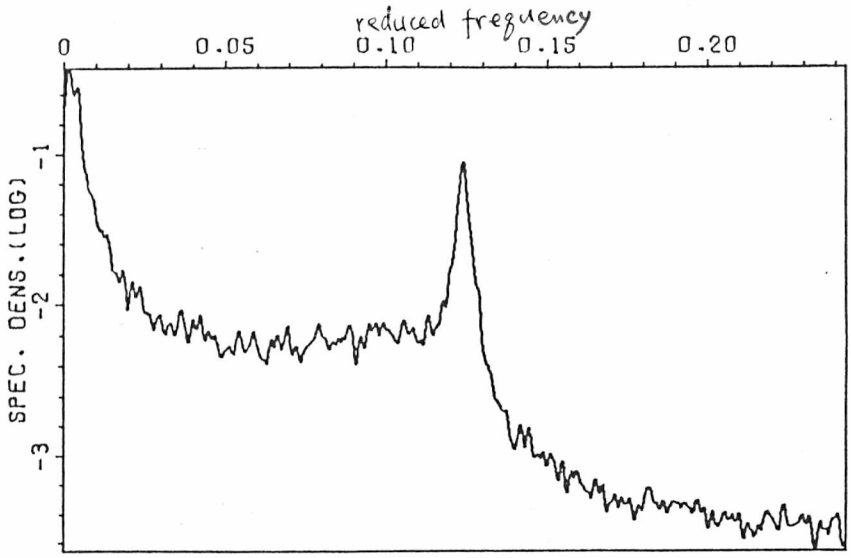
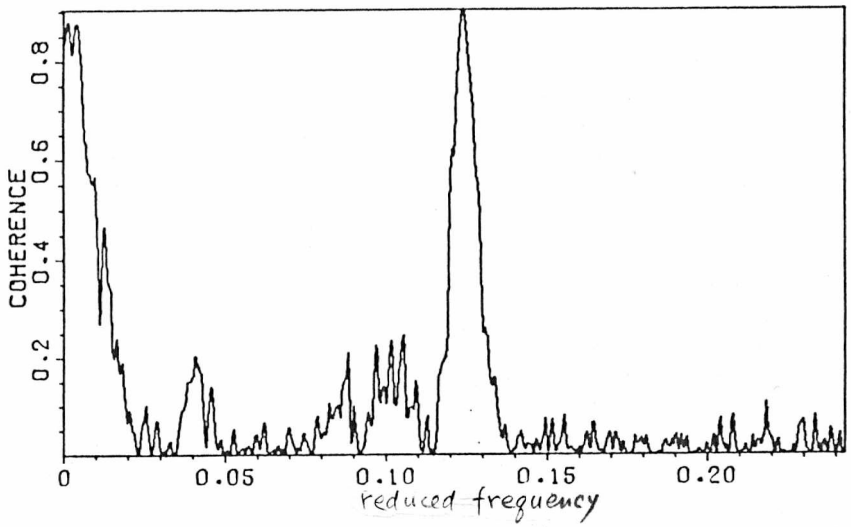



Figure 3.1.8 Analysis of velocity fluctuations behind the ring model of d/w = 4.5

(a) $S_{xx}$ $(S_t)$




(b) $\gamma_{xy}$ $(S_t)$




(c) $\theta_{xy}$ $(S_t)$

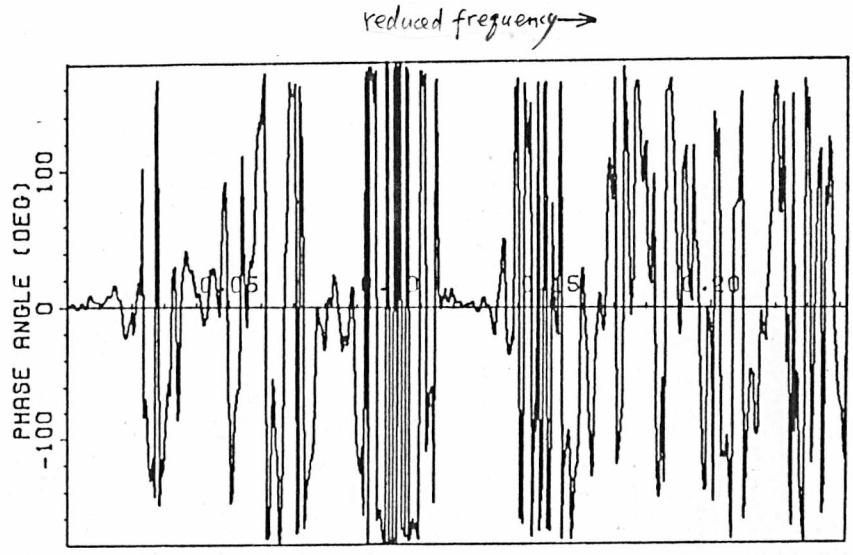
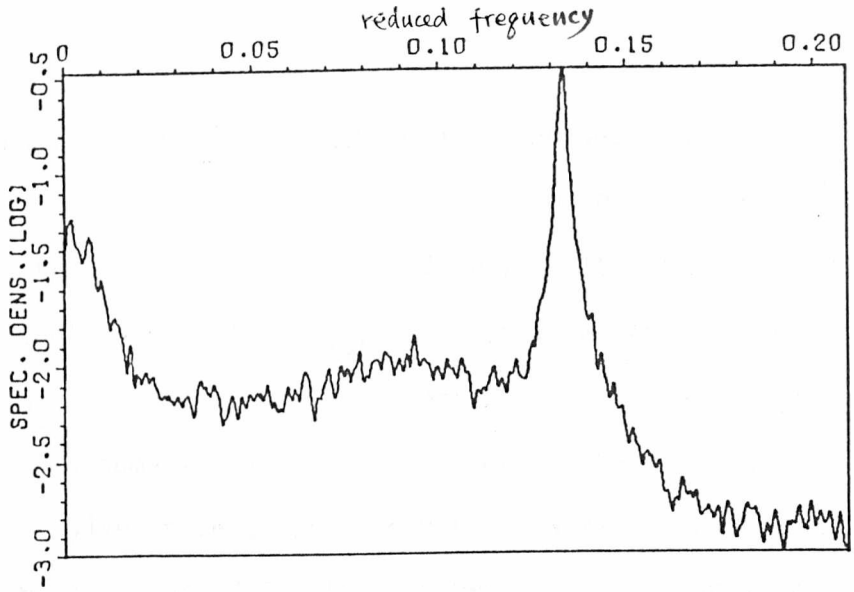
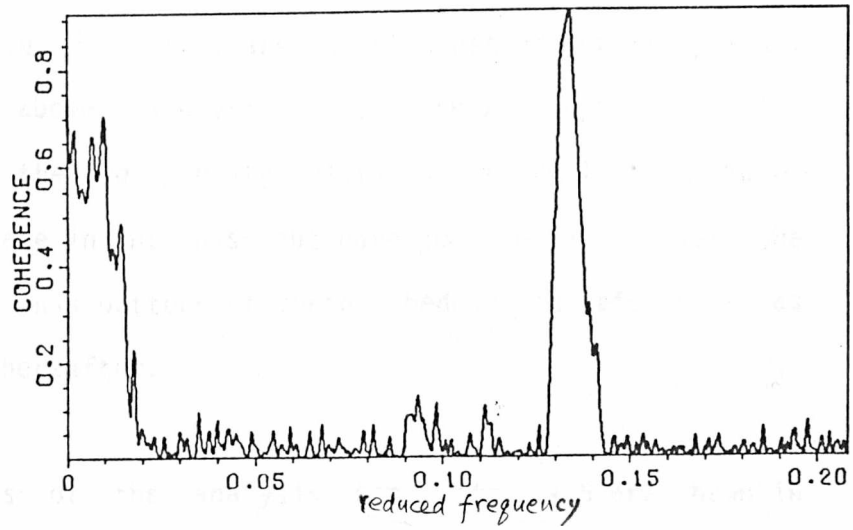



Figure 3.1.9 Analysis of velocity fluctuations behind the ring model of d/w = 5.0

(a) $S_{xx}$ $(S_t)$




(b) $\gamma_{xy}$ $(S_t)$




(c) $\theta_{xy}$ $(S_t)$

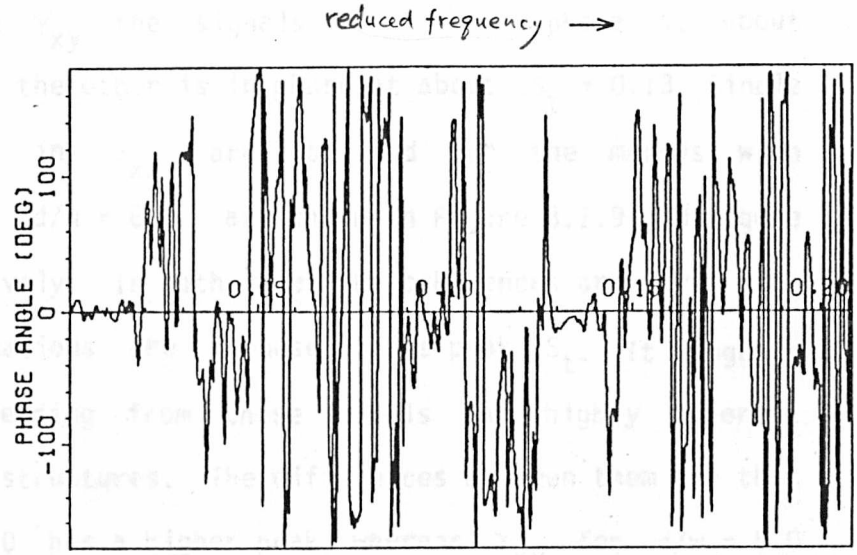



Figure 3.1.10 Analysis of velocity fluctuations behind the ring model of d/w = 6.0

turbulence spectrum. Also, a weak coherence between the two hot-wire signals at the peak $S_t$, with a $180^o$ phase difference, can be recognised from Figure 3.1.7 (b) and (c). It should be noted that the spectral density, $P_{xy}$, is negative at frequencies around the peak $S_t$, but the quadrature spectral density, $Q_{xy}$, is almost zero and has some small fluctuations around zero at other frequencies. This gives rise to the large fluctuations between $\theta_{xy} = \pm 180^o$ shown in Figure 3.1.7 (c). Robert (1973) found that velocity fluctuations at the two opposite positions behind a solid circular disk, i.e. $\theta = 180^o$, are in antiphase at the predominant frequency. The above analysis also shows that velocity fluctuations at the two opposite positions outside the ring model with d/w = 4.0 are in antiphase but have poor regularity, at the peak frequency. This pattern of vortex shedding is referred to as the 'disk-mode' hereafter.

The results of the analysis for d/w = 4.5 are shown in Figure 3.1.8. There are two peaks in $S_{xx}$ and $\gamma_{xy}$, respectively, at one peak in $\gamma_{xy}$ the signals are in antiphase at about $S_t = 0.10$ and the other is in phase at about $S_t = 0.13$. Single pronounced peaks in $S_{xx}$ are obtained for the models with d/w = 5.0 and d/w = 6.0 as shown in Figure 3.1.9 and Figure 3.1.10, respectively. In both cases the coherences are very high and the fluctuations are inphase at the peak $S_t$. It suggests that vortex shedding from these models has highly coherent axisymmetrical structures. The differences between them are that $S_{xx}$ for d/w = 6.0 has a higher peak, whereas $\gamma_{xy}$ for d/w = 5.0

is higher at low $S_t$. Therefore, the ring model with d/w = 6.0 is supposed to have more regular vortex wake structure, although the correlations for d/w = 5.0 and d/w = 6.0 are about the same degree as shown earlier in Figure 3.1.4. The two peaks in Figure 3.1.8 suggests that the pattern of vortex shedding from the ring model with d/w = 4.5 is changing intermittently between the 'disk-mode' and the axisymmetrical mode.

Figure 3.1.11 shows records of the velocity fluctuations detected by one of the two single hot-wires used for the above analyses. It can also be recognised from these waveforms that the regularity of velocity fluctuations caused by vortex shedding improves with increasing d/w. It is an interesting feature that the low frequency modultion of velocity fluctuations, which is observed even in a regular vortex shedding from a two-dimensional bluff body, is inphase and relatively high coherent, as shown in Figures 3.1.7 to 3.1.10, although the mechanism of the modulation is not clear.

The frequency of velocity fluctuations measured on the axis of symmetry behind the ring models with d/w = 5.0 and d/w = 6.0 were the same as those measured outside the ring wakes (the same position for the correlation measurement). Figure 3.1.12 shows $S_{xx}$ of velocity fluctuations measured on the axis of symmetry 3.4 w downstream of the ring models with d/w = 4.0 and d/w = 4.5. It is suggested that the velocity fluctuations on the

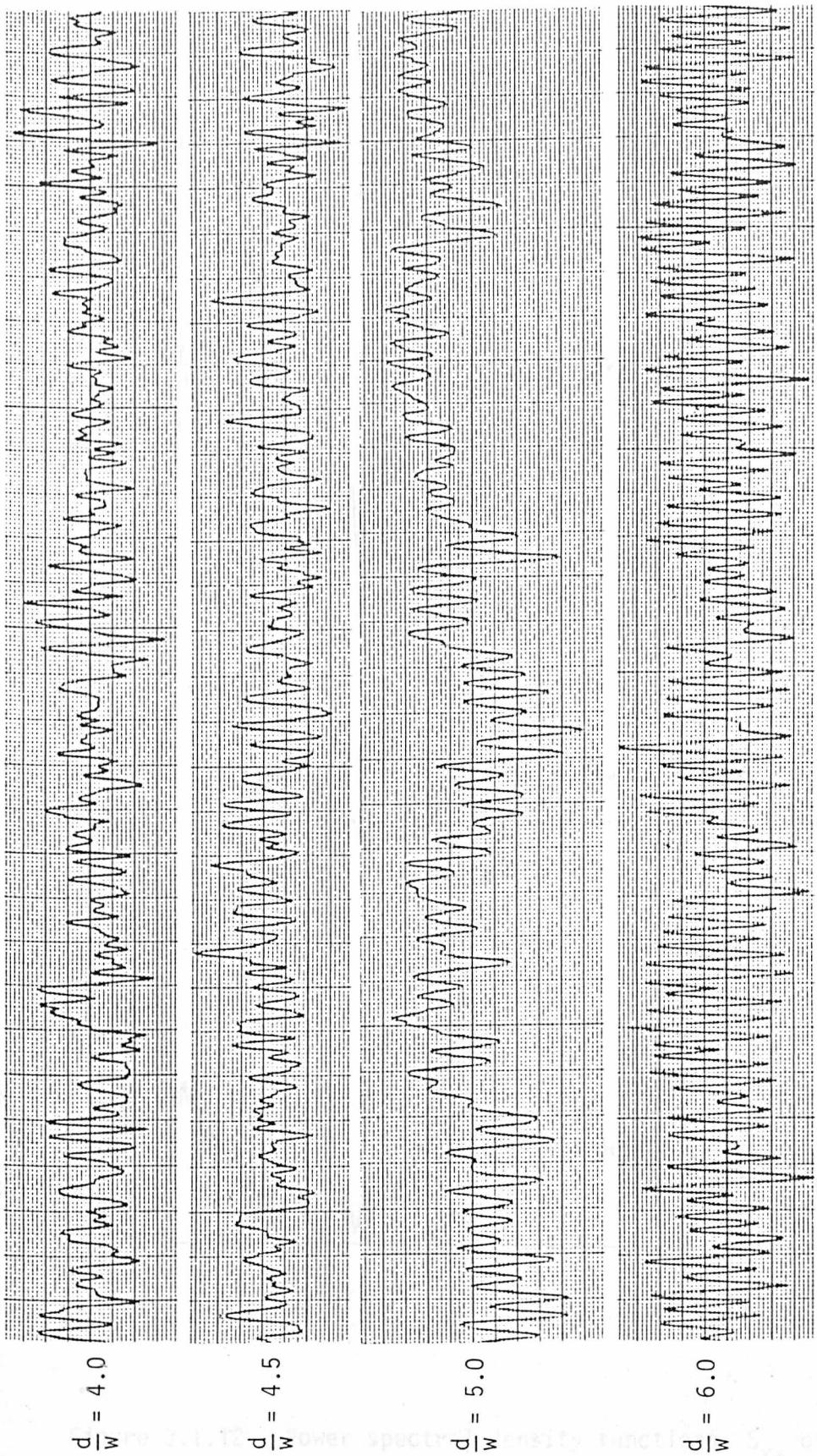
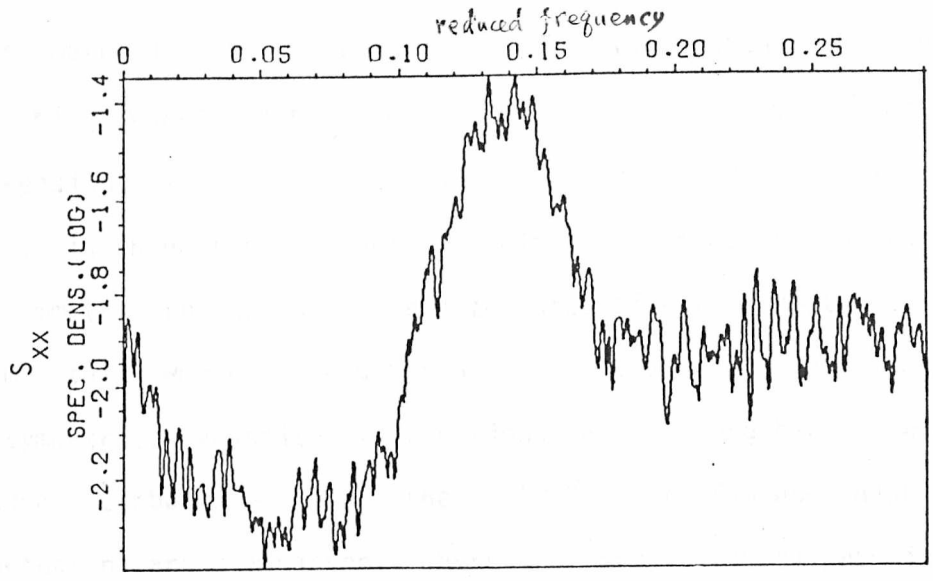
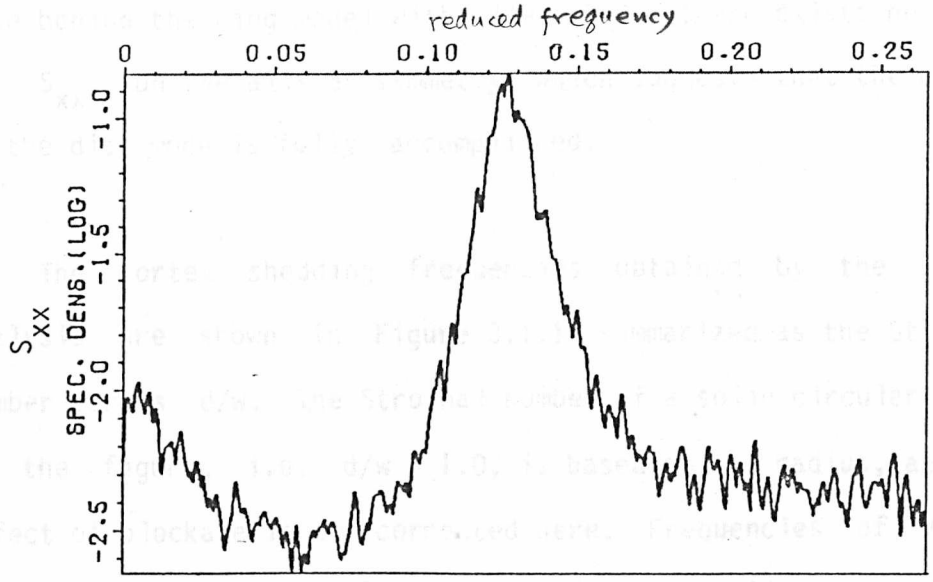



Figure 3.1.11 Records of velocity fluctuations detected by the hot-wire located outside the ring wakes (Amplitude; arbitrary scale) $R_e = 2.0 \times 10^4 - 2.9 \times 10^4$.




(a) $\frac{d}{w} = 4.0$

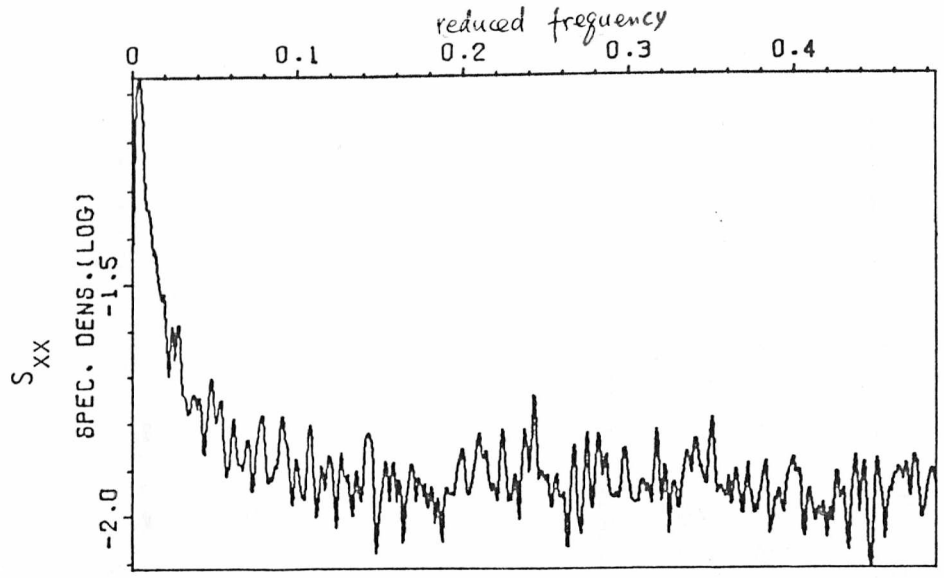



(b) $\frac{d}{w} = 4.5$

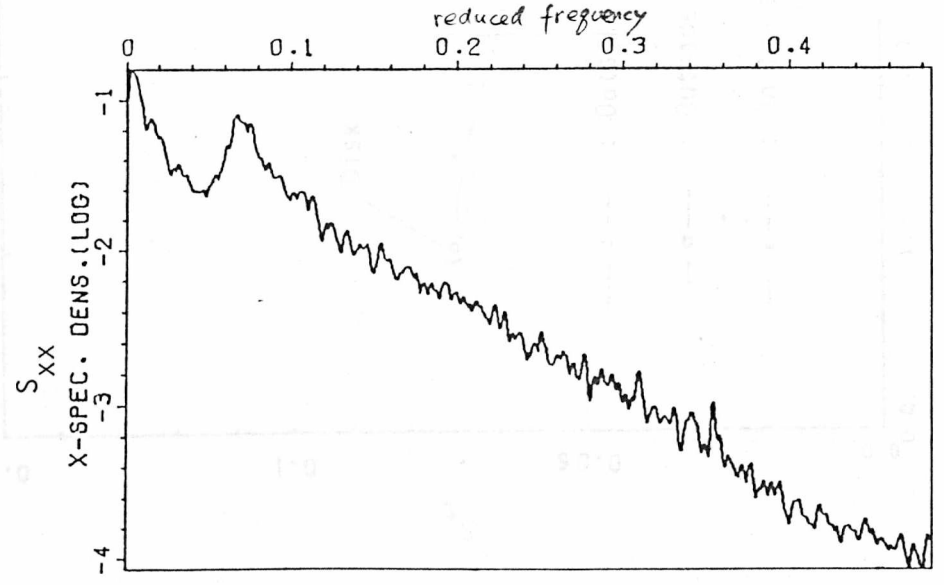
Figure 3.1.12 Power spectral density functions $S_{XX}$ of velocity fluctuations measured on the axis of symmetry behind the ring model of d/w = 4.0 and d/w = 4.5.

axis of symmetry may be similar to those obtained in the axisymmetrical mode, whereas, the velocity fluctuations outside the ring wakes have already changed to the disk mode with decreasing d/w as shown in Figures 3.1.7 and 3.1.8. The main reason is thought to be that the velocity fluctuations on the axis of symmetry are caused by the integrated effect of vortex shedding from the whole circumference of the ring model, hence, axisymmetrical velocity fluctuations are strengthened, whereas random turbulence and the $180^{o}$ out-of-phase disk mode fluctuatons are diminished. Therefore, the low level peak in $S_{xx}$ at d/w = 4.0 shown in Figure 3.1.12 (a) suggests that the change in the mode is still not complete. Figure 3.1.13 shows $S_{xx}$ of velocity fluctuations on the axis of symmetry and outside the ring wake behind the ring model with d/w = 2.0. There exists no peak in $S_{xx}$ on the axis of symmetry, which suggests that the change to the disk mode is fully accomplished.

The vortex shedding frequencies obtained by the above analysis are shown in Figure 3.1.14 summarized as the Strouhal number versus d/w. The Strouhal number of a solid circular disk in the figure, i.e. d/w = 1.0, is based on the radius, and the effect of blockage is not corrected here. Frequencies of vortex shedding from two flat plates arranged side-by-side measured by a hot-wire outside the wake 5w or 6w downstream of the bluff bodies are shown in Figure 3.1.15, reproduced by Andreopoulos (1972). Although he did not find the discontinuous change of the mode, the characteristics of $S_t$ versus d/w measured outside




(a) On the axis of symmetry




(b) Outside of the ring wake

Figure 3.1.13 $S_{XX}$ of velocity fluctuations measured on the axis of symmetry and outside the ring wake behind the ring model of d/w = 2.0.

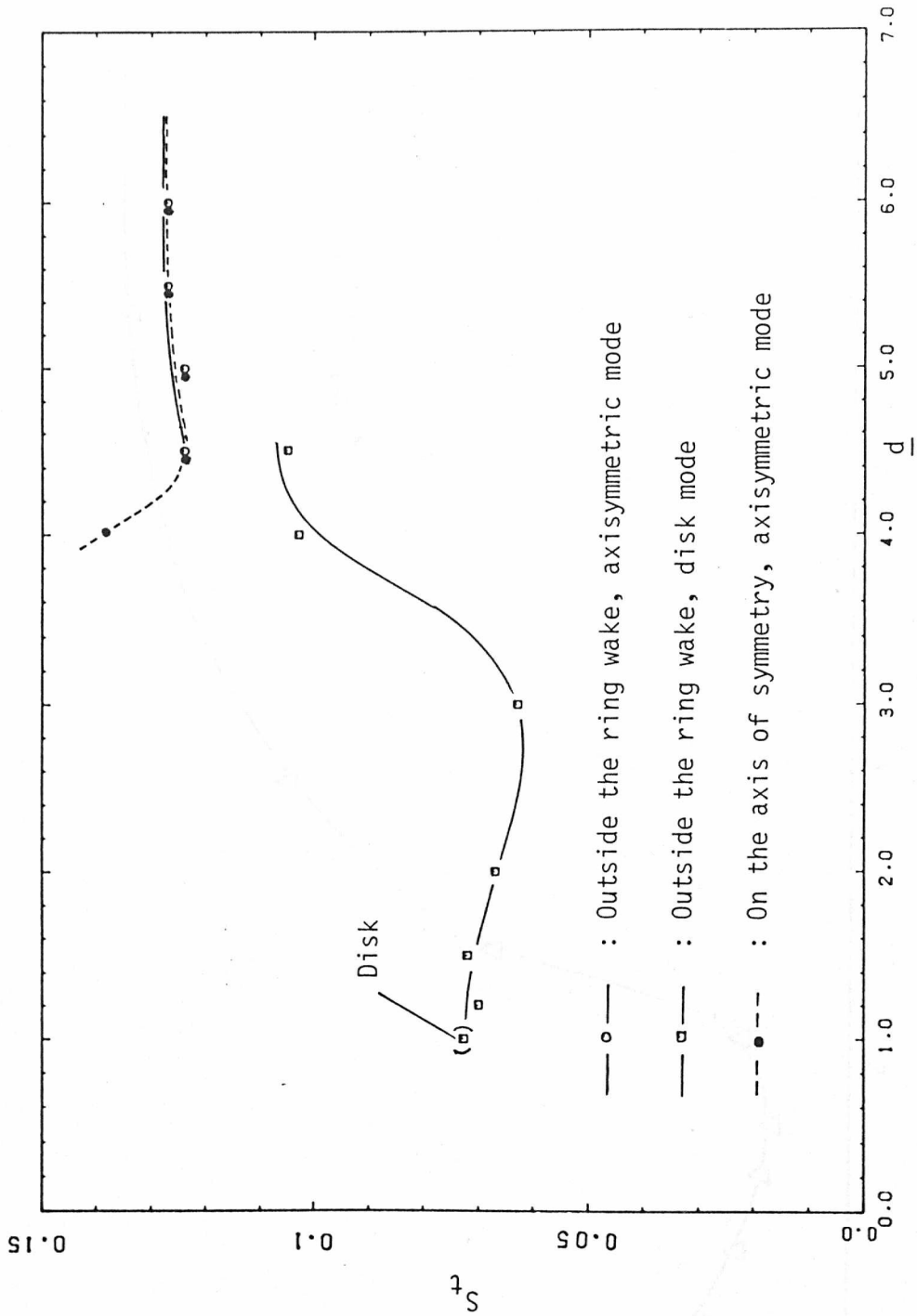



Figure 3.1.14 Frequencies of vortex shedding from the ring model
(the effect of blockage is not corrected)

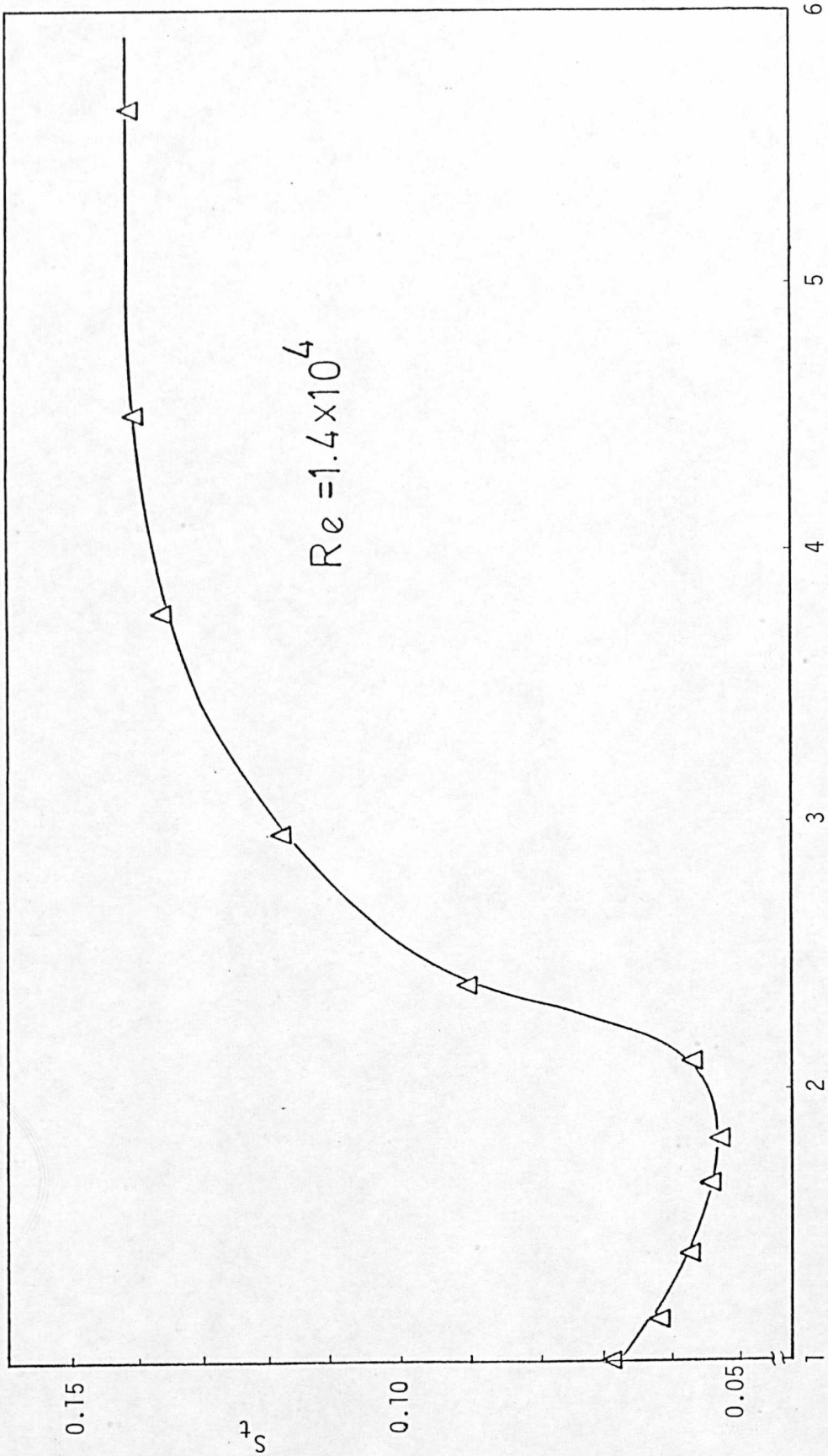



Figure 3.1.15 Frequencies of vortex shedding from the two flat plates arranged side-by-side, measured by a hot-wire located outside the wake. Reproduced from Andreopoulos (1972).

the wakes of the two flat plates model and the ring models have a close similarity. The $S_t$ for both models is lower than that of an isolated flat plate, and gradually decreases with increasing d/w at low d/w range, then it experiences a rapid increase followed by a gradual increase at higher d/w range. Figure 3.1.16 shows frequencies of vortex shedding from two circular cylinders arranged side-by-side, and Figure 3.1.17 shows correlations of velocity fluctuations across the cylinder pair, which are reproduced from Bearman and Wadcock (1973). They observed that $S_t$ measured outside the wake 6w downstream of the bluff bodies has a low value at a low d/w range compared with a high d/w range except at about d/w = 1.8, whereas $S_t$ measured outside the ring wake increases continuously with d/w. They also showed from correlation measurements the change in the mode where velocity fluctuations are symmetric about the axis of the gap in the range d/w > 2.0 and $180^{o}$ out-of-phase at the very small cylinder separation range. But they were unable to clarify the flow structure at intermediate d/w values where $S_t$ rapidly changes with d/w as the measurements of the correlation were scattered. Also, a sudden increase and decrease of $S_t$ were measured by them at the centre of the gap between the two cylinders at small separations, whereas only a slightly higher value of $S_t$ at d/w = 4.0 and no other predominant frequency is recognised on the axis of symmetry in the present measurements. The cause of the difference is not clear, but the two circular cylinders experience different base pressures caused by a marked

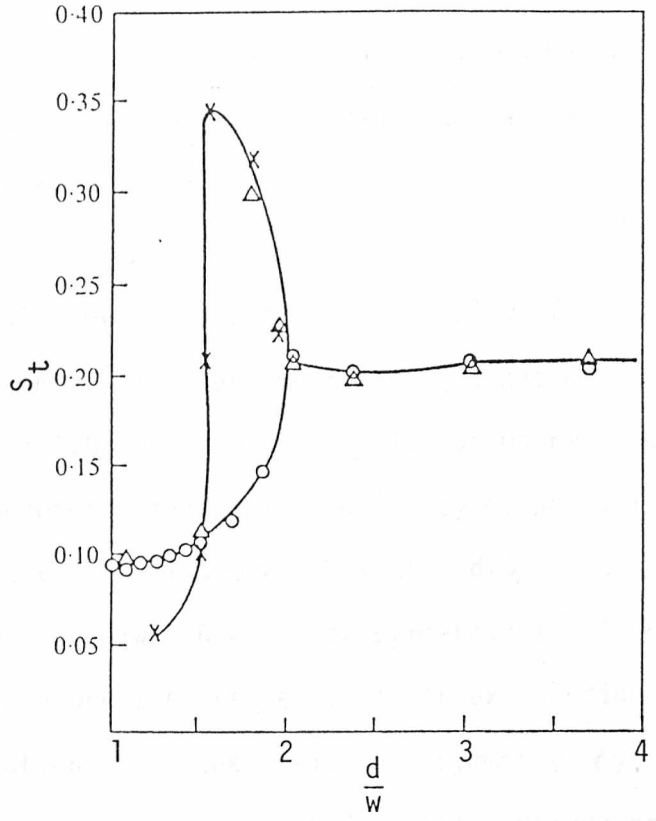



Figure 3.1.16 Strouhal number versus cylinder separation. o, hot wire 6 diameters downstream of cylinder pair, outside the wake; Δ, hot wire at outer $90^{o}$ point; x, hot wire on gap centre line, reproduced from Bearman and Wadcock (1973).

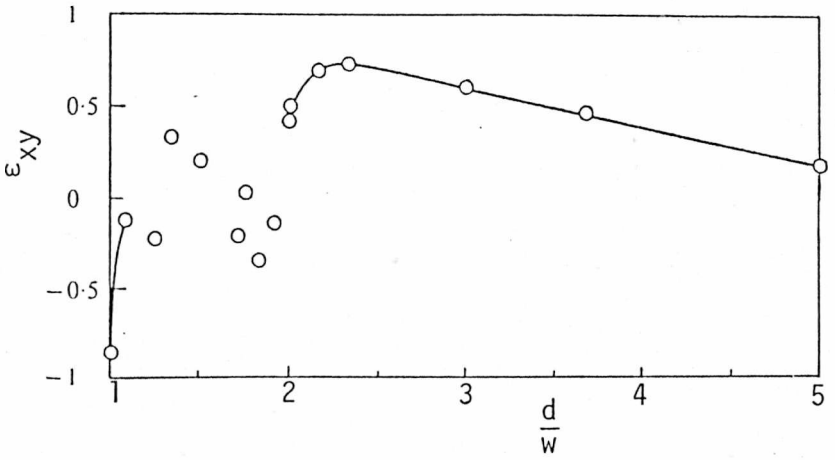



Figure 3.1.17 Correlation across the cylinder pair versus cylinder separation, reproduced from Bearman and Wadcock (1973).

asymmetric mean flow when the gap is small, which may give rise to some substantial differences between the wakes of the two cylinders and the ring model.

Figure 3.1.18 shows comparisons of velocity fluctuations on the axis of symmetry and outside the ring wakes behind the ring models with d/w = 4.0 and d/w = 6.0. It can be recognised from the recorded waveforms that the regularity of periodic velocity fluctuations on the axis of symmetry with d/w = 6.0 is high, since the mode of d/w = 6.0 is axisymmetrical. Therefore, it was possible to measure the frequency of vortex shedding from the velocity fluctuations on the axis of symmetry by using an electrical counter and a band-pass filter set. Measurements with d/w = 6.0, 8.0 and 10.0 were carried out at $R_e = 2 \times 10^4$ and the results are shown in Table 3.1.1. It is supposed that the Maskell's formulae can be applied for blockage correction of $S_t$ here.

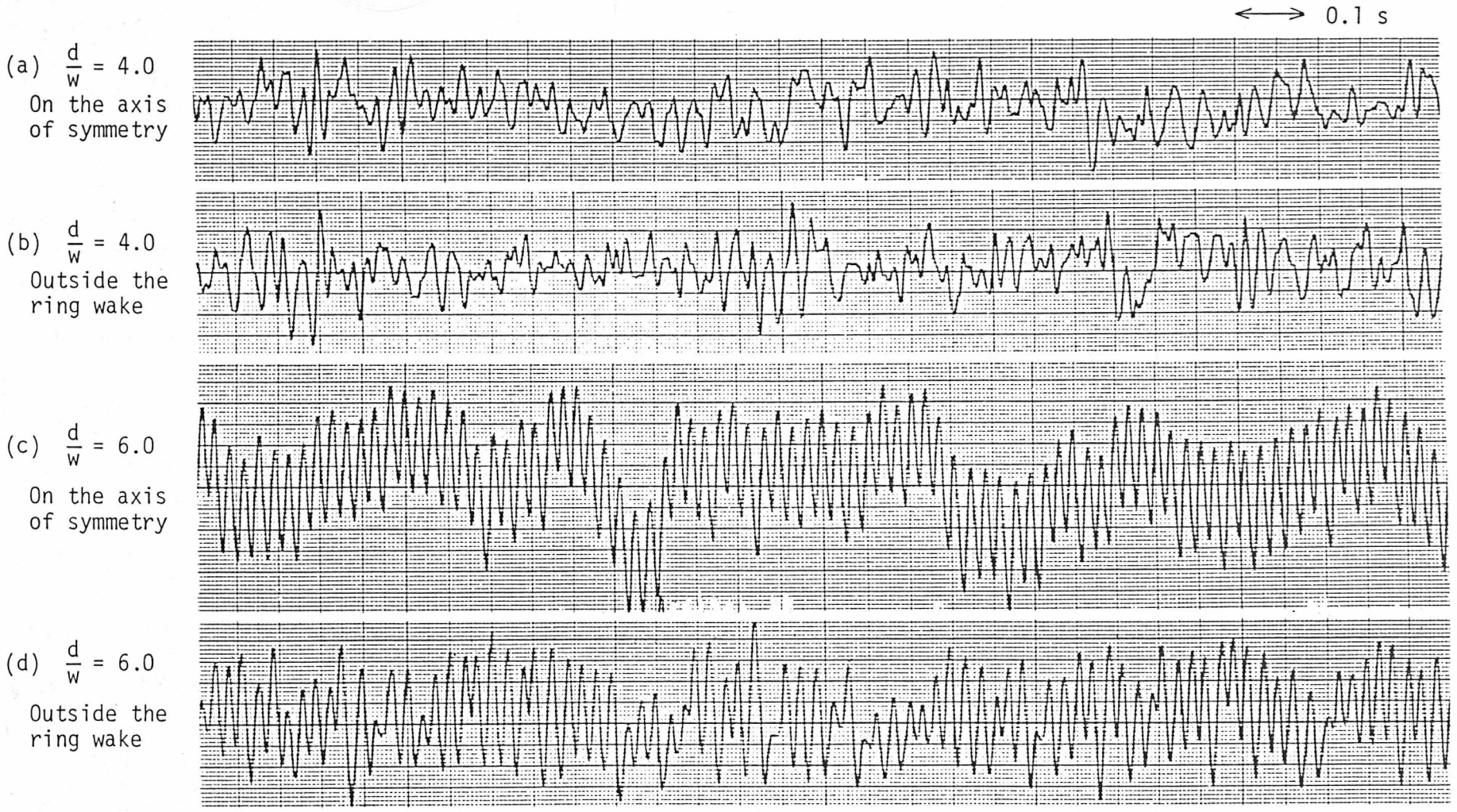



Figure 3.1.18 Records of velocity fluctuations detected by the hot-wire located on the axis of symmetry and outside the ring wakes. (Amplitude: arbitrary scale)
$R_e = 2.0 \times 10^4 - 2.9 \times 10^4$

## TABLE 3.1.1

| Bluff body | d/w | $S_t$* | $R_e$ |
|---|---|---|---|
| Ring | 6.0 | 0.123 | $2x10^4$ |
| Ring | 8.0 | 0.135 | $2x10^4$ |
| Ring | 10.0 | 0.136 | $2x10^4$ |
| Flat Plate | - | 0.142** | $2x10^4$ |

* Effect of blockage is corrected.

** Reproduced from Davies (1975)

### 3.1.3 Results of conditional averaging

The periodic component due to vortex shedding from the thin sharp-edged cross-section ring model with $d/w = 6.0$ was extracted from the turbulent velocity fluctuations of the u and v records by using the conditional averaging technique described in Section 2.5. Cross-wire probes were traversed from $y = 0$ to $y = 20$ cm on a plane normal to the axis of symmetry at $x = 3.4$ w and $x = 8.0$ w. The step length, $\Delta y$, was 0.5 cm, therefore there were 41 measurement points in the y direction. At each y position, analogue signals of u(t) and v(t) were sampled and converted into digital values at the rate of about 50 points per vortex shedding cycle. The reference velocity fluctuation used for control of conditioning was measured near the axis of symmetry. Although the reference signal appeared fairly regular, only about 60 to 70% of the measured periods between the two consecutive maxima of the signal coincided with the expected vortex shedding cycle. A vortex shedding cycle was accepted if the period was within about $\pm$4% of the mean and the others were rejected.

Elimination of the effect of random fluctuations from the conditionally averaged velocity fluctuations depends on the number of cycles averaged and the sampling position. Figure 3.1.19 shows examples of the convergence of the averaged values of the velocity fluctuations which were measured in the wakes of the thin sharp-edged cross-section and the rectangular cross-section ring

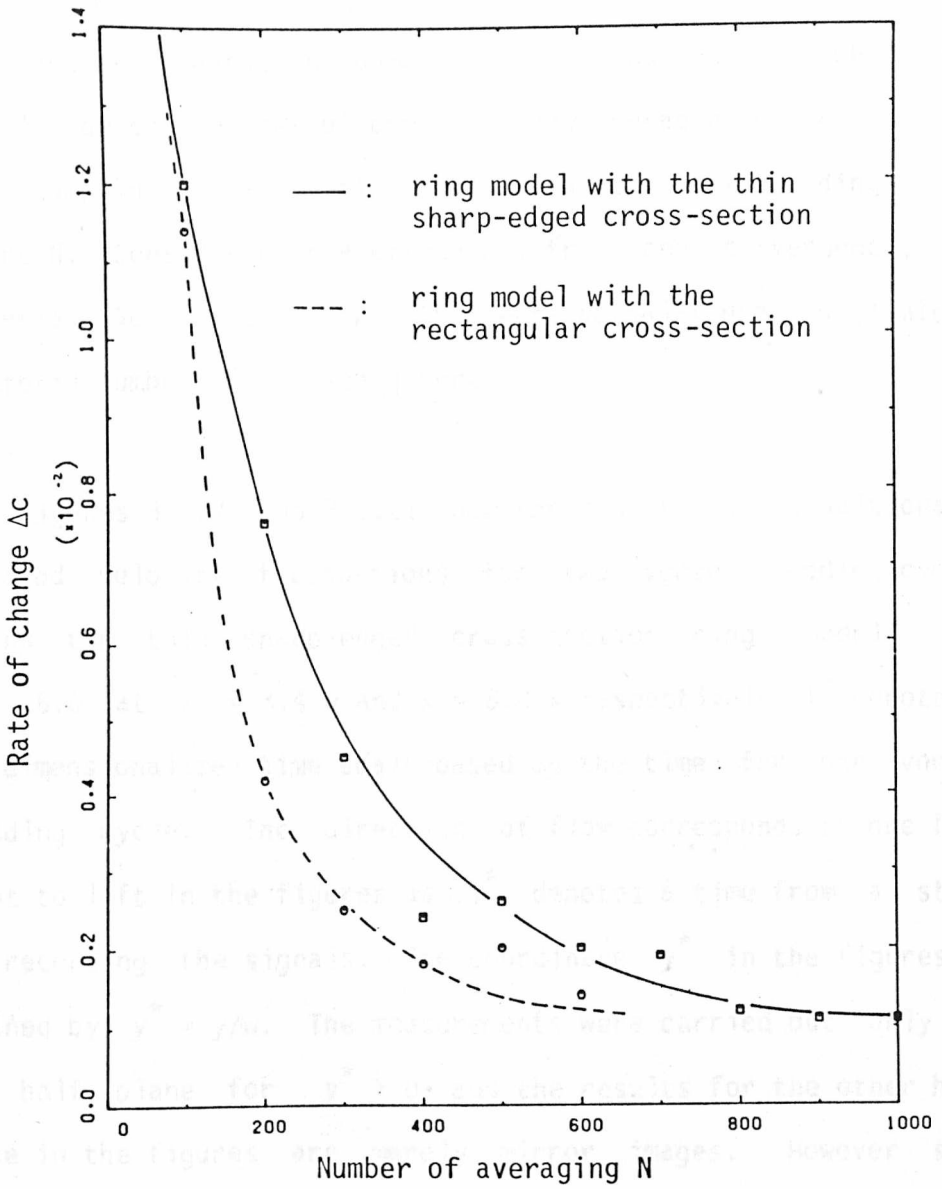


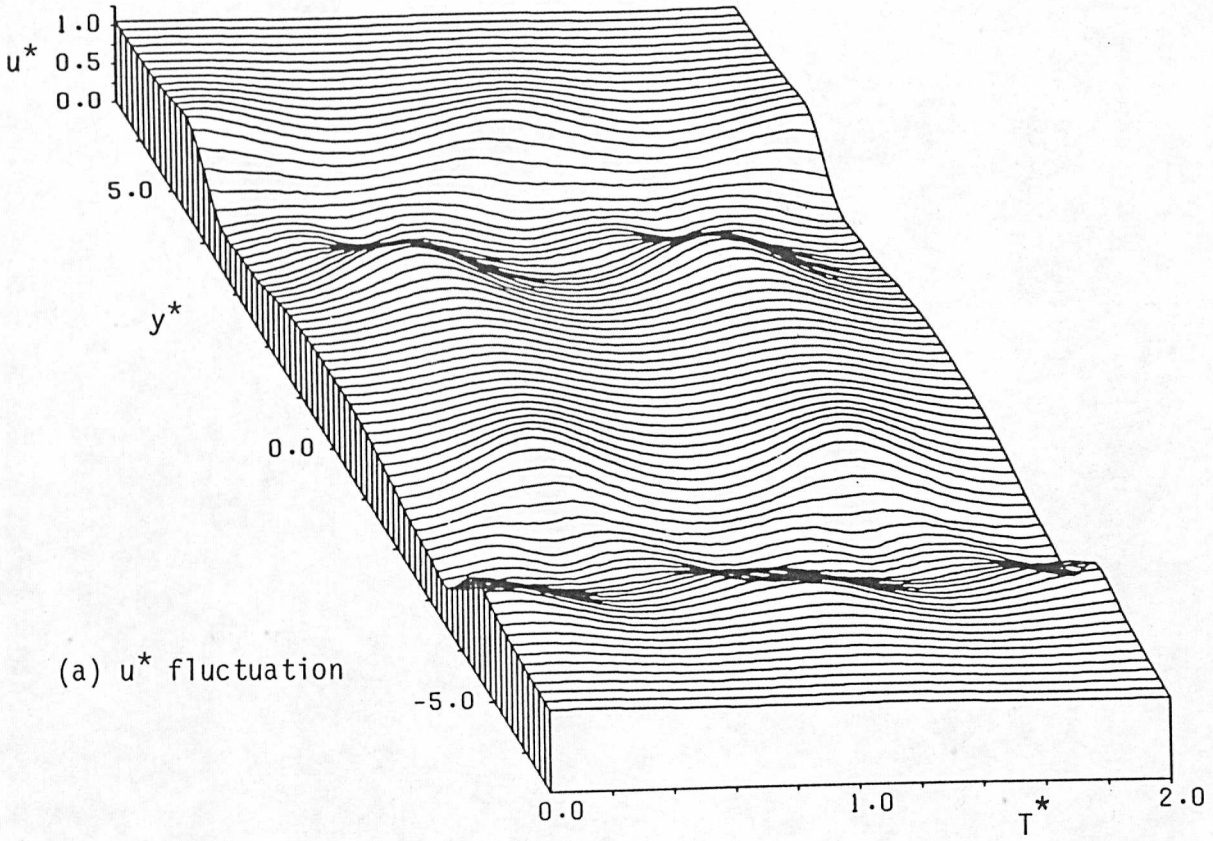

Figure 3.1.19 Convergence rates of the averaged values of velocity fluctuations measured in the wakes of ring models with d/w = 6.0.

models with $d/w = 6.0$ at $x = 3.4$ w and $y = 3.0$ w, respectively. In the figure, the rates of changes $\Delta c(N)$ defined by the following equation

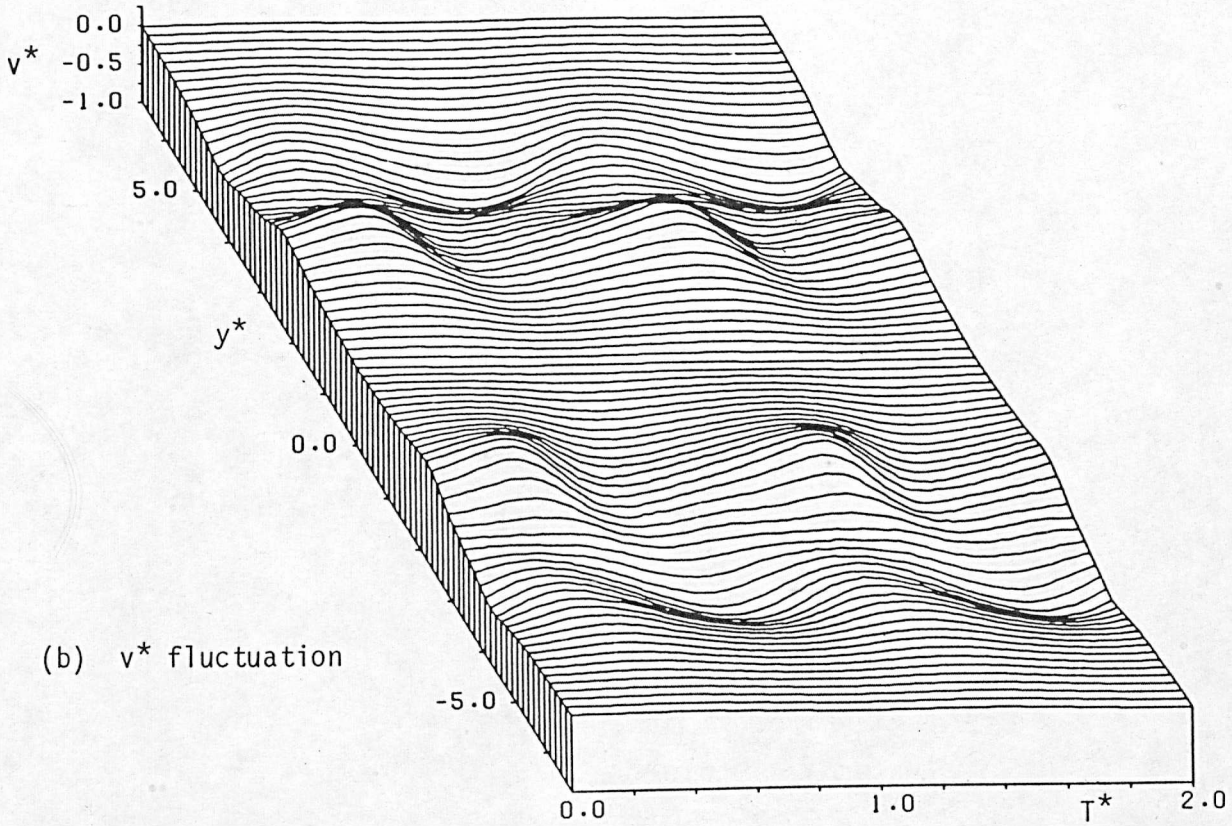
$$\Delta c = \left( \sum \Delta u_i^2 + \sum \Delta v_i^2 \right)^{0.5} \qquad (3.1.1)$$

are plotted against the number of averaging cycles N, where $\Delta u_i$ and $\Delta v_i$ denote changes of conditionally averaged u and v at each sampling time within three averaged vortex shedding cycles around N. Considering the efficiency from the convergence, the criteria $\Delta c = 0.001$ or $N = 1000$ were actually used for limiting the total number of averaging here.

Figures 3.1.20 and 3.1.21 show the results of conditionally averaged velocity fluctuations for two vortex shedding cycles behind the thin sharp-edged cross-section ring model with $d/w = 6.0$ at $x = 3.4$ w and $x = 8.0$ w respectively. $T^*$ denotes a non-dimensionalized time scale based on the time for one vortex shedding cycle. The direction of flow corresponds to one from right to left in the figures as $T^*$ denotes a time from a start of recording the signals. The coordinate $y^*$ in the figures is defined by $y^* = y/w$. The measurements were carried out only in the half plane for $y^* \geq 0$ and the results for the other half plane in the figures are merely mirror images. However some measurements at $y^* < 0$ showed that the conditionally averaged velocity fluctuations were completely symmetric about the axis of $y^* = 0$. The velocity fluctuation $v^*$ is positive in the figures when $v^*$ is directed radially outwards.

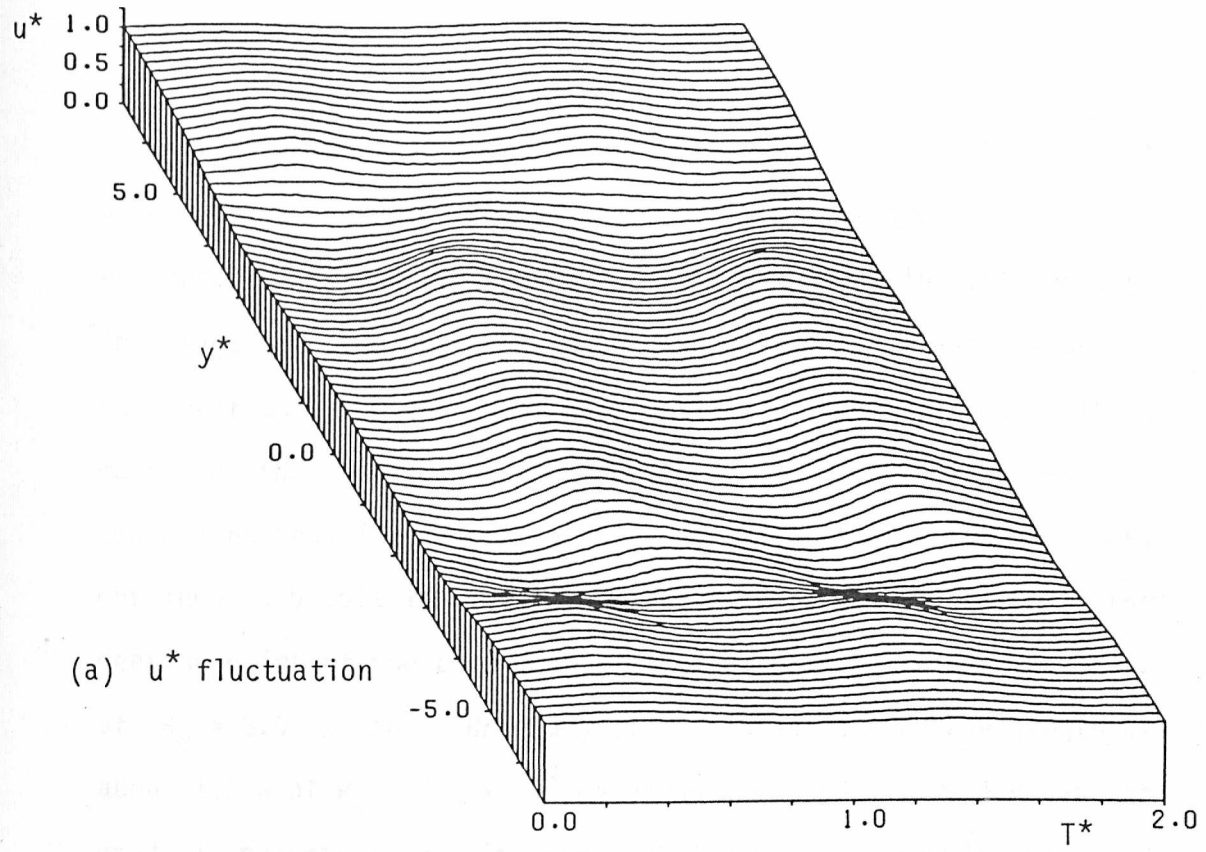



(a) u* fluctuation




(b) v* fluctuation

Figure 3.1.20 Conditionally averaged velocity fluctuations in the wake behind the thin sharp-edged cross-section ring model with d/w = 6.0 at x = 3.4 w, U = 10 m/s.



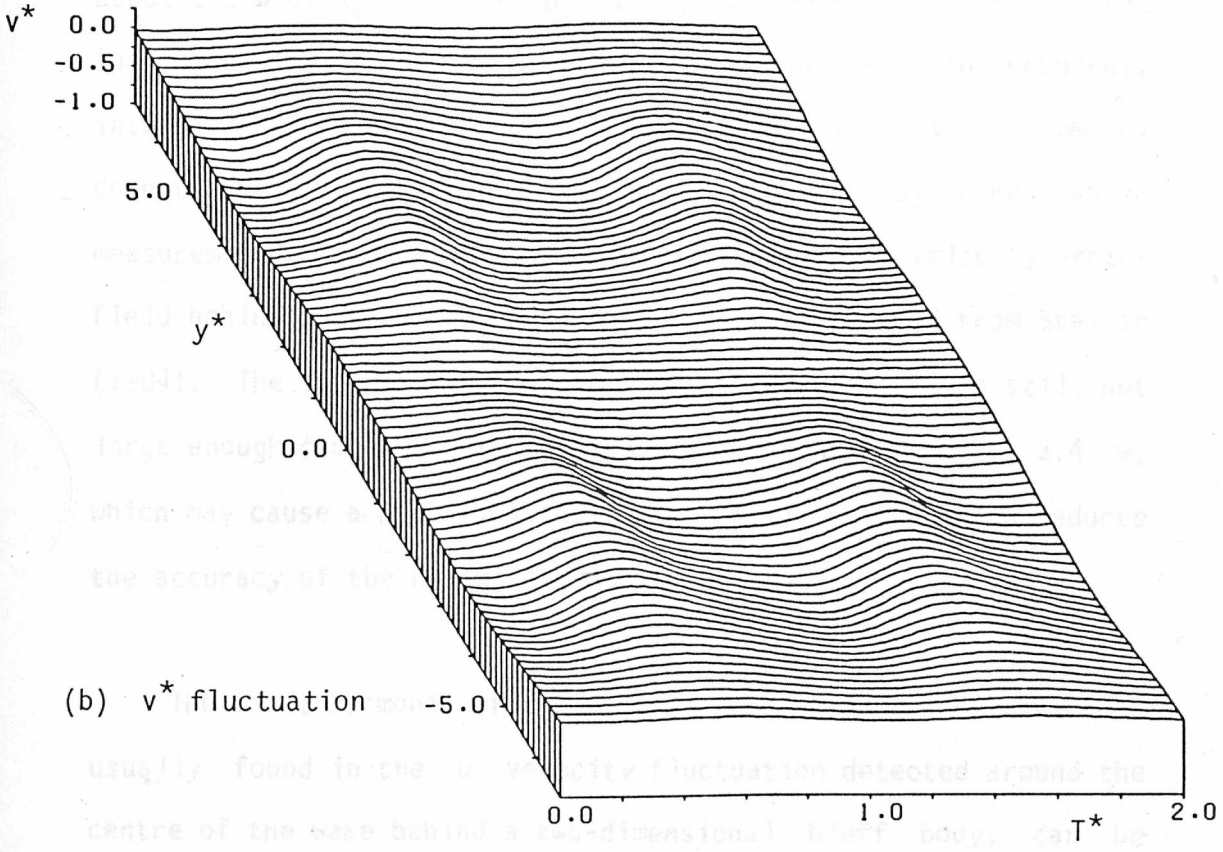




Figure 3.1.21 Conditionally averaged velocity fluctuations in the wake behind the thin sharp-edged cross-section ring model with d/w = 6.0 at x = 8.0 w, U = 10 m/s.

It is known that there are problems associated with using hot wires in a near wake region. The difficulties are caused by the existence of strong turbulence and reverse flow. In the present investigation two positions were chosen, x = 3.4 w and x = 8.0 w, to investigate the change of wake pattern. Fail et al. (1957) measured the time-mean flow pattern of the near wake behind a two-dimensional flat plate by using a Pitot-static tube. They obtained a bubble length, the distance from the flat plate to the meeting point of the time-mean free shear layers, of about 2.8 w at $R_e = 8.9 \times 10^4$. Bradbury (1976) obtained a bubble length of about 1.9 w at $R_e = 2.5 \times 10^4$ by using a pulsed-wire which can be used in reverse flow. Steiner (1984) obtained a bubble length of about 2.2 w at $R_e = 2 \times 10^4$ by using a flying hot-wire. This instrument can be used to make accurate measurements in turbulent, intermittent reversed flow. The position x = 3.4 w is someway downstream of the bubble boundary obtained by the above measurements. Figure 3.1.22 shows a time-mean velocity vector field behind a two-dimensional flat plate, reproduced from Steiner (1984). The velocity $u^*$ shown in the Figure 3.1.22 is still not large enough compared with the velocity $v^*$ at around x = 3.4 w, which may cause a high flow angle when vortices shed which reduces the accuracy of the hot-wire measurements.

The first harmonic of the vortex shedding frequency, which is usually found in the u velocity fluctuation detected around the centre of the wake behind a two-dimensional bluff body, can be

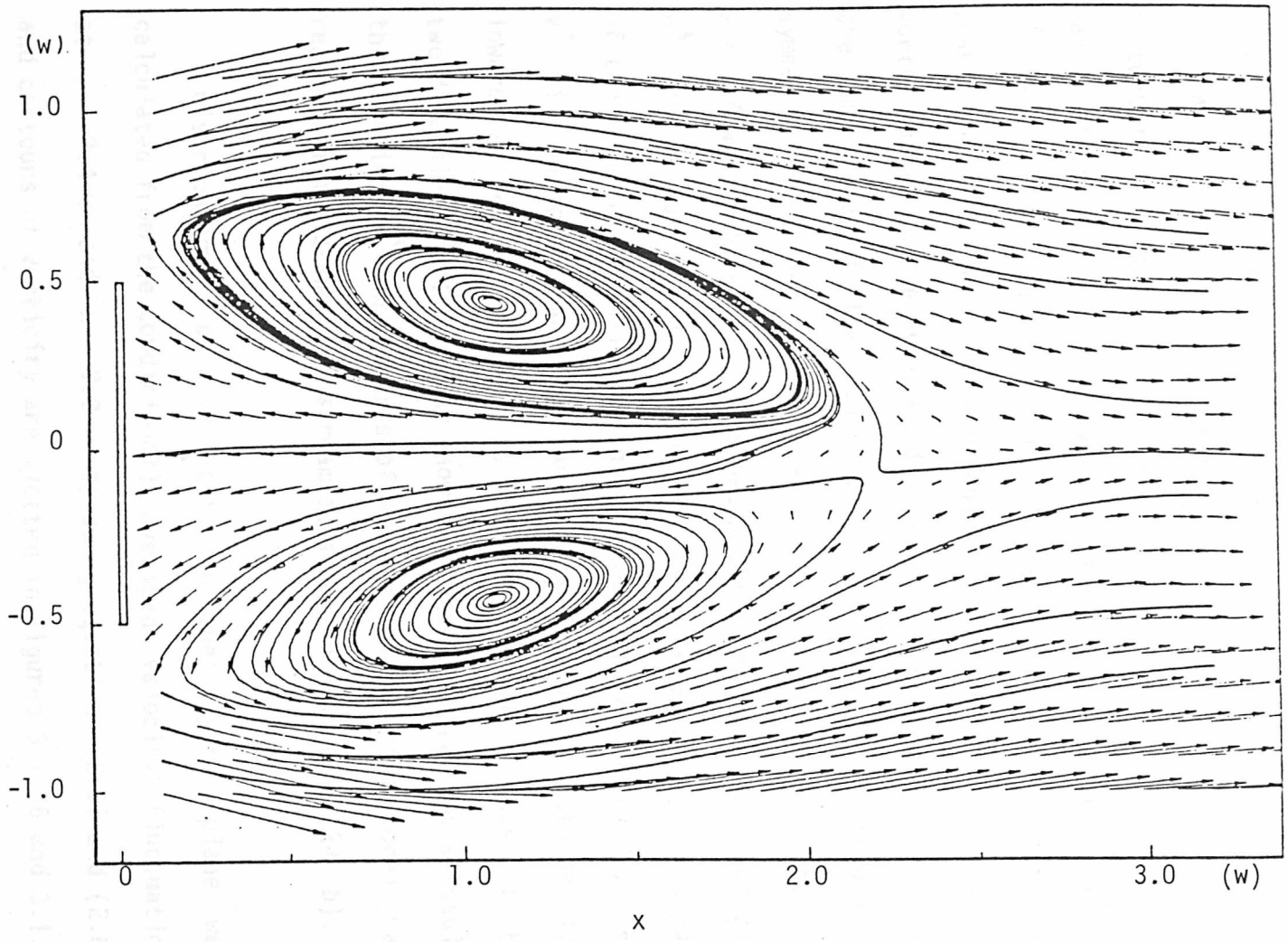
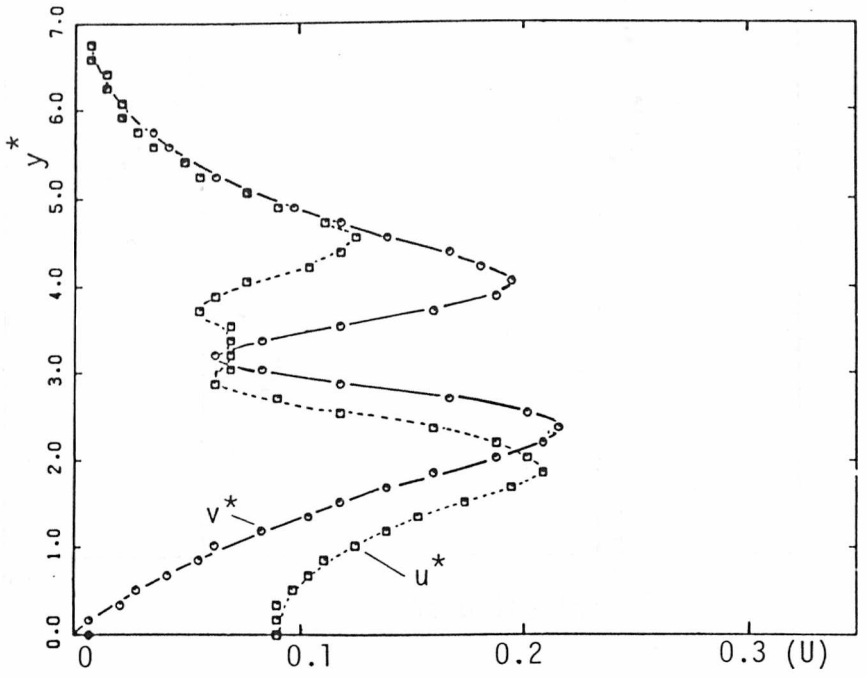



Figure 3.1.22 Time-mean velocity vector field and integrated streamline pattern behind a two-dimensional flat plate, reproduced from Steiner (1984)

clearly recognised in Figure 3.1.20 (a). However it can not be seen in Figure 3.1.21 (b), which suggests a substantial change in the arrangement of vortices in the wake. The patterns of conditionally averaged velocity fluctuations at x = 8.0 w shown in Figure 3.1.21 are smoother on the whole compared with those at x = 3.4 w, which suggests that flow in the wake is mixed rapidly by turbulence. Figure 3.1.23 shows profiles of root-mean-square values of the conditionally averaged velocity fluctuations $u^*$ and $v^*$ at x = 3.4 w and x = 8.0 w respectively. There exists clear peaks at x = 3.4 w which are caused by the inside and outside vortex rings. On the other hand, the peaks are less pronounced and the amplitude of the velocity fluctuation $u^*$ on the axis of symmetry is larger at x = 8.0 w compared with those at x = 3.4 w. Figure 3.1.24 shows profiles of the mean velocities $u^*$ and $v^*$ at x = 3.4 w and x = 8.0 w respectively. The part of the wake on the inside of the ring model flows outwards, i.e. $v^*$ is positive, and the part of the wake on the outside flows inwards at x = 3.4 w, which is similar to the near wake of the two-dimensional bluff body shown in Figure 3.1.22. As a result, the velocity $u^*$ on the axis of symmetry of the ring model wake reduces with distance downstream as shown in Figure 3.1.24 (b).

Distributions of vorticity in the (y,t) plane were calculated from the conditionally averaged velocity fluctuations at x = 3.4 w and x = 8.0 w by using equations (2.5) and (2.6), and contours of vorticity are plotted in Figures 3.1.25 and 3.1.26 respectively. The patterns of the contours at x = 3.4 w are

(a) x = 3.4 w




(b) x = 8.0 w

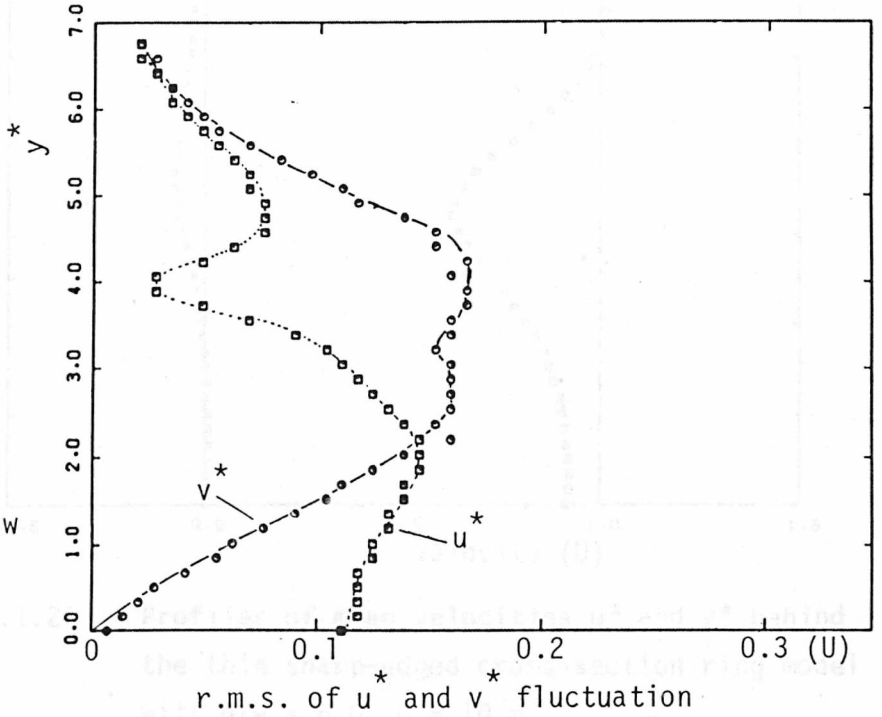
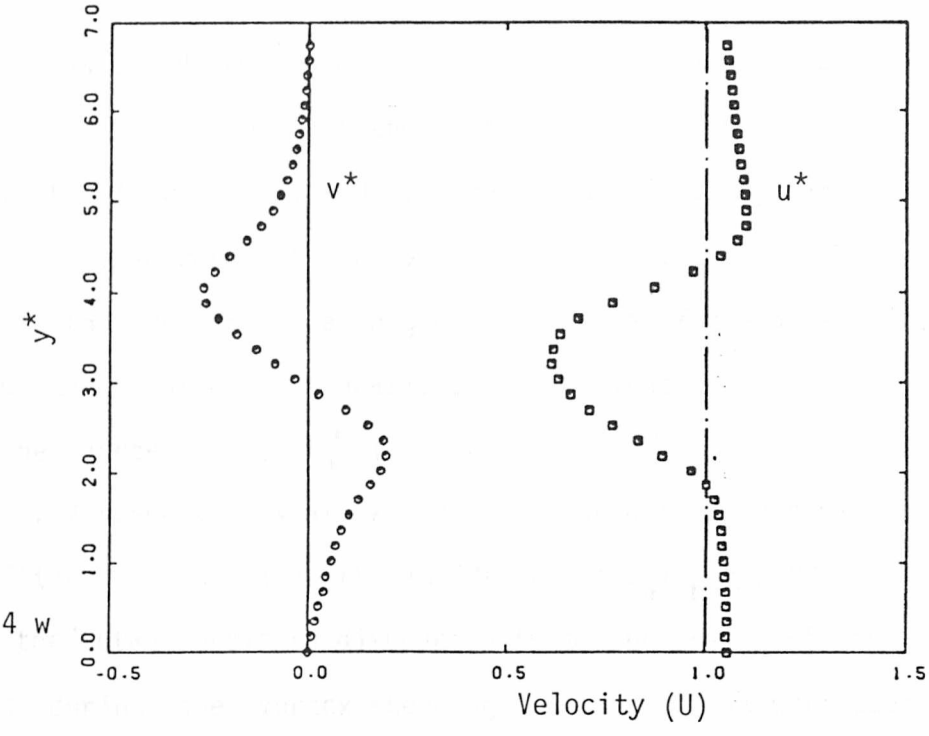
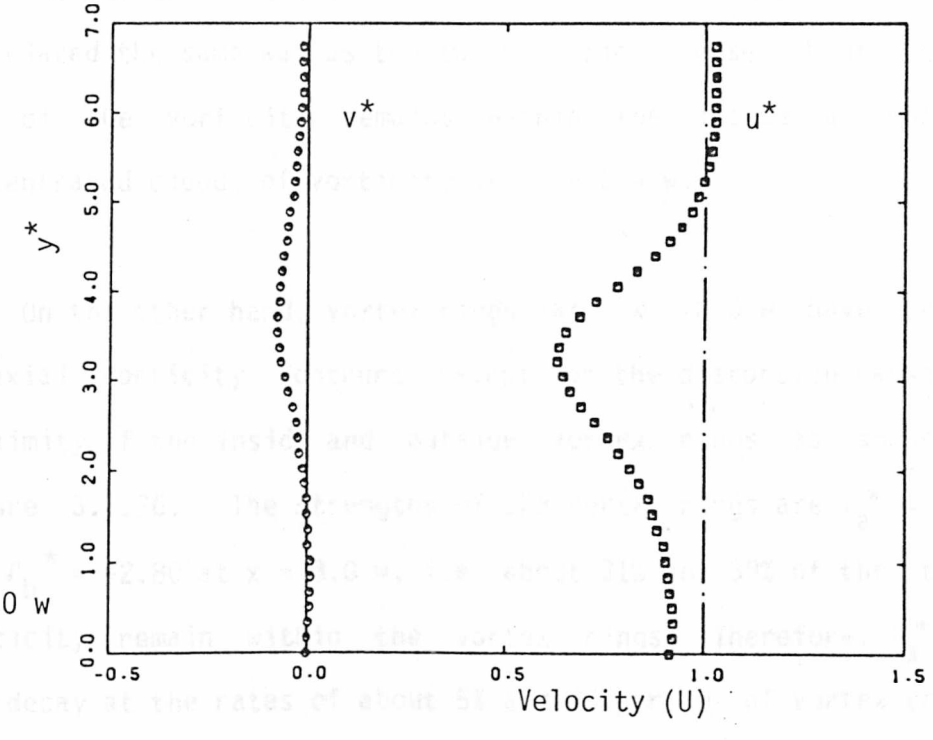



Figure 3.1.23 Root-mean-square profiles of conditionally averaged velocity fluctuations $u^*$ and $v^*$ in the wake behind the thin sharp-edged cross-section ring model, $R_e = 2.0 \times 10^4$.




(a)
x = 3.4 w




(b)
x = 8.0 w

Figure 3.1.24 Profiles of mean velocities u* and v* behind the thin sharp-edged cross-section ring model with d/w = 6.0, U = 10 m/s.

fairly distorted from co-axial circles as the shear layers seem to have a strong influence on the vortex rings in the near wake. The strengths of the inside and outside vortex rings, $\Gamma_a$ and $\Gamma_b$, were obtained by integrating the vorticity distributions. The lowest 5% of the vorticity was neglected because of the uncertainty of the boundary for the integration. Non-dimensionalized strengths of the vortex rings $\Gamma_a^*$ (= $\Gamma_a/Uw$) and $\Gamma_b^*$ (= $\Gamma_b/Uw$) are 2.75 and -3.17 respectively at $x = 3.4$ w. The outside vortex ring is a little stronger than the inside one ($-\Gamma_a/\Gamma_b = 0.87$). Compared with the total vorticity discharged from one side of the ring model during one vortex shedding cycle, which is estimated from the measurement of the base pressure provided vorticity discharged from the inside and outside of the ring model is equal and can be calculated the same way as the two-dimensional case, about 38% and 44% of the vorticity remains within the inside and outside concentrated clouds of vorticity at $x = 3.4$ w.

On the other hand, vortex rings at $x = 8.0$ w have fairly co-axial vorticity contours except for the distortion caused by proximity of the inside and outside vortex rings as shown in Figure 3.1.26. The strengths of the vortex rings are $\Gamma_a^* = 2.19$ and $\Gamma_b^* = -2.80$ at $x = 8.0$ w, i.e. about 31% and 39% of the total vorticity remain within the vortex rings. Therefore, $\Gamma_a^*$ and $\Gamma_b^*$ decay at the rates of about 5% and 3% per w of vortex travel between $x = 3.4$ w and $x = 8.0$ w respectively. Cantwell and Coles (1983) measured a vorticity distribution in the wake of a circular cylinder at $R_e = 1.4 \times 10^5$ by using a flying hot-wire

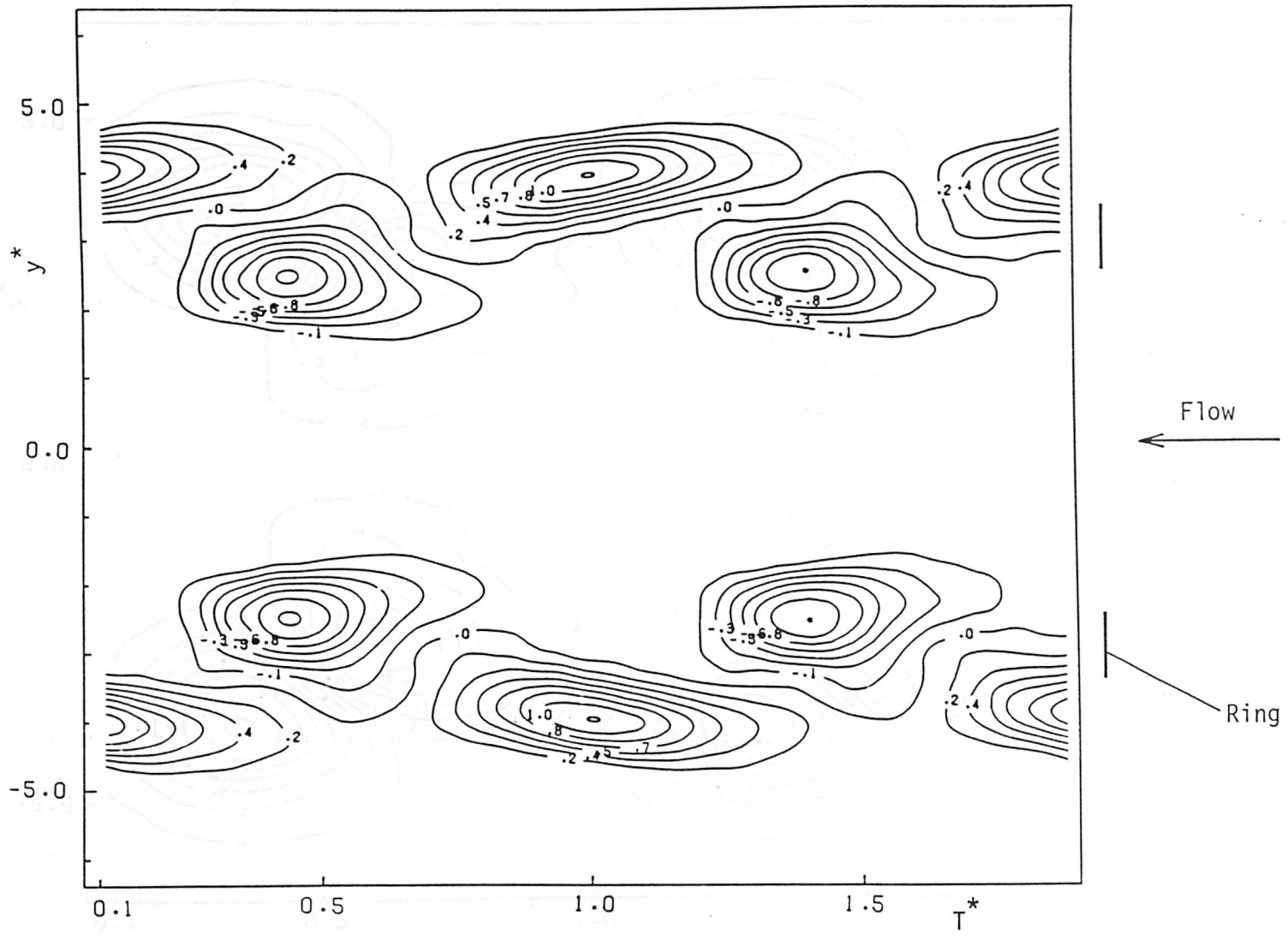



Figure 3.1.25 Vorticity distribution in the wake behind the thin sharp-edged cross-section ring model with d/w = 6.0, x = 3.4 w, $R_e$ = 2.0 x $10^4$

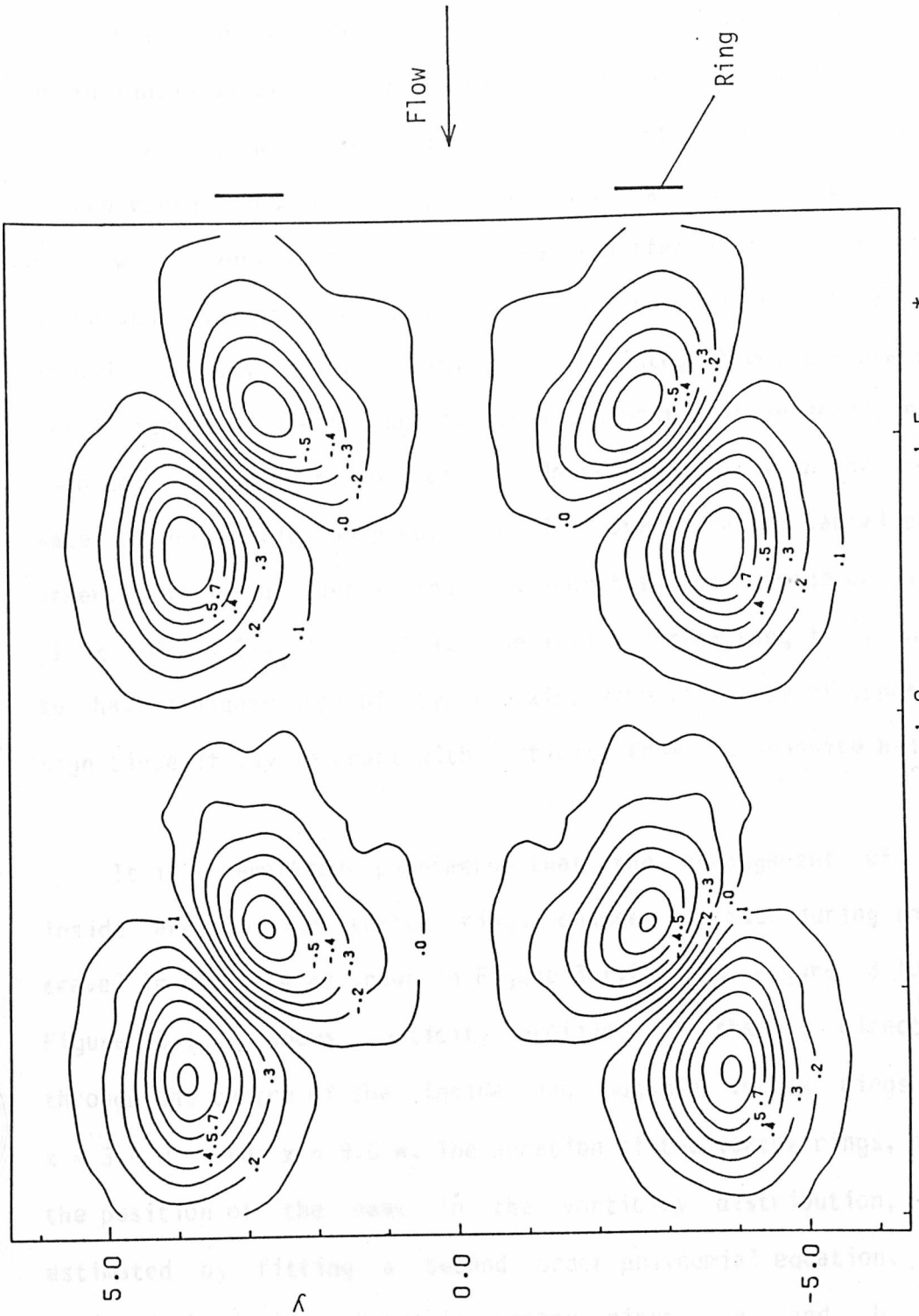



Figure 3.1.26 Vorticity distribution in the wake behind the thin sharp-edged cross-section ring model with $d/w = 6.0$, $x = 8.0\ w$, $R_e = 2.0 \times 10^4$

and the conditional averaging technique. They found that non-dimensional strength of vortices reaches a maximum of 2.58 at about $x = 3.6\ w$, where about 44% of the total vorticity remains in the vortex, and then decays slowly with $x$ at the rate of 8% per $w$ of vortex travel. In spite of differences in bluff body shape and Reynolds number, as well as an uncertainty about the actual boundary of vorticity for the integration, the present result agrees well with theirs. It is thought that generally more than half of the total vorticity is destroyed quickly in the near wake as vorticities with opposite signs are mixed and cancel each other. The inside vortex ring is weaker than the outside one also at $x = 8.0\ w$ ($-\Gamma_a/\Gamma_b = 0.78$). The inside vortex ring is thought to have a higher probability of mixing with vorticity of opposite sign since it may interact with vorticity from its opposite half.

It is a remarkable phenomenon that the arrangement of the inside and outside vortex rings changes so much during their travel in the wake as shown in Figure 3.1.25 and Figure 3.1.26. Figure 3.1.27 shows vorticity profiles in the $y$ direction through the centre of the inside and outside vortex rings at $x = 3.4\ w$ and $x = 8.0\ w$. The location of the vortex rings, i.e. the position of the peak in the vorticity distribution, was estimated by fitting a second order polynomial equation. The radii of the inside and outside vortex rings, $a$ and $b$, are about $2.5\ w$ and $3.9\ w$ at $x = 3.4\ w$ and about $2.7\ w$ and $3.9\ w$ at $x = 8.0\ w$ respectively. The radii of both vortex

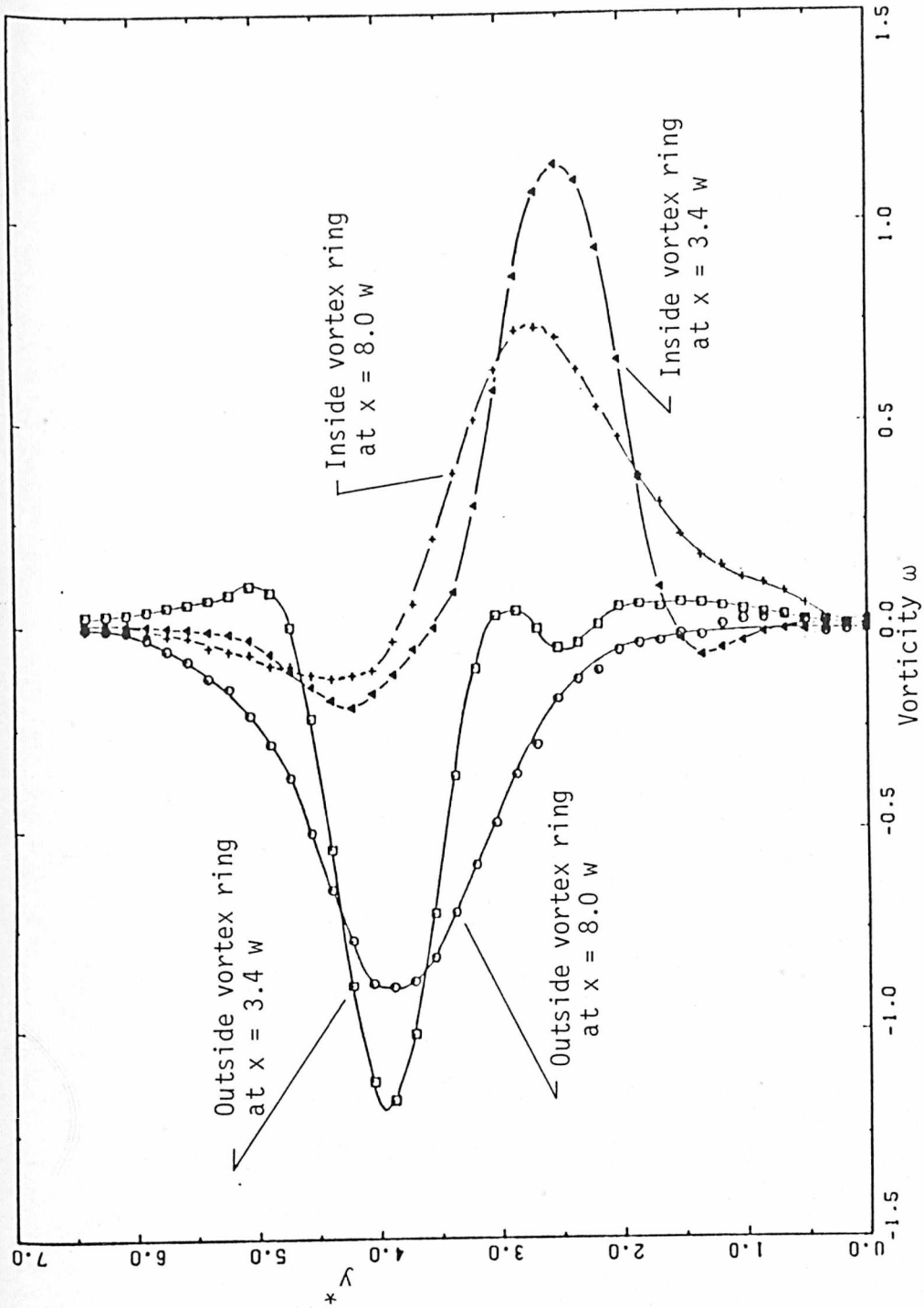



Figure 3.1.27 Vorticity profiles through the centres of vortex rings at x = 3.4 w and x = 8.0 w.

rings are expected to grow during their travel in the wake from consideration of the induced velocity of the vortex rings, however, the radius of only the inside vortex ring actually increased and the radius of the outside one kept almost constant. The reason is not clear, but cancellation of vorticity caused by the proximity of the inside and outside vortex rings and the distorted vorticity distribution may have had some influence on the change of radii. Figure 3.1.28 shows the variation of vorticity with time at the $y^*$ positions where the centres of vortex rings pass through at $x = 3.4$ w and $x = 8.0$ w respectively. The phase difference between the inside and outside vortex rings at $x = 3.4$ w is nearly $180^0$ out of phase, whereas at $x = 8.0$ w the phase difference becomes quite small. The ratio $h/\ell$ is about 0.45 at $x = 3.4$ w and 0.27 at $x = 8.0$ w, where $\ell$ is the longitudinal spacing of both inside and outside vortex rings and h is the lateral spacing between adjacent inside and outside vortex rings. A vortex ring has a self-induced velocity (Batchelor 1967), and this is thought to be the main cause of the difference in the arrangements between axisymmetrical vortices and vortices behind two-dimensional bluff bodies. The vortices shed from the inside and outside of the ring models, alternately at nearly $180^0$ out of phase, quickly get closer to each other because their self-induced velocities are in the opposite directions.

The clouds of vorticity in the wake flow with the fluid and have a relative velocity to the fluid which is induced by the

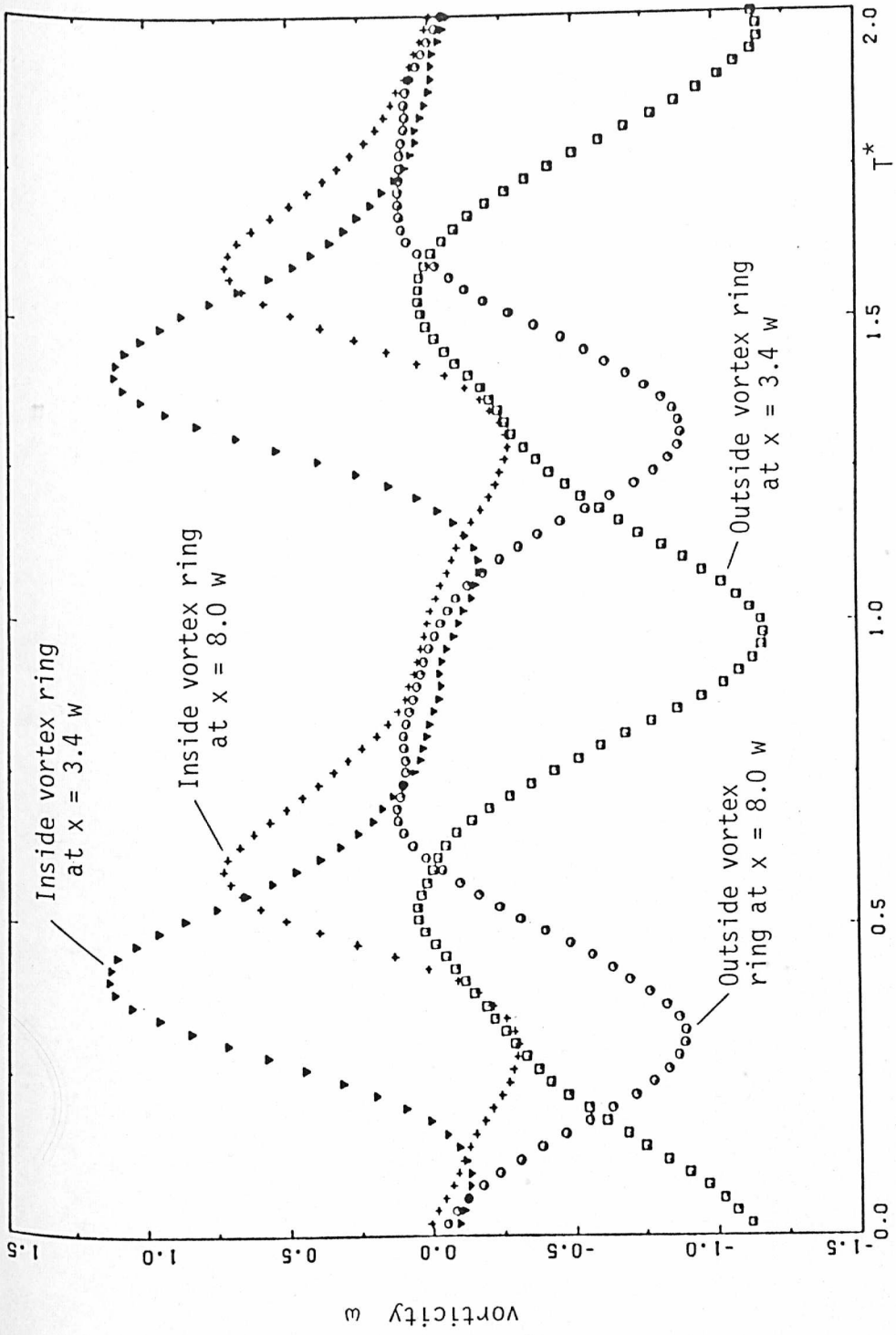
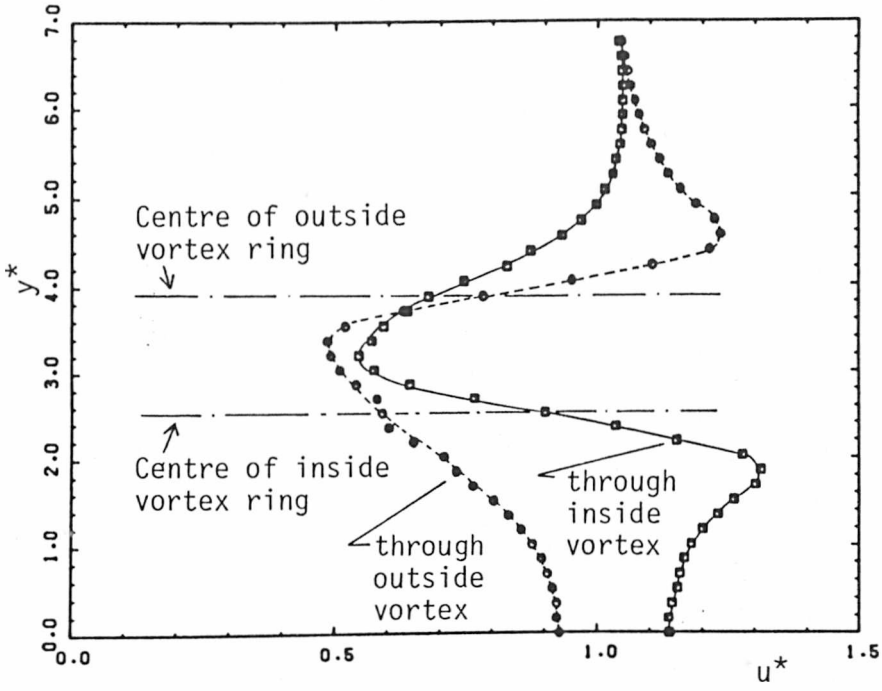
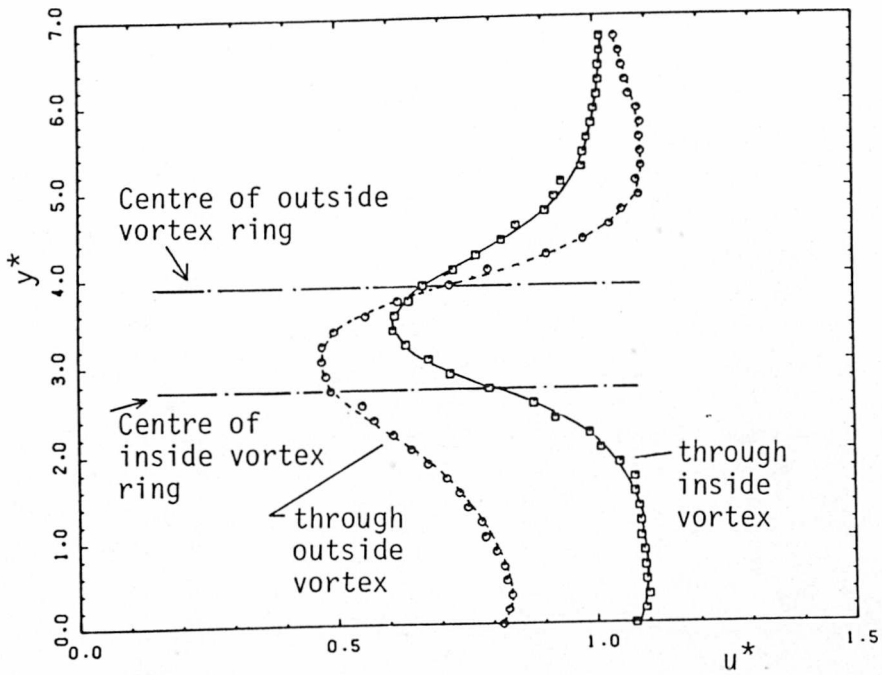



Figure 3.1.28 Variations of vorticity with time at the paths of the centre of vortex rings, x = 3.4 w and x = 8.0 w.

vorticity field. The convection velocity $u_c$ of an ideal infinite row of staggered point vortices was given theoretically by Karman (1911) and values of $u_c$ of vortices from two-dimensional bluff bodies have been estimated by many people. Simmons (1974) used a method to determine $u_c$ which measured the phase difference between the signals from two hot-wires separated in the wake in the direction of mean flow. He found that the two hot-wires should be located close to the paths of the centres of vortices in the wake for a good estimate of $u_c$ and the region in which $x < 3.0$ w or more than 1.5 w away from the centre line of the wake behind a two-dimensional bluff body, cannot be used to obtain a representative value for $u_c$. In fact, an accurate and consistent measurement of $u_c$ is not so easy. Davies (1975) measured $u_c$ in the wake behind a two-dimensional flat plate and the results obtained at $x = 6.0$ w and within 1.0 w from the centre line of the wake were scattered between 0.72 U and 0.87 U. Furthermore, measurement of $u_c$ in a three-dimensional wake is more sensitive to position, since each vortex has a curvature which gives rise to a self-induced velocity. Therefore, $u_c$ values for vortex rings have been taken from the conditionally averaged velocities at the centres of each of the vortices in the present experiment. Figure 3.1.29 shows velocity profiles of $u^*$ through the centres of the inside and outside vortex ring at $x = 3.4$ w and $x = 8.0$ w respectively. The $u_c$ of the inside and outside vortex rings are 0.90 U and 0.78 U at $x = 3.4$ w and 0.79 U and 0.72 U at $x = 8.0$ w respectively. The measurements for vortex rings in the wake behind the thin sharp-edged




(a) x = 3.4 w




(b) x = 8.0 w

Figure 3.1.29 Velocity profiles through centres of vortex rings

cross-section ring model with $d/w = 6.0$ at $x = 3.4\ w$ and $x = 8.0\ w$ are shown summarized in Table 3.1.2.

Figures 3.1.30 and 3.1.31 show conditionally averaged velocity vector fields at $x = 3.4\ w$ and $x = 8.0\ w$ respectively. Vortex rings can be clearly recognised in the velocity vector fields plotted in Figure 3.1.32 and Figure 3.1.33 in which the convection velocity of the inside vortex ring has been subtracted from the total velocity. It is an interesting observation that there exists a fairly large area around the centre where the fluid moves at almost the same velocity as the centre of the inside vortex ring at both $x = 3.4\ w$ and $x = 8.0\ w$.

### 3.1.4 Effect of afterbody shapes

The special ring models with the triangular cross-section and the rectangular cross-section of $\delta/w = 0.6$ shown in Figure 2.2 were tested here and compared with the thin sharp-edged cross-section ring model with $d/w = 6.0$ to examine the effect of afterbody shape.

The base pressure of the special ring models was measured in the same way as previously described and the effect of wind tunnel blockage was corrected by using Maskell's formulae, in which $C_D$

## TABLE 3.1.2

Vortex rings from the thin sharp-edged cross-section ring model with d/w = 6.0

| Downstream Position x | 3.4 w | 8.0 w |
|---|---|---|
| $\Gamma_a^*$ (Inside Vortex) | 2.75 | 2.19 |
| $\Gamma_a$ / Total Vorticity | 38% | 31% |
| $\Gamma_b^*$ (Outside Vortex) | -3.17 | -2.80 |
| $\Gamma_b$ / Total Vorticity | 44% | 39% |
| $-\Gamma_a / \Gamma_b$ | 0.87 | 0.78 |
| a (Inside Vortex Radius) | 2.5 w | 2.7 w |
| b (Inside Vortex Radius) | 3.9 w | 3.9 w |
| $h/\ell$ (Spacing Ratio) | 0.45 | 0.27 |
| $u_c$ of Inside Vortex | 0.90 U | 0.79 U |
| $u_c$ of Outside Vortex | 0.78 U | 0.72 U |

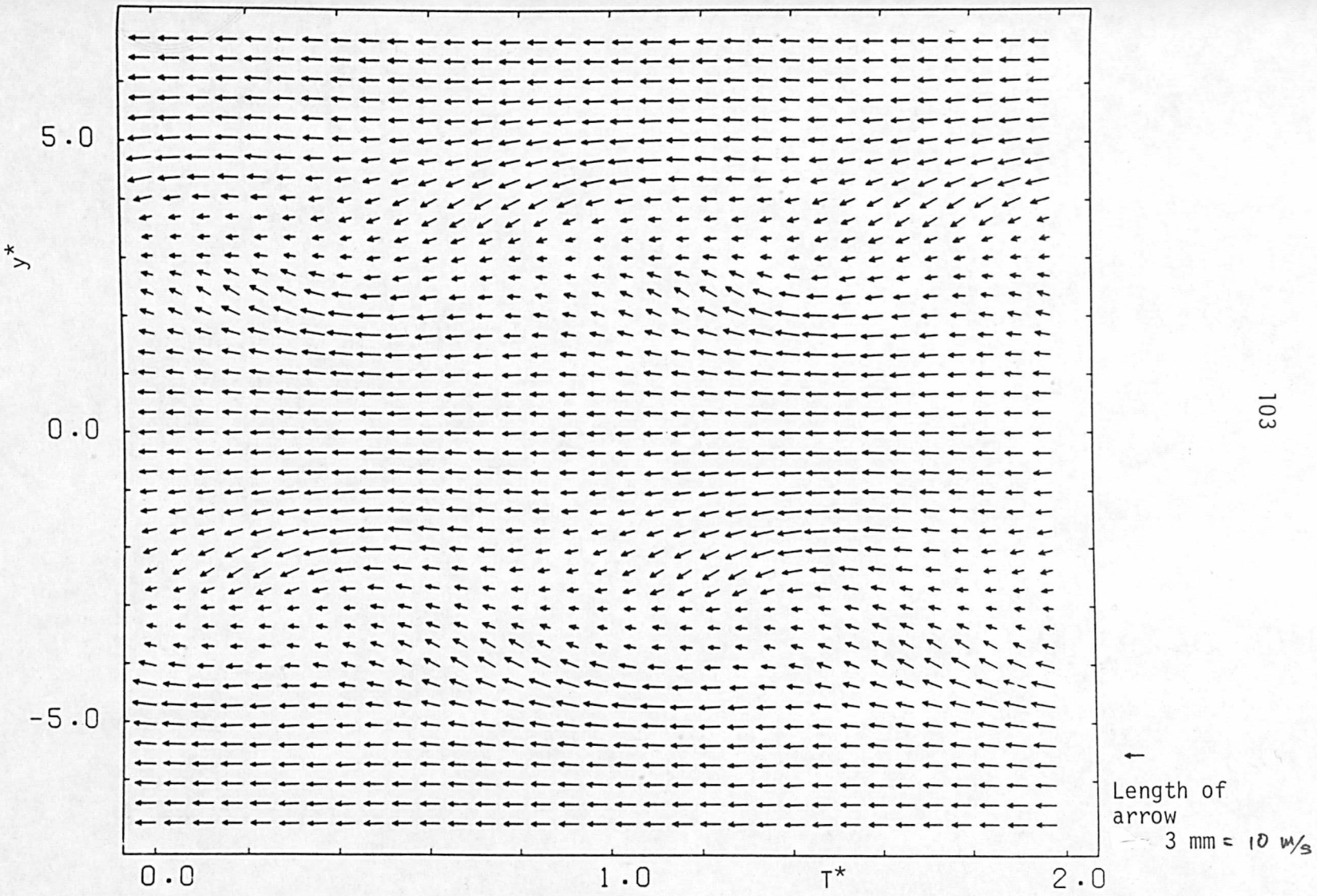



Figure 3.1.30 Velocity vector field in the wake behind the thin sharp-edged cross-section ring model with d/w = 6.0 at x = 3.4 w, U = 10 m/s.

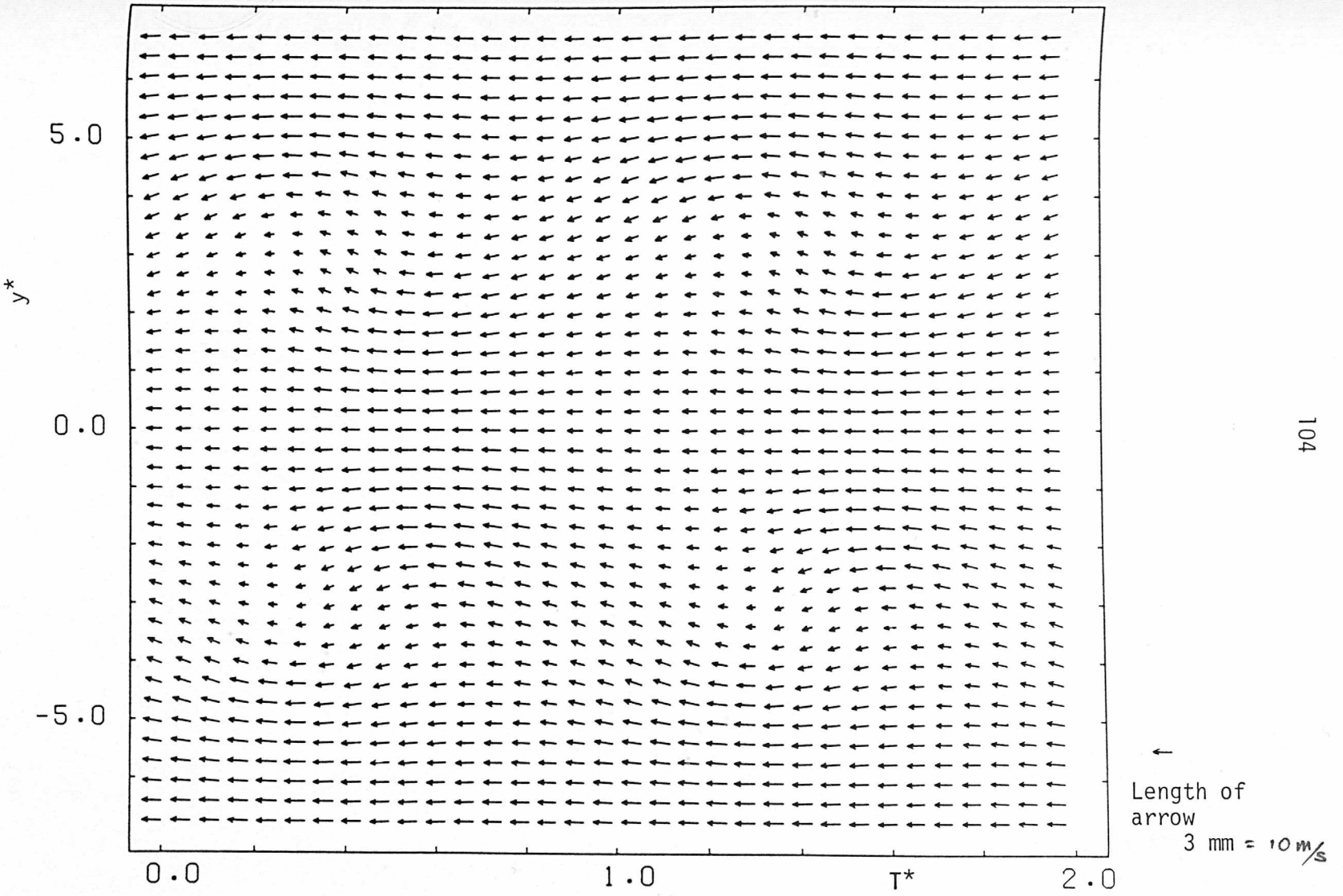



Figure 3.1.31 Velocity vector field in the wake behind the thin sharp-edged cross-section ring model with d/w = 6.0 at x = 8.0 w, U = 10 m/s.

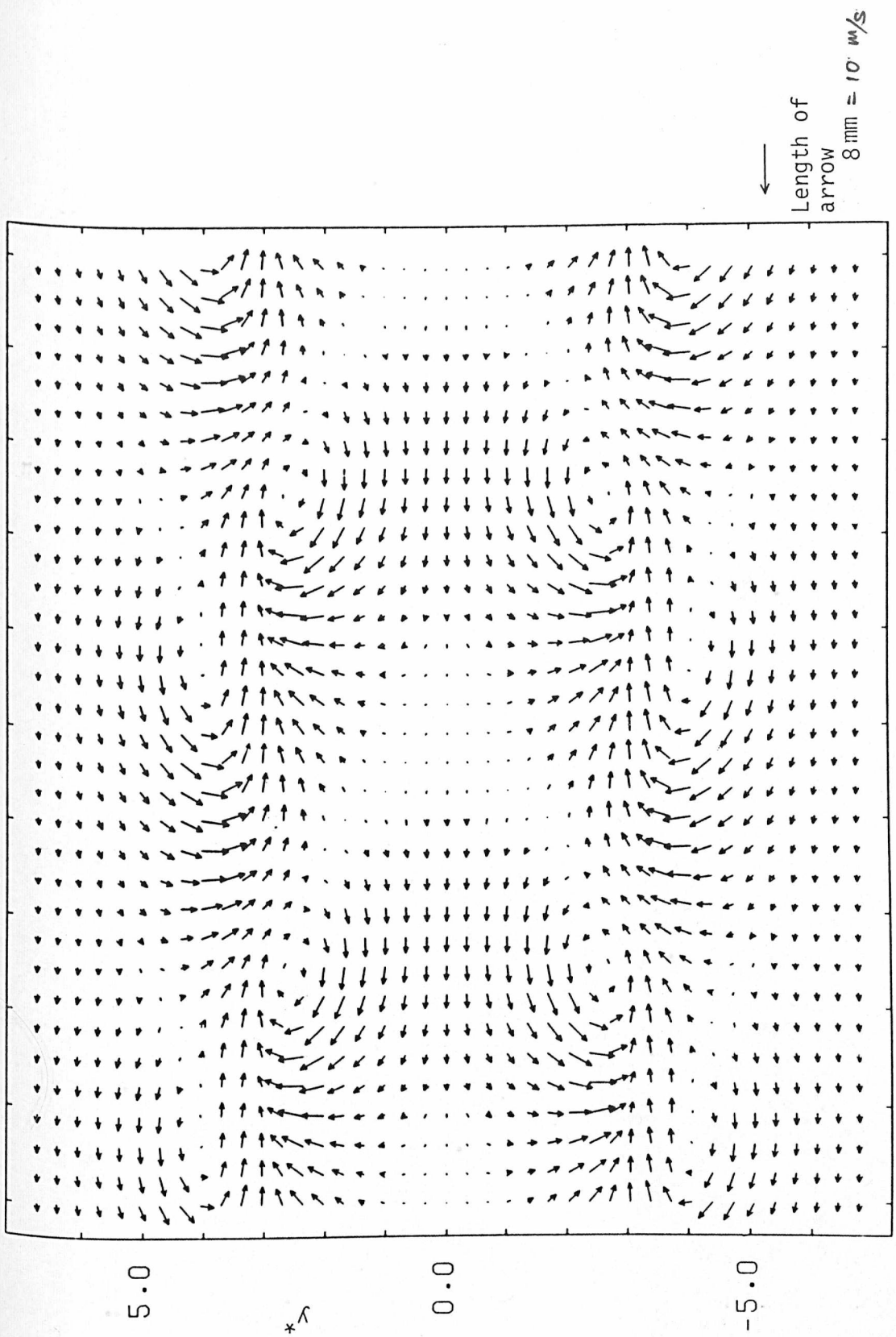



Figure 3.1.32 Velocity vector field in the wake behind the thin sharp-edged cross-section ring model with d/w = 6.0 at x = 3.4 w, $u_c$ = 0.90U removed, U = 10 m/s.

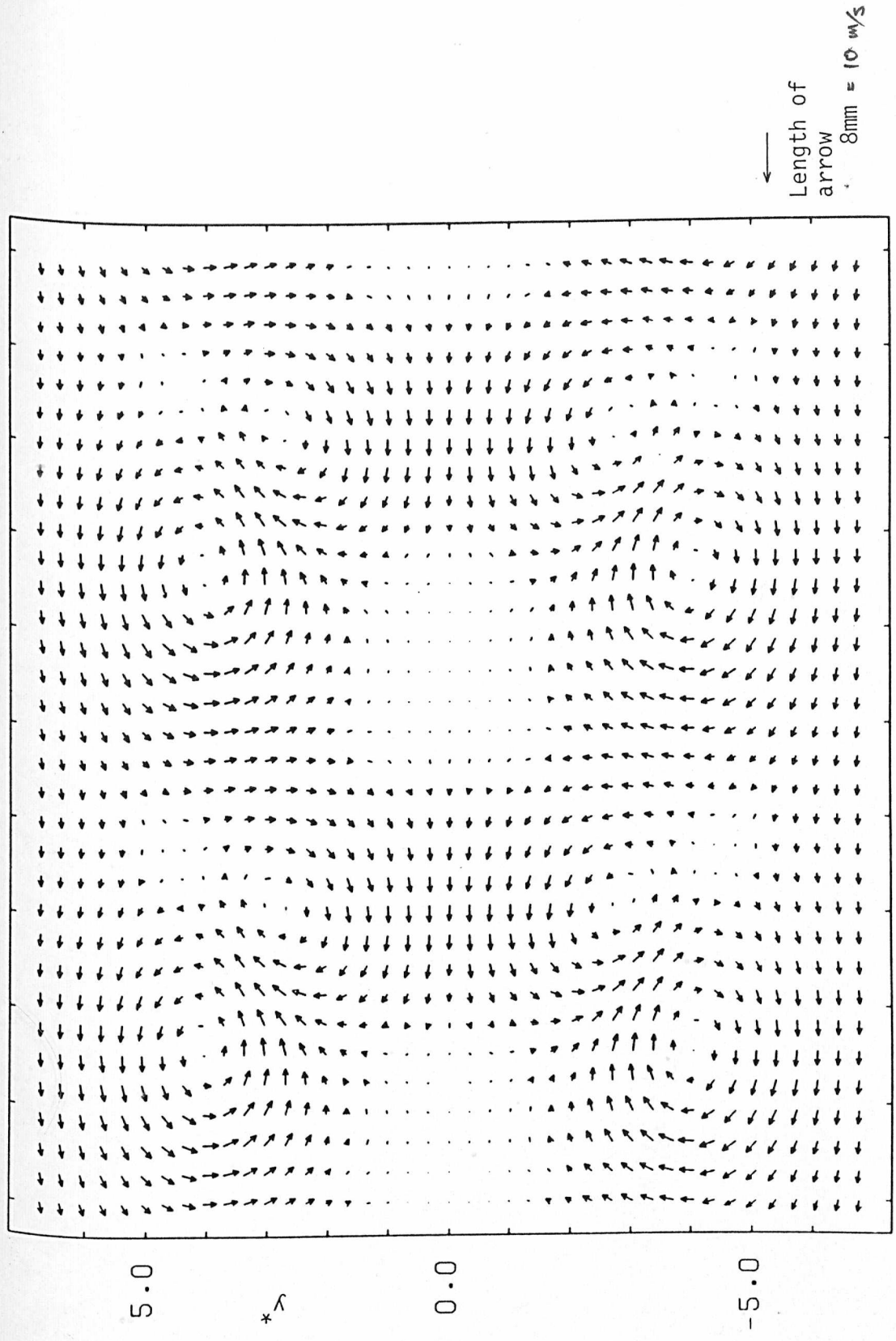



Figure 3.1.33 Velocity vector field in the wake behind the thin sharp-edged cross-section ring model with d/w = 6.0 at x = 8.0 w, $u_c$ = 0.79U removed, U = 10 m/s.

was approximated by 0.8 - $C_{pb}$. The corrected value is $C_{pb}$ = -0.97 for the triangular cross-section ring model, which is a little lower than the thin sharp-edged cross-section ring model which has $C_{pb}$ = -0.91. On the other hand, the rectangular cross-section ring model has a remarkable low value of $C_{pb}$ = -1.83, though it is a little higher than the value of -2.18 measured on the two-dimensional cylinder with the same cross-section by Bearman and Trueman (1972). The results of the measurements are summarized in Table 3.1.3.

Figure 3.1.34 shows the correlations of velocity fluctuations in the wakes behind the special ring models versus angular separation. The degree of correlation of the rectangular cross-section ring model is markedly high and there is no significant difference between the triangular cross-section ring modeland the thin sharp-edged cross-section ring model. The low base pressure and the high correlation suggest that very strong vortex rings with a highly coherent structure are shed from the rectangular cross-section ring model. Figure 3.1.35 shows a comparison between the ring model and the two-dimensional cylinder with the same cross-section of $\delta/w$ = 0.6, in which the correlation coefficients are plotted along a spanwise separation. The data for the cylinder are reproduced from Bearman and Trueman (1972). The correlation coefficient of the ring model is still high even at a large spanwise separation as there exists no disturbance from the ends of the bluff body.

## Table 3.1.3

**Measurements of base pressure**

| Model | Cross-Section | Measured $C_{pb}$ | Corrected $C_{pb}$ | $R_e$ |
|---|---|---|---|---|
| Ring with d/w = 6.0 | thin sharp-edged | -0.98 | -0.91 | $2.0 \times 10^4$ |
| Ring with d/w = 6.0 | triangular | -1.04 | -0.97* | $2.0 \times 10^4$ |
| Ring with d/w = 6.0 | rectangular $\delta/w = 0.6$ | -1.91 | -1.83* | $2.0 \times 10^4$ |
| Two-dimensional cylinder | rectangular $\delta/w = 0.6$ | - | -2.18** | $3.4 \times 10^4$ |

* $C_D = 0.8 - C_{pb}$ is assumed for blockage correction purposes

** Reproduced from Bearman and Trueman (1972)

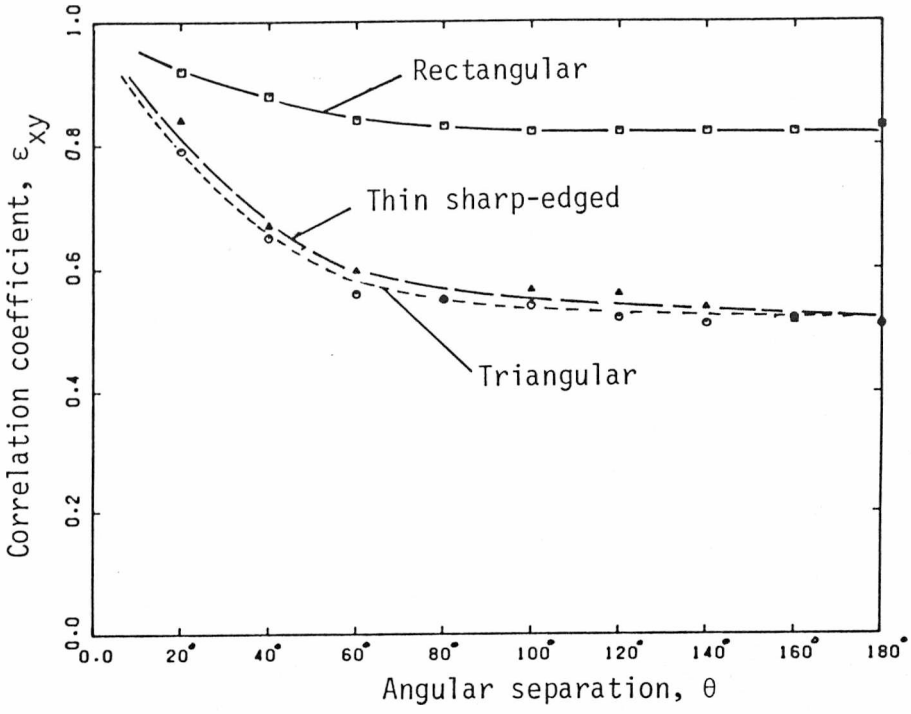



Figure 3.1.34 Correlations of velocity fluctuations behind ring models with various cross-sections.

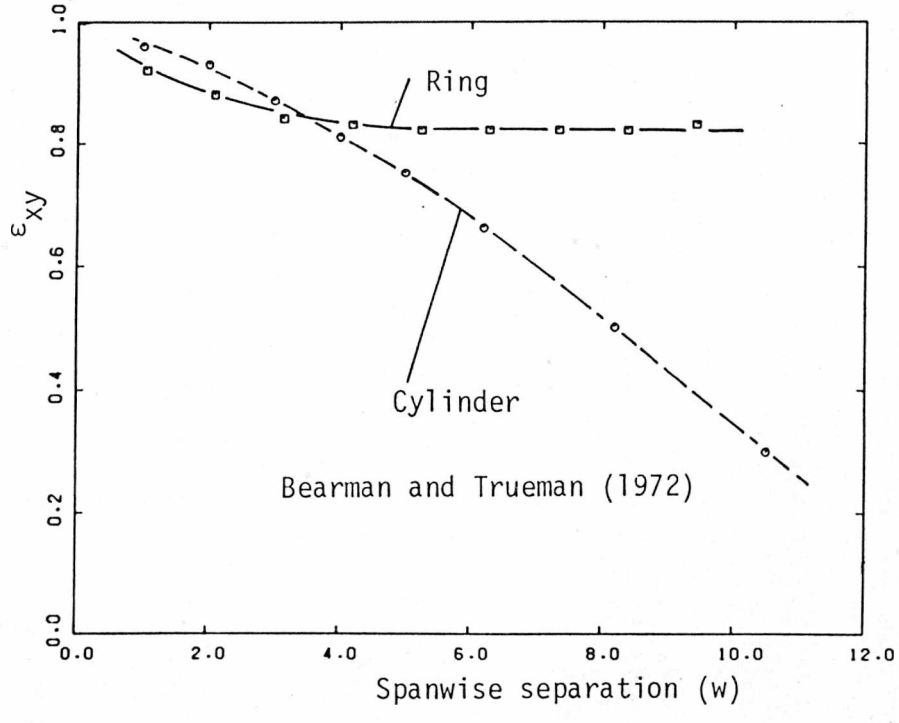
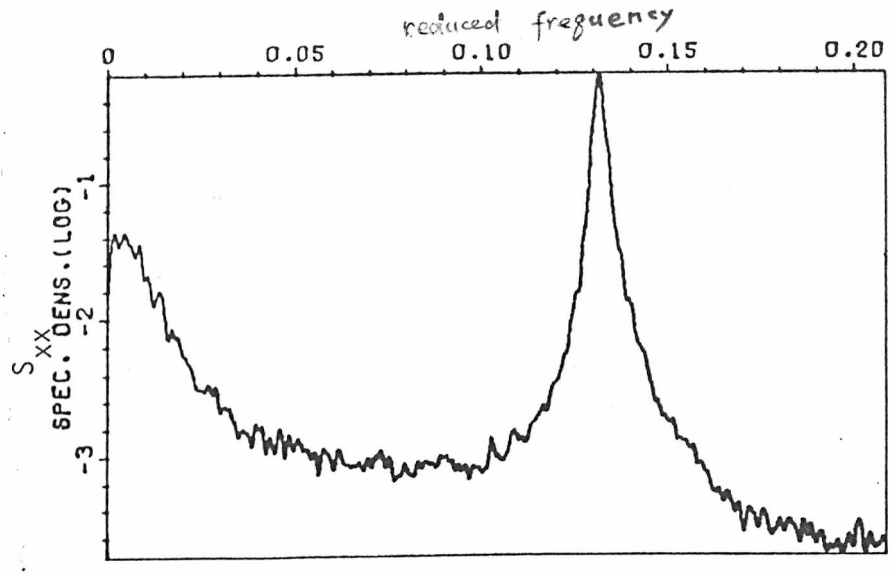



Figure 3.1.35 Correlations of the ring model and the two-dimensional cylinder with the same rectangular cross-section of $\delta/w = 0.6$ along the spanwise separation.

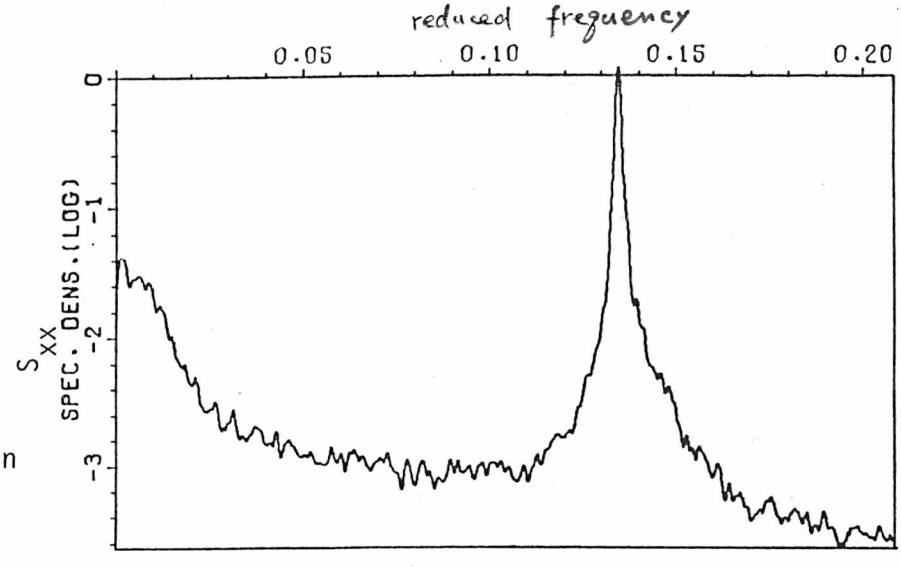
Figure 3.1.36 shows power spectral density functions $S_{xx}$ of velocity fluctuations detected on the axis of symmetry in the wake behind the ring models. The $S_{xx}$ of the thin sharp-edged cross-section ring model shown in Figure 3.1.36 (a) has a little higher peak against the background turbulence spectrum compared with the $S_{xx}$ measured outside the wake of the same ring model shown in Figure 3.1.10 (a). This is thought to be due to the fact that velocity fluctuations caused by axisymmetric vortex shedding is strengthened on the axis of symmetry. The $S_{xx}$ of the triangular cross-section ring model shown in Figure 3.1.36 (b) has a little narrower peak compared with that of the thin sharp-edged ring model, but there is no substantial difference between the two. The random fluctuations in the wake of the rectangular cross-section ring model at low frequencies is small, as shown in Figure 3.1.36 (c). It can also be recognised in the records of the wave forms of velocity fluctuations shown in Figure 3.1.37.

The remarkably regular periodic velocity fluctuation found behind the rectangular cross-section ring model is thought to have a great potential value for industrial applications. The relation between the standard deviation of time intervals between successive pulses and the repeatability of a flowmeter, which has a pulse (frequency) output proportional to a flow rate, has been investigated by Robinson (1985) who has made a numerical simulation by using a Monte Carlo method. Hayward and Jelffs (1986) have pointed out that the repeatability of the vortex

(a) Thin sharp-edged cross-section




(b) Triangular cross-section




(c) Rectangular cross-section

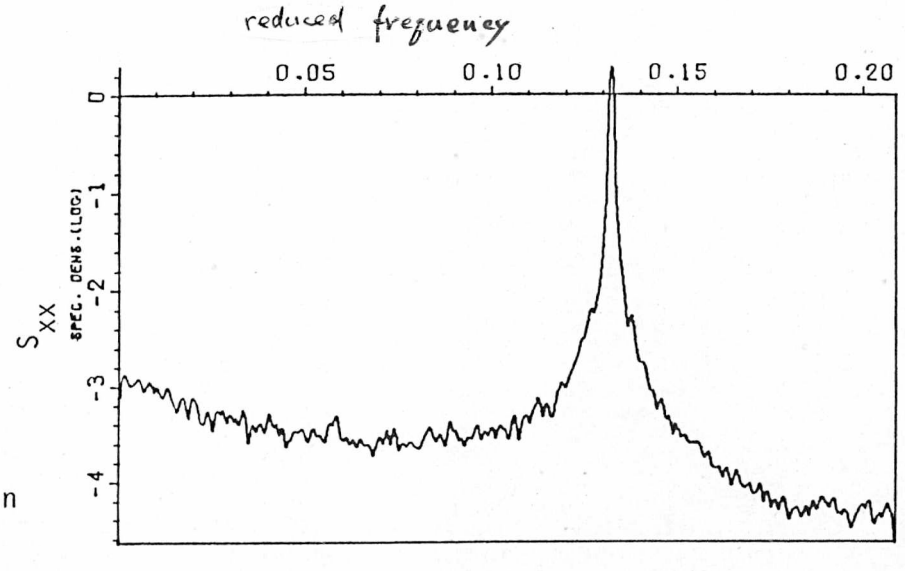



Figure 3.1.36 Power spectral density functions of velocity fluctuations measured on the axis of symmetry behind the ring models with various cross-sections, x = 3.4 w, d/w = 6.0, $R_e$ = 2.0 x $10^4$.

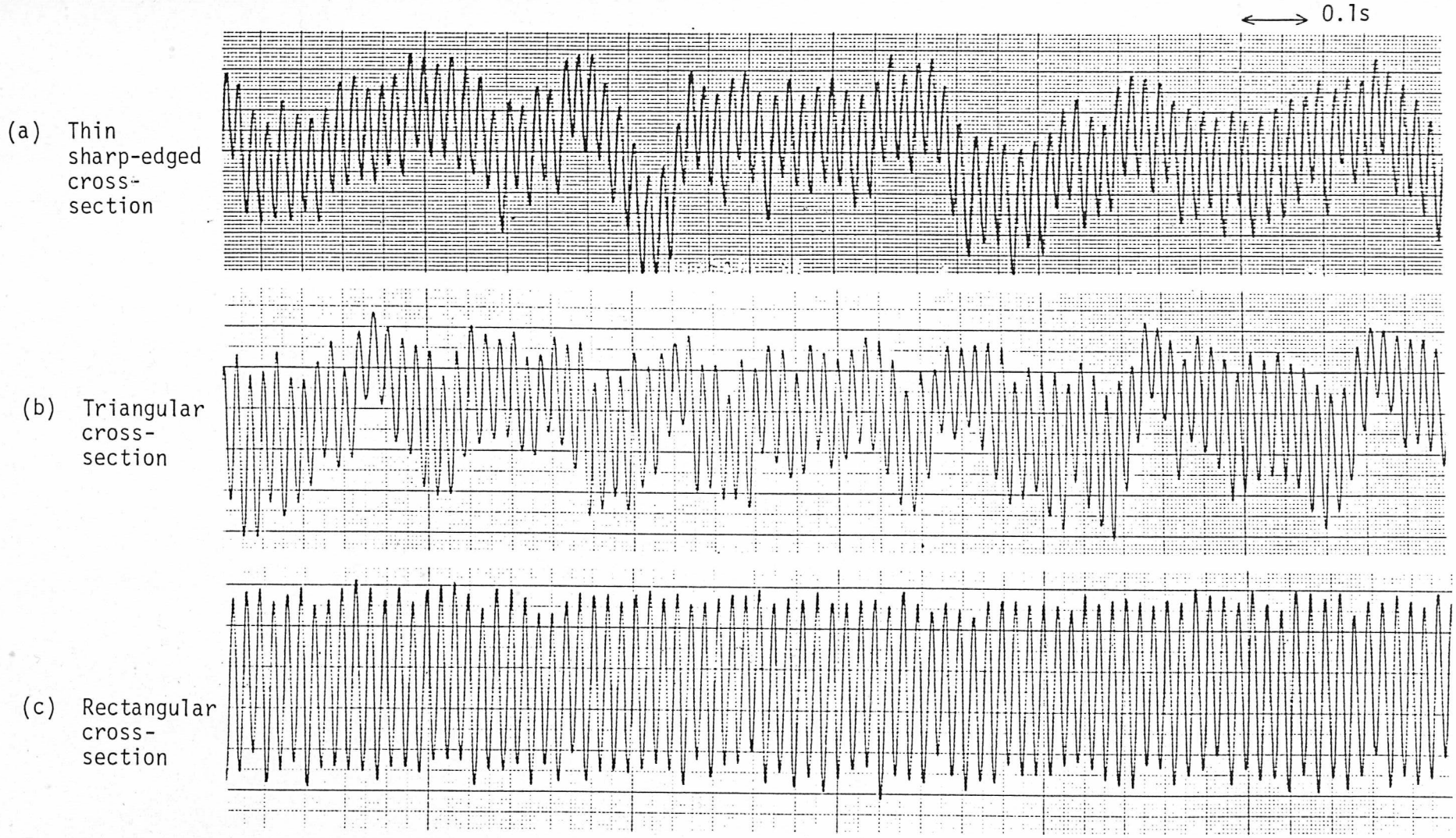
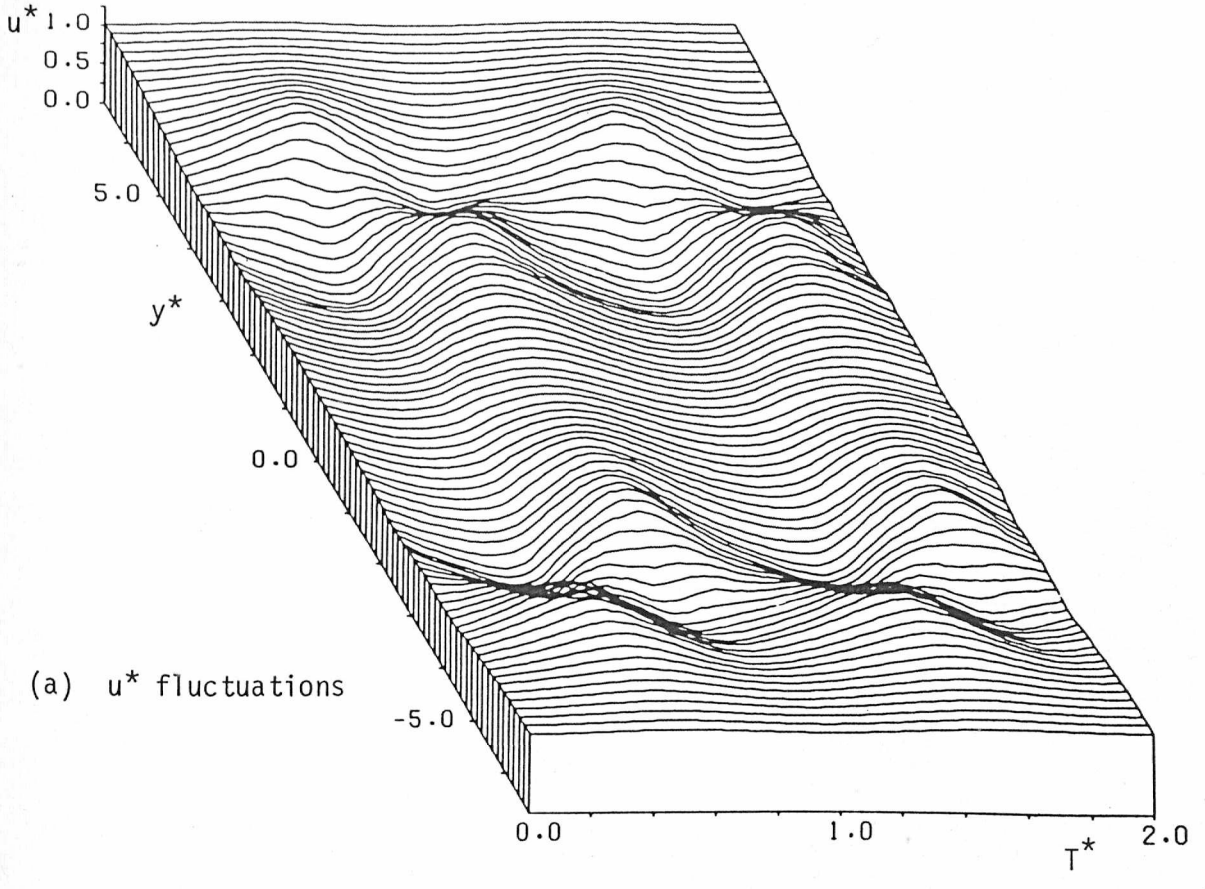


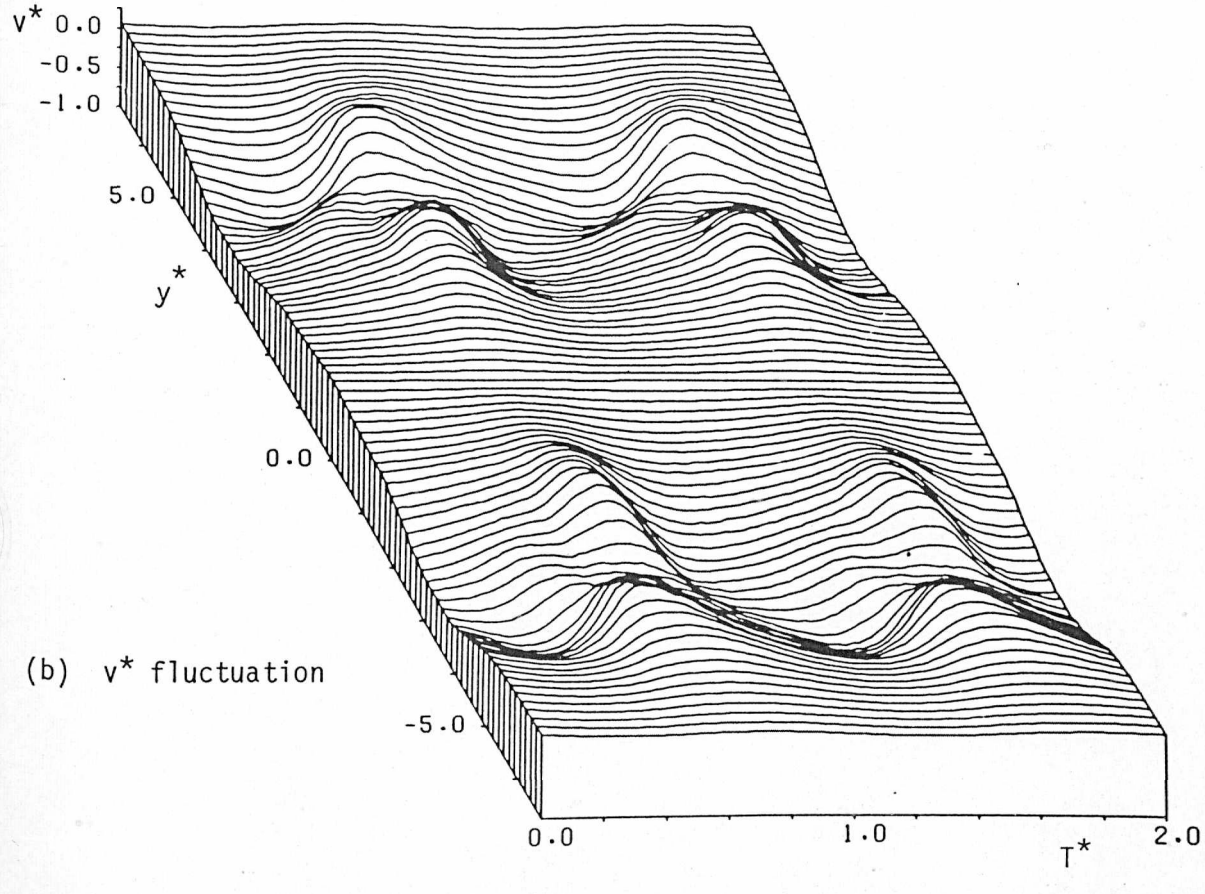

Figure 3.1.37 Records of velocity fluctuations detected by a single hot-wire on the axis of symmetry in the wakes of ring models with various cross-sections, $R_e = 2.0 \times 10^4$ (Amplitude : arbitrary scale)

shedding flowmeter is the only obstacle to its use as a standard flowmeter. They have demonstrated experimentally that the standard deviation of shedding times is the major factor governing the repeatability. The standard deviation of shedding times of vortex shedding flowmeters is typically around 10% of the mean shedding time, but the remarkably regular velocity fluctuations shown in Figure 3.1.37 suggests the possibility of a substantial reduction in the standard deviation. Although it was not carried out in the present experiment, an investigation into the industrial application of the ring model as a bluff body for a flowmeter would be very useful.

As the correlation and base pressure measurements have proved that the wake of the rectangular cross-section ring model is fairly different from that of the thin sharp-edged cross-section ring model, the wake structure was investigated by using the conditional averaging technique. Figures 3.1.38 and 3.1.39 show the results of conditionally averaged velocity fluctuations for two vortex shedding cycles behind the rectangular cross-section ring model at $x = 3.4\ w$ and $x = 8.0\ w$ respectively. The amplitudes of the velocity fluctuations are larger and the patterns are more complicated at $x = 3.4\ w$ compared with that of the thin sharp-edged cross-section ring model shown in Figure 3.1.20. Especially, wave forms of velocity fluctuations of $v^*$ around the paths of the vortex rings are distorted and quite different from the sinusoidal waves. It is also suggested that the velocity fluctuations due to vortices spreads outside the

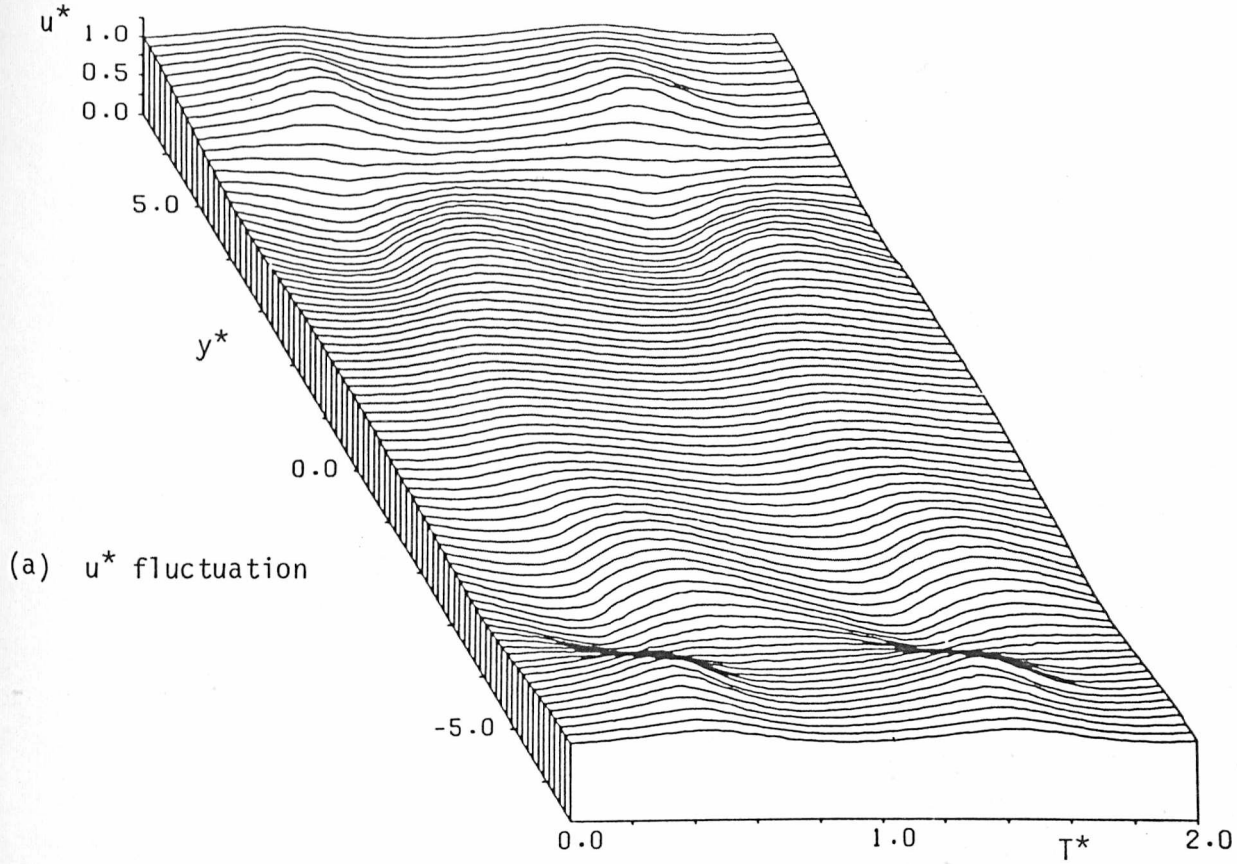



(a) u* fluctuations

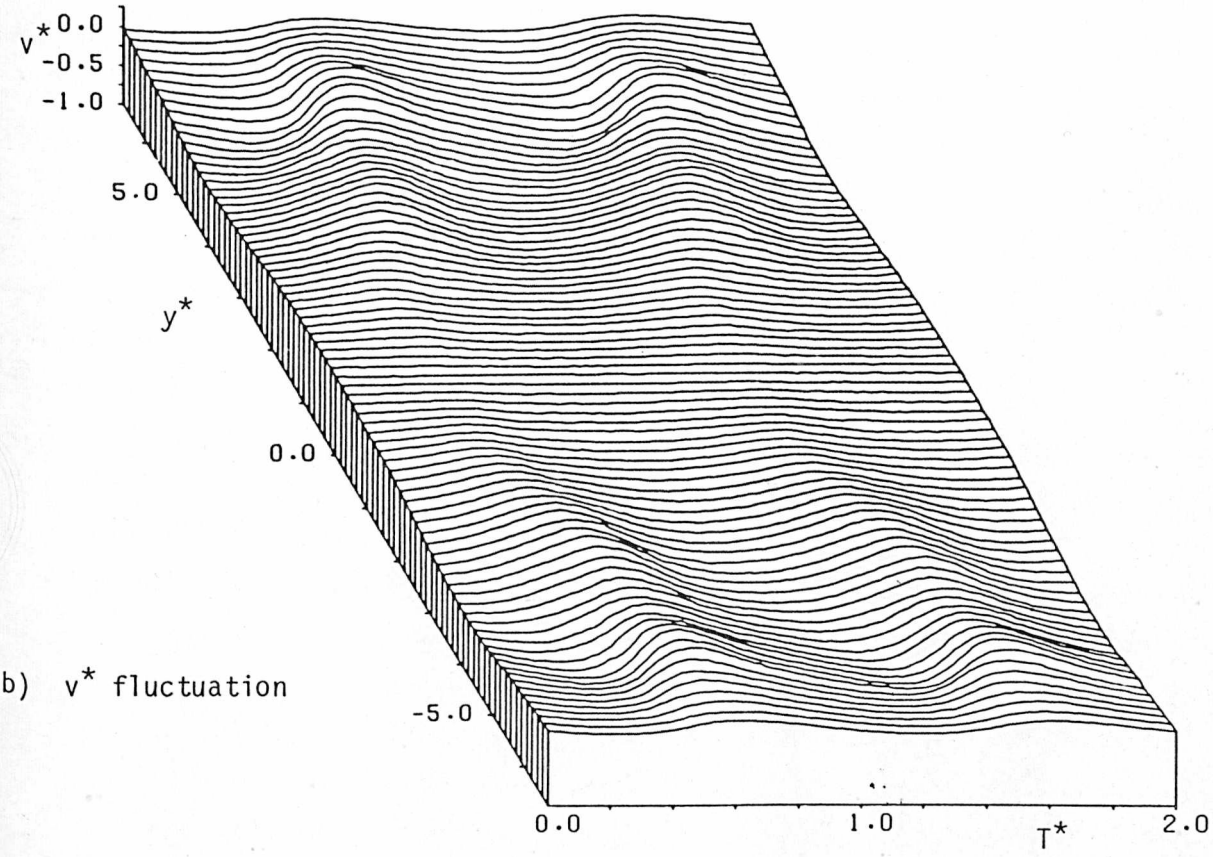



(b) v* fluctuation

Figure 3.1.38 Conditionally averaged velocity fluctuations in the wake behind the rectangular cross-section ring model at x = 3.4 w, U = 10 m/s.




(a) u* fluctuation



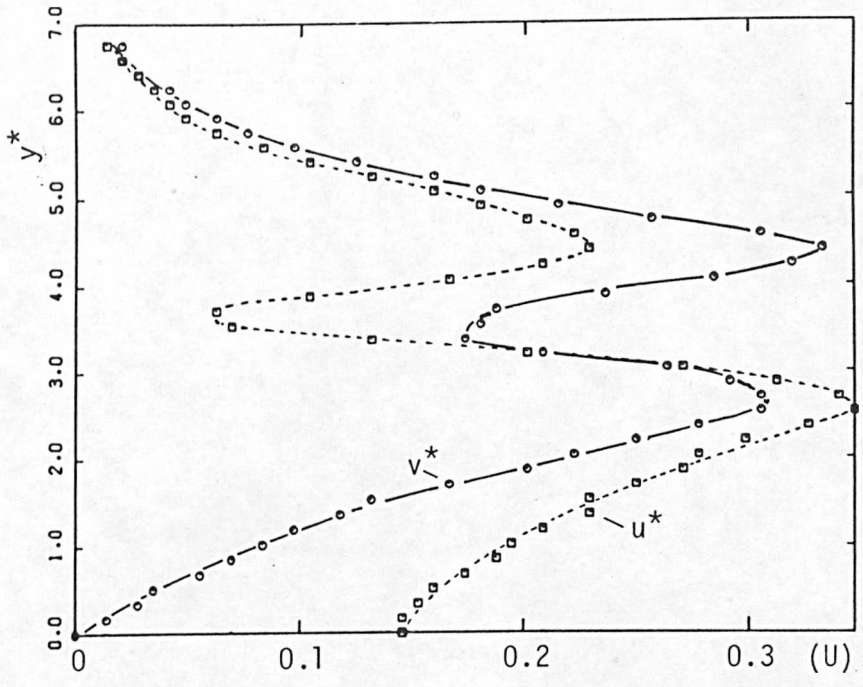

(b) v* fluctuation

Figure 3.1.39 Conditionally averaged velocity fluctuations in the wake behind the rectangular cross-section ring model at x = 8.0 w, U = 10 m/s.

traverse area at $x = 8.0$ w. Figure 3.1.40 shows profiles of root-mean-square values of conditionally averaged velocity fluctuations at $x = 3.4$ w and $x = 8.0$ w respectively. The patterns of the profiles are little different, but the root-mean-square values at $x = 3.4$ w are about 50% higher compared with the thin sharp-edged cross-section ring model shown in Figure 3.1.23. Figure 3.1.41 shows profiles of mean velocities of $u^*$ and $v^*$ at $x = 3.4$ w and $x = 8.0$ w respectively. It is recognised that the positions of minimum velocities move towards the outside at the downstream position, and the velocity $u^*$ near the centre at $x = 3.4$ w is lower than U whereas $u^*$ is higher than U in the wake of the thin sharp-edged cross-section ring model as shown in Figure 3.1.24.

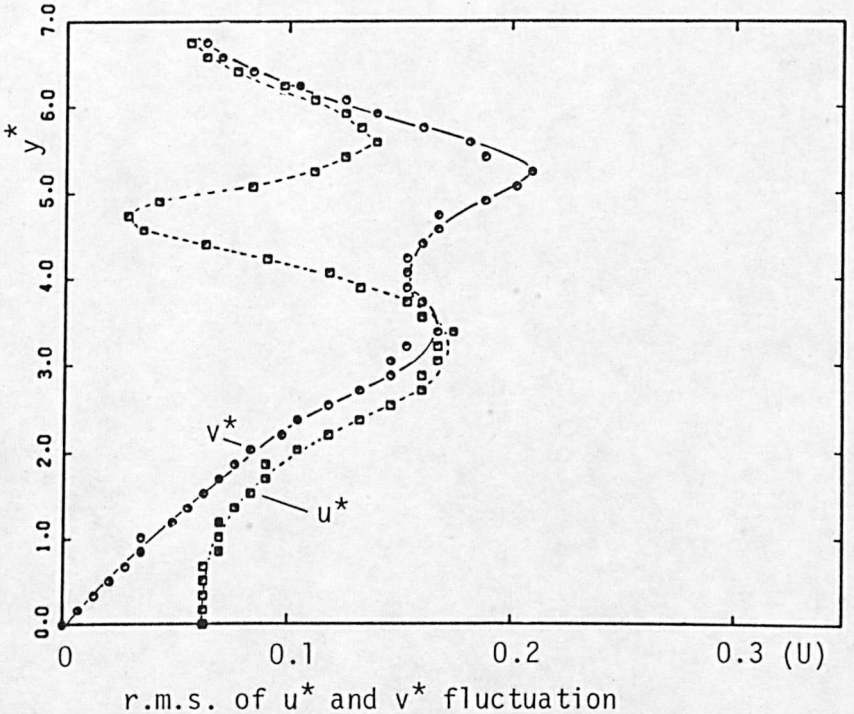
Figure 3.1.42 and Figure 3.1.43 show contours of vorticity distributions behind the rectangular cross-section ring model calculated from the conditionally averaged velocity fluctuations at $x = 3.4$ w and $x = 8.0$ w respectively. The vorticity distribution of the outside vortex ring is very distorted and has a small second peak inside the vorticity cloud at $x = 3.4$ w. It is not clear whether the distorted vorticity distribution is formed from the beginning or a result of interaction between the inside and outside vortex rings. However, it is certain that there exists a stronger mixing in the near wake, which gives rise to cancellation of the opposite signed vortices. Also the inside vortex ring approaches the outside vortex ring more quickly compared with the wake behind the thin sharp-edge cross-section

(a) x = 3.4 w




r.m.s. of u* and v* fluctuation

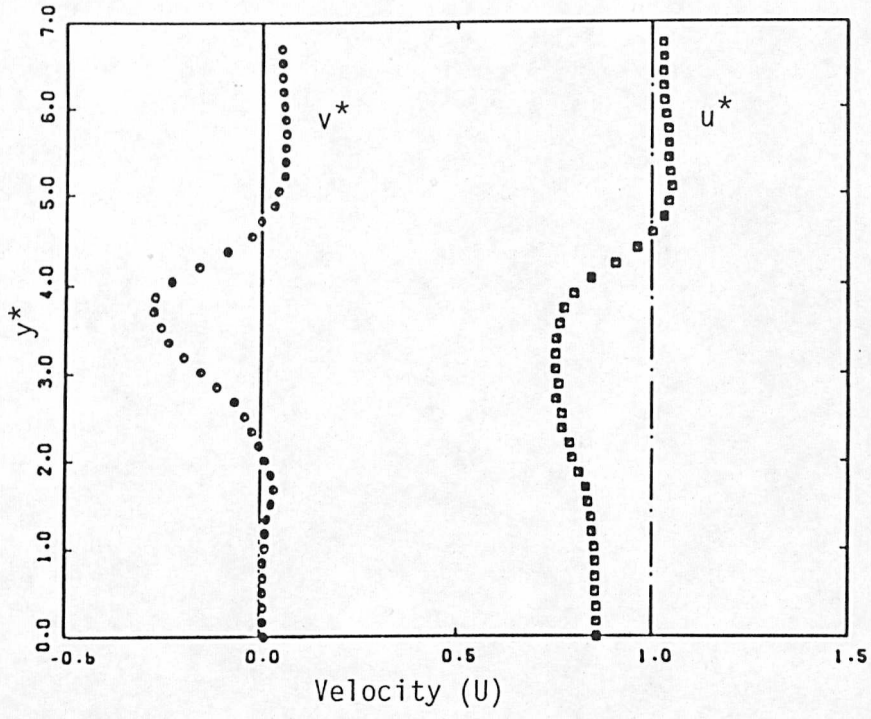
(b) x = 8.0 w




r.m.s. of u* and v* fluctuation

Figure 3.1.40 Root-mean-square profiles of conditionally averaged velocity fluctuations u* and v* in the wake behind the rectangular cross-section ring model, $R_e = 2.0 \times 10^4$.

(a) x = 3.4 w




(b) x = 8.0 w

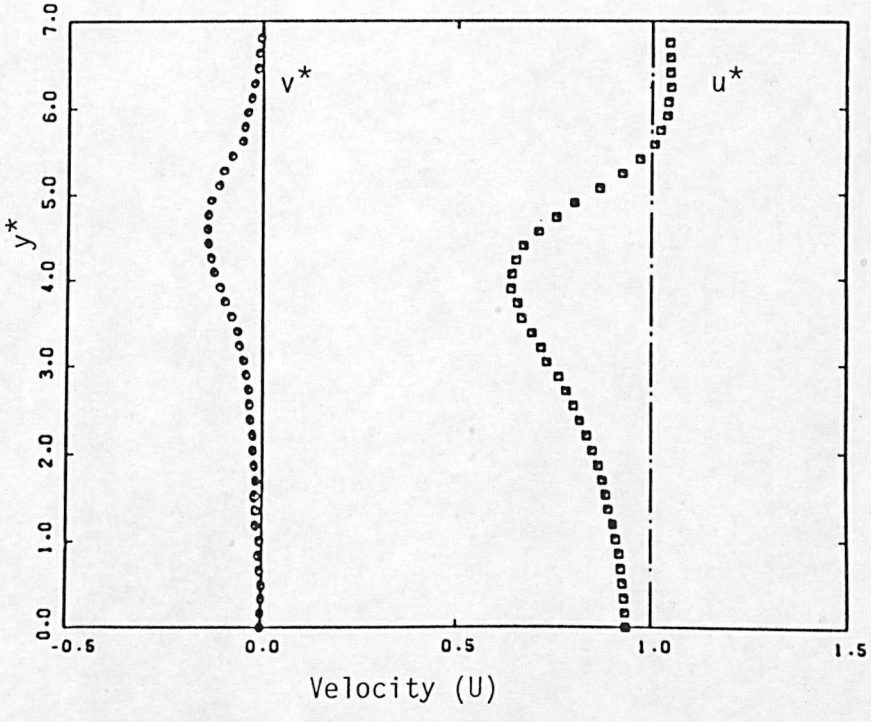



Figure 3.1.41 Profiles of mean velocities u* and v* hehind the rectangular cross-section ring model, U = 10 m/s.

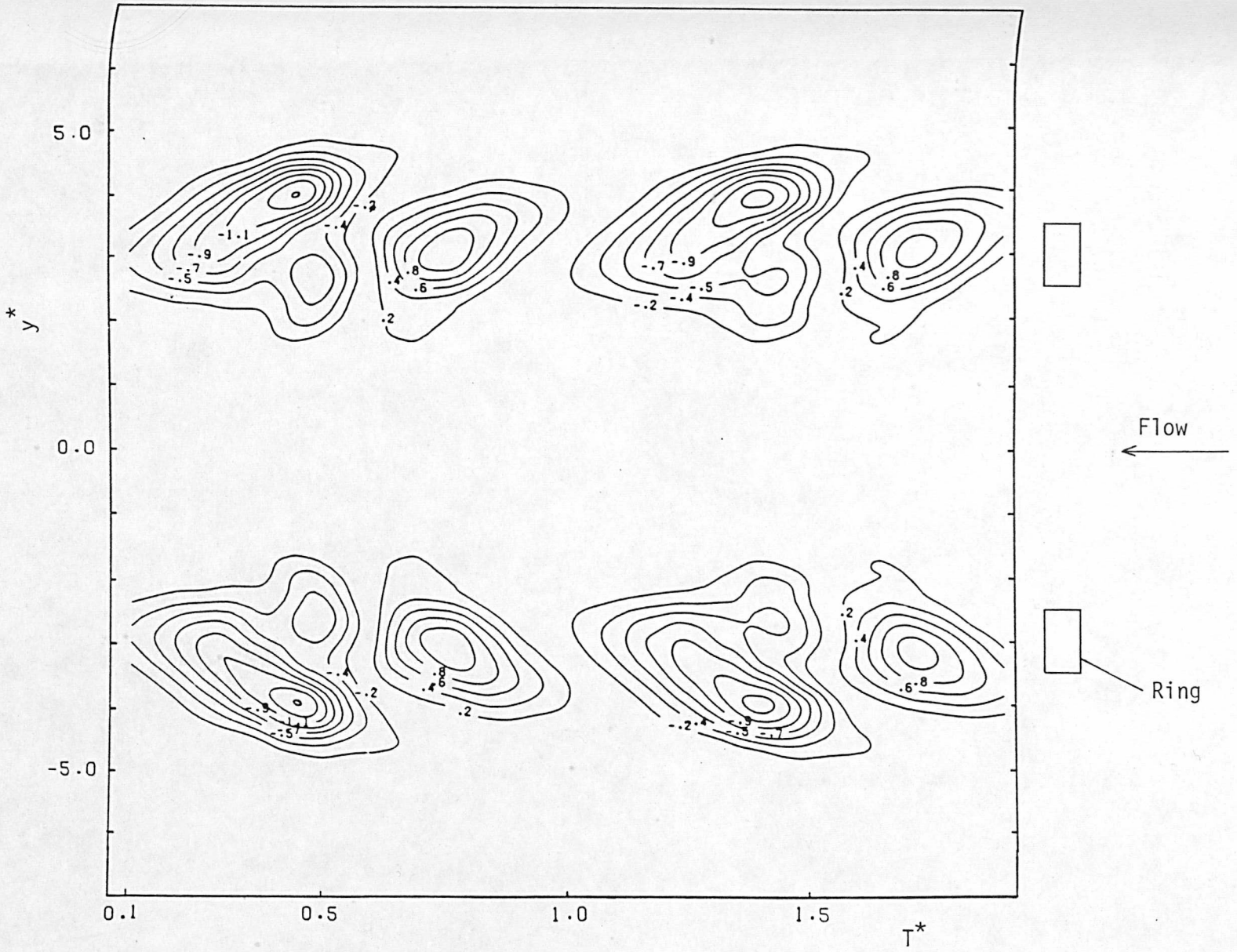



Figure 3.1.42 Vorticity distribution in the wake behind the rectangular cross-section ring model at x = 3.4 w, $R_e$ = 2.0 x $10^4$.

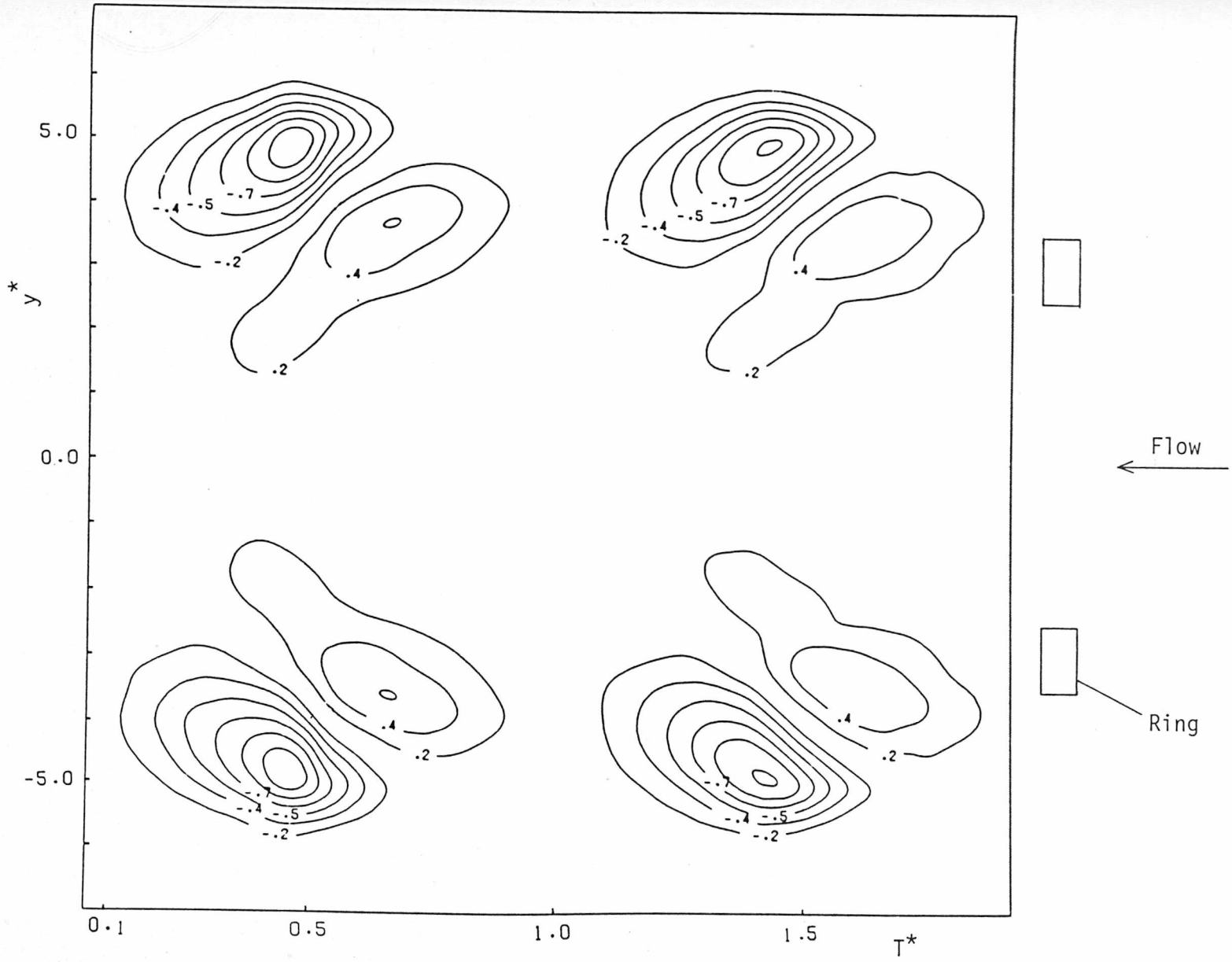



Figure 3.1.43 Vorticity distribution in the wake behind the rectangular cross-section ring model at $\dot{x}$ = 8.0 w, $R_e$ = 2.0 x $10^4$.

ring model. The radii of the vortex rings are a = 3.2 w and b = 4.0 w at x = 3.4 w. Therefore the radius of the inside vortex ring has already expanded further than the mean radius of the ring model. Also, the spacing ratio of the vortices is $h/\ell$ = 0.35, i.e. the inside and outside rings is already not $180^{o}$ out of phase. The strengths of the vortices are $\Gamma_a^*$ = 2.83 and $\Gamma_b^*$ = -4.10 ($-\Gamma_a/\Gamma_b$ = 0.69), i.e. about 27% and 39% of the total vorticity remain within the inside and outside concentrated clouds of vorticity respectively at x = 3.4 w. Therefore, the outside vortex ring is much stronger and larger percentages of the totally available vorticity are lost, especially from the inside vortex ring, compared with the case of the thin sharp-edged cross-section ring model.

The inside and outside vortex rings get closer to each other and spread further, but the inside vortex does not pass through the outside one at x = 8.0 w as shown in Figure 3.1.43. The radii of the vortex rings are a = 3.7 w and b = 4.9 w, both of which are about 1.0 w larger than those from the thin sharp-edged cross-section ring model at the same position, and the spacing ratio of the vortices is $h/\ell$ = 0.20. The clouds of vorticity are diffusing to a bigger area and the strengths of the vortex rings are $\Gamma_a^*$ = 2.23 and $\Gamma_b^*$ = 3.22 ($-\Gamma_a/\Gamma_b$ = 0.69), i.e. only about 21% and 30% of the total vorticity remain within each cloud of vorticity at x = 8.0 w. Therefore, $\Gamma_a^*$ and $\Gamma_b^*$ decay at the rates of about 4% and 5% per w of vortex travel between x = 3.4 w and x = 8.0 w respectively, and larger percentages of

vorticity are lost on the whole compared with the wake of the thin sharp-edged cross-section ring model. Davies (1975) measured the strength of a vortex in the wake of a D-shape cylinder by calculating a line integral of the conditionally averaged velocity around a contour which enclosed the vortex and passed through points of zero vorticity. He obtained a non-dimensional strength of 2.39 at $x = 8.0\ w$ which was 26% of the total vorticity shed. The base pressure coefficient of the cylinder was $C_{pb} = -1.4$. Although the shape of the afterbody is different, the magnitudes of his results are comparable with the present results. The convection velocity of the inside and outside vortex ring are 1.0 U and 1.03 U at $x = 3.4\ w$ and 0.83 U and 0.84 U at $x = 8.0\ w$. The results for the vortex rings behind the rectangular cross-section ring model are shown summarized in Table 3.1.4.

Figure 3.1.44 and Figure 3.1.45 show conditionally averaged velocity vector fields, in which the convection velocity of the inside vortex rings have been subtracted from the total velocity, at $x = 3.4\ w$ and $x = 8.0\ w$ respectively. It is clearly recognised that the inside vortex ring is weaker than the outside one and that the radii of both vortex rings are larger than those behind the thin sharp-edged cross-section ring model shown in Figure 3.1.33 at $x = 8.0\ w$. Also in this case there exists a fairly large area around the centre where the fluid moves with the same velocity of the inside vortex ring.

## TABLE 3.1.4

Vortex rings from the rectangular cross-section ring model with d/w = 6.0

| Downstream Position x | 3.4 w | 8.0 w |
|---|---|---|
| $\Gamma_a^*$ (Inside Vortex) | 2.83 | 2.23 |
| $\Gamma_a$ / Total Vorticity | 27% | 21% |
| $\Gamma_b^*$ (Outside Vortex) | -4.10 | -3.22 |
| $\Gamma_b$ / Total Vorticity | 39% | 30% |
| $-\Gamma_a / \Gamma_b$ | 0.69 | 0.69 |
| a (Inside Vortex Radius) | 3.2 w | 3.7 w |
| b (Inside Vortex Radius) | 4.0 w | 4.9 w |
| $h/\ell$ (Spacing Ratio) | 0.35 | 0.20 |
| $u_c$ of Inside Vortex | 1.00 U | 0.83 U |
| $u_c$ of Outside Vortex | 1.03 U | 0.84 U |

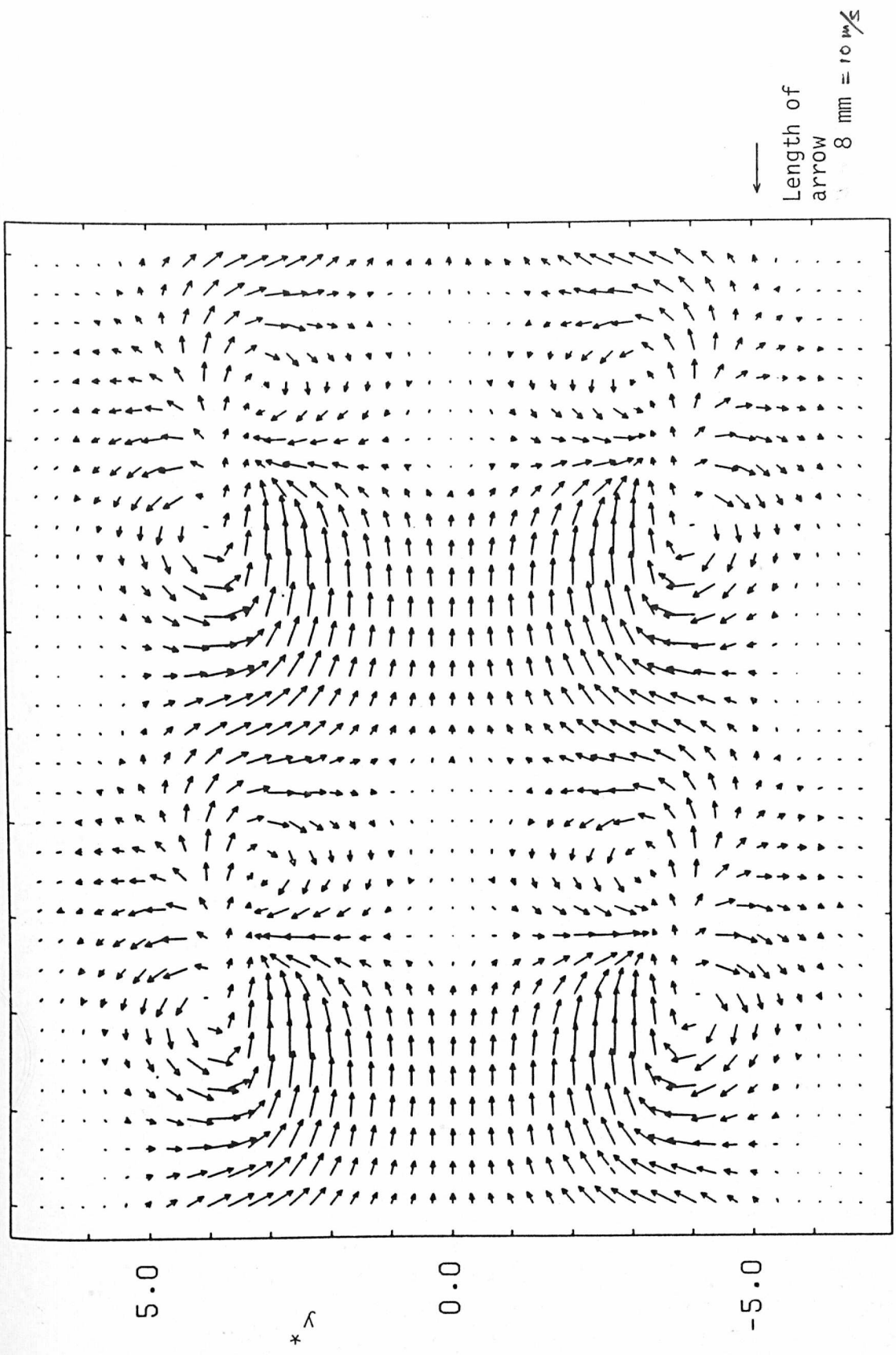



Figure 3.1.44 Velocity vector field in the wake behind the rectangular cross-section ring model at x = 3.4 w, $u_c$ = 1.00 U removed. U = 10 m/s.

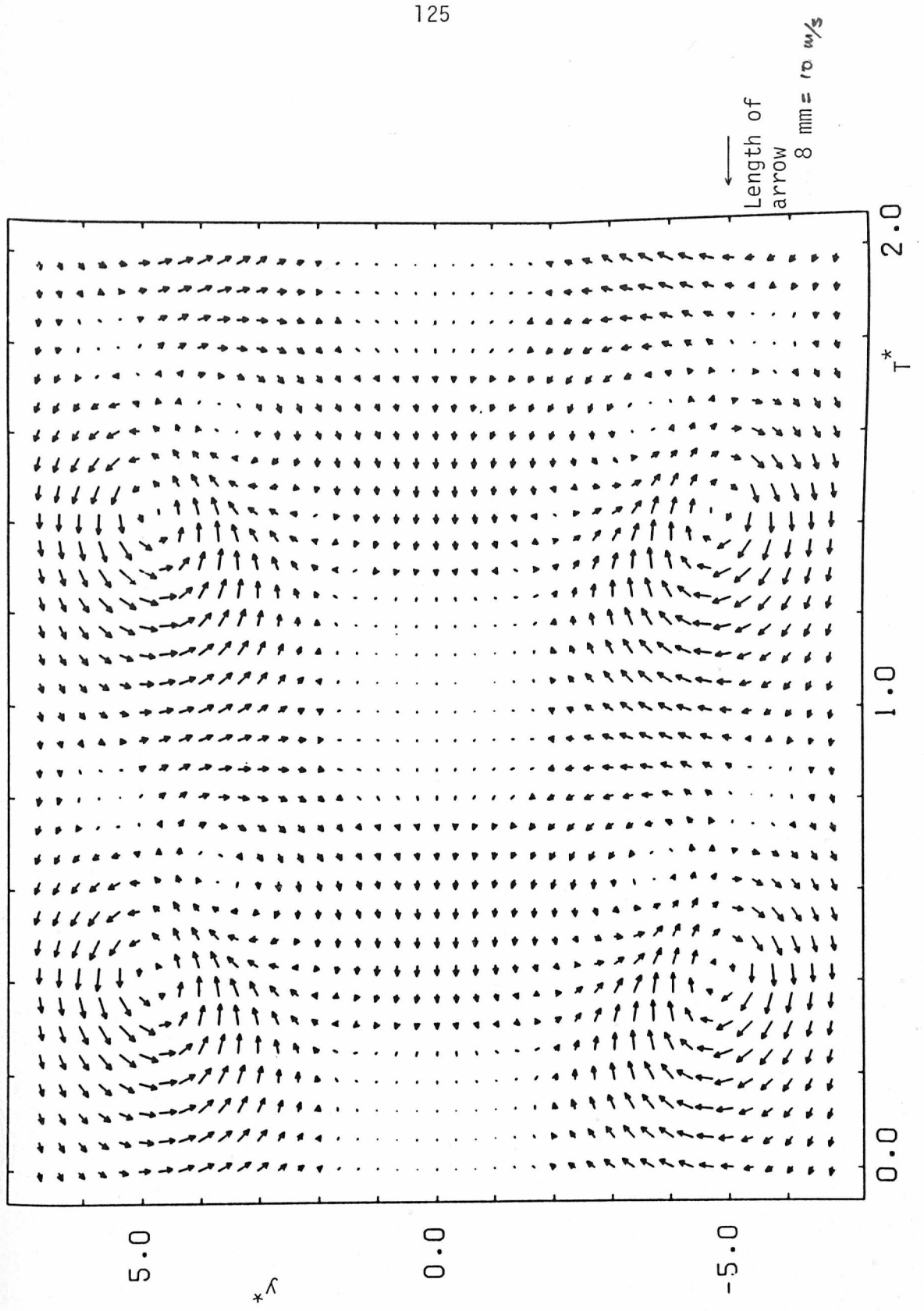
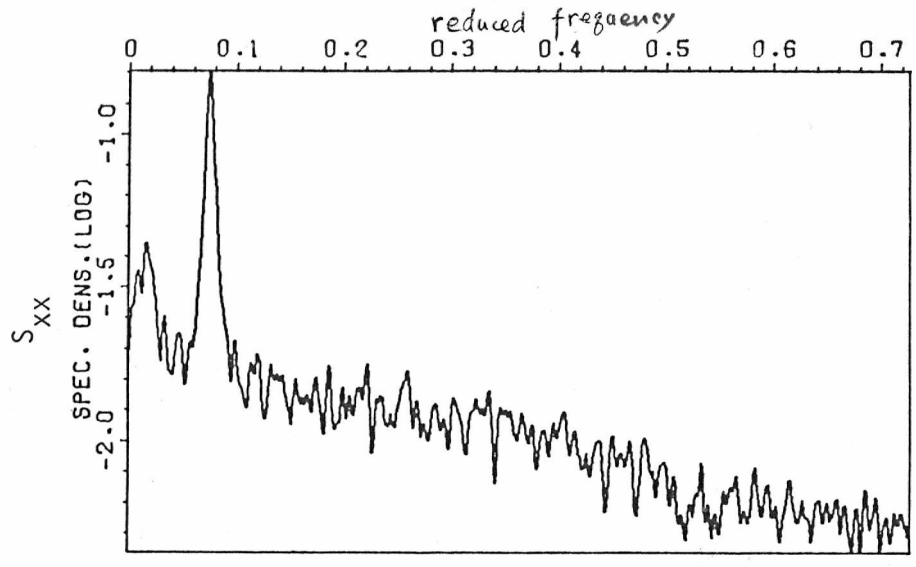



Figure 3.1.45 Velocity vector field in the wake behind the rectangular cross-section ring model at x = 8.0 w, $u_c$ = 0.83 U removed, U = 10 m/s.

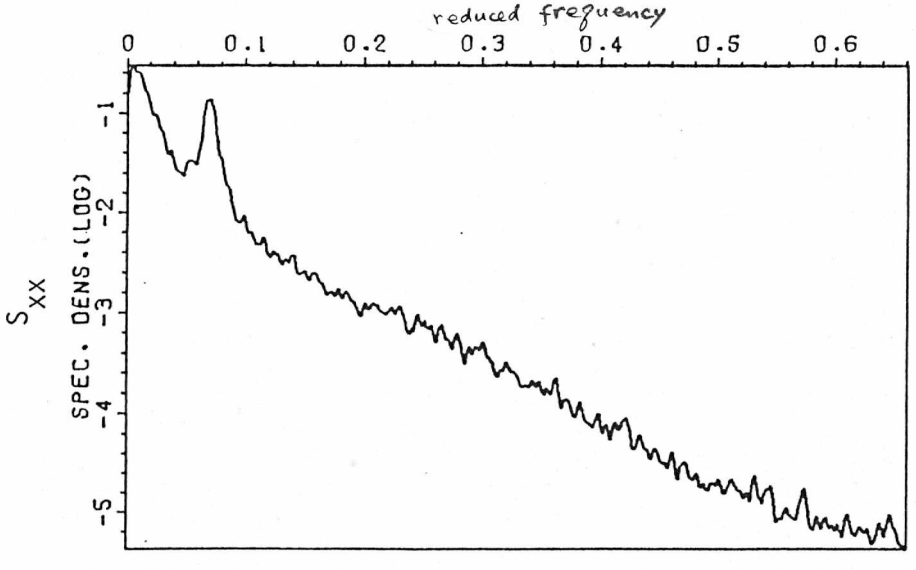
## 3.2 Wake structure of a solid circular disk

Measurements of the wake structure of a solid circular disk, which can be thought as a special shape of the ring model with d/w = 1.0, were carried out for comparison. The periodic component in the wake of the solid circular disk model described in Table 2.1 was extracted from the turbulent velocity fluctuations measured by the cross-wires in the wake by using the conditional averaging technique. Here, the three-dimensional coordinate system (x,y,z) with the origin at the centre of the disk and y and z normal to x, the free stream direction, is used. Here the coordinates $y^*$ and $z^*$ are non-dimensionalised by the diameter D of the disk.

There exists a fairly predominant frequency in the velocity fluctuations in the wake of the solid circular disk. Figure 3.2.1 (a) shows the power spectral density function of the velocity fluctuation measured by a single hot-wire outside the wake behind the disk at x = 3.4 D, in which the Strouhal number is based on the radius of the disk. A clear peak is recognised in the figure, though the background turbulence is also at a relatively high level. It is very interesting that the ring model with d/w = 1.2, a disk with a small hole at the centre, has a very different power spectral density function as shown in figure 3.2.1 (b). The fluctuations decrease very much at high frequencies and increase at very low frequencies compared with the solid circular disk.




(a) Solid circular disk at x = 3.4 D




(b) Ring model with d/w = 1.2 at x = 3.4 w

Figure 3.2.1 Power spectral density functions $S_{XX}$ of velocity fluctuations measured outside the wakes of a solid circular disk and a ring model with d/w = 1.2 at x = 3.4 w. $R_e$ = 6.2 - 6.8 x $10^4$.

The cross-wires were traversed from $y = -25$ cm to $y = 25$ cm on the plane normal to the axis of symmetry behind the disk at $x = 3.4$ D and $z = 0$. The traverse step $\Delta y$ was about 9.6 mm, therefore there were 53 measurement positions altogether in the $y$ direction. At each $y$ position, the analogue signals of the velocity fluctuations recorded by the cross-wires were sampled at the rate of about 36 points per cycle. The reference velocity fluctuation used for control of conditioning was measured outside the wake behind the disk near $x = 3.4$ D, $y = -1.25$ D and $z = 0$. A conditional averaged signal was extracted at the predominant frequency shown in Figure 3.2.1 (a). However only 30 to 40 percent of the total records of the velocity fluctuations were available for the averaging as the reference signal is not so regular as that of the ring model. As the shedding frequency was very low (7 Hz), only about 500 samples were averaged at each measurement point.

Figure 3.2.2 shows the results of conditionally averaged velocity fluctuations for two cycles behind the solid circular disk of $x = 3.4$ D. The velocity fluctuation $v^*$ is plotted positive when the flow is in the $y$ direction in the figure. The conditionally averaged velocity fluctuations are not so smooth as those of the ring model because of the high level of background turbulence and the small numbers of samples used for averaging. However the periodic features are clearly shown in the figure. The amplitude of the fluctuations are smaller compared with those of the ring model. The conditionally averaged velocity

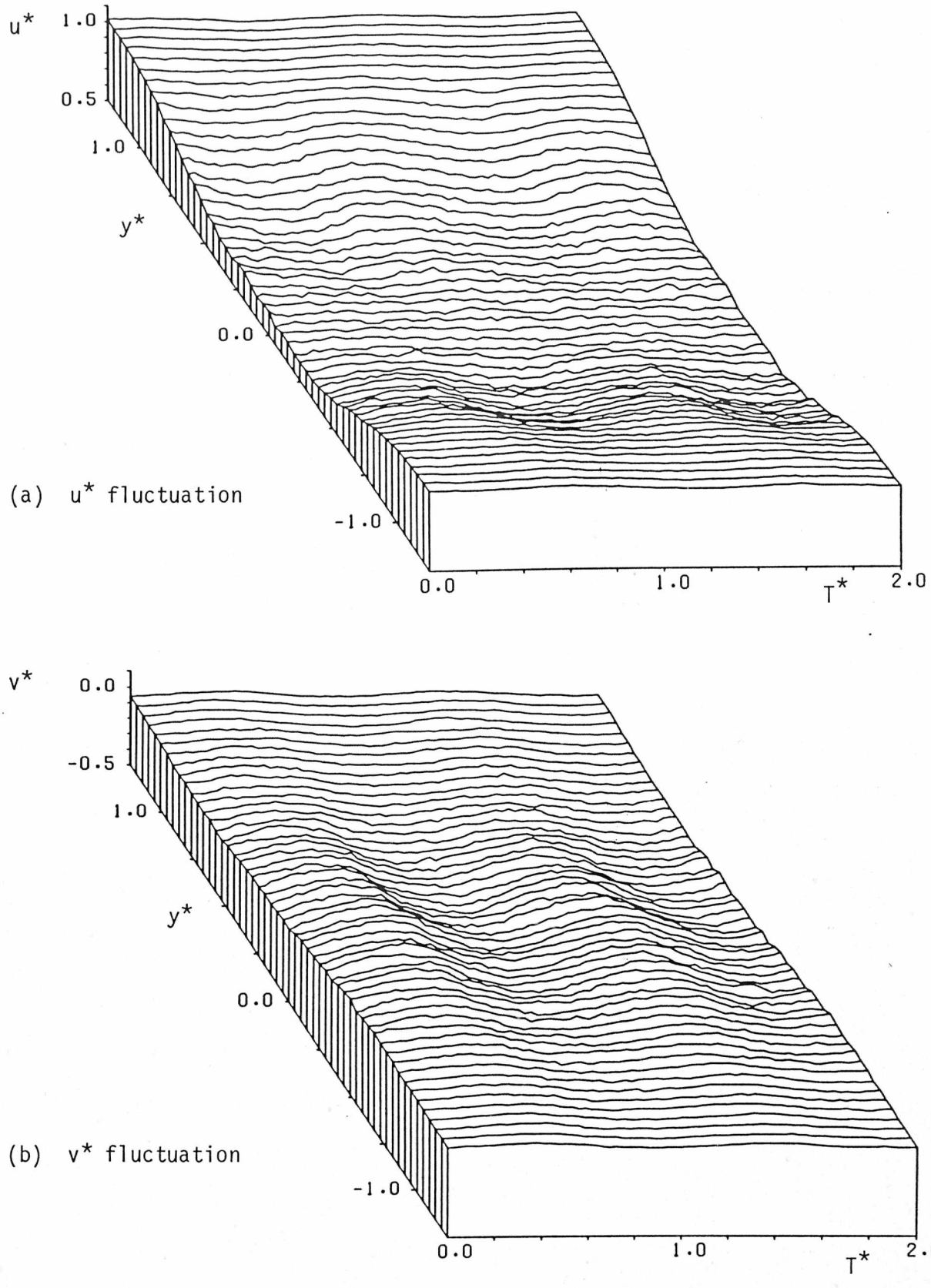



Figure 3.2.2 Conditionally averaged velocity fluctuations in the wake behind the solid circular disk at x = 3.4 D z = 0, U = 10 m/s.

fluctuation $u^*$ at positions $y^* > 0$ and $y^* < 0$ are out of phase. This agrees with the results of Roberts (1973) and Fuch et al. (1979) who observed a high negative correlation of the components of the velocity fluctuations at the predominant frequency between two opposite positions behind a solid circular disk. The pattern of velocity fluctuations of $v^*$ is similar to the one usually observed in the wake of an isolated two-dimensional bluff body, but the first harmonics of the fluctuation $u^*$ cannot be recognised in the figure around the centre of the wake. This suggests some differences in the wake structure of the solid circular disk from the wake of two-dimensional bluff body.

Figure 3.2.3 shows contours of vorticity distribution in the (y,t) plane behind the solid circular disk at $x = 3.4$ D and $z = 0$, in which both positive and negative peak areas of vorticity are shown hatched. The vorticity distribution is distorted by the effect of strong shear in the near wake, however, the nearly staggered array of vortices can be recognised in the figure. The strength of the vortices is not calculated as the vorticity is continuously distributed. The values of vorticity at the peaks are only about half that found in the wake of the thin sharp-edged ring model at the same downstream position.

Figure 3.2.4 shows conditionally averaged velocity vector field in the wake behind the solid circular disk at $x = 3.4$ D and $z = 0$, in which the convection velocity of 0.83 U, the velocity at

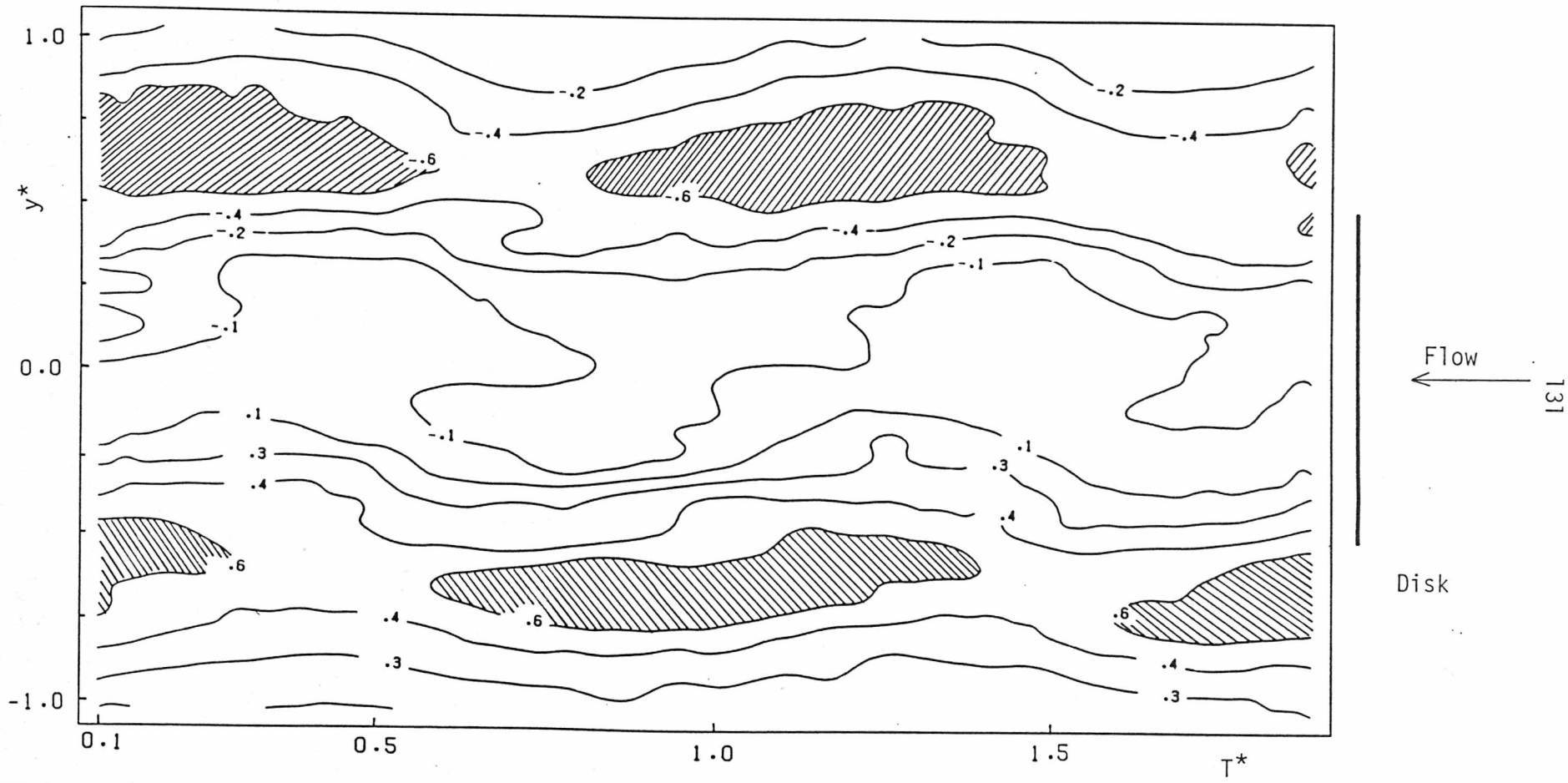



Figure 3.2.3 Vorticity distribution in the wake behind the solid circular disk at x = 3.4 D, Z = 0, $R_e = 6.8 \times 10^4$.

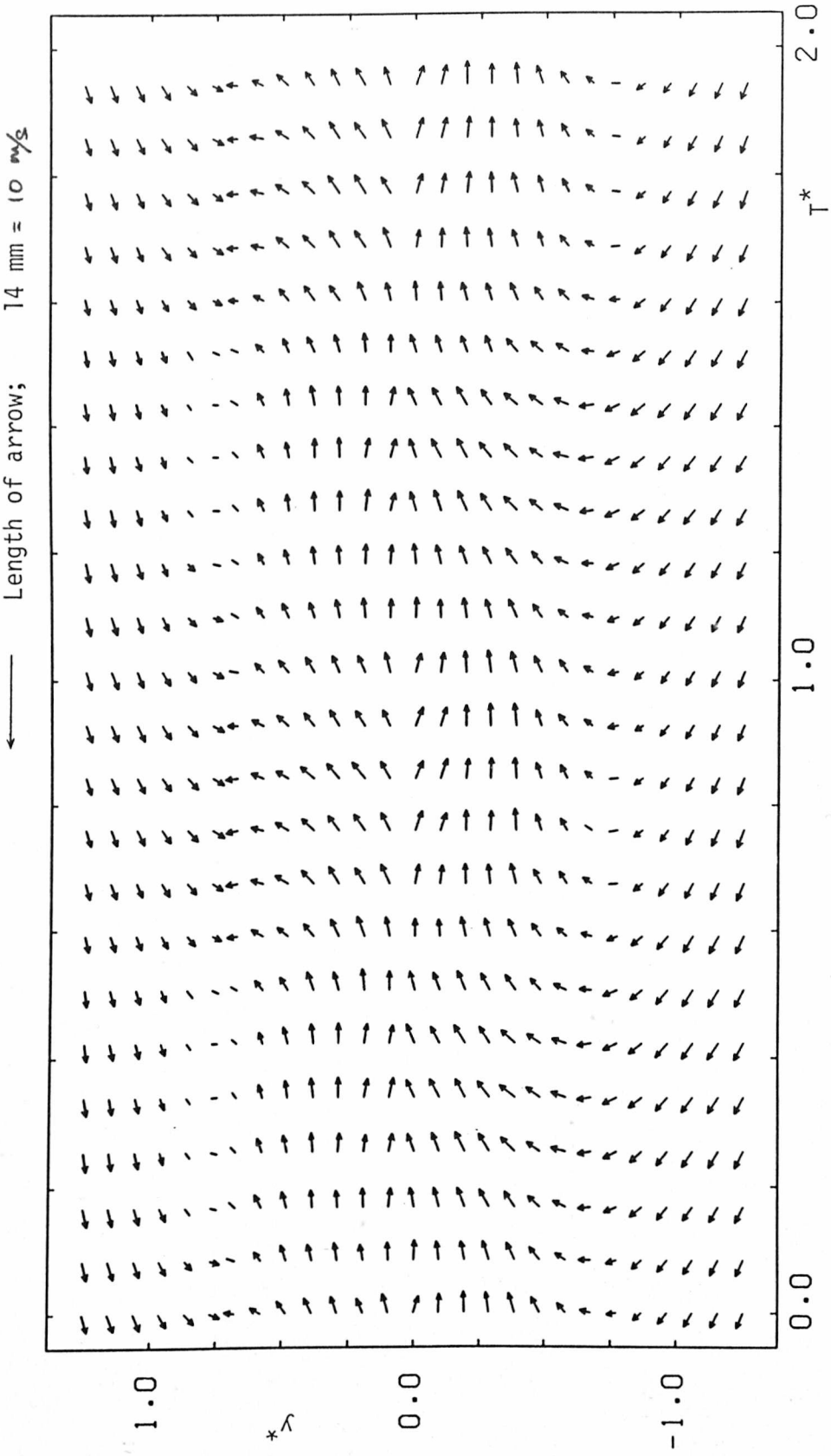
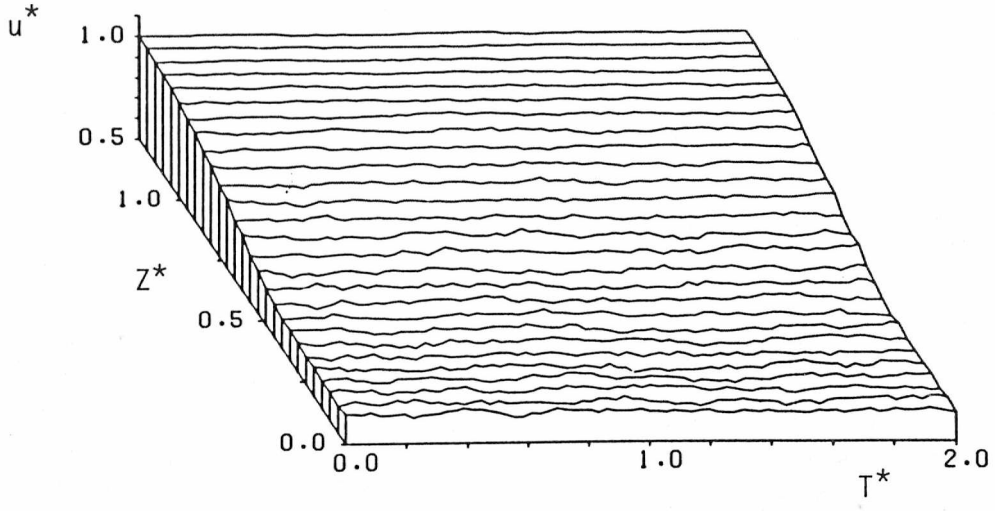



Figure 3.2.4 Velocity vector field in the wake behind the solid circular disk at x = 3.4 W, z = 0, U = 10 m/s, 0.83 U removed.

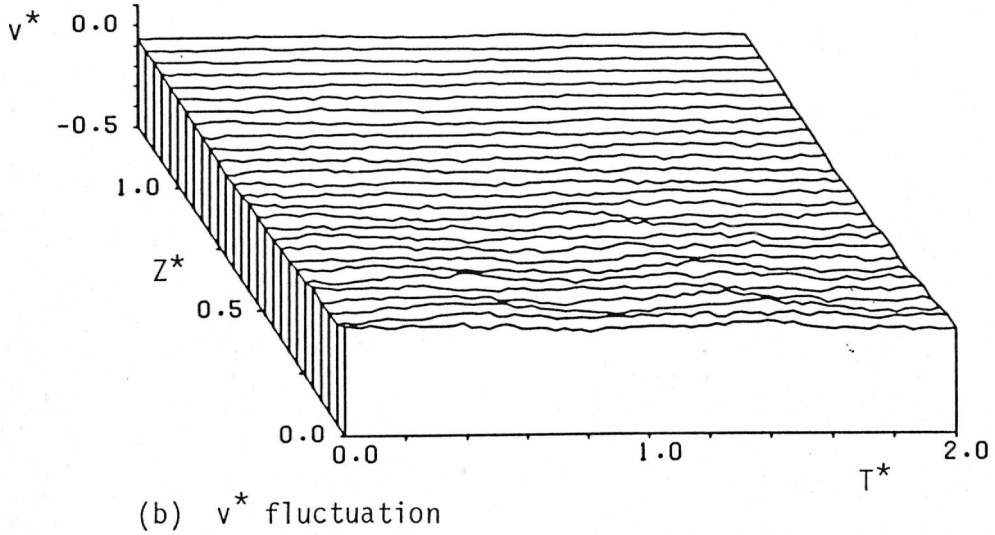
the peak of the vorticity distribution, is subtracted. Although the centres of vortices are not clear, it can be recognised that vortices shed from the two opposite sides of the axis of symmetry of the disk are out of phase and have opposite signs of rotation.

The cross-wires were traversed also on the z-axis, normal to the x-axis and y-axis, from z = 0 to z = 1.25 D. The conditional averaging technique was again employed to extract the periodic component from the measured turbulent velocity fluctuations in the (z,t) plane which is normal to the previous (y,t) plane. The reference signal for control of conditioning was measured at the same position as in the previous measurements. Figure 3.2.5 shows the results of the conditionally averaged velocity fluctuations of two cycles in the wake behind the solid circular disk. The velocity fluctuation $v^*$ is plotted positive when the flow is in the positive z direction. There exists no periodic feature at the vortex shedding frequency in the figure, which agrees with the result of Roberts (1973). He observed no correlation of the velocity fluctuation components at the predominant frequency between two positions located at the same x, the same radial distance from the axis of symmetry and at an angular separation of $90^{o}$.

In spite of the existence of a predominant frequency in the velocity fluctuations measured in the (z,t) plane, a periodic component could not be extracted by using the conditional averaging technique. There are two possibilities; one is that the




(a) $u^*$ fluctuation




(b) $v^*$ fluctuation

Figure 3.2.5 Conditionally averaged velocity fluctuations in the wake behind the solid circular disk at $x = 3.4\ D$, $y = 0$, $U = 10$ m/s.

velocity fluctuations at the shedding frequency in the (z,t) plane are completely uncoupled with the reference velocity fluctuation at the same frequency measured in the (y,t) plane. The other possibility is that the velocity fluctuations at the predominant frequency can be divided into two modes and that both modes have correlations with the reference velocity fluctuation, but they are out of phase with each other and hence they cancel each other when they are averaged together, assuming the two modes occur equally.

The second possibility was examined by dividing the velocity fluctuations into two modes and applying the conditional averaging technique to each mode individually. When the reference signal could sense the clear start and the end of a vortex shedding cycle as shown in Figure 3.2.6, the averages of both the first half and the second half of cycles of the velocity fluctuation $u^*$ were calculated. Figure 3.2.7 shows an example of a series of cycles indicating the mode depending on which half cycle has larger averages. For convenience, the ($+90^o$) mode denotes the velocity fluctuation for which the average of the first half cycle is larger than the other and ($-90^o$) mode denotes vice versa hereafter. It is recognised from the figure that both modes occur intermittently and randomly at about an even rate and the mode lasts only one cycle in many cases, but sometimes it lasts a few cycles.

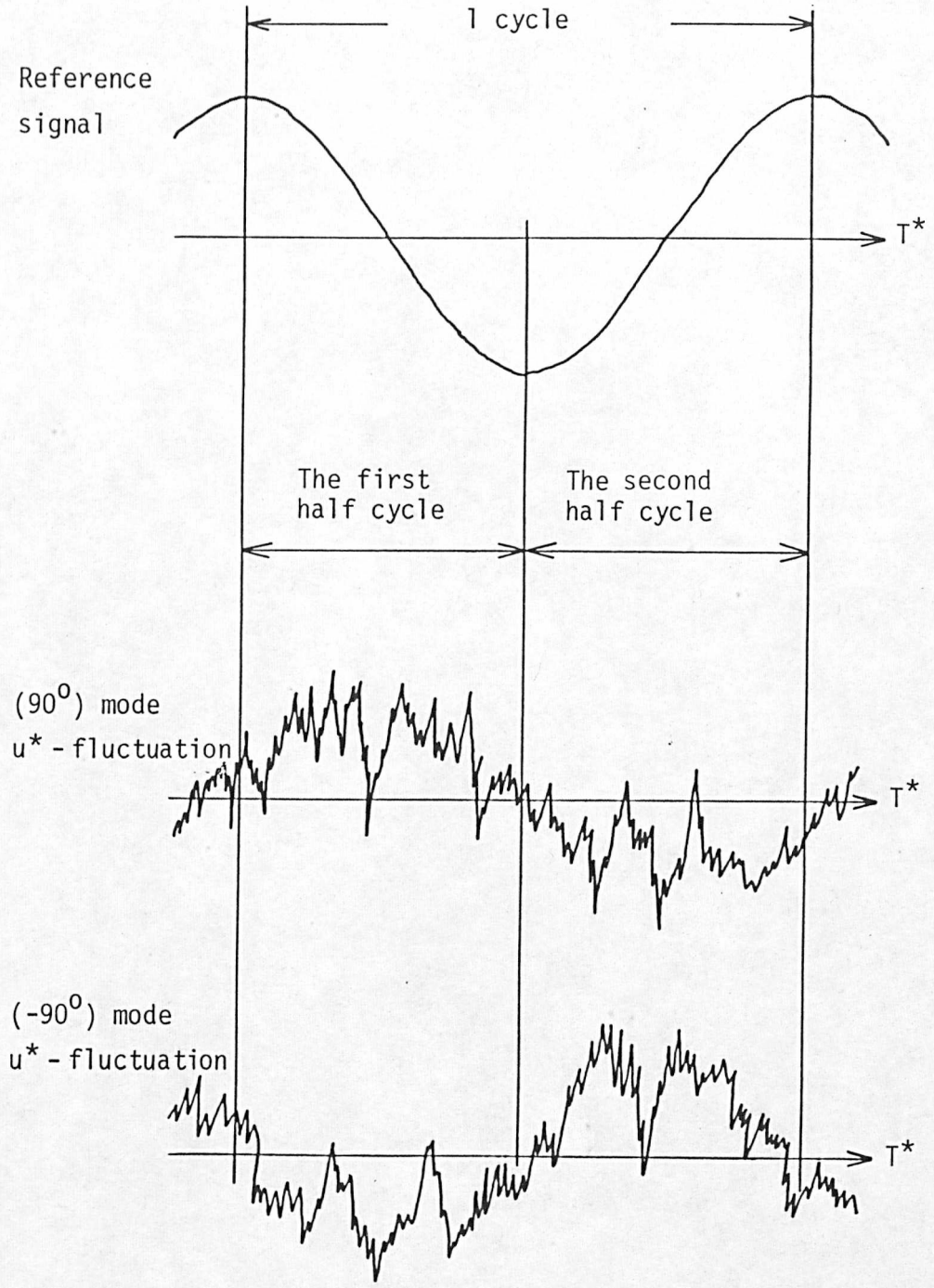



Figure 3.2.6 Division of ($90^{o}$) mode and ($-90^{o}$) mode of velocity fluctuation $u^*$ by comparing the averages of two half cycles.

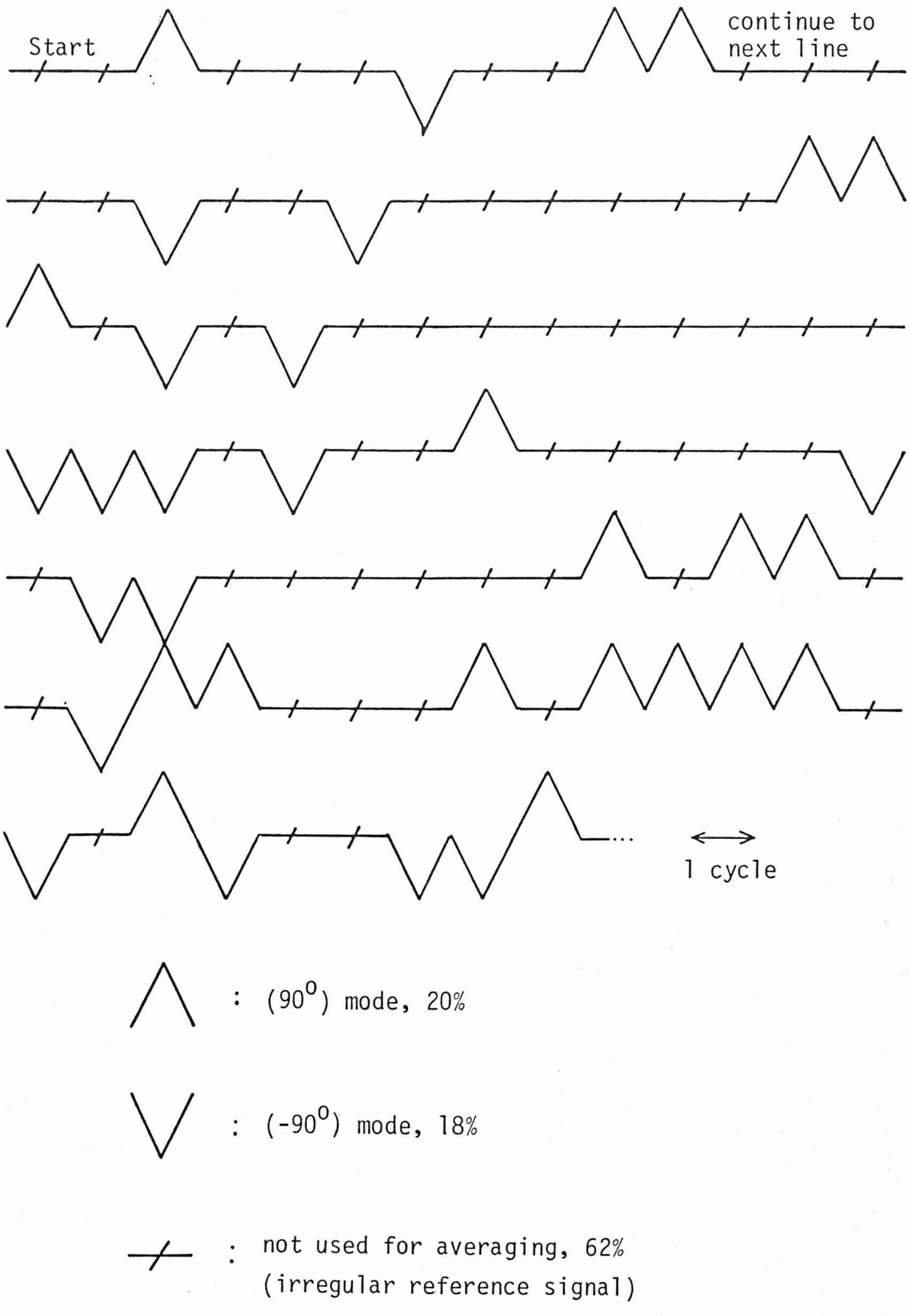
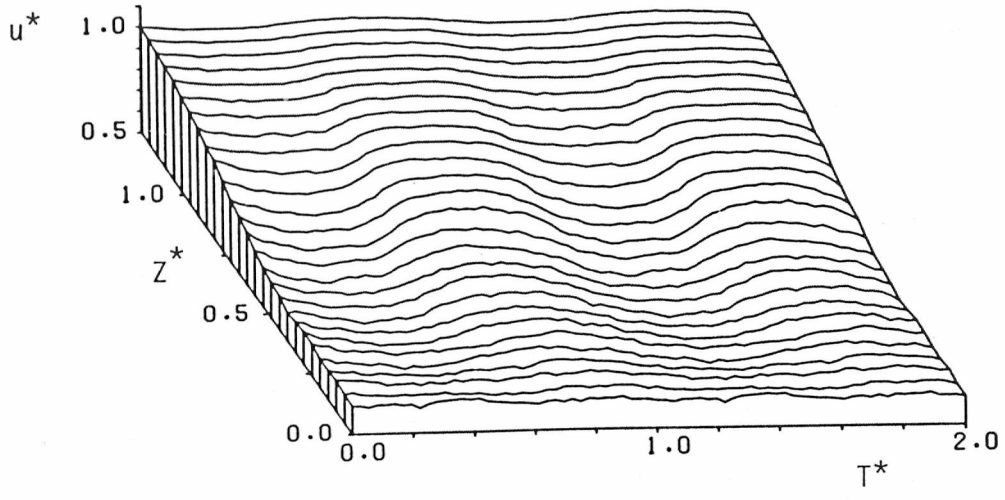


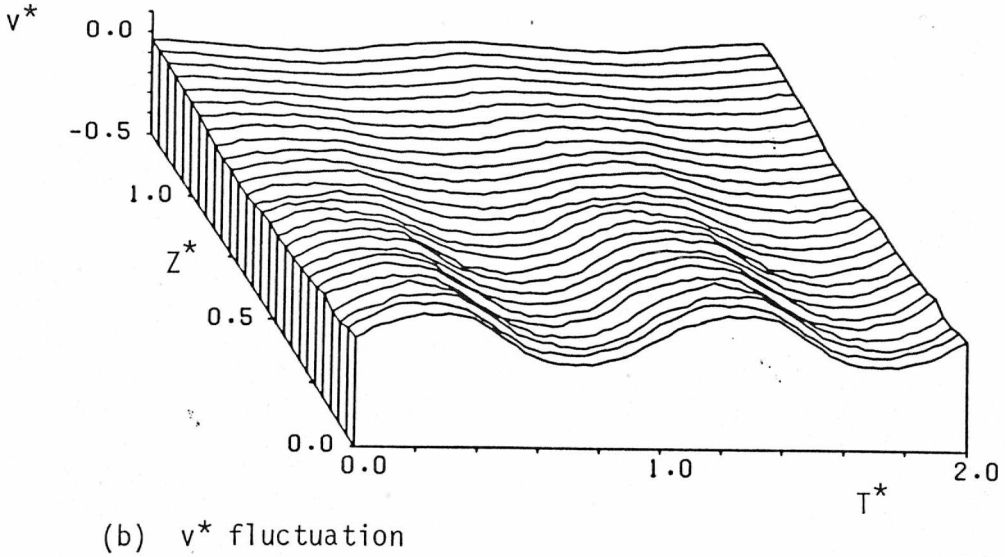

Figure 3.2.7 Example of a series of cycles of velocity fluctuations $u^*$ at x = 3.4 D, y = 0, z = 1.0 D.

Figure 3.2.8 and Figure 3.2.9 show the results of conditionally averaged ($+90^{o}$) mode and ($-90^{o}$) mode velocity fluctuations in the $(z,t)$ plane in the wake behind the solid circular disk. Although the division into modes was based on the velocity fluctuation of $u^{*}$, the same portions of the cycles of velocity fluctuation of $v^{*}$ were conditionally averaged as the same mode. It is recognised from the figure that the periodic features of both ($+90^{o}$) mode and ($-90^{o}$) mode of $u^{*}$ and $v^{*}$ are clearly extracted and that both modes have almost the same level of amplitude and are $180^{o}$ out of phase with each other. Also the patterns and the amplitudes of both modes are almost the same as those measured in the $(y,t)$ plane shown in Figure 3.2.2. The vorticity distributions of both ($+90^{o}$) mode and ($-90^{o}$) mode are calculated from the conditionally averaged velocity fluctuations and the contours of the distributions are shown plotted in Figure 3.2.10. The patterns of the distributions are similar and $180^{o}$ out of phase with each other. Also, both patterns and the levels of vorticity are almost the same as that in the $(y,t)$ plane shown in Figure 3.2.3. The phase between the vorticity distributions for the ($+90^{o}$) mode and ($-90^{o}$) mode and the area of $y^{*} < 0$ in the $(y,t)$ plane are roughly $90^{o}$ and $-90^{o}$ respectively.

The present measurements may be insufficient to describe the whole wake structure of the solid circular disk. However, the following fundamental periodic features of the wake were disclosed by applying the conditional averaging technique to the turbulent

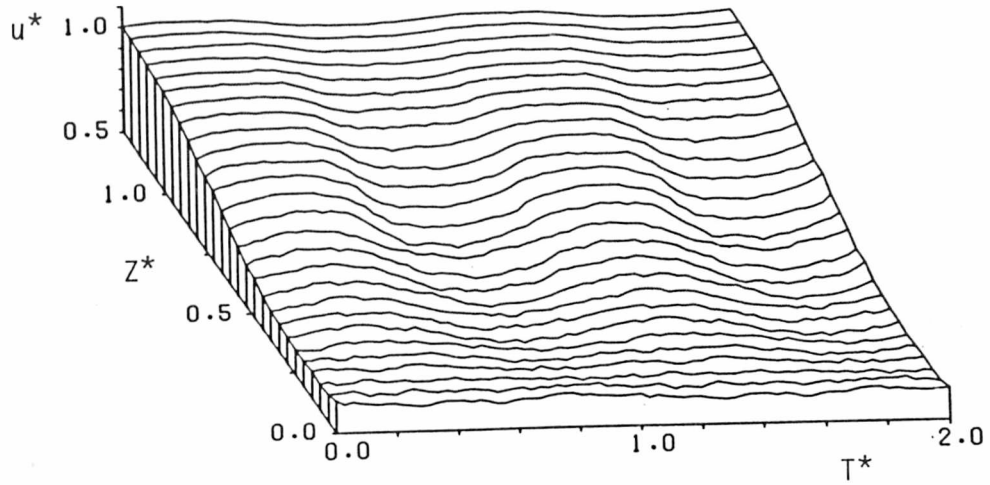



(a) $u^*$ fluctuation

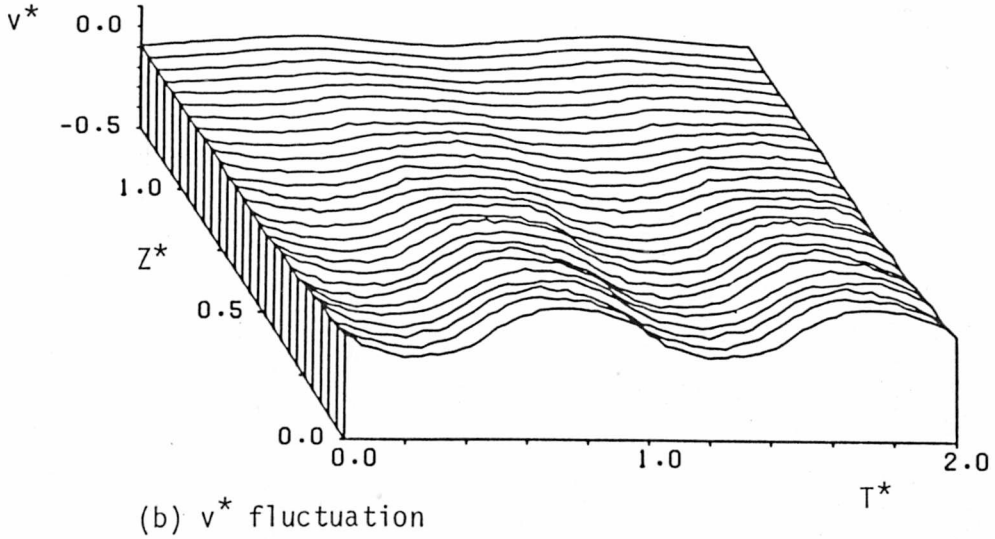



(b) $v^*$ fluctuation

Figure 3.2.8 Conditionally averaged velocity fluctuations of ($+90^{o}$) mode in the (z,t) plane in the wake of the solid circular disk at x = 3.4 D, y = 0, U = 10 m/s.

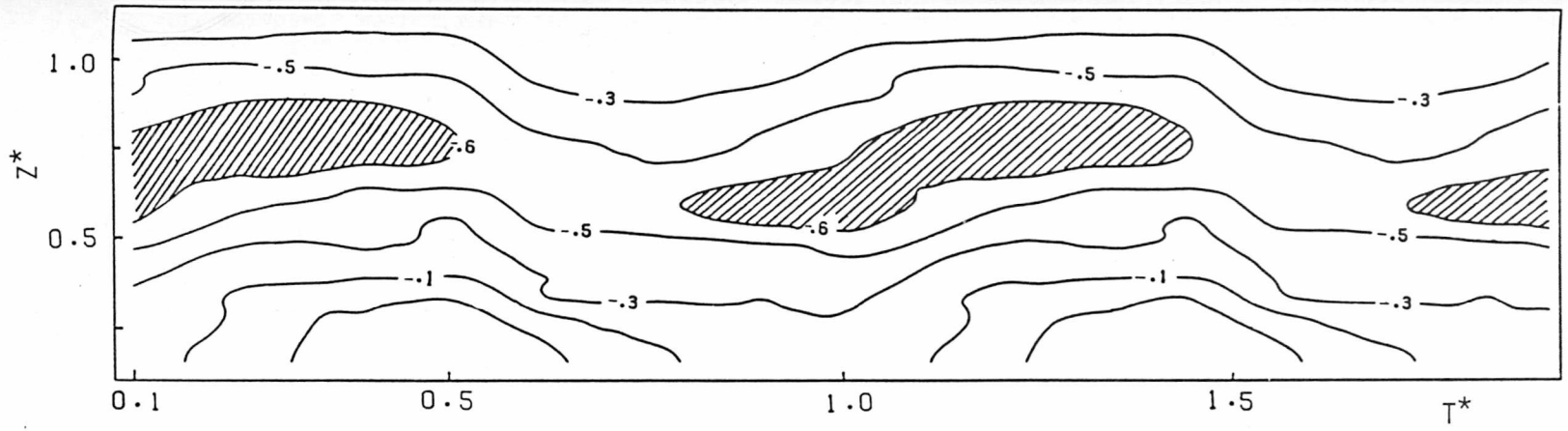



(a) u* fluctuation

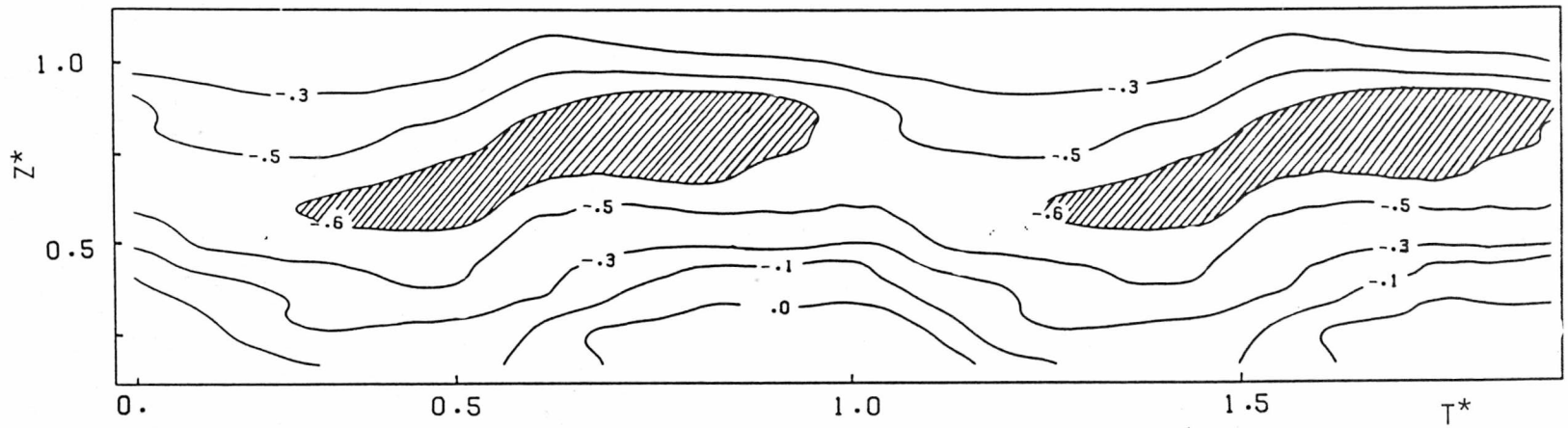



(b) v* fluctuation

Figure 3.2.9 Conditionally averaged velocity fluctuations of ($-90^{o}$) mode in the (z,t) plane in the wake of the solid circular disk at x = 3.4 D, y = 0, U = 10 m/s.




(a) ($-90^{o}$) mode




(b) ($90^{o}$) mode

Figure 3.2.10 Velocity distributions in the (z,t) plane in the wake behind the solid circular disk at x = 3.4 D, y = 0, $R_e = 6.8 \times 10^4$.

wake flow: (i) the clouds of vorticity shed from any two opposite sides of the disk are roughly $180^{o}$ out of phase with each other at $x = 3.4\ D$, (ii) extracted periodic clouds of vorticity in the (y,t) plane and (z,t) plane can be either $90^{o}$ or $-90^{o}$ out of phase with each other. The simplest interpretation of the above limited information would be that an unstable helical counterrotating vortex pair is shed intermittently. The direction of the helices change from clock-wise to anticlock-wise or vice versa frequently and randomly. This structure should be confirmed by further measurements at various positions in the wake.

## 3.3 Wake structure of a two flat plates arranged side-by-side

If we consider the cross-sectional view of vortex shedding from a ring model in a plane containing the axis of symmetry, then its two-dimensional analogue is vortex shedding from two flat plates placed normal to a free stream in a side-by-side arrangement. Measurements of base pressure, drag, correlation of velocity fluctuations and vortex shedding frequencies of two circular cylinders or two flat plates arranged side-by-side, with various gaps, have been carried out by several investigators. In the present research periodic components were extracted from turbulent velocity fluctuations measured by cross-wires in the wakes behind the two flat plates with end plates described in Table 2.1 and Figure 2.1. The conditional averaging technique was used in the present experiment and the results are compared with

those from the wake of the thin sharp-edged ring model. The wakes of two flat plates arranged side-by-side with spacings of $d/w = 4.0$ and $d/w = 6.0$, where $w$ is the width of the flat plate and $d$ is the distance between the centres of the two flat plates, were examined. Measurements of the reference velocity fluctuation, the velocity fluctuation of $u$ and $v$ and the conditional averaging were achieved in the same way as for the thin sharp-edged ring model described in Section 3.1.3. The two-dimensional coordinate system $(x,y)$ is used and the symbols employed here are the same as those used for the ring model in the last two sections, except that the discriminating symbol (') is used.

Biermann and Herrnstein (1933) demonstrated experimentally that the interference drag of two circular cylinders arranged side-by-side with a spacing of $d/w = 4.0$ is very small and that the interference drag is practically zero for spacings greater than that. Andreopoulos (1972) measured the base pressure on each of two sharp-edged cross-section flat plates arranged side-by-side and found that the flat plates experienced asymmetric flow in the range of spacing up to $d/w = 3.0$, as shown in Figure 3.3.1. This is a larger range of gap size than that found for asymmetric flow around two circular cylinders. Bearman and Wadcock (1973) observed that vortex shedding from two circular cylinders arranged side-by-side is symmetric about the axis of the gap when the spacing is $d/w > 2.0$. Although it is not clear what is the upper limit of spacing for antiphase (symmetric) vortex shedding from two flat plates, Williamson (1985) visualised the antiphase

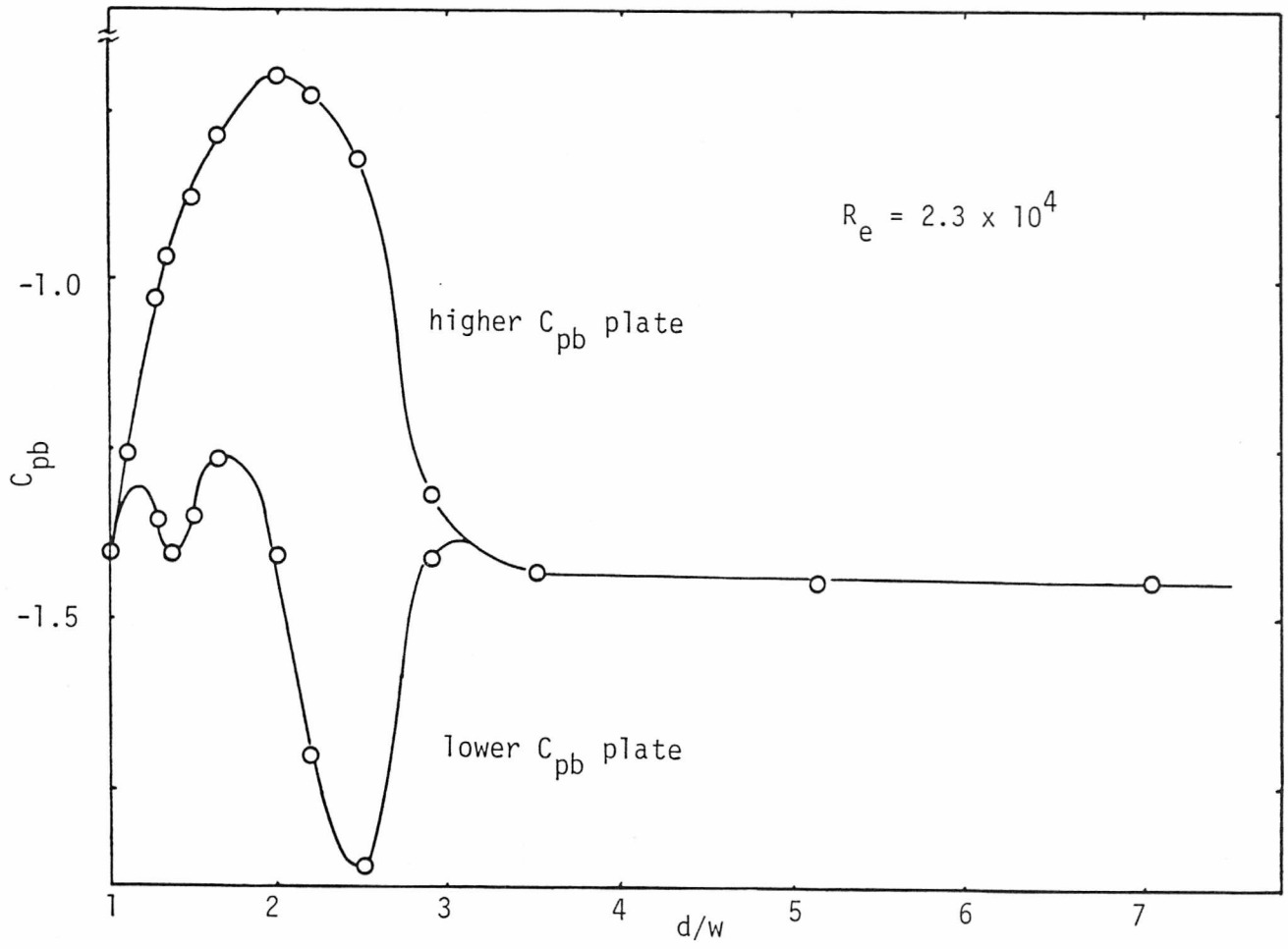
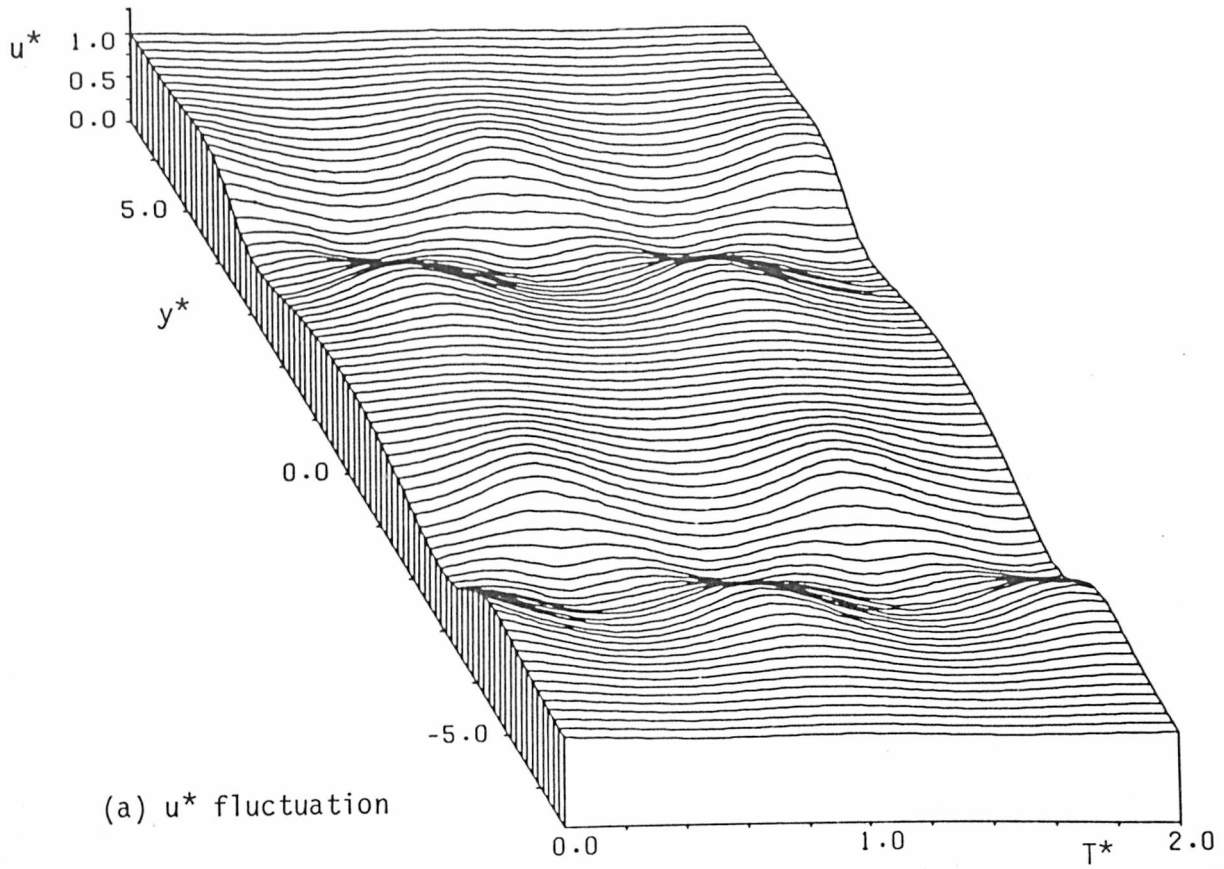


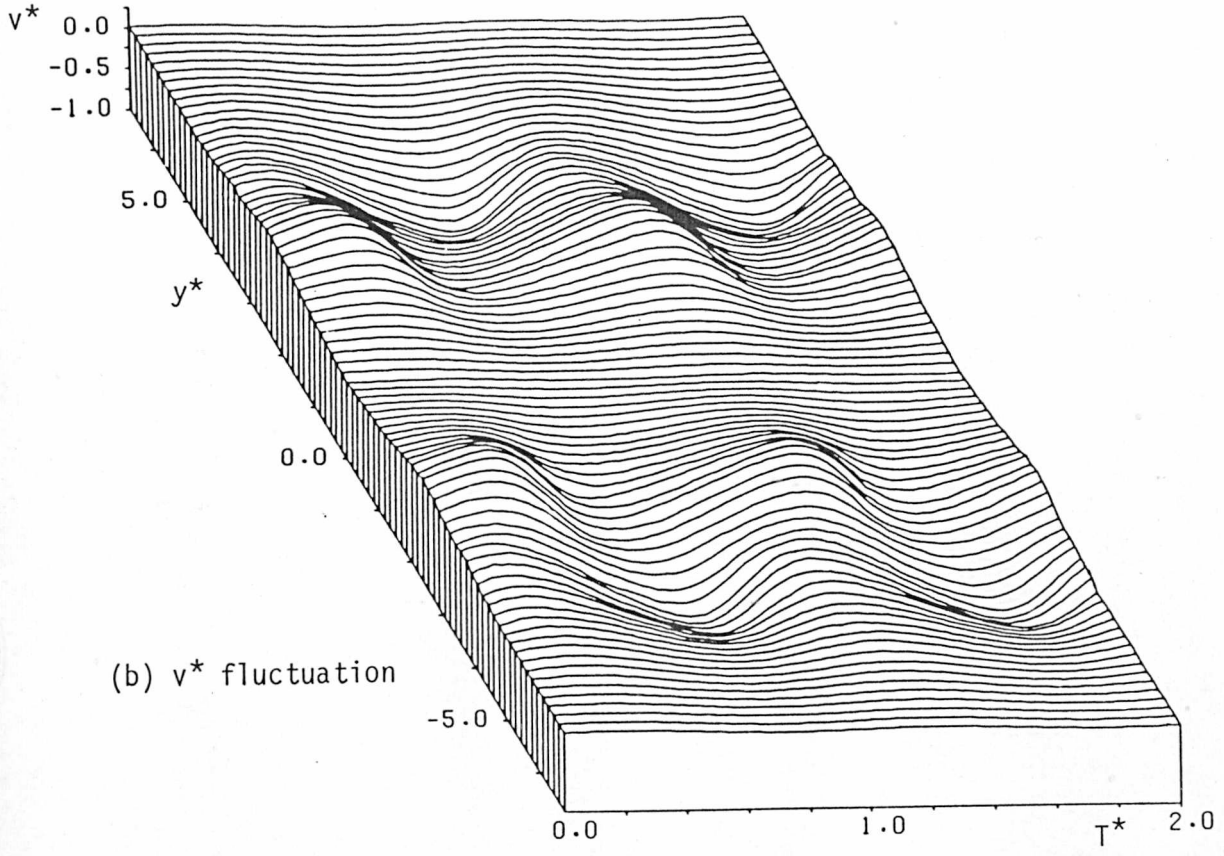

Figure 3.3.1 Measurement of base pressure of two flat plates arranged side-by-side, reproduced from Andreopoulos (1972).

synchronization of vortex shedding from two circular cylinders with d/w = 6.0 at a low Reynolds number. He also observed that vortex shedding synchronization occurs either in phase or in anticphase in the range between d/w = 2.0 and d/w = 6.0. Preliminary measurements of conditionally averaged velocity fluctuations in the wakes behind two flat plates with d/w = 4.0 and d/w = 6.0 were made at several positions in the present experiment. These showed that vortex shedding from the two flat plates is in antiphase on the whole, although some asymmetric vortex shedding,which disappeared in the process of averaging over a large number of cycles, was also observed.

Figure 3.3.2 to Figure 3.3.4 show the conditionally averaged velocity fluctuations of two vortex shedding cycles behind the two flat plates arranged side-by-side with d/w = 6.0 at x = 3.4 w, 8.0 w and 16.0 w respectively. The patterns of the velocity fluctuations are similar to those measured in the wake of the thin sharp-edged cross-section ring model shown in Figures 3.1.20 and 3.1.21, except for the pattern of the velocity fluctuation of $v^*$ between the paths of the inside and outside vortices at x = 3.4 w. The difference may be caused by the difference in the spacing between the rows of inside and outside vortices, which can be seen from the distribution of vorticity presented later. Figures 3.3.5 and 3.3.6 show root-mean-square and mean conditionally averaged velocity fluctuations profiles at x = 3.4 w, 8.0 w and 16.0 w respectively. The profiles of r.m.s. values at the three positions are almost symmetric about $y^*$ = 3.0, whereas the profiles of the thin sharp-edged cross-section ring model shown in




(a) u* fluctuation




(b) v* fluctuation

Figure 3.3.2 Conditionally averaged velocity fluctuations in the wake behind the two flat plates arranged side-by-side with d/w = 6.0 at x = 3.4 w, U = 10 m/s.

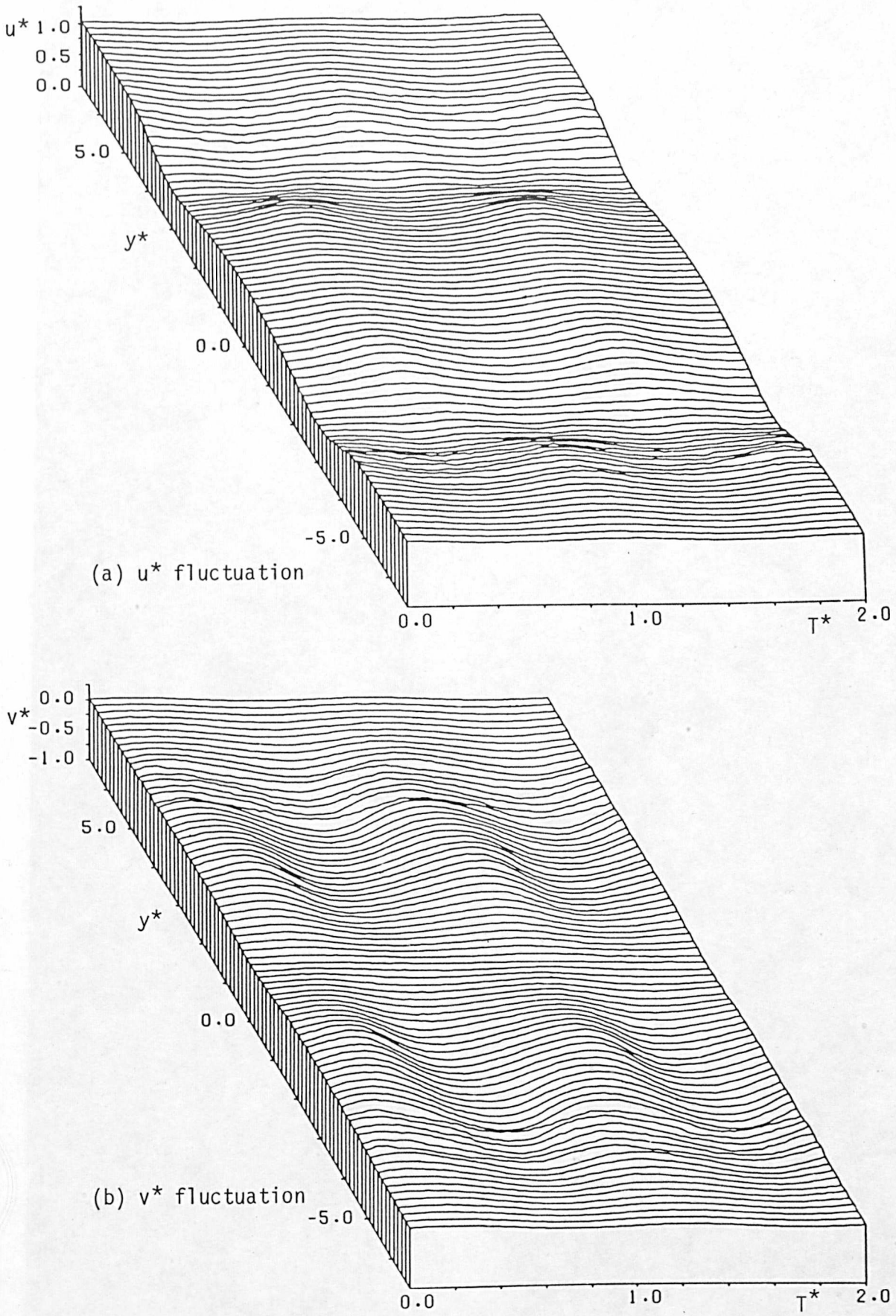
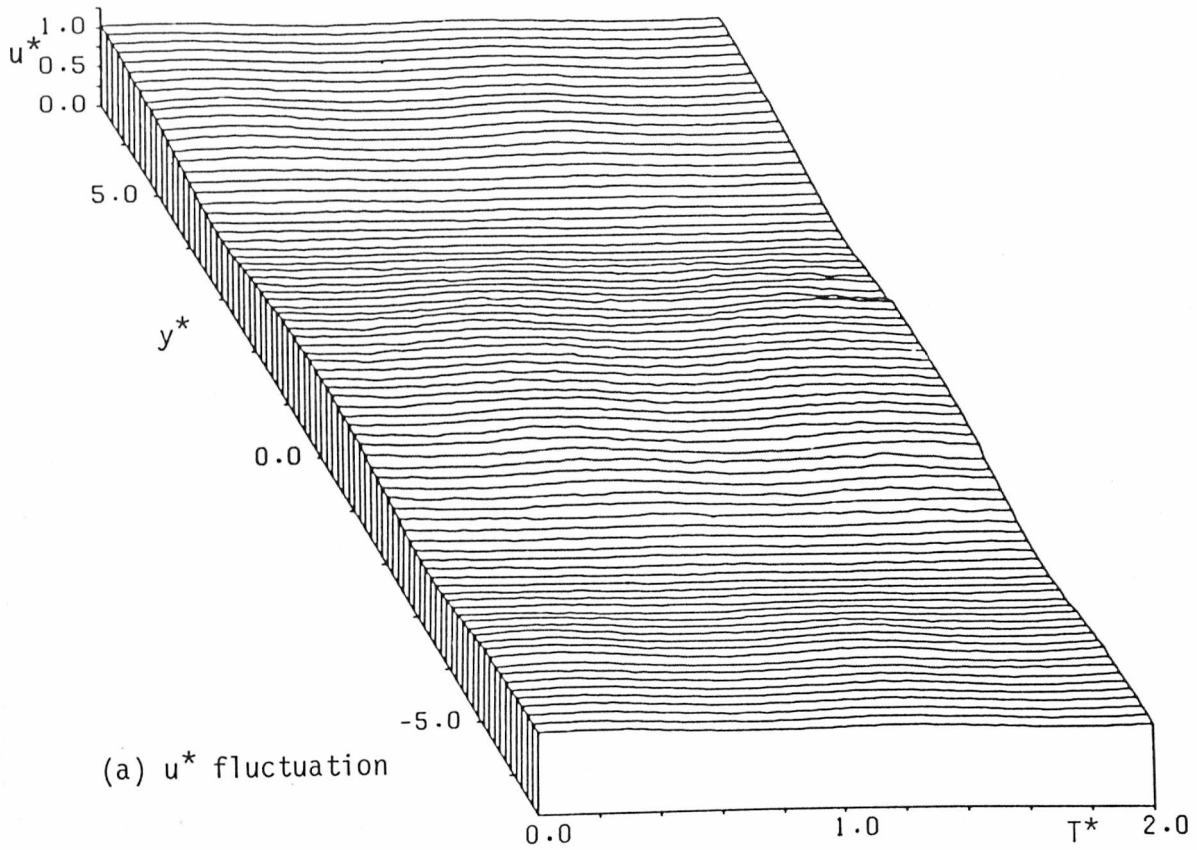
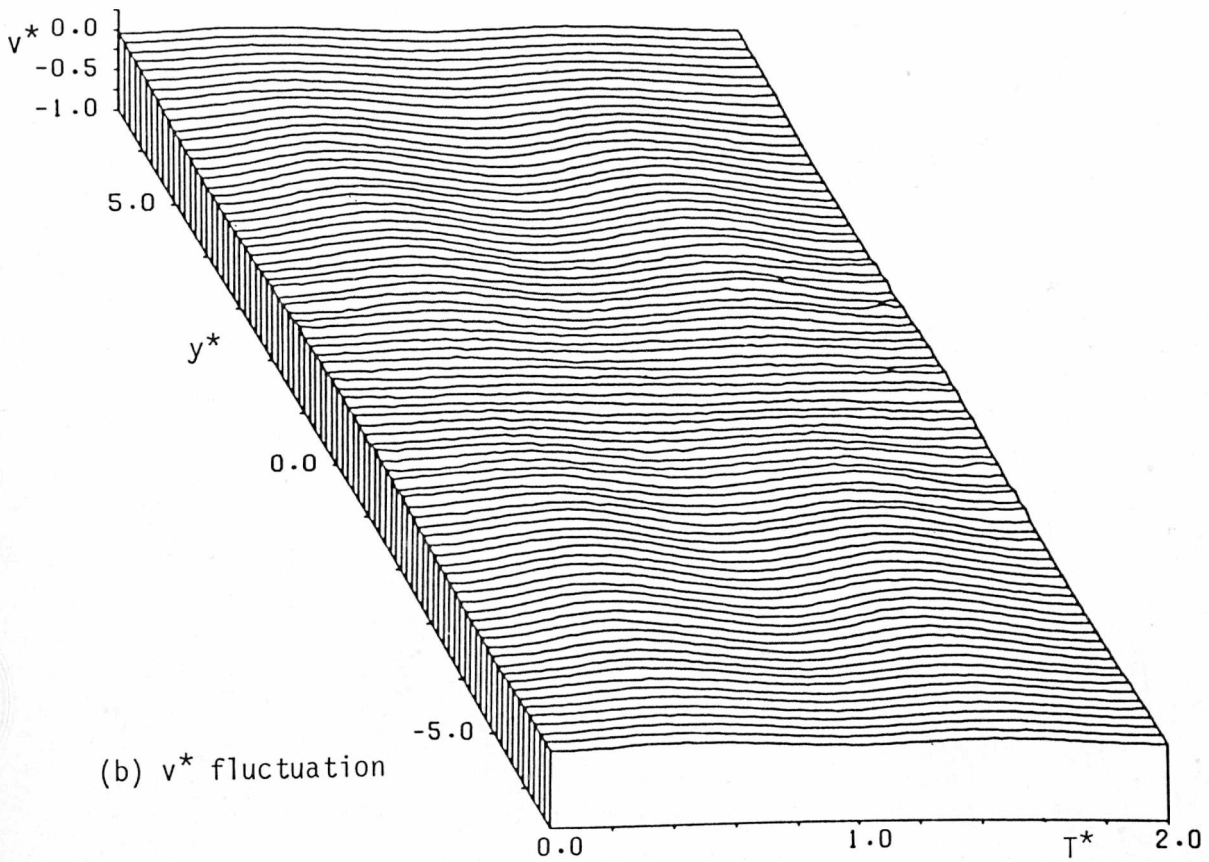



Figure 3.3.3 Conditionally averaged velocity fluctuations in the wake behind the two flat plates arranged side-by-side with d/w = 6.0 at x = 8.0 w, U = 10 m/s.

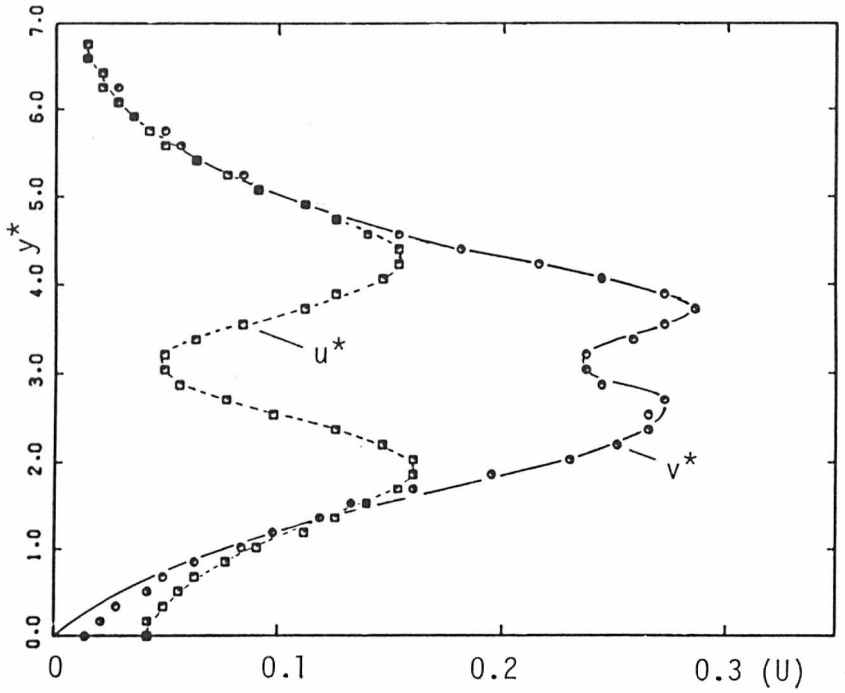



(a) u* fluctuation



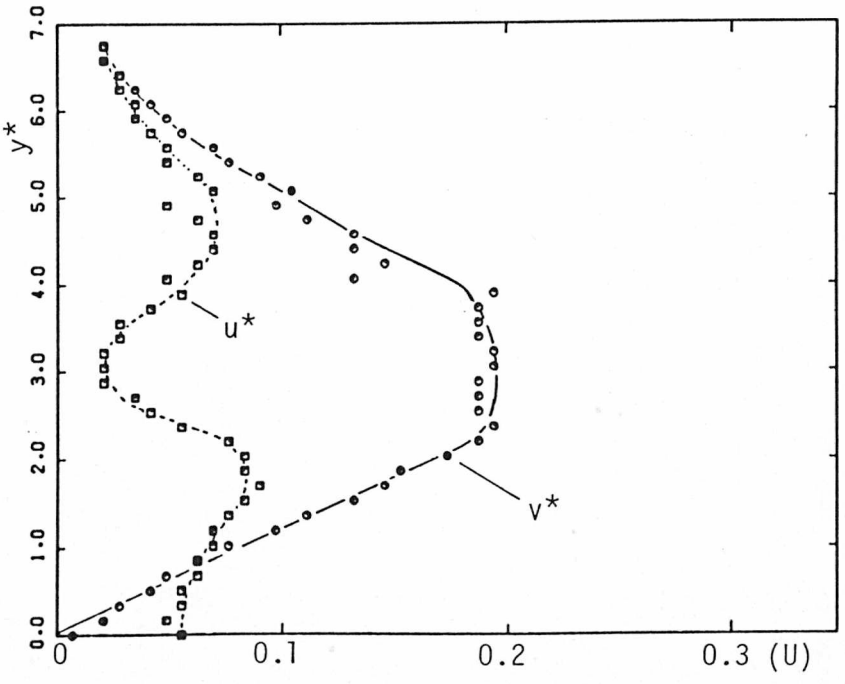

(b) v* fluctuation

Figure 3.3.4 Conditionally averaged velocity fluctuations in the wake behind the two flat plates arranged side-by-side with d/w = 6.0 at x = 16.0 w, U = 10 m/s.




r.m.s. of u* and v* fluctuation

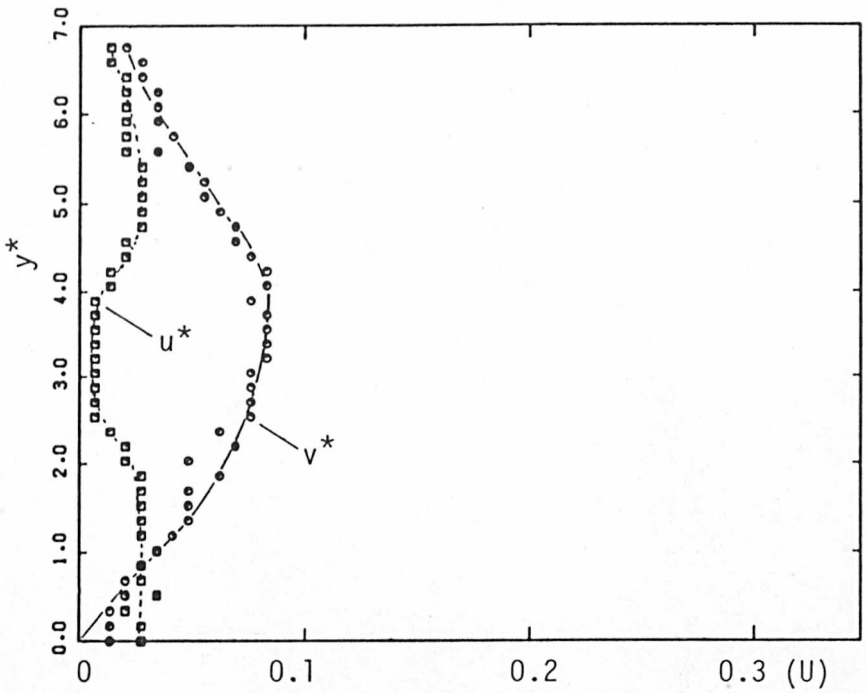
(a) x = 3.4 w




r.m.s. of u* and v* fluctuation

(b) x = 8.0 w

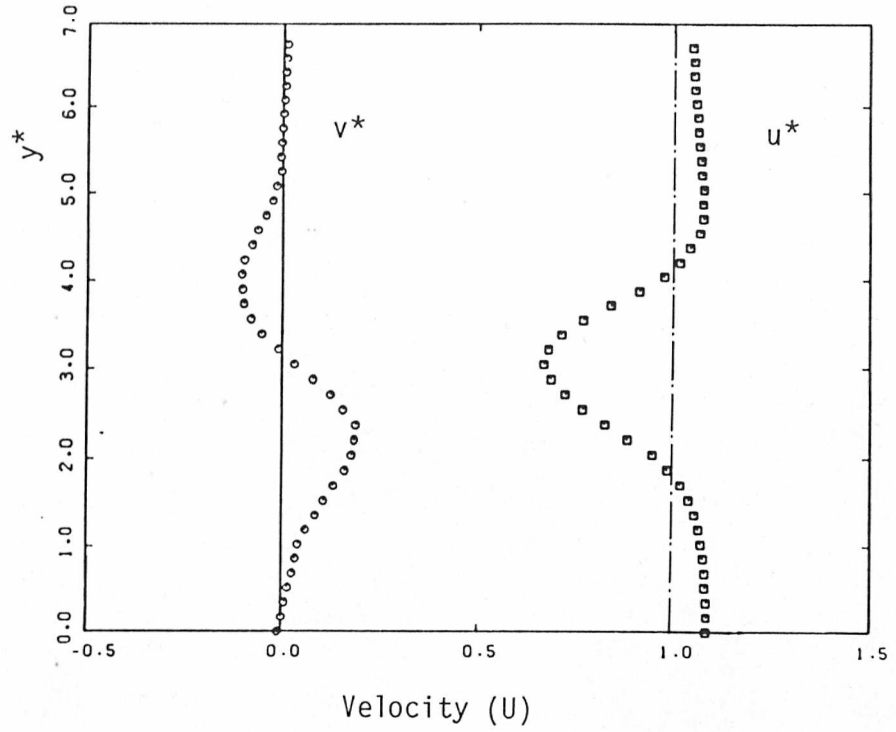
Figure 3.3.5



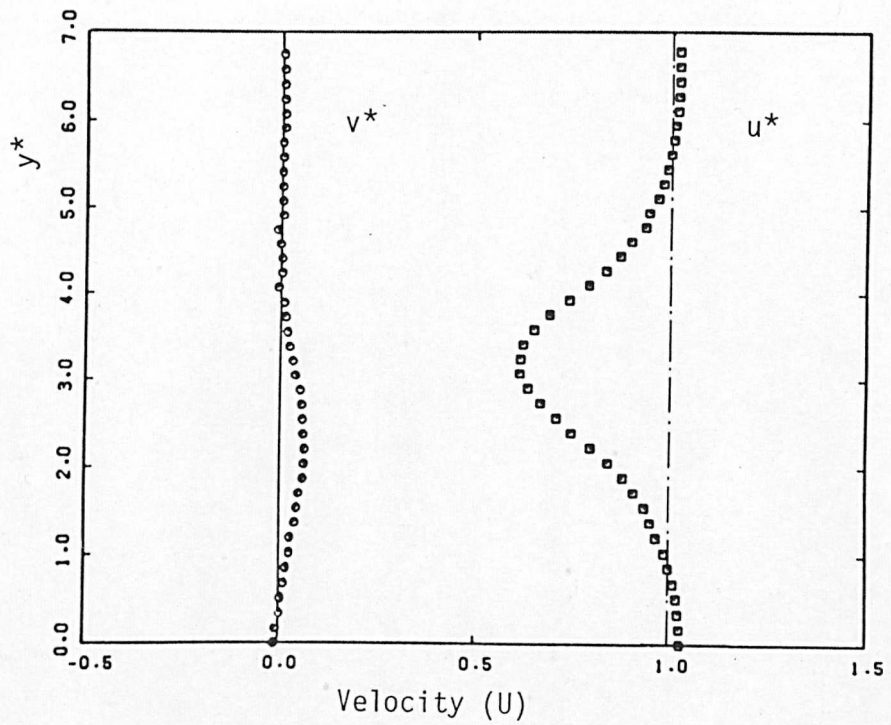

r.m.s. of $u^*$ and $v^*$ fluctuation

(c) x = 16.0 w.

Figure 3.3.5 Root-mean-square profiles of conditionally averaged velocity fluctuations $u^*$ and $v^*$ in the wake behind the two flat plates arranged side-by-side with d/w = 6.0, $R_e = 2.0 \times 10^4$.

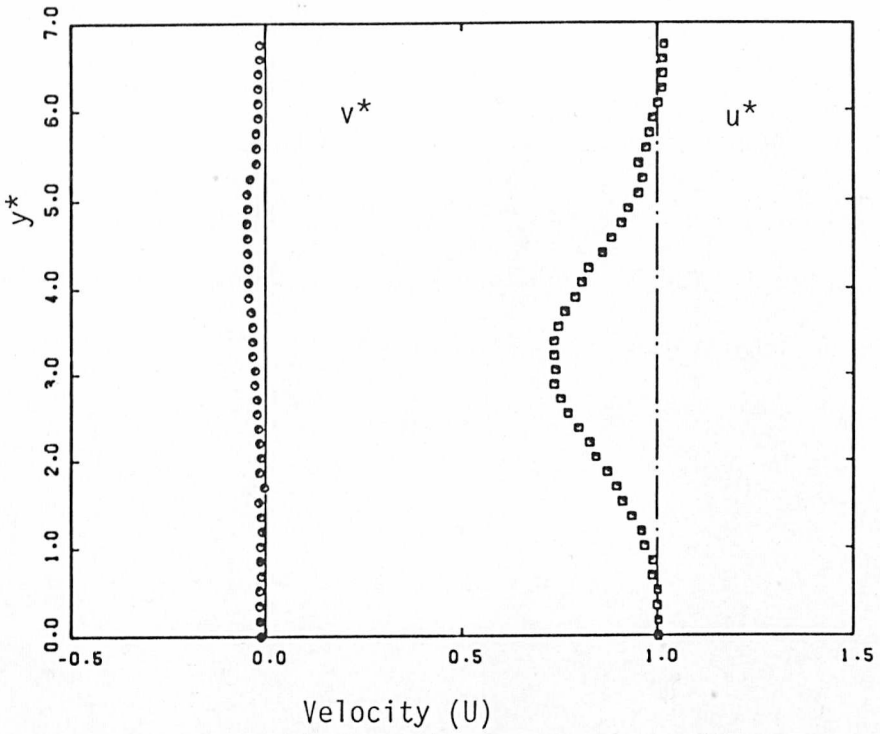



(a) x = 3.4 w




(b) x = 8.0 w

Figure 3.3.6




(c) x = 16.0 w

Figure 3.3.6 Profiles of mean velocities u* and v* in the wake behind the two flat plates arranged side-by-side with d/w = 6.0, U = 10 m/s.

Figure 3.1.23 are not. It suggests that vortex shedding from each of the two flat plates is almost symmetric about the centre of each flat plate and is not affected much by the existence of vortex shedding from the other plate except for the synchronization of the phase of vortex shedding. Also the r.m.s. values of $v^*$ fluctuations are about twice as large as that of the $u^*$ fluctuations at the three positions, whereas the r.m.s. values of $u^*$ and $v^*$ fluctuations of the thin sharp-edged cross-section ring model are almost at the same level. The profiles of mean velocities are almost the same as those of the thin sharp-edged cross-section ring model as shown in Figure 3.1.24.

Figures 3.3.7 to 3.3.9 show vorticity contours behind the two flat plates arranged side-by-side with $d/w = 6.0$ at $x = 3.4$ w, 8.0 w and 16.0 w respectively. The patterns of the vorticity distributions of the inside and outside vortices and their arrangements at the three positions in the wake are almost the same except for the effect of diffusion of vorticity which spreads the vortices with distance downstream. The strengths of the inside and outside vortices at $x = 3.4$ w are $\Gamma_a'^* = 3.08$ and $\Gamma_b'^* = -2.97$ and their ratio is $-\Gamma_a'/\Gamma_b' = 1.03$. Therefore, about 41% and 40% of the total vorticity remain within each concentrated cloud of vorticity. These values are between those for the inside and outside vortex rings measured at the same position in the wake of the thin sharp-edged cross-section ring model. The spacing ratio of the vortices is $h'/\ell' = 0.51$, i.e. vortices of about the

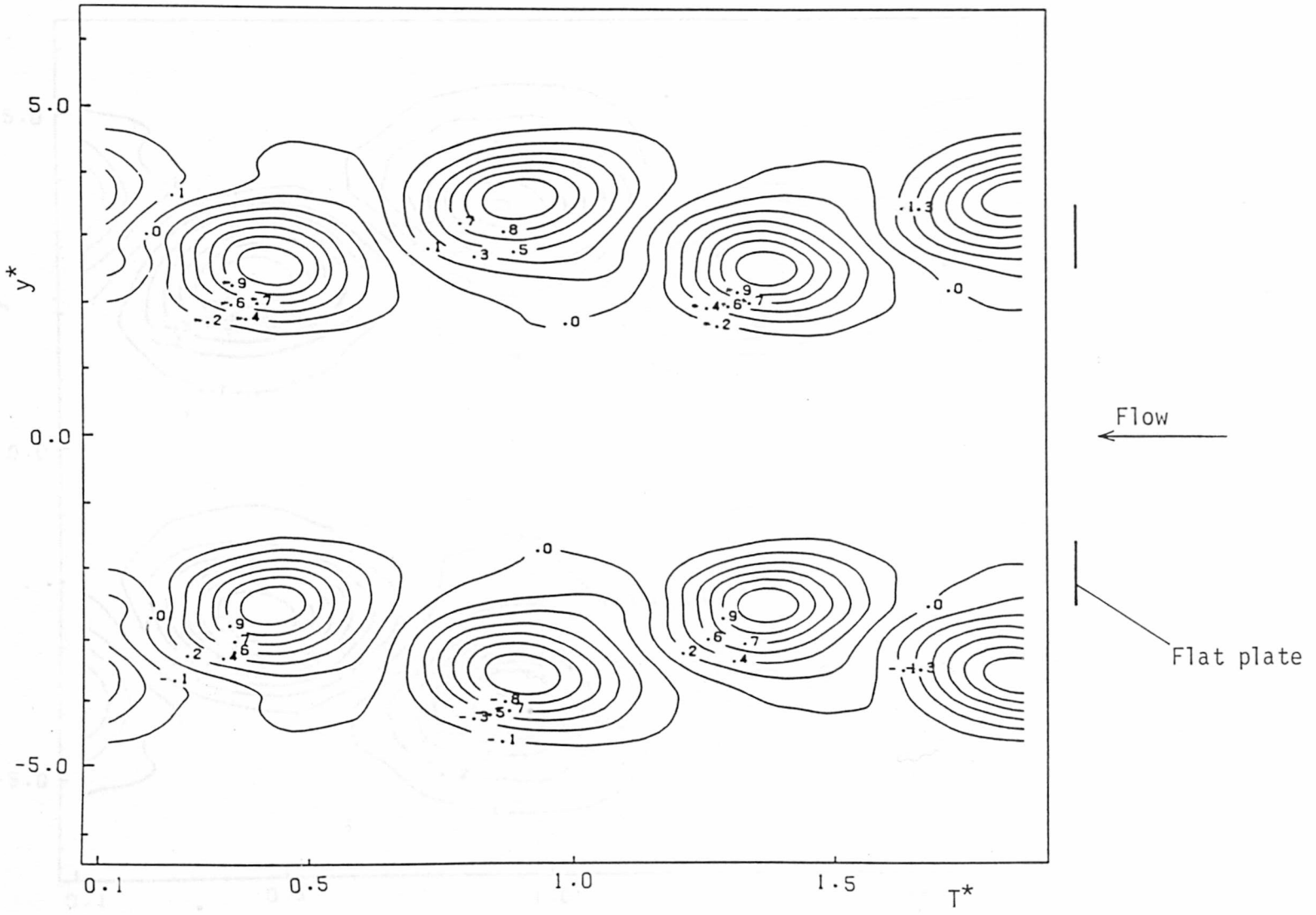



Figure 3.3.7 Vorticity distribution in the wake behind the two flat plates arranged side-by-side with d/w = 6.0 at x = 3.4 w, $R_e$ = 2.0 x $10^4$

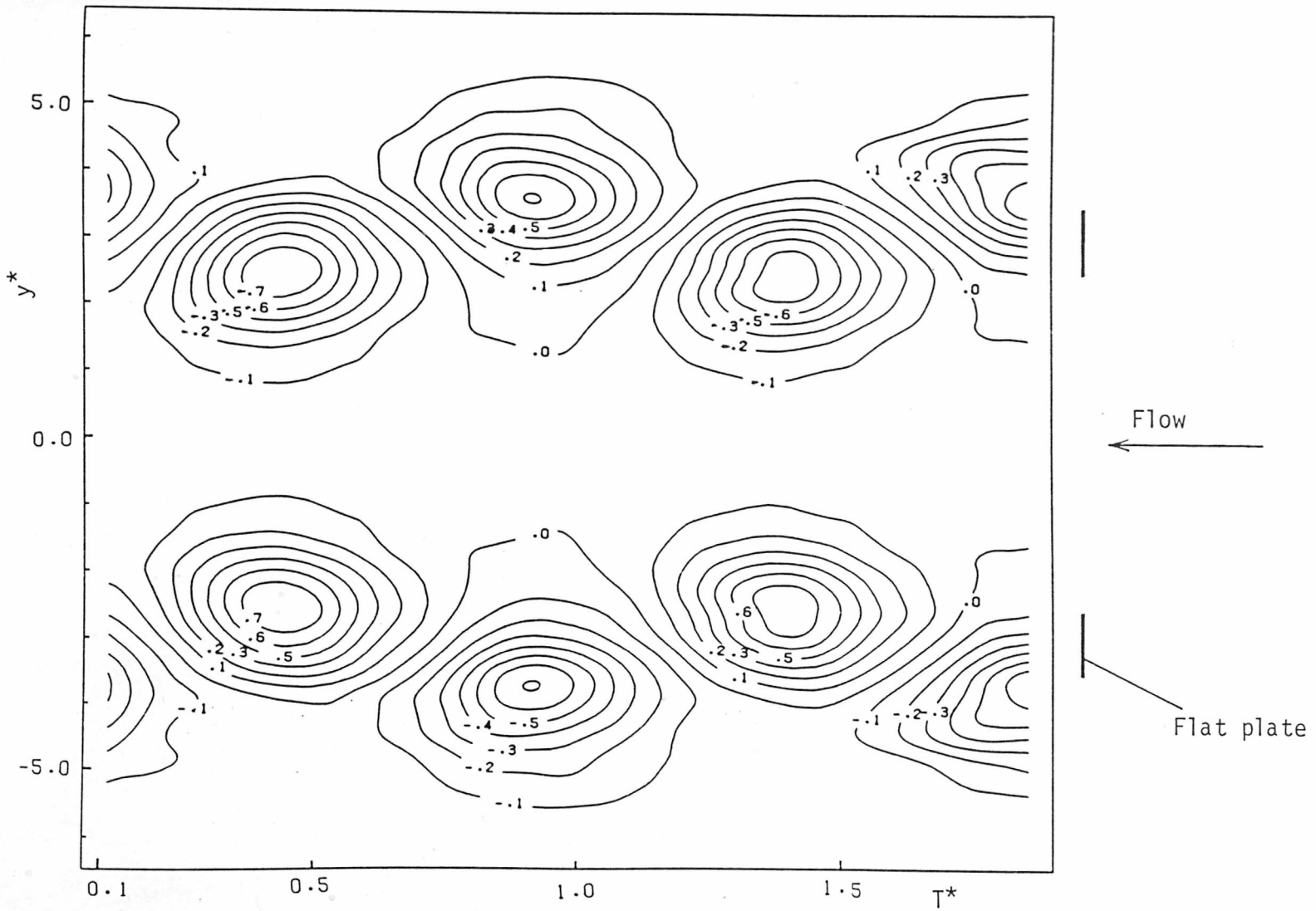



Figure 3.3.8 Vorticity distribution in the wake behind the two flat plates arranged side-by-side with d/w = 6.0 at x = 8.0 w, $R_e = 2.0 \times 10^4$

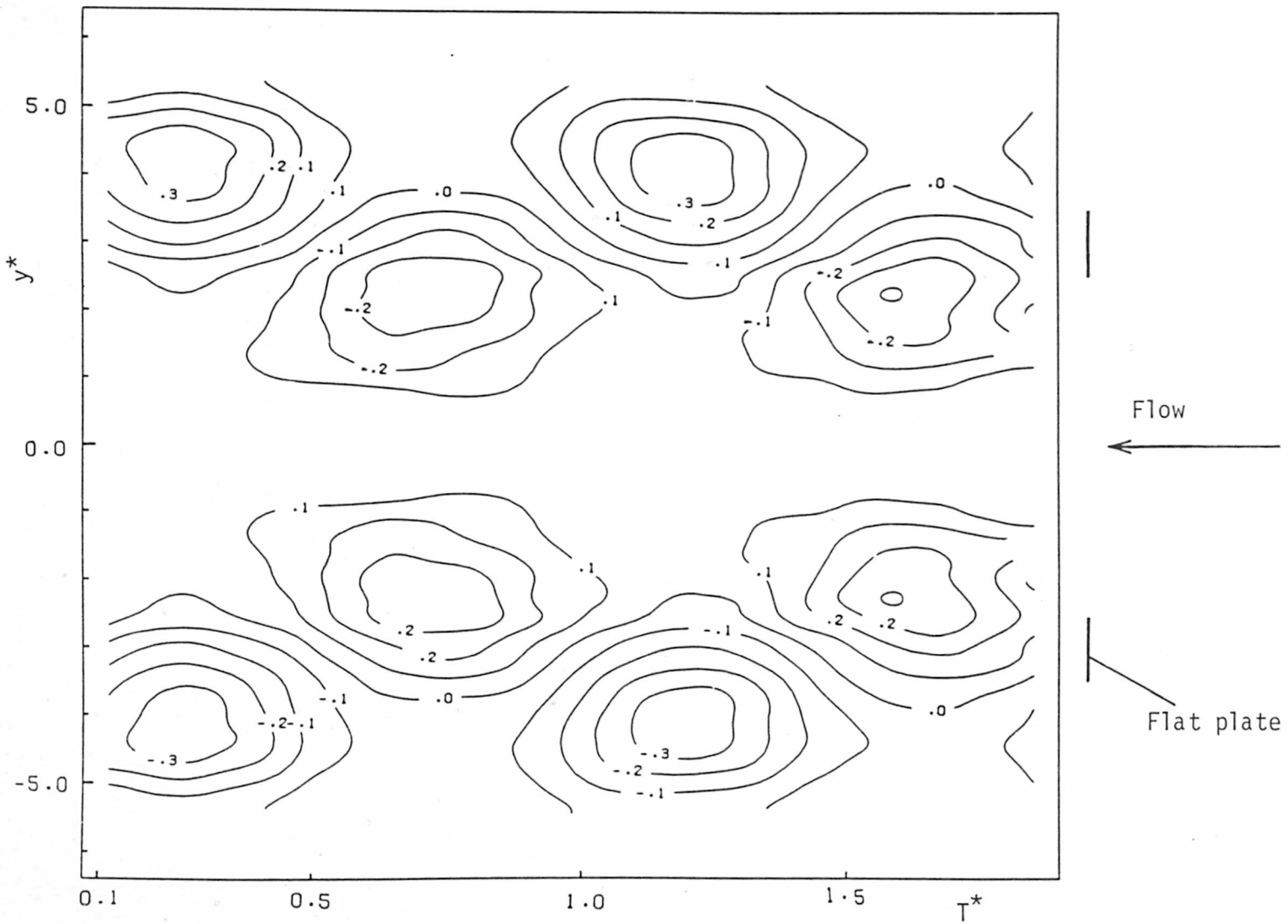



Figure 3.3.9 Vorticity distribution in the wake behind the two flat plates arranged side-by-side with d/w = 6.0 at x = 16.0 w, $R_e$ = 2.0 x $10^4$

same strength shed from alternate sides of the flat plate with nearly $180^{o}$ out of phase difference. Half the spacing between the two rows of inside vortices and between the two rows of outside vortices is a' = 2.5 w and b' = 3.5w respectively. Therefore, the spacing between the rows of the inside and outside vortices is b' - a' = 1.0 w, which is smaller than that of the ring model of b - a = 1.4 w at the same position. At x = 8.0 w the strengths of the vortices decrease to $\Gamma_a'^* = 2.57$ and $\Gamma_b'^* = -2.58$ ($-\Gamma_a'/\Gamma_b' = 1.00$) at decay rates of 4% and 3% per w of vortex travel. However the arrangement of vortices changes very little. Davies (1975) meaured the wake of an isolated D-shaped cylinder at x =8.0 w. He obtained a non-dimensional strength of a vortex of 2.39 which was 26% of the total vorticity shed and a convection velocity of 0.8 U. The magnitudes of his results are comparable with the present results. The regular symmetric arrangement of vortices can still be recognised at x = 16.0 w, although a considerable diffusion of vorticity has taken place. The strengths of vortices decrease to $\Gamma_a'^* = 1.59$ and $\Gamma_b'^* = -1.64$ ($-\Gamma_a'/\Gamma_b' = 0.97$), i.e. only about 21% and 22% respectively of the total vorticity remains within the concentrated clouds. The decay rate of both vortices is 6% per w vortex travel between x = 8.0 w and x = 16.0 w. Therefore, vortices in the wake of the two flat plates and the ring models decay at almost the same rate. The width of the wake increases with distance downstream and at x = 16.0 w the arrangement of vortices are $h'/\ell' = 0.43$, with a' = 2.4 w and b' = 4.4 w. The results of the present measurements, which are summarized in Table 3.3.1, suggest that

## Table 3.3.1.

Vortices from the two flat plates arranged side-by-side with d/w = 6.0.

| Downstream Position x | 3.4 w | 8.0 w | 16.0 w |
|---|---|---|---|
| $\Gamma'_a{}^*$ (Inside Vortex) | 3.08 | 2.57 | 1.59 |
| $\Gamma'_a$ / Total Vorticity | 41% | 34% | 21% |
| $\Gamma'_b{}^*$ (Outside Vortex) | -2.97 | -2.58 | -1.64 |
| $\Gamma'_b$ / Total Vorticity | 40% | 34% | 22% |
| $-\Gamma_a'/\Gamma_b'$ | 1.03 | 1.00 | 0.97 |
| a' | 2.5 w | 2.5 w | 2.4 w |
| b' | 3.5 w | 3.6 w | 4.4 w |
| h'/ℓ' (Spacing Ratio) | 0.51 | 0.50 | 0.43 |
| $u_c$ of Inside Vortex | 0.96 U | 0.84 U | 0.81 U |
| $u_c$ of Outside Vortex | 0.91 U | 0.76 U | 0.88 U |

vortices shed from one of the two flat plates arranged side-by-side with $d/w = 6.0$ are little affected by vortices from the other flat plate, since there exists little difference between the inside and outside vortices. The only major interaction between the wakes of the two flat plates is the synchronization of vortex shedding. However, it is thought that synchronization can be induced by quite small fluctuations in the flow field since the vortex shedding frequencies of both flat plates are the same.

Figures 3.3.10 to 3.3.12 show conditionally averaged velocity vector fields, in which the convection velocity of the inside vortex is subtracted, at $x = 3.4\ w$, $8.0\ w$ and $16.0\ w$ respectively. Inside and outside vortices, $180^{o}$ out of phase with each other, can be clearly recognised in the three figures. Also the strengths of the inside and outside vortices appear about the same from considering the scales and circumferential velocities of the vortices. There is no area near the axis of symmetry between the wakes where fluid moves with the same velocity as the inside vortices in contrast to the case of the ring models.

The wakes of the two flat plates arranged side-by-side with a narrower spacing of $d/w = 4.0$ was also measured in the same way for comparison. Figure 3.3.13 shows conditionally averaged velocity fluctuations at $x = 8.0\ w$. Figure 3.3.14 and Figure 3.3.15 show the profiles of root-mean-square values and mean values of conditionally averaged velocity fluctuatuons $u^{*}$ and $v^{*}$ respectively. The patterns of the velocity fluctuations are

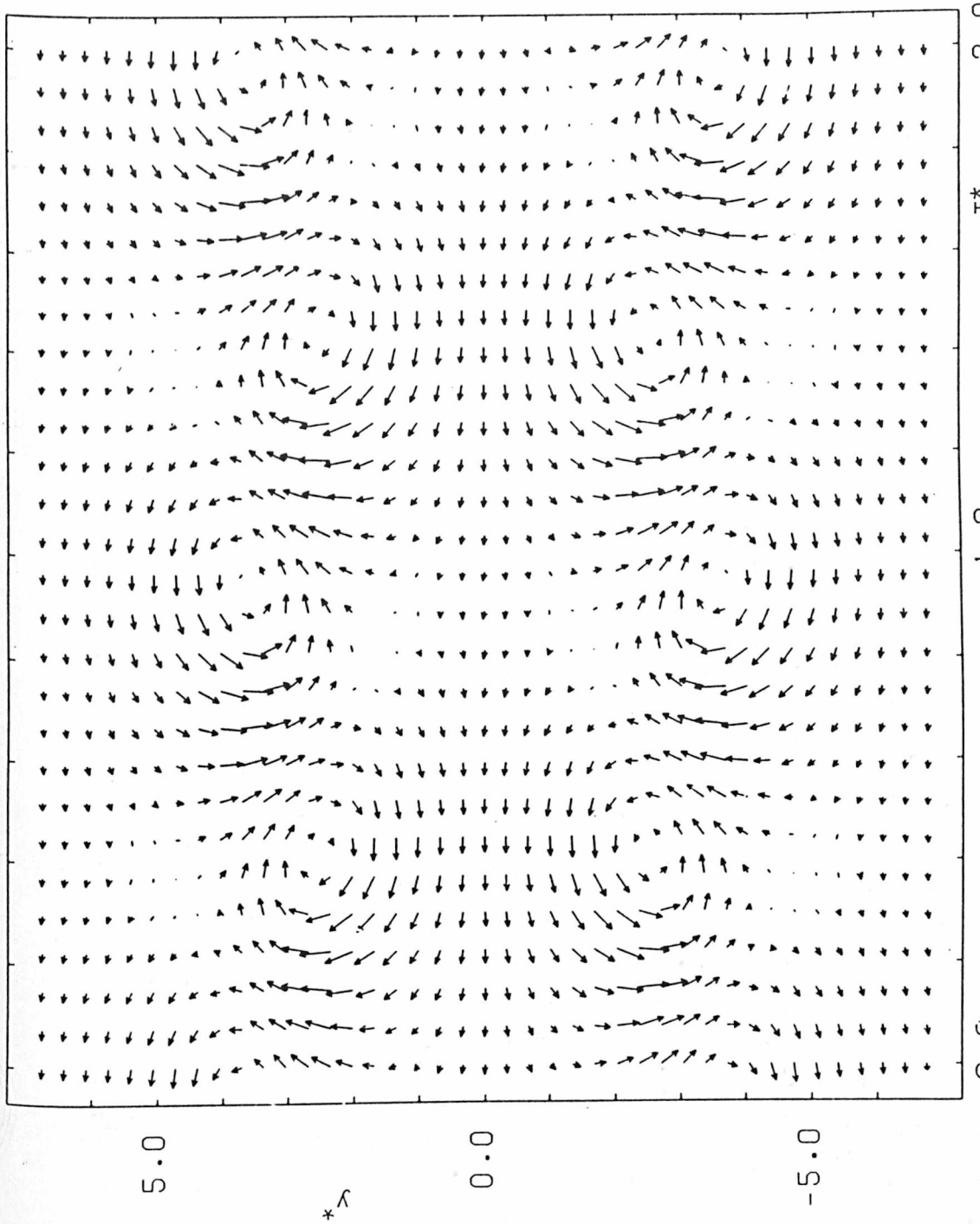



Figure 3.3.10 Velocity vector field in the wake behind the two flat plates arranged side-by-side with d/w = 6.0 at x = 3.4 w, $u_c$ = 0.96 U removed, U = 10 m/s.

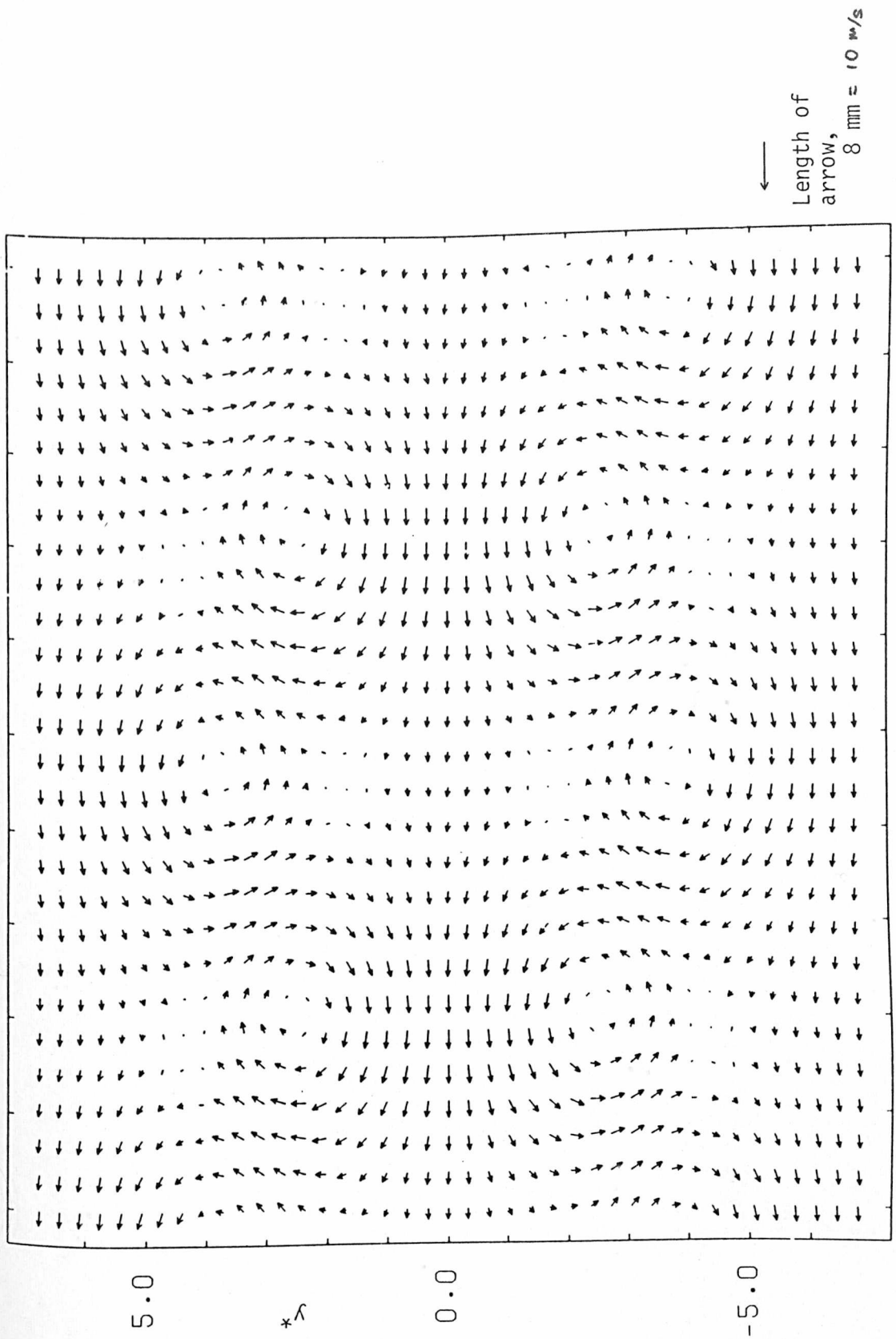



Figure 3.3.11 Velocity vector field in the wake behind the two flat plates arranged side-by-side with d/w = 6.0 at x = 8.0 w, $u_c$ = 0.84 U removed, U = 10 m/s.

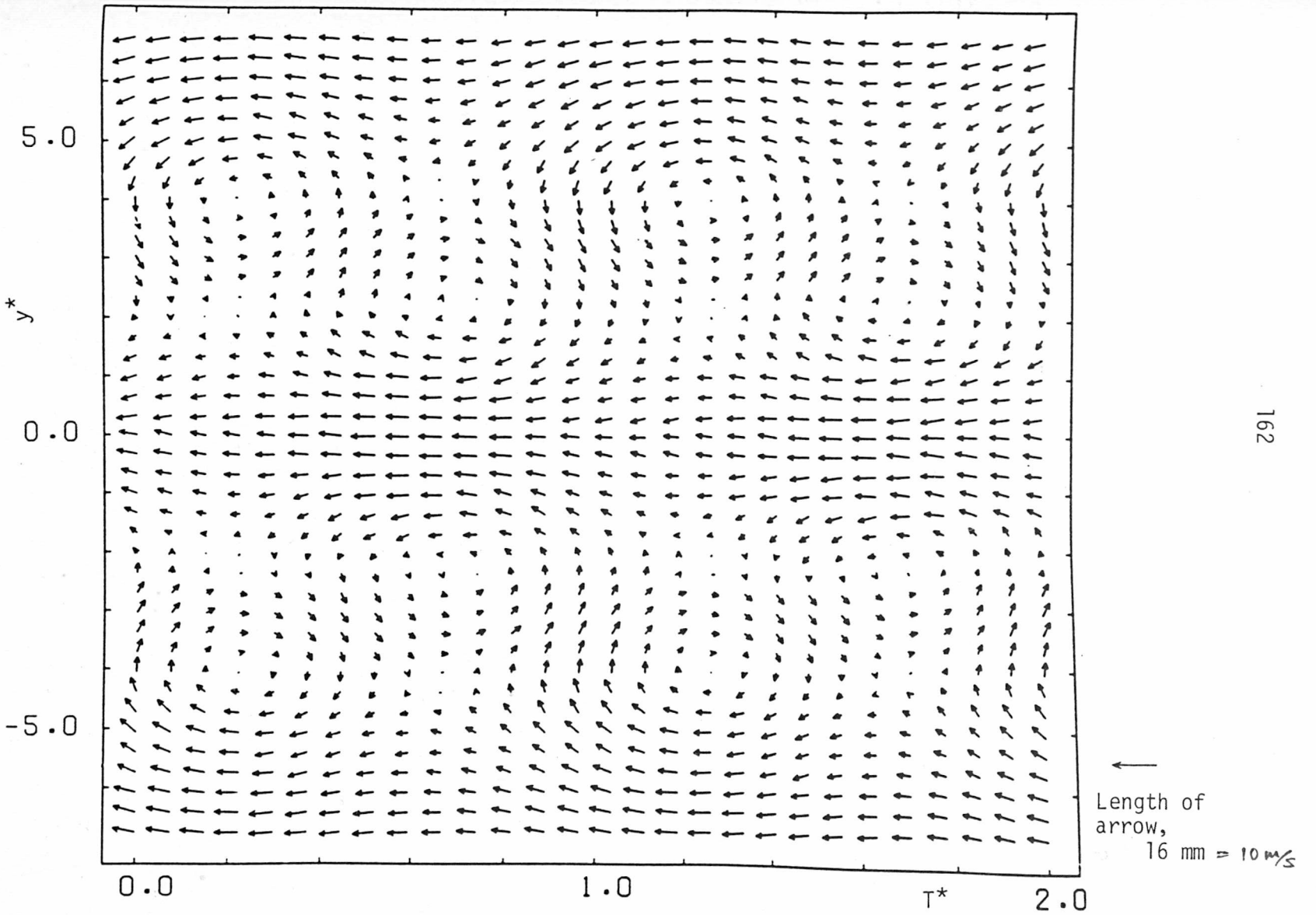
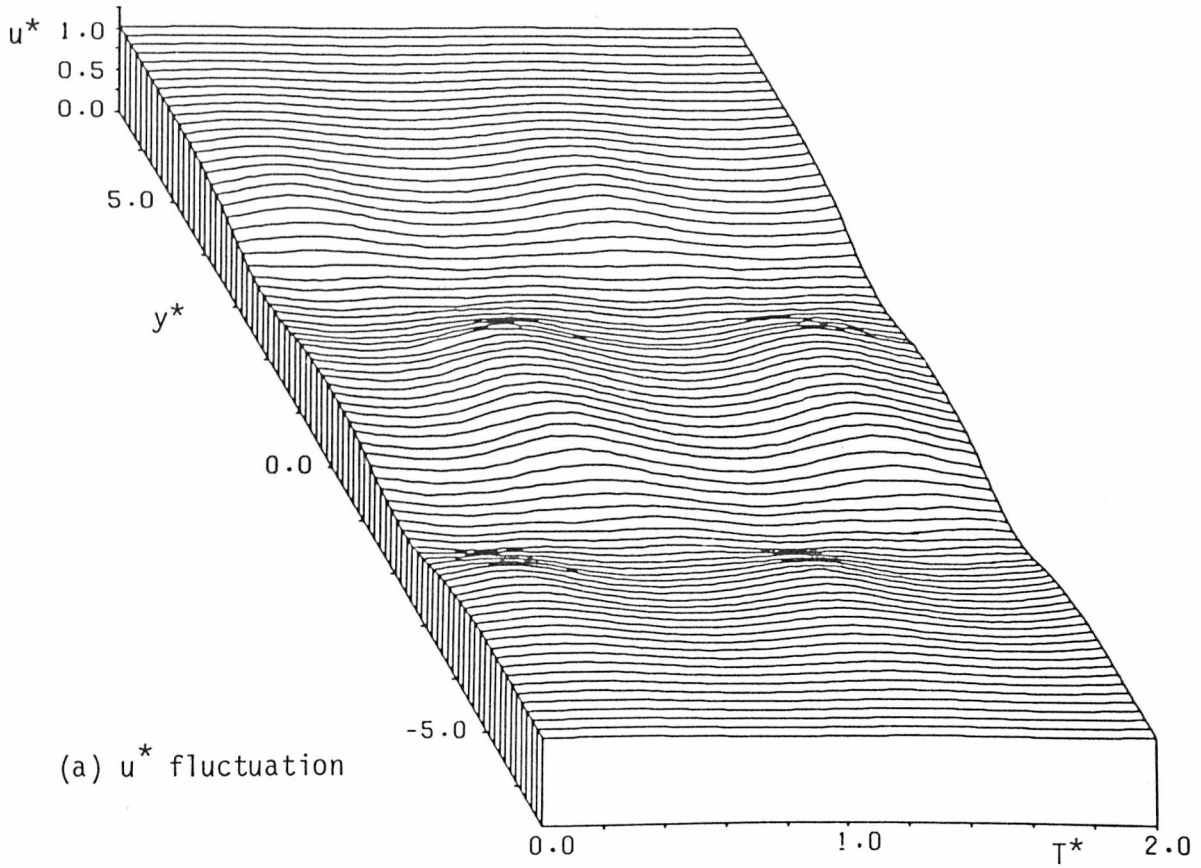
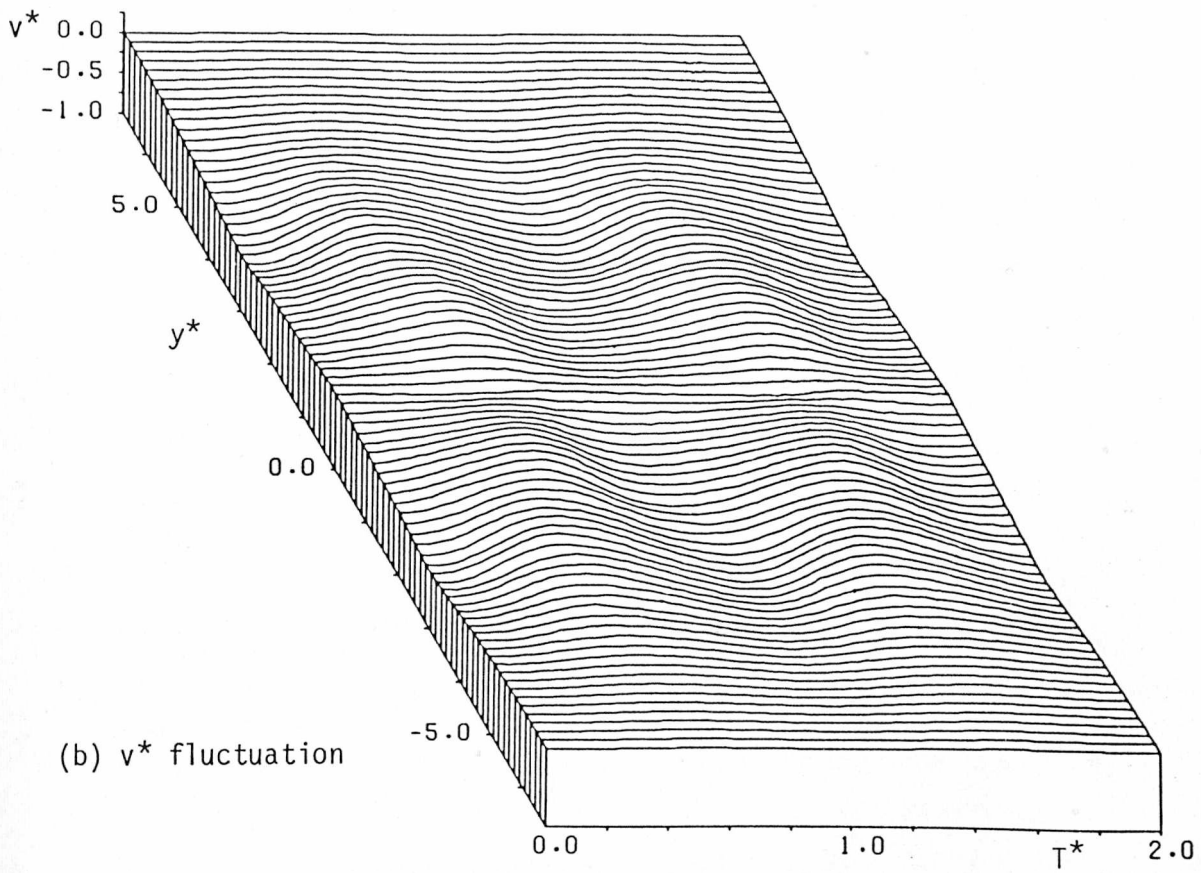



Figure 3.3.12 Velocity vector field in the wake behind the two flat plates arranged side-by-side with d/w = 6.0 at x = 16.0 w, $u_c$ = 0.81 U removed, U = 10 m/s.




(a) $u^*$ fluctuation




(b) $v^*$ fluctuation

Figure 3.3.13 Conditionally averaged velocity fluctuations in the wake behind the two flat plates arranged side-by-side with d/w = 4.0 at x = 8.0 w, U = 10 m/s.

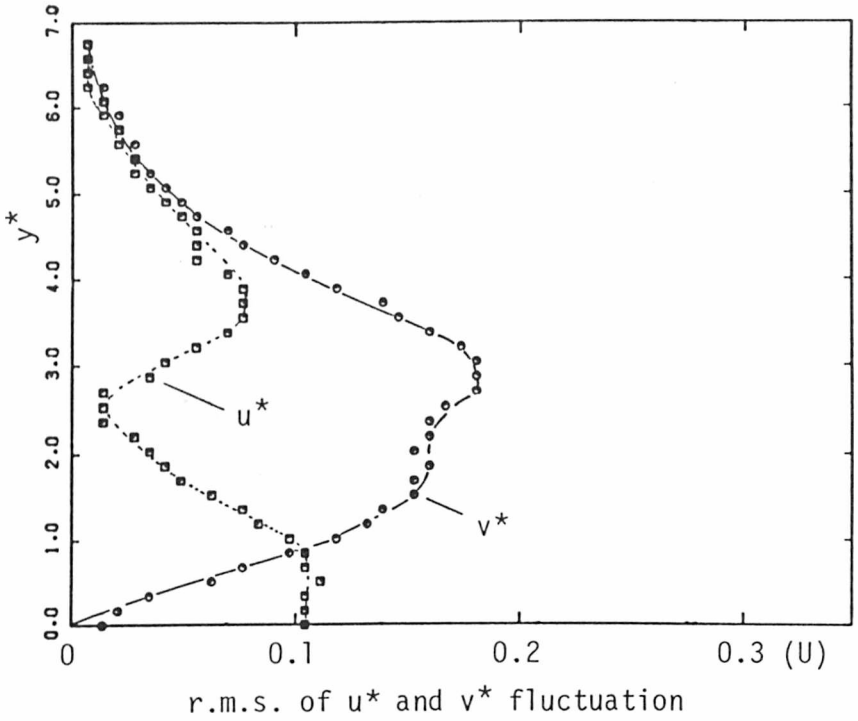



Figure 3.3.14 Root-mean-square profiles of conditionally averaged velocity fluctuation behind the two flat plates with d/w = 4.0 at x = 8.0 w, $R_e$ = 2.0 x $10^4$.

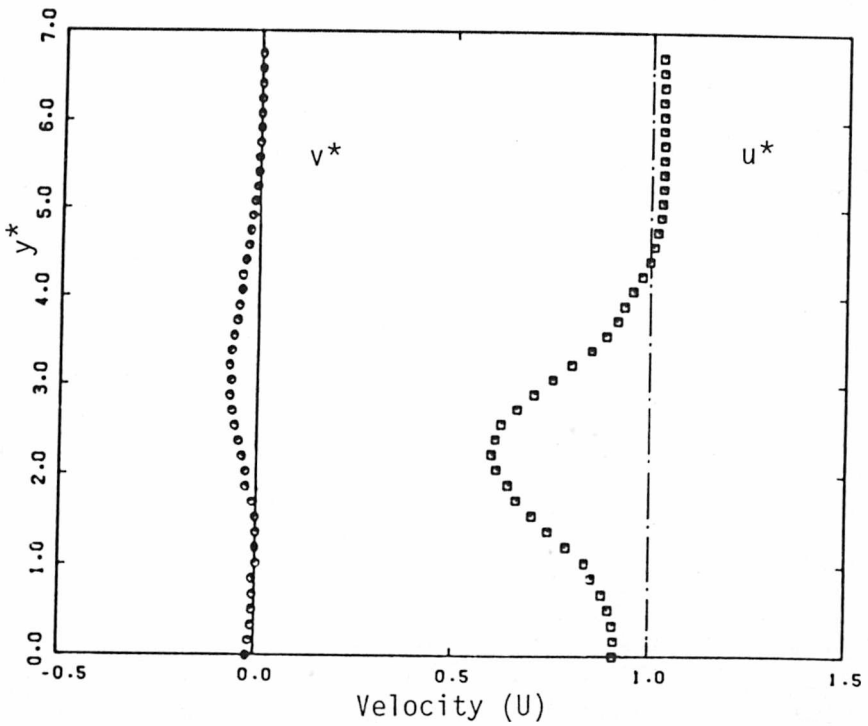



Figure 3.3.15 Profiles of mean velocities u* and v* in the wake behind the two flat plates with d/w = 4.0 at x = 8.0 w, $R_e$ = 2.0 x $10^4$.

almost the same as those of the two flat plates with d/w = 6.0. Figure 3.3.16 shows contours of vorticity distribution at x = 8.0 w calculated from the conditionally averaged velocity fluctuations. Regular symmetric vortices are seen in the wake of two flat plates with d/w = 4.0, whereas there exists no regular vortex shedding from the ring model with d/w = 4.0. The strengths of the inside and outside vortices are $\Gamma_a'^* = 2.10$ and $\Gamma_b'^* = -2.60$ ($-\Gamma_a'/\Gamma_b' = 0.81$), i.e. about 28% and 35% of the total vorticity remain within the concentrated clouds of vorticity respectively. Therefore, almost the same level of total vorticity remains within the outside clouds, but a smaller amount remains within the inside clouds compared with the wake of the two flat plates with d/w = 6.0 at the same downstream position. The reason is thought to be that since the inside vortices shed from the two flat plates are counterrotating the rate of cancellation between them is higher when the gap between the two flat plates is narrower. The arrangements of the inside and outside vortices are $h'/\ell' = 0.44$, $a' = 1.5$ w and $h' = 2.9$ w. The results of measurements are summarized in Table 3.2.2. Figure 3.3.17 shows conditionally averaged velocity vector field, in which the convection velocity of the inside vortex is subtracted, in the wake of the two flat plates with d/w = 4.0 at x = 8.0 w. It is recognised from the figure that the inside and outside vortices are nearly $180^{o}$ out of phase, and there exists an area on the axis of symmetry where the fluid moves at almost the same velocity as the centre of the inside vortex.

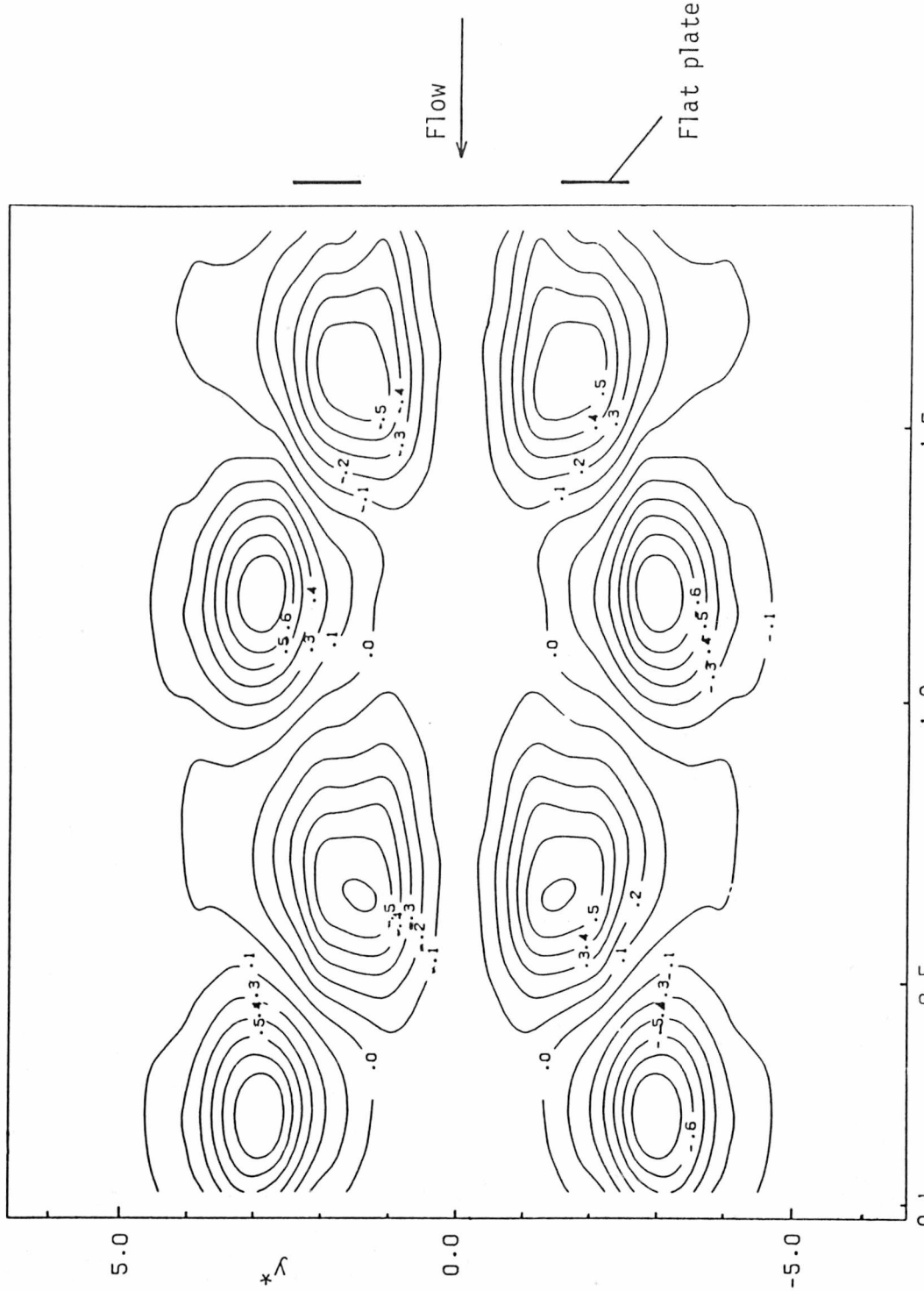



Figure 3.3.16 Vorticity distribution in the wake behind the two flat plates arranged side-by-side with d/w = 4.0 at x = 8.0 w, $R_e$ = 2.0 x $10^4$.

Table 3.3.2.

Vortices from the two flat plates arranged side-by-side with d/w = 4.0

| Downstream Position x | 8.0 w |
|---|---|
| $\Gamma'_a$* (Inside Vortex) | 2.10 |
| $\Gamma'_a$ / Total Vorticity | 28% |
| $\Gamma'_b$* (Outside Vorticity) | -2.60 |
| $\Gamma'_b$ / Total Vorticity | 35% |
| $-\Gamma_a'/\Gamma_b'$ | 0.81 |
| a' | 1.5 w |
| b' | 2.9 w |
| h'/ℓ' (Spacing Ratio) | 0.44 |
| $U_c$ of Inside Vortex | 0.85 U |
| $U_c$ of Outside Vortex | 0.82 U |

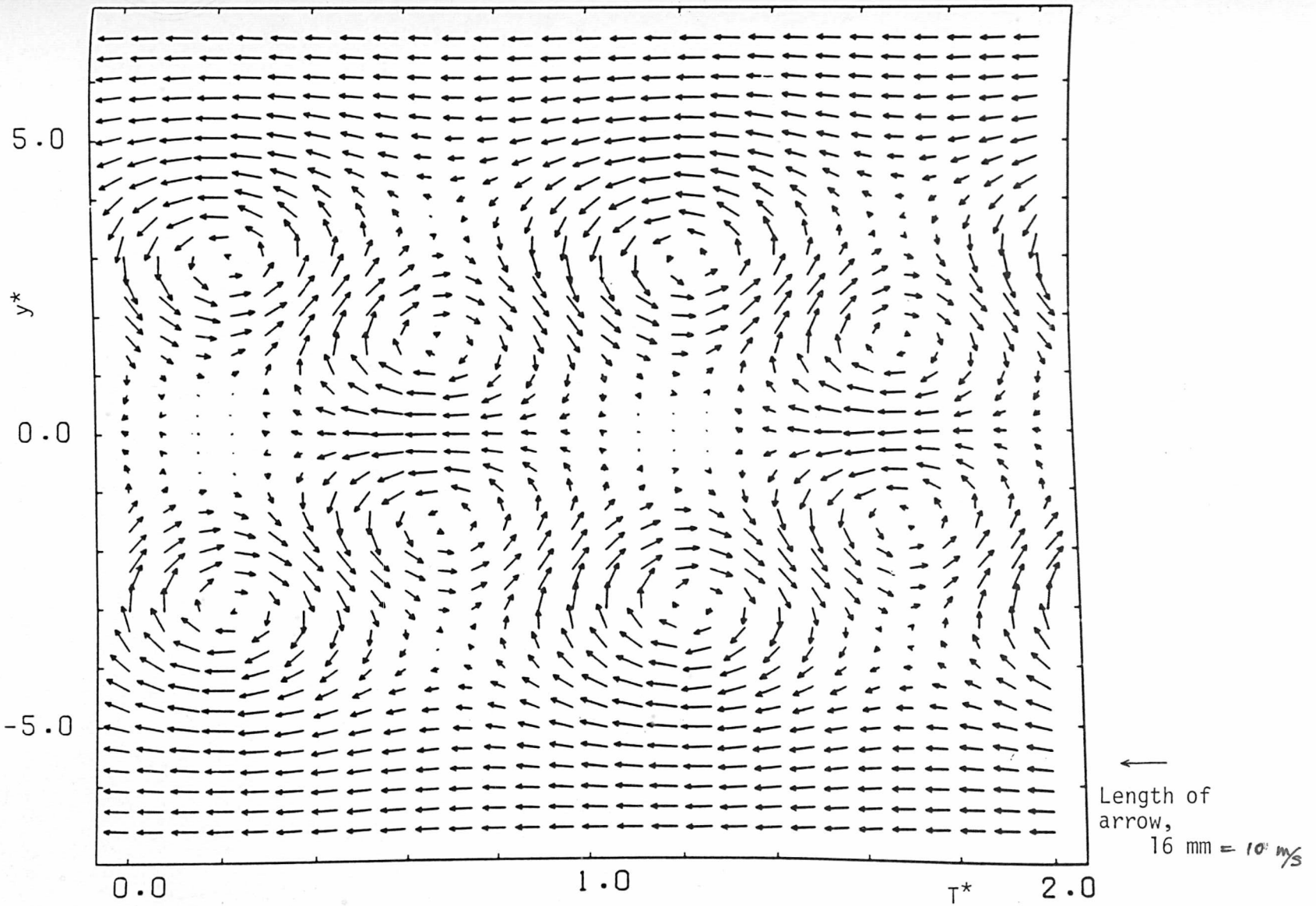



Figure 3.3.17 Conditionally averaged velocity vector field in the wake behind the two flat plates arranged side-by-side with d/w = 4.0 at x = 8.0 w, convection velocity of the inside vortices 0.85 U is removed, U = 10 m/s.

# CHAPTER FOUR

# VORTEX WAKE MODEL

Stable vortex ring shedding from a ring with $d/w \geq 5$ has been observed in the experiments described in Chapter 3. This chapter describes a simple vortex wake model of a ring, which consists of a pair of infinite rows of counterrotating coaxial vortex rings. Also, vortex wake of two flat plates in a side-by-side arrangement, which consists of two parallel vortex streets in antiphase, is modelled. The time sequences of the arrangements of the models are numerically simulated and compared with the experimental results.

## 4.1 Modelling of the vortex wake of a ring

Vortex rings are assumed to be circular line vortices for the simplicity of the modelling, except for the calculation of self-induced velocity of the vortex ring, which depends on the distribution of vorticity in the core of the vortex. A viscous vortex model is used to match the vorticity profile in the core, and initial values for the model simulation are taken from the experimental results for the thin sharp-edged ring with $d/w = 6$.

4.1.1. Isolated vortex ring

Let us suppose that the velocity, $\vec{u}$, of the fluid at the position, $\vec{x}$, is specified by the vorticity, $\vec{\omega}$, in the fluid where the rate of expansion is zero everywhere, then the following equations can be written:

$$\vec{\omega} = \text{rot } \vec{u} \tag{4.1.1}$$

$$\text{div } \vec{u} = 0 \tag{4.1.2}$$

For an arbitrary vector, $\vec{B}$, vector analysis shows that

$$\text{div rot } \vec{B} = 0 \tag{4.1.3}$$

Therefore, the vector potential of $\vec{u}$ is defined from (4.1.2) such that

$$\vec{u} = \text{rot } \vec{B} \tag{4.1.4}$$

We difine $\vec{B}$ such that div $\vec{B} = 0$

From (4.1.1) and (4.1.4), the following relation is obtained.

$$\vec{\omega} = \text{rot rot } \vec{B}$$

$$= \text{grad div } \vec{B} - \nabla^2 \vec{B}$$

$$= - \nabla^2 \vec{B} \tag{4.1.5}$$

This is the well-known Poisson's equation, and the solution of $\vec{B}$ at $\vec{x}$ is given by

$$\vec{B}(\vec{x}) = \frac{1}{4\pi} \iiint \frac{\vec{\omega}(\vec{x}')}{s} \, dV(\vec{x}') \tag{4.1.6}$$

$$s = |\vec{x} - \vec{x}'| \tag{4.1.7}$$

where $s$ is the distance between $\vec{x}$ and $\vec{x}'$ where the vorticity is distributed. The volume integral in (4.1.6) is taken over the region occupied by the fluid. Equations (4.1.4) and (4.1.6) have an analogy in electromagnetic theory, where they are related to the Biot-Savart's law.

If the flow has symmetry about an axis, the stream function, $\psi$, can be defined, in terms of cylindrical coordinates ($x$, $r$, $\theta$) with corresponding velocity components ($u$, $v$, 0). The axis of symmetry being the line $r = 0$, such that

$$u = \frac{1}{r} \frac{\partial \psi}{\partial r} \tag{4.1.8}$$

$$v = -\frac{1}{r} \frac{\partial \psi}{\partial x} \tag{4.1.9}$$

The vector potential in this case is given from (4.1.4), (4.1.8) and (4.1.9), such that

$$B_\theta = \frac{\psi}{r} \tag{4.1.10}$$

where

$$\vec{B} = (0,\ 0,\ B_\theta) \tag{4.1.11}$$

Now we consider a vortex ring at x = 0 in a cylindrical coordinate system, as shown in Figure 4.1. For simplicity of

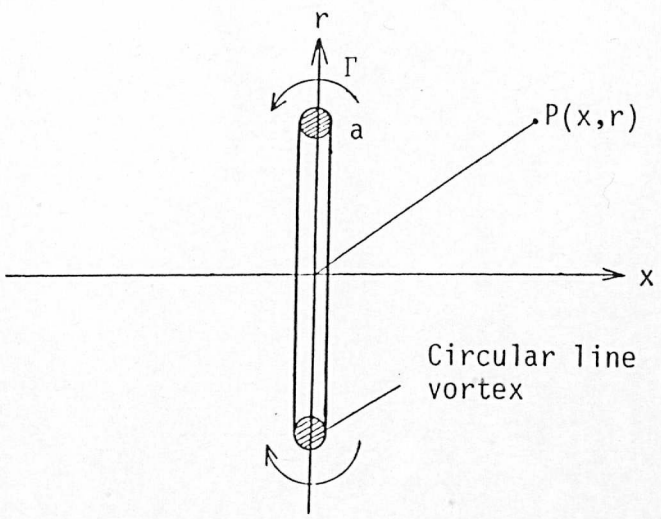



Figure 4.1 Vortex ring

calculation the vortex ring is approximated by a single circular line vortex of radius, a , and circulation strength $\Gamma$. The approximation is thought to be acceptable if the point, p(x,r), under consideration is not close to the vortex filament. Then, in the usual way, the elements of the integration in equation (4.1.6) can be written as (Batchelor 1967)

$$\omega(x',r')\, dx'dr' = \Gamma \tag{4.1.12}$$

$$s = (x^2+r^2+a^2 - 2ar\cos\theta)^{\frac{1}{2}} \tag{4.1.13}$$

From equations (4.1.6), (4.1.10), (4.1.12) and (4.1.13) the stream function $\psi(x,r)$ at point P(x,r) is given by

$$\psi(x,r) = \frac{\Gamma ar}{4\pi} \int_0^{2\pi} \frac{\cos\theta\, d\theta}{(x^2+r^2+a^2 - 2ar\cos\theta)^{\frac{1}{2}}}$$

$$= \frac{\Gamma(ar)^{\frac{1}{2}}}{4\pi} \left\{ \left(\frac{2}{k} - k\right) K(k) - \frac{2}{k} E(k) \right\} \tag{4.1.14}$$

where K(k) and E(k) are the so-called complete elliptic integrals of the first and second kind, and

$$k^2 = \frac{4ar}{x^2 + (r+a)^2} \tag{4.1.15}$$

$$K(k) = \int_0^{\frac{\pi}{2}} (1 - k^2\sin^2\theta)^{-\frac{1}{2}} \, d\theta \tag{4.1.16}$$

$$E(k) = \int_0^{\frac{\pi}{2}} (1 - k^2\sin^2\theta)^{\frac{1}{2}} \, d\theta. \tag{4.1.17}$$

There is no azimuthal motion and the other velocity components of the flow are calculated from (4.1.8), (4.1.9) and (4.1.14) as

$$u = \frac{\Gamma}{8\pi r} \left\{ \left(\frac{a}{r}\right)^{\frac{1}{2}} \frac{k^3}{1 - k^2} E(k) - \left(\frac{r}{a}\right)^{\frac{1}{2}} G(k) \right\} \tag{4.1.18}$$

$$v = \frac{\Gamma}{8\pi r} \left(\frac{a}{r}\right)^{\frac{1}{2}} \left(\frac{x}{a}\right) G(k), \tag{4.1.19}$$

where

$$G(k) = k\left\{\frac{2 - k^2}{1 - k^2}\ E(k) - 2K(k)\right\}. \qquad (4.1.20)$$

Detailed calculations are presented in Appendix B.

## 4.1.2. Self-induced velocity of a vortex ring

There is a singularity in the velocity distribution at points on the approximated circular line vortex in the equations (4.1.18)

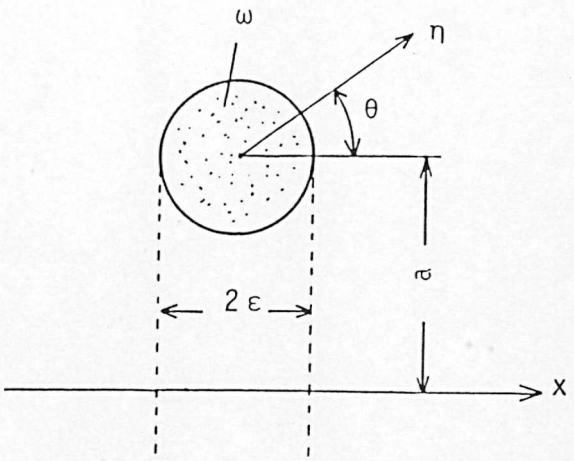



Figure 4.2 Core of a vortex ring

and (4.1.19). It is necessary to examine the value of the velocity in the core area of the vortex ring in order to estimate the self-induced velocity of the vortex ring. This velocity depends on the vorticity profile in the core. When the diameter of the vortex core is small, compared with the vortex ring diameter, and the vorticity is distributed uniformly inside the core of radius, $\varepsilon$, Lamb (1945) gives a proof of Kelvin's formula for the self-induced velocity, $u_{xs}$, in the x-direction, of the vortex ring. The velocity is given by

$$u_{sx} = \frac{\Gamma}{4\pi a} \left( \log \frac{8a}{\varepsilon} - \frac{1}{4} \right) \tag{4.1.21}$$

where

$$\varepsilon << a \tag{4.1.22}$$

When the length of the vortex core model is stretched as shown in Figure 4.3, and the volume of the vortex core and the strength of circulation remain constant, the following relations are obtained.

$$2\pi^2 a \varepsilon^2 = \text{const} \tag{4.1.23}$$

$$\pi \omega \varepsilon^2 = \text{const} \tag{4.1.24}$$

Experimental measurements of the vorticity distribution in the core of a vortex ring shows the effect of viscous diffusion and the vorticity distribution is far from the uniform one used in the Kelvin's formula. The two-dimensional vorticity equation for a viscous fluid is written in terms of radial coordinates $(\eta, \theta)$ such that

$$\frac{\partial \omega}{\partial t} = \nu \left( \frac{\partial^2 \omega}{\partial \eta^2} + \frac{1}{\eta} \frac{\partial \omega}{\partial \eta} \right) \tag{4.1.25}$$

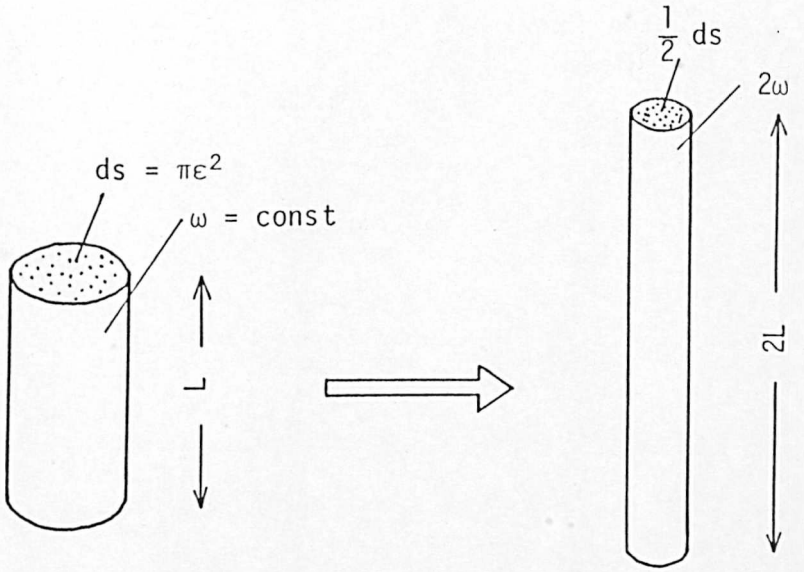



Figure 4.3 Stretch of a vortex core

where $\nu$ is kinematic viscosity and $\eta = 0$ is chosen as the centre of the core, as shown in Figure 4.2. The vorticity diffuses rapidly in a turbulent flow, but turbulent viscosity is not applied here for the simplicity of the modelling. If the diffusion in the core is solely viscous the solution of equation (4.1.25) is given by

$$\omega = \frac{\Gamma}{4\pi\nu t} \exp\left(-\frac{\eta^2}{4\nu t}\right)$$

$$= \frac{1.26\,\Gamma}{R_o^2} \exp\left(-\frac{1.26\,\eta^2}{R_o^2}\right) \qquad (4.1.26)$$

$$R_o^2 = 5.04\ \nu t \qquad (4.1.27)$$

where $\Gamma$ is the initial circulation and $t$ is the "age" of the vortex, and $R_o$ denotes the radial distance from the core centre to the maximum in the circumferential velocity, $u_\theta$, given by

$$u_\theta = \frac{\Gamma}{2\pi\eta}\left\{1 - \exp\left(-\frac{\eta^2}{4\nu t}\right)\right\}. \qquad (4.1.28)$$

Frankel (1970) and Saffman (1970) have extended Kelvin's formula to a vortex ring with an arbitrary vorticity distribution in the core. Saffman (1970) evaluated $u_{sx}$ for a viscous vortex ring expressed by equation (4.1.26), and gave the result

$$u_{sx} = \frac{\Gamma}{4\pi a}\left(\log\frac{8a}{\sqrt{4\nu t}} - 0.558\right)$$

$$= \frac{\Gamma}{4\pi a}\left(\log\frac{8.98a}{R_o} - 0.558\right) \qquad (4.1.29)$$

where

$$R_o << a \qquad (4.1.30)$$

When the diameter of the vortex ring changes only a little, the following relation given by equation (4.1.23) can be used.

$$aR_o^2 = \text{const} \qquad (4.1.31)$$

### 4.1.3. Double rows of vortex rings of infinite extent

Let us consider a stable vortex wake model of a ring, which consists of an infinite array of alternate sign vortex rings on a common axis of symmetry. The inside and outside vortex rings are approximated by circular line vortices of radii a and b with circulation strengths $\Gamma_a$ and $\Gamma_b$ respectively. The line r = 0 is chosen as the axis of symmetry in terms of cylinderical coordinates (x, y, θ). The longitudinal spacing of both the inside and outside rings is ℓ and the spacing between adjacent inside and outside vortex rings is h as shown in Figure 4.4. The induced velocity components u and v at a point P(x,r) are given by superimposing the induced velocities of the isolated vortex ring (4.1.18) and (4.1.19).

$$u = \frac{\Gamma_a}{8\pi r}\left\{ \left(\frac{a}{r}\right)^{\frac{1}{2}} \sum_{-\infty}^{\infty} \frac{k_m^3}{1-k_m^2} E(k_m) - \left(\frac{r}{a}\right)^{\frac{1}{2}} G(k_m)\right\}$$

$$+ \frac{\Gamma_b}{8\pi r}\left\{ \left(\frac{b}{r}\right)^{\frac{1}{2}} \sum_{-\infty}^{\infty} \frac{k_n^3}{1-k_n^2} E(k_n) - \left(\frac{r}{b}\right)^{\frac{1}{2}} G(k_n)\right\} \qquad (4.1.32)$$

$$v = \frac{\Gamma_a}{8\pi r}\left(\frac{a}{r}\right)^{\frac{1}{2}} \sum_{-\infty}^{\infty} \left\{\frac{x - m\ell}{a}\right\} G(k_m)$$

$$+ \frac{\Gamma_b}{8\pi r}\left(\frac{b}{r}\right)^{\frac{1}{2}} \sum_{-\infty}^{\infty} \left\{\frac{x-h-n\ell}{b}\right\} G(k_n) \qquad (4.1.33)$$

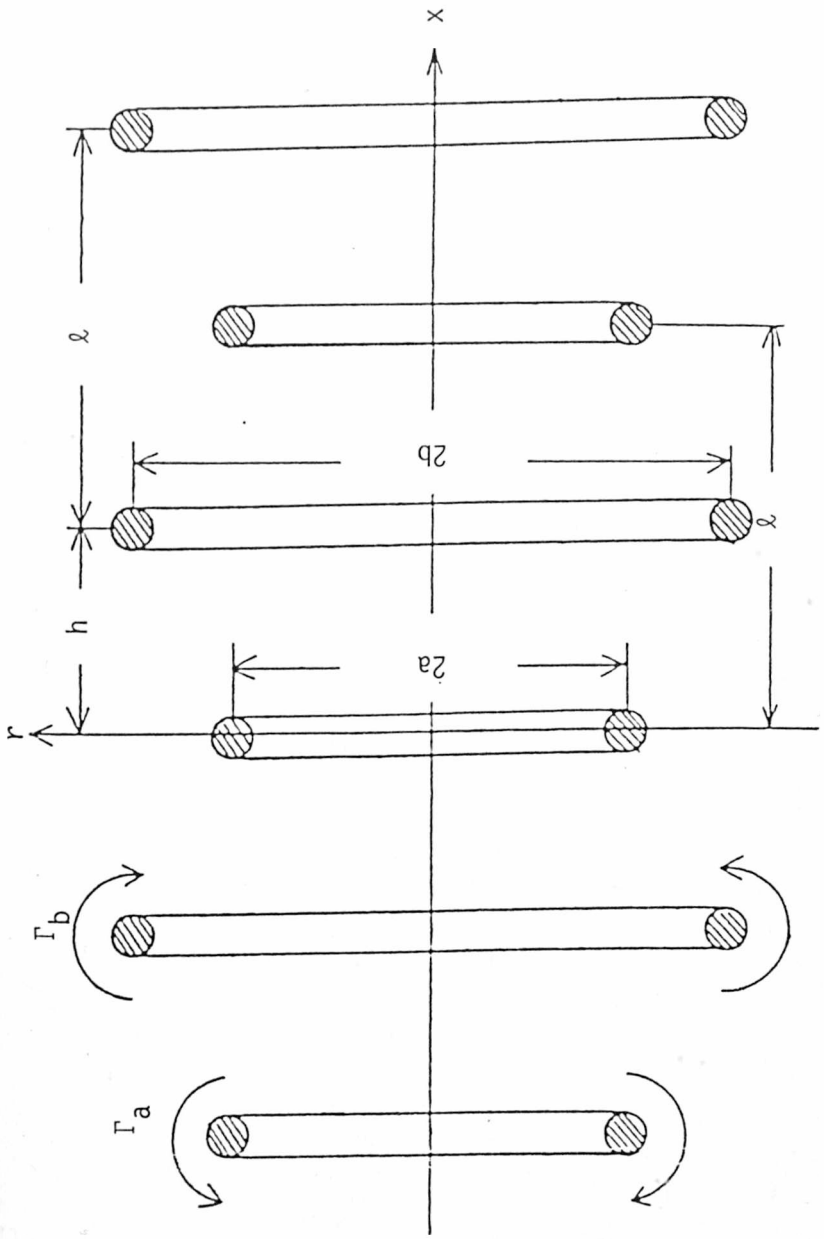



Figure 4.4 Double rows of infinite vortex rings

where

$$k_m^2 = \frac{4ar}{(x - m\ell)^2 + (a+b)^2} \tag{4.1.34}$$

$$k_n^2 = \frac{4br}{(x-h-n\ell)^2 + (a+b)^2} \tag{4.1.35}$$

Then the velocity components of the inside and outside vortex ring rows, $(u_a, v_a)$ and $(u_b, v_b)$ are given by

$$u_a = \frac{\Gamma_a}{8\pi a}\left\{\sum_{\substack{-\infty \\ m\neq o}}^{\infty} \frac{k_{am}^3}{1-k_{am}^2} E(k_{am}) - \sum_{\substack{-\infty \\ m\neq o}}^{\infty} G(k_{am})\right\}$$

$$+ \frac{\Gamma_b}{8\pi a}\left\{\left(\frac{b}{a}\right)^{\frac{1}{2}} \sum_{-\infty}^{\infty} \frac{k_{an}^3}{1-k_{an}^2} E(k_{an}) - \left(\frac{a}{b}\right)^{\frac{1}{2}} \sum_{-\infty}^{\infty} G(k_{an})\right\}$$

$$+ \frac{\Gamma_a}{4\pi a}\left[\log \frac{8.98a}{R_{oa}} - 0.558\right] \tag{4.1.36}$$

$$v_a = -\frac{\Gamma_b}{8\pi a}\left(\frac{b}{a}\right)^{\frac{1}{2}} \sum_{-\infty}^{\infty} \left[\frac{h + n\ell}{b}\right] G(k_{an}) \tag{4.1.37}$$

$$u_b = \frac{\Gamma_a}{8\pi b}\left\{ \left(\frac{a}{b}\right)^{\frac{1}{2}} \sum_{-\infty}^{\infty} \frac{k_{bm}^{\,3}}{1-k_{bm}^{\,2}} E(k_{bm}) - \left(\frac{b}{a}\right)^{\frac{1}{2}} \sum_{-\infty}^{\infty} G(k_{bm}) \right\}$$

$$+ \frac{\Gamma_b}{8\pi b}\left\{ \sum_{\substack{-\infty \\ n\neq o}}^{\infty} \frac{k_{bn}^{\,3}}{1-k_{bn}^{\,2}} E(k_{bn}) - \sum_{\substack{-\infty \\ n\neq o}}^{\infty} G(k_{bn}) \right\}$$

$$+ \frac{\Gamma_b}{4\pi b}\left( \log \frac{8.98b}{R_{ob}} - 0.558 \right) \qquad (4.1.38)$$

$$v_b = \frac{\Gamma_a}{8\pi b} \left(\frac{a}{b}\right)^{\frac{1}{2}} \sum_{-\infty}^{\infty} \left(\frac{h-m\ell}{a}\right) G(k_{bm}) \qquad (4.1.39)$$

where

$$k_{am}^{\,2} = \frac{4a^2}{(m\ell)^2 + 4a^2} \qquad (4.1.40)$$

$$k_{an}^{\,2} = \frac{4ab}{(h+n\ell)^2 + (a+b)^2} \qquad (4.1.41)$$

$$k_{bm}^{\,2} = \frac{4ab}{(h-m\ell)^2 + (a+b)^2} \qquad (4.1.42)$$

$$k_{bn}^{\,2} = \frac{4b^2}{(n\ell)^2 + 4b^2} \qquad (4.1.43)$$

where suffixes a and b imply the inside and outside vortex rings respectively.

4.1.4. Numerical simulation

The time sequence of the arrangement of vortex rings in the wake of a ring is numerically simulated by using the model of double rows of infinite vortex rings considered in the last section. First the parameters of the viscous vortex model expressed by (4.1.26) are evaluated from the vorticity profiles of the inside and outside vortex rings obtained by the conditional averaging technique described in Section 3.1.3. The profiles of the thin sharp-edged ring with d/w = 6 at x = 8.0 w are used, since they have less distorted vorticity distribution comparing with those at x = 3.4 w. The non-dimensional form of equation (4.1.26) is written as

$$\omega^* = \frac{1.26\Gamma^*}{\pi R_o^{*2}} \exp\left(-\frac{1.26\eta^{*2}}{R_o^{*2}}\right) \qquad (4.1.44)$$

where

$$\omega^* = \frac{\omega w}{U}$$

$$\Gamma^* = \frac{\Gamma}{Uw}$$

$$\eta^* = \frac{\eta}{w}$$

$$R_o^* = \frac{R_o}{w} \qquad (4.1.45)$$

The experimental results at x = 8.0 w are matched to equation (4.1.44) by the least-square-error method and are shown in Figure 4.5. The following values of the parameters are obtained

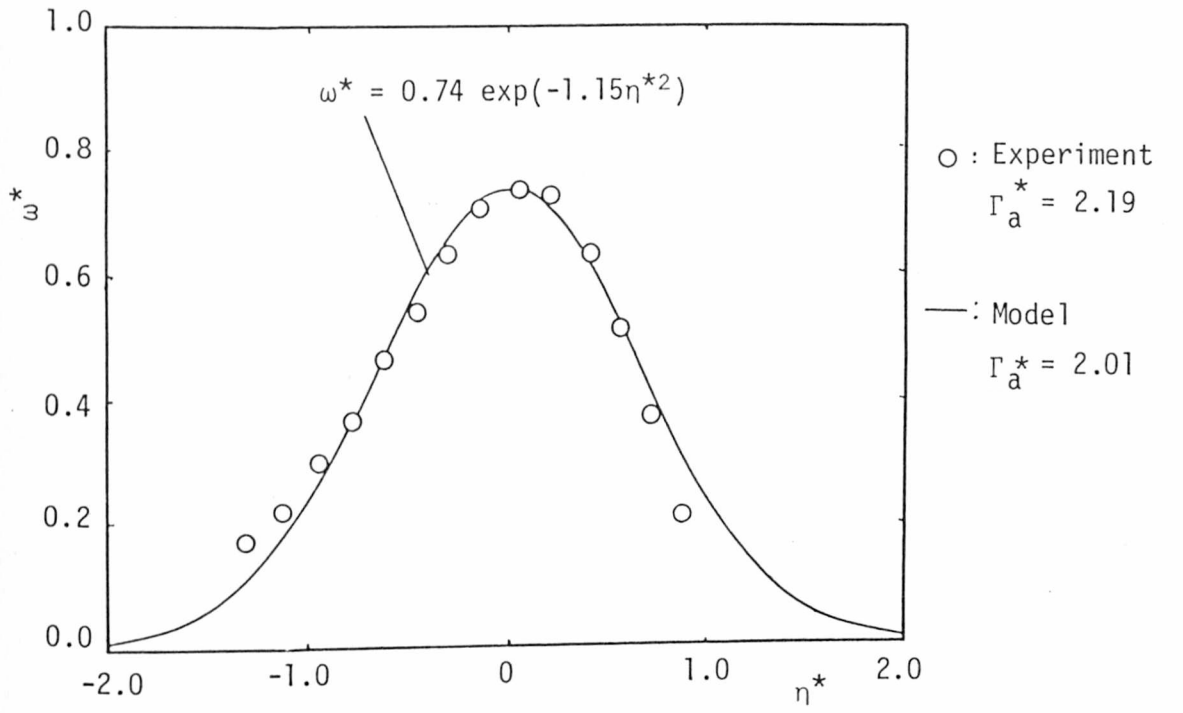
$$R_{oa}^* = 1.05 \qquad \frac{a^*}{R_{oa}^*} = 2.67$$

$$R_{ob}^* = 1.12 \qquad \frac{b^*}{R_{ob}^*} = 3.48$$

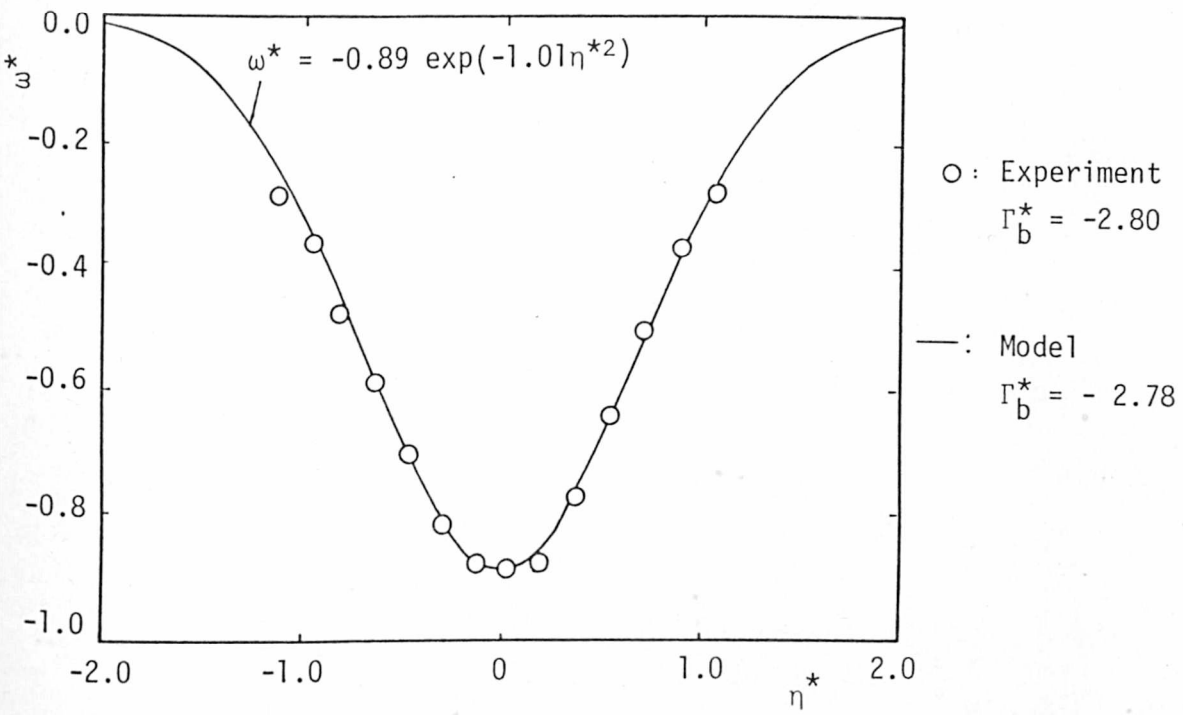
$$\Gamma_a^* = 2.01$$

$$\Gamma_b^* = 2.78 \qquad (4.1.46)$$

where $R_{oa}^*$ and $R_{ob}^*$ are the values of $R_o^*$ for the inside and outside vortex rings respectively. It should be noted that these




(a) Inside vortex ring




(b) Outside vortex ring

Figure 4.5 Modelling of vorticity distributions in the cores of a vortex ring. Thin sharp-edged ring with d/w = 6.0. x = 8w.

values do not satisfy the condition (4.1.30) of the approximation in the calculation of the self-induced velocity (4.1.29), although the values of $\Gamma_a^*$ and $\Gamma_b^*$ almost agree with the experimental values, 2.19 and -2.80 respectively.

The time sequence of the arrangement of vortex rings iteratively calculated by the following equations.

$$a_{i+1}^* = a_i^* + u_a^* \Delta t^* \tag{4.1.47}$$

$$b_{i+1}^* = b_i^* + u_b^* \Delta t^* \tag{4.1.48}$$

$$h_{i+1}^* = h_i^* - (u_a^* - u_b^*) \Delta t^* \tag{4.1.49}$$

where $^*$ denotes non-dimensionalized values by w or U and $\Delta t^*$ is the step of non-dimensional time $t^*$ expressed by

$$t^* = \frac{tU}{w} \tag{4.1.50}$$

In the calculation, $\Delta t^*$ is set to 0.2 and 100 inside and 100 outside vortex rings are taken into account. The initial values for the calculation are taken from the experimental result at

$x = 3.4\ w$ ($t^* = 0$) except for the vortex core models which are taken at $x = 8.0\ w$ (see 4.1.46). The comparison between the model simulation and the experimental results at $x = 3.4\ w$ and $x = 8.0\ w$ ($t^* = 5.8$, i.e. the convection velocity of 0.8 U is used here) is shown in Table 4.1, and the changes of $a^*$, $b^*$ and $h/\ell$ with $t^*$ are shown in Figure 4.6. Although calculated values do not coincide exactly with the experimental results, the order of the changes and the trends are well predicted by this simple model. The tendencies for the inside and outside vortex rings get close to each other and the radii to increase with time, are also clearly seen in the flow visualization experiments to be described in the next chapter. The inside vortex ring never passes through the outside vortex ring in the experiment nor in this simulation. However the simulation is thought not to be accurate enough to predict such a phenomenon, because when the cores of the inside and outside vortex rings get close to each other, the approximation of a line vortex gives rise to a large error in the calculation of induced velocities. The calculated vorticity distributions in the cores of the vortex rings and the velocity fluctuations are shown in Figures 4.7, 4.8 and 4.9. The velocity fluctuation in the core areas is not plotted in Figure 4.9 because of a large error caused by the approximation to a line vortex. The general features of the model simulation agree well with the experimental result at $x = 8.0\ w$.

The approximation of the actual vortex ring to the simple circular line vortex in the calculation of the stream function,

## TABLE 4.1

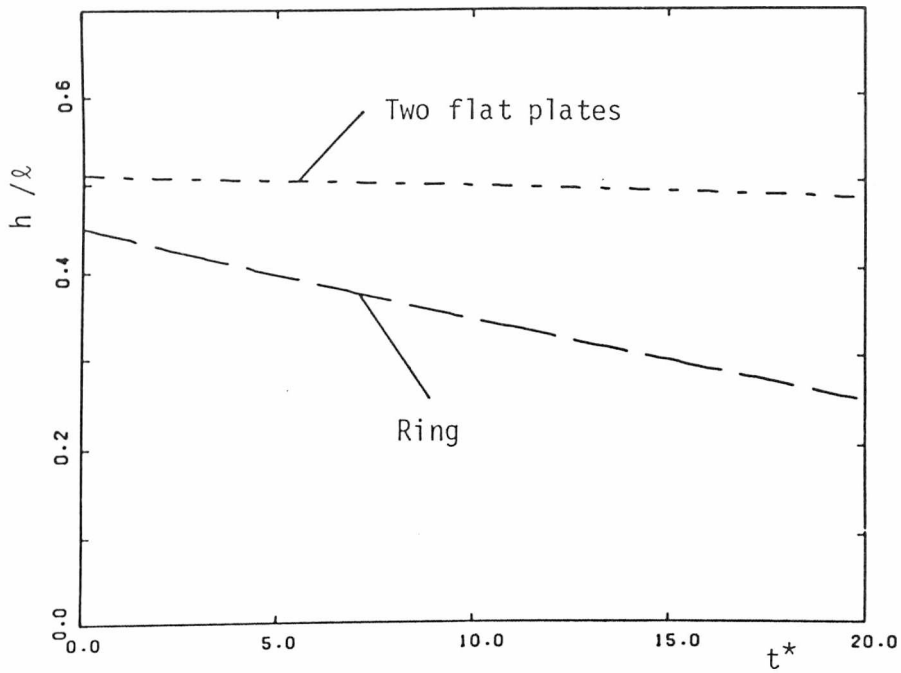
Comparison of experimental and model simulation results

Bluff body model: thin sharp-edged ring with d/w = 6.0

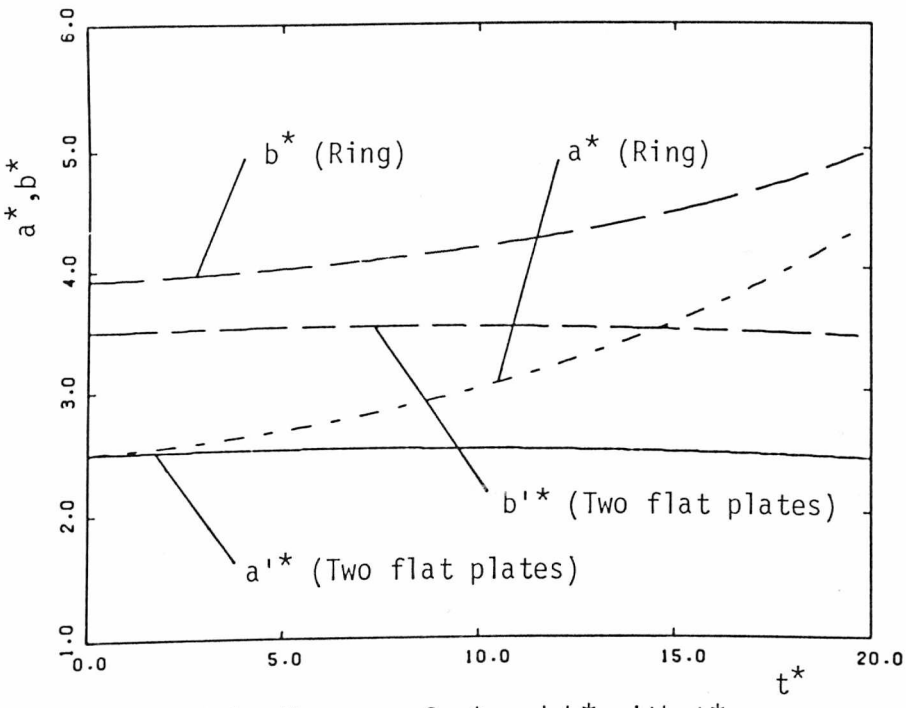
| | Experiment | | Model simulation | |
|---|---|---|---|---|
| x | 3.4 W | 8.0 W | (3.4 W) | (8.0 W) |
| $t^*$ | (0.0) | (5.8)*** | 0.0 | 5.8*** |
| $a^*$ | 2.5 | 2.7 | 2.5 | 2.7 |
| $b^*$ | 3.9 | 3.9 | 3.9 | 4.0 |
| $h/\ell$ | 0.45 | 0.27 | 0.45 | 0.38 |
| $\Gamma_a^*$ | 2.75 | 2.19 | 2.01** | 2.01 |
| $\Gamma_b^*$ | -3.19 | -2.80 | -2.78** | -2.78 |
| $R_{oa}^*$ | - | 1.05 | 1.05** | 0.91 |
| $R_{ob}^*$ | - | 1.12 | 1.12** | 1.04 |

** These values are modelled from the experimental results at x = 8.0 w (see 4.1.46)

*** Convection velocity of 0.8 U is used.




(a) Change of $h^*/\ell^*$ with $t^*$




(b) Changes of $a^*$ and $b^*$ with $t^*$

Figure 4.6 Results of numerical simulation

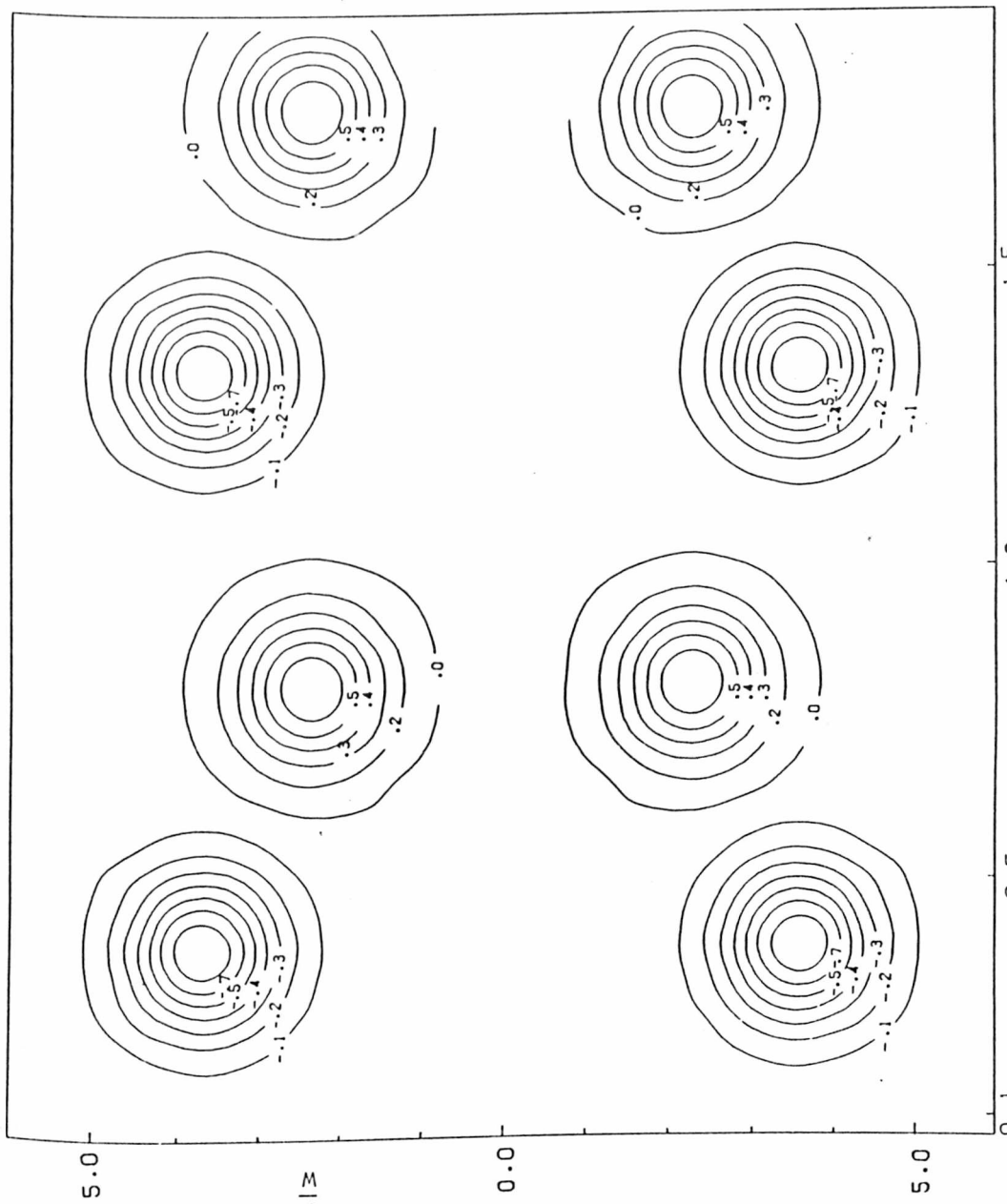



Figure 4.7 Vorticity distribution by model simulation at $t^* = 0.0$

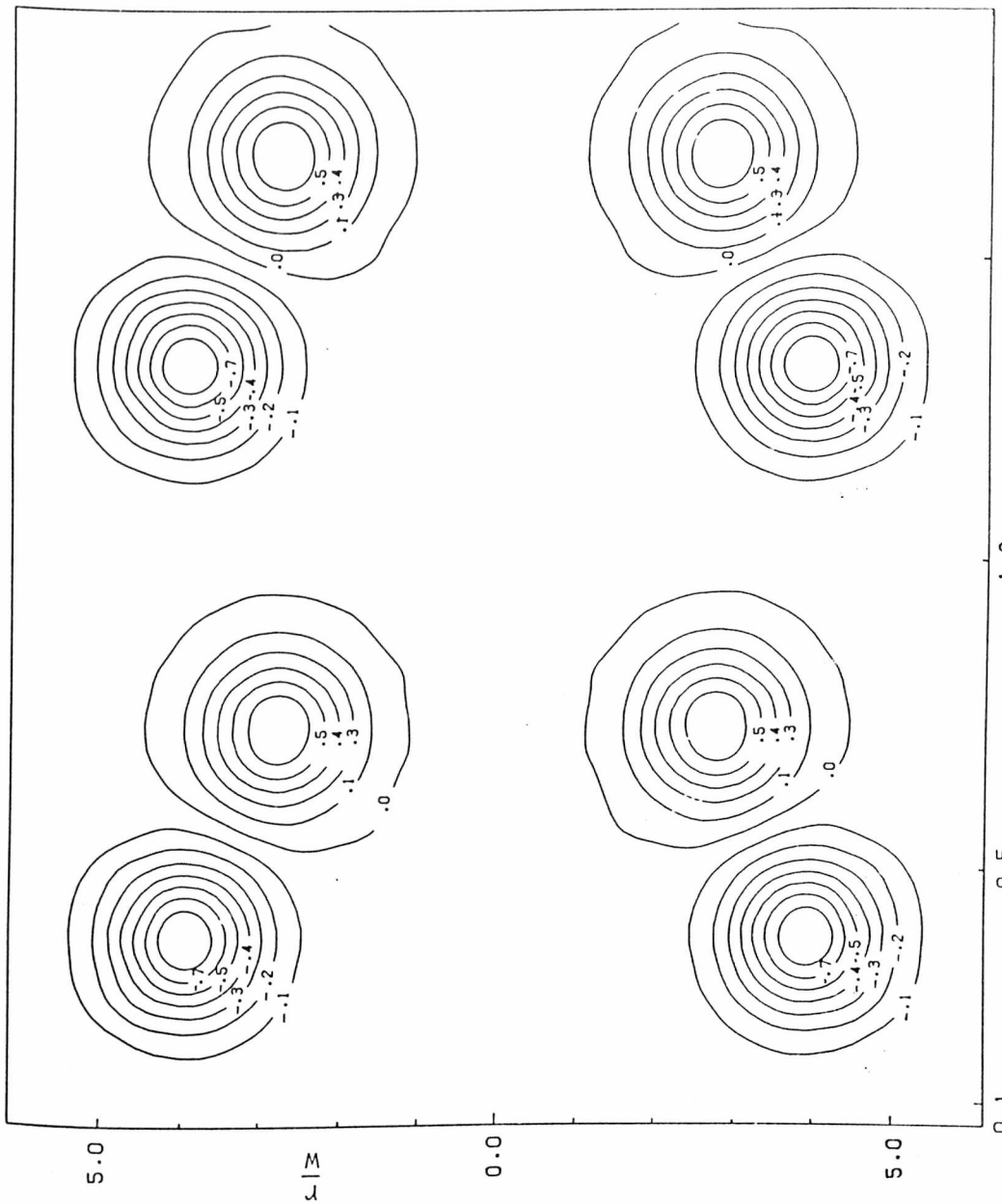
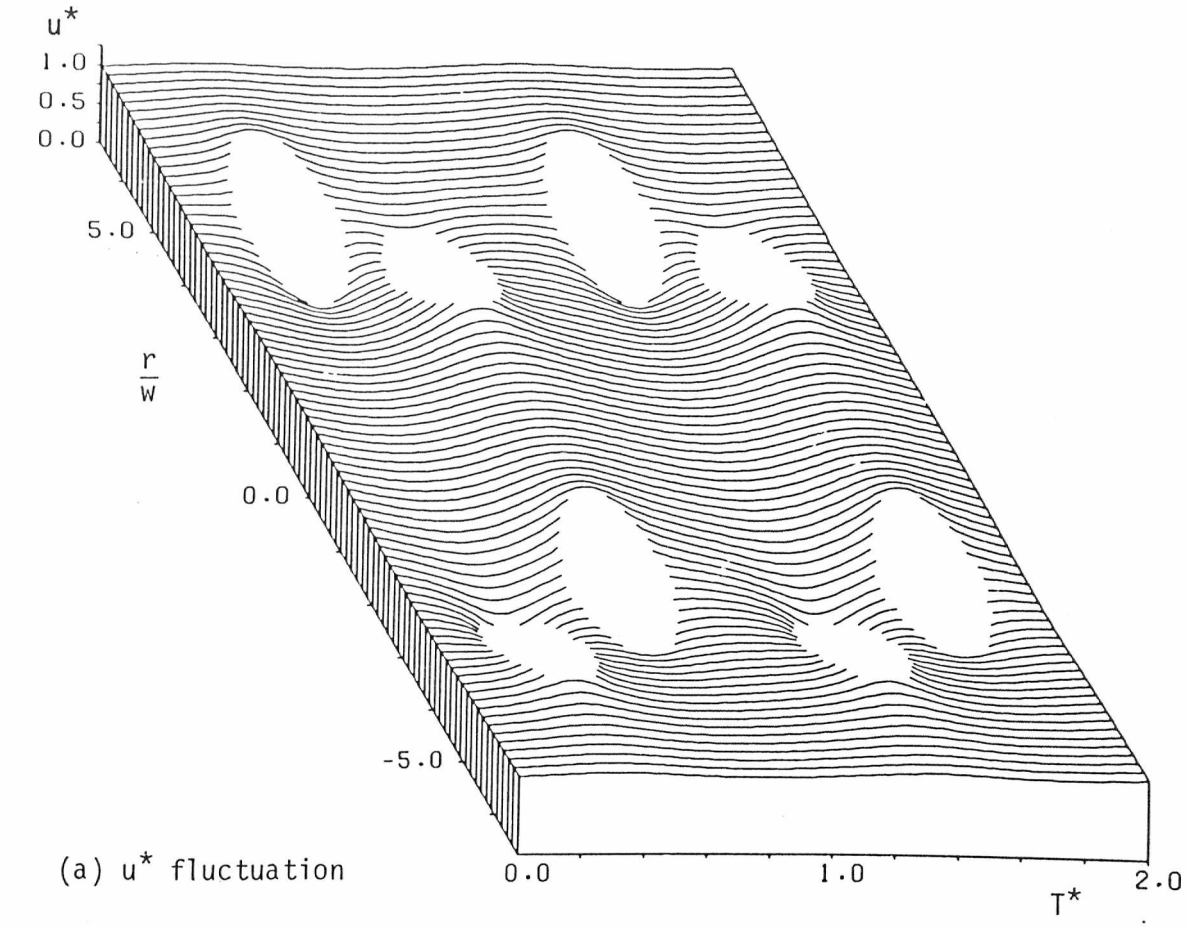
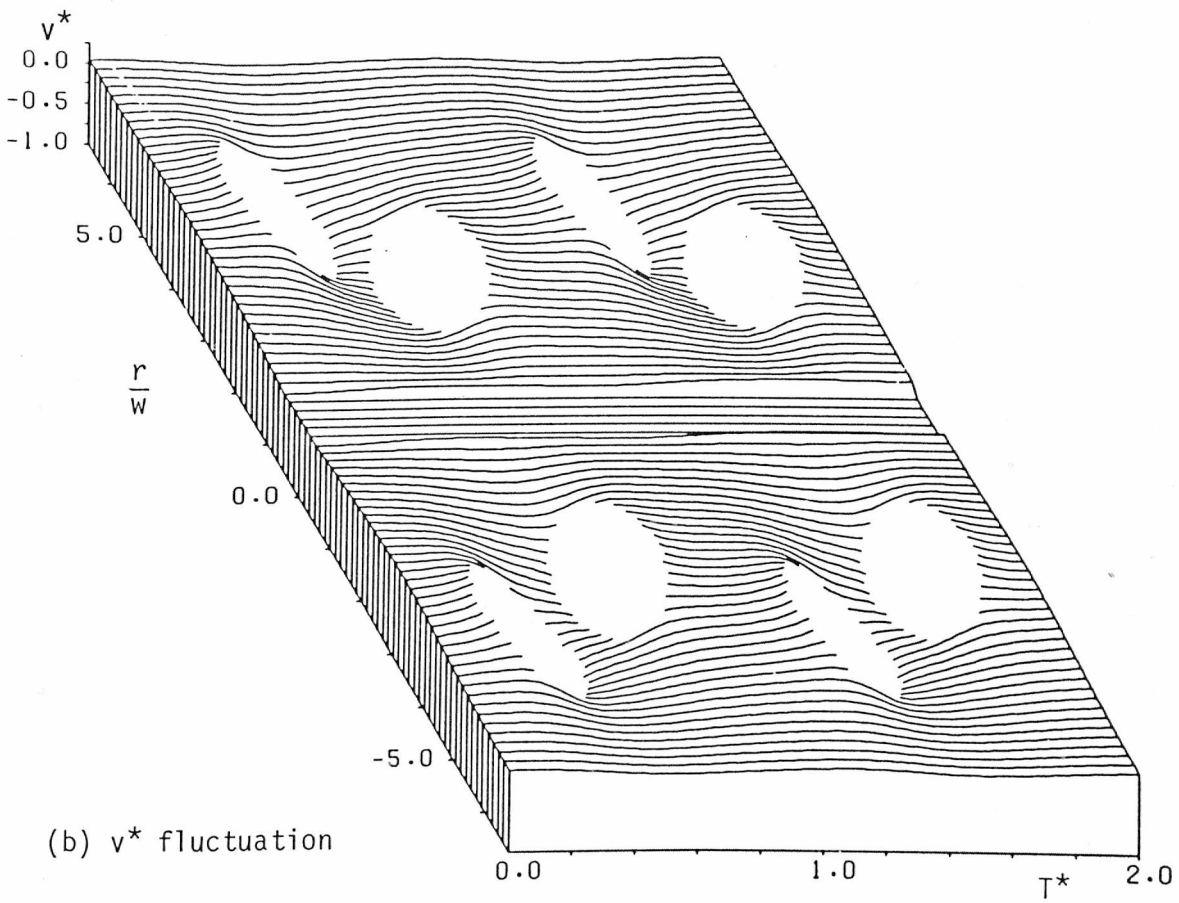



Figure 4.8 Vorticity distribution by model simulation at $t^* = 5.8$.




(a) $u^*$ fluctuation




(b) $v^*$ fluctuation

Figure 4.9 Velocity fluctuations by model simulation at $t^* = 5.8$.

(4.1.14) and the assumption that the core of the vortex ring has a very small cross-sectional area in the calculation of the self-induced velocity (4.1.29), provide a certain limitation to the accuracy of this simulation model. Nevertheless, even an exact calculation using the model would not yield the values obtained by the experiment, since vortices just shed from the bluff body are in fact the beginning of some finite vortex street, also the existence of the bluff body affects the arrangement of vortices in a real wake. Therefore, a more sophisticated model is necessary to simulate the actual vortex wake behind the ring, and also vorticity diffusion by turbulence must be taken into account. However this simple model is thought to be adequate for the consideration of the fundamental nature of the vortex ring wake.

## 4.2 Modelling of the vortex wake of two flat plates in a side-by-side arrangement.

The double vortex streets in antiphase which are shed from two flat plates in a side-by-side arrangement are modelled by 4 rows of infinite two-dimensional point vortices in the (x,y) plane as shown in Figure 4.10. The symbols used here are the same as for the axisymmetrical case in the last section, except the discriminating symbol (') is used and $x = 0$ is the axis of symmetry. The complex potential function f(z) is given by

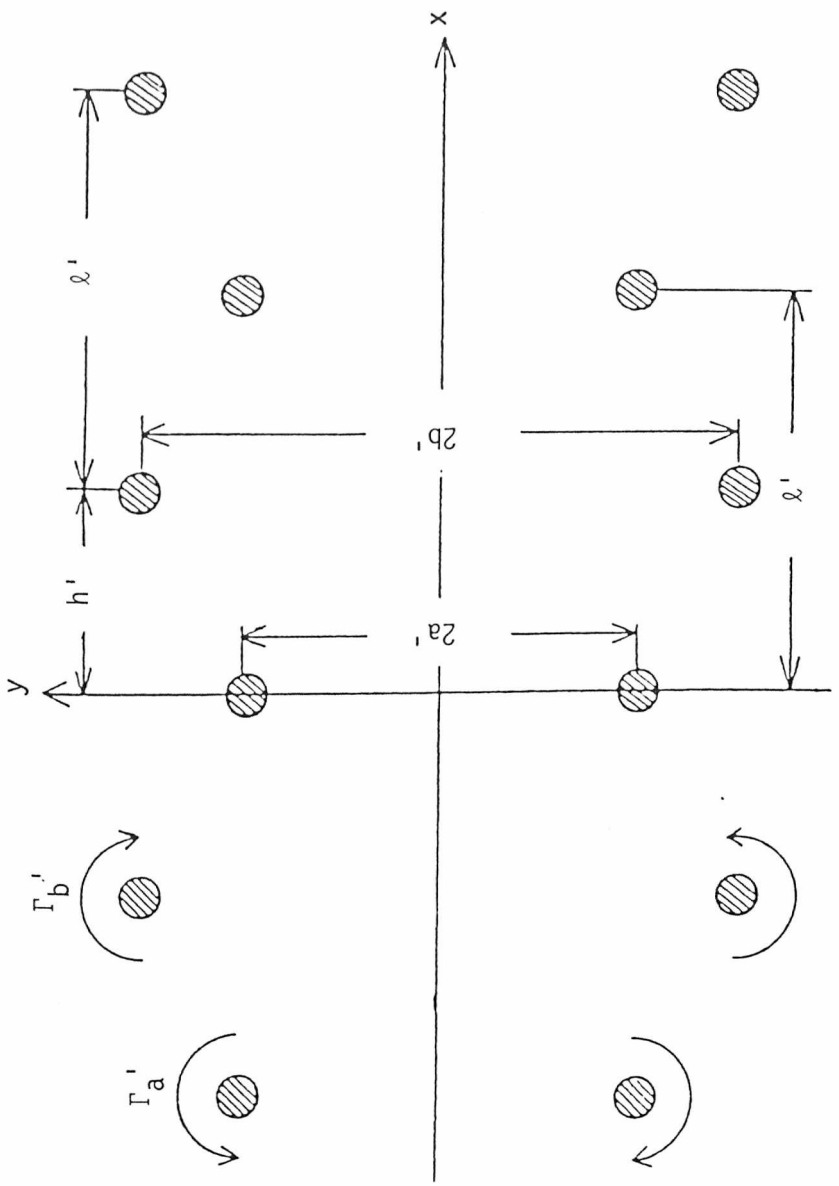



Figure 4.10 Model of 4 rows of infinite two-dimensional point vortices.

$$f(z) = \frac{\Gamma_a'}{2\pi i} \log \frac{\sin \frac{\pi(z-a')}{\ell'}}{\sin \frac{\pi(z+a')}{\ell'}} + \frac{\Gamma_b'}{2\pi i} \log \frac{\sin \frac{\pi(z-b')}{\ell'}}{\sin \frac{\pi(z+b')}{\ell'}} \qquad (4.2.1)$$

and the velocity components of the inside and outside vortices $(u_a', v_a')$ and $(u_b', v_b')$ are given by

$$u_a' = \frac{\Gamma_a'}{2\ell'} \coth \frac{2\pi a'}{\ell'} + \frac{\Gamma_b'}{2\ell'} \left[ H(a'+b') + H(b'-a') \right] \qquad (4.2.2)$$

$$v_a' = - \frac{\Gamma_b'}{2\ell'} \left[ I(b'-a') - I(a'+b') \right] \qquad (4.2.3)$$

$$u_b' = \frac{\Gamma_b'}{2\ell'} \coth \frac{2\pi b'}{\ell'} + \frac{\Gamma_a'}{2\ell'} \left[ H(a'+b') - H(b'-a') \right] \qquad (4.2.4)$$

$$v_b' = \frac{\Gamma_a'}{2\ell'} \left[ I(b'-a') - I(a'+b') \right] \qquad (4.2.5)$$

where

$$H(a) = \frac{\sinh \frac{2\pi a'}{\ell'}}{\cosh \frac{2\pi a'}{\ell'} - \cos \frac{2\pi h'}{\ell'}} \qquad (4.2.6)$$

$$I(a) = \frac{\sin \frac{2\pi h'}{\ell'}}{\cosh \frac{2\pi a'}{\ell'} - \cos \frac{2\pi h'}{\ell'}} \qquad (4.2.7)$$

The time sequence of the arrangement of the modelled double vortex streets is numerically calculated by the following iterative equations.

$$a'^{*}_{i+1} = a'^{*}_{i} + v'^{*}_{a} \Delta t^{*} \qquad (4.2.8)$$

$$b'^{*}_{i+1} = b'^{*}_{i} + v'^{*}_{b} \Delta t^{*} \qquad (4.2.9)$$

$$h'^{*}_{i+1} = h'^{*}_{i} - (u'^{*}_{a} - u'^{*}_{b}) \Delta t^{*} \qquad (4.2.10)$$

The initial values for the calculation are taken from the experimental result for two flat plates of d/w = 6 at x = 3.4 w ($t^{*}$ = 0). The comparison between the results of the model simulation and the experimental results at x = 3.4 w and x = 8.0 w ($t^{*}$ = 5.3, i.e. the convection velocity of 0.87 U is used here) is shown in Table 4.2. Also the change of $a'^{*}$, $b'^{*}$ and $h'^{*}$ are

## TABLE 4.2

Comparison of experimental and model simulation results

Bluff body model: two flat plates, d/w = 6.0

| | Experiment | | Model simulation | |
|---|---|---|---|---|
| x | 3.4 w | 8.0 w | (3.4 w) | (8.0 w) |
| $t^*$ | (0.0) | (5.3)** | 0.0 | 5.3** |
| $a'^*$ | 2.5 | 2.5 | 2.5 | 2.5 |
| $b'^*$ | 3.5 | 3.6 | 3.5 | 3.5 |
| $h'/\ell'$ | 0.51 | 0.50 | 0.51 | 0.50 |
| $\Gamma'^*_a$ | 3.08 | 2.57 | 3.08 | 3.08 |
| $\Gamma'^*_b$ | -2.97 | -2.58 | -2.97 | -2.97 |

** Convection velocity of 0.87 U is used here.

compared with the previous axisymmetrical case in Figure 4.6. It is found that the predicted changes for the plates are negligibly small compared with the case of the ring, which agreed well with the experimental results, including the flow visualization in Chapter 5.

# CHAPTER FIVE

# FLOW VISUALIZATION

This chapter describes flow visualizations of the wakes of various ring models and two flat plates arranged side-by-side. The experiments were carried out in a low Reynolds number range, in a water tank by using dye and powder. The visualized wakes are compared with results obtained in the experiments in the wind tunnel in the high Reynolds number range.

## 5.1 Experimental apparatus and flow visualization techniques

Flow visualizations were carried out in a water tank of 0.5 m width, 0.5 m depth and 2 m length. The bluff body model was suspended from a towing carriage on the water tank by a thin streamline-shaped support. A schematic diagram of the apparatus is shown in Figure 5.1. The towing carriage shown in Photo 5.1 can move with highly constant speeds up to 5 m/s. Although the system is complicated and requires a long waiting time for the water in the tank to become still after each run of the experiment, it has great advantages for flow visualization compared with a conventional water circulating channel, especially in a low Reynolds number range. In this facility the velocity profile is uniform and there exists no turbulence. The surface of

water was slightly heated for stability of thermal convection. The bluff bodies used for the experiment were ring models of d/w = 4.0, 6.0 and 12.0 and two flat plates of d/w = 4.0 and 6.0. Most of the models had the same rectangular cross-section of w = 10 mm and $\delta$ = 3 mm. Two other models were rings of d/w = 6.0 and w = 10 mm with a thin sharp-edged cross-section and with a rectangular cross-section of $\delta$/w = 0.6, which were used to examine the effect of the afterbody shape. The Reynolds number range based on w was 62 to 95.

Two methods were employed for the flow visualizations, one was the electrolytic precipitation method which can visualize a streakline and the other was the aluminimum powder method which can visualize particle paths.

For the electrolytic precipitation method, the bluff body models were electroplated with tin in a solution of tin sulphate beforehand. Then, water in the tank was electrolysed using the model as a positive electrode, and the precipitation from the model was used as a dye to visualize a streakline. Although this method requires strong lighting for pictures with good contrast, since the dye is fairly thin, it is easy to control the dye electrically. Another advantage of this method is that the dye is generated from within the boundary layer of the bluff body model, which makes it easy to observe rolling up of the separated shear layers. A conventional method that emits a dye upstream of the bluff body model may disturb the flow field (Taneda et al. 1974).

The streakline method provides a clear picture, but its interpretation needs some care. It should be noted that a streakline merely indicates some time-integrated 'history' of a marked mass of fluid and the pattern of the dye at any position does not necessarily prove the actual existence of such movement of fluid at the moment observed. Photographs of streaklines were taken by a camera fixed to the towing carriage.

It is also useful to visualize particle paths which gives more accurate instantaneous information about the flow field, although the picture may not be so clear as that of a streakline. The particle paths were obtained by taking a photograph with a certain time exposure of the movement of the aluminium powder. To be exact, a particle of aluminium powder is a fine film fragment and tends to lie parallel to the flow in a shear layer (Taneda 1952). Therefore, it starts and stops reflecting frequently in the wake as it changes its direction, which affects the particle paths in the picture. But an overall picture of particle paths is accurate enough to identify the arrangement of vortices in the wake, as it shows the average movement of numerous particles.

Photographs of particle paths were taken with the camera fixed outside the water tank, although it is better to move the camera with the convection speed of the vortices. A cross-sectional plane was obtained by using a thin sheet of light generated by cylinderical lenses.

## 5.2 Flow visualization of wakes behind ring models

The three-dimensional streakline of the wake behind the ring model with d/w = 4.0, and a cross-sectional view, are shown in Photo 5.2 and Photo 5.5, and also the particle paths of the wake are shown in Photo 5.11. These flow patterns show that there exists no regular vortex shedding from the model in this low Reynolds number range. The flow passing through the ring model shown in the photographs is not biased in any direction in the near wake, whereas, a biased gap flow is observed in the two-dimensional case of two cylinders arranged side-by-side with a narrow gap (Ishigai et al. 1971).

The streaklines and the particle paths of the wakes behind the ring model of d/w = 6.0 are shown in Photographs 5.3, 5.6, 5.7, 5.8, 5.9 and 5.12, in which regular axisymmetrical vortex ring shedding alternatively from the inside and outside of the ring model can be clearly recognised. The ring model was impulsively started from rest with a constant velocity. Photo 5.7 shows a time sequence of vortex development in the initial stage. At first, twin vortex rings are formed at the same plane normal to the axis of symmetry, just behind the ring model, as shown in Photo 5.7 (a) and (b). Then, the inside vortex ring moves quickly by a self-induced velocity in the downstream direction as shown in Photo 5.7 (c) and (d), and gets out of the influence of the outside vortex ring which would have the effect of moving it in the opposite direction. The inside vortex ring always sheds first

and moves independently to far downstream at an early stage, as shown in Photo 5.3(a). Once the inside vortex ring sheds, alternate vortex shedding from the inside and outside of the ring model continues as shown in Photo 5.7 (e) and (f). Photo 5.12 shows that the phase difference between the inside and outside vortex rings is nearly $180^{o}$ when they shed from the ring model, but the inside vortex ring catches up with the outside one with passage downstream. However, the inside vortex ring never passes through the outside vortex ring. The diameters of the vortex rings grow slightly as they move downstream in the wake. Although it is very difficult to judge definitely from the photograph, the strength of the inside and outside vortex rings seem to be the same level where the vortex rings are near to the ring model, but the strength of vorticity of the inside vortex ring seems to be weaker than that of the outside vortex ring as they move downstream in the wake, considering the length of the particle paths shown in the photograph. There exists large amplitude, periodic velocity fluctuations on the axis of symmetry, and its regularlity can be expected to be high as it is caused by a coherent axisymmetrical vortex shedding. Photo 5.8 and Photo 5.9 show streaklines of the wakes behind the ring models of $d/w = 6.0$ with the thin sharp-edged cross-section and the rectangular cross-section of $\delta/w = 0.6$, respectively. The difference between the ring models with the thin sharp-edged cross-section and the rectangular cross-section of $\delta/w = 0.3$ shown in Photo 5.6 is not considerable, which is also suggested from the

result obtained by Bearman and Trueman (1972) who have measured drag and base pressure of rectangular cross-section cylinders of various $\delta/w$ as shown in Figure 5.2. However, the diameters of the vortex rings shed from the ring model with the rectangular cross-section of $\delta/w = 0.6$ increase more rapidly as they move downstream in the wake. On the whole, the results of the arrangement for the ring models with $d/w = 6.0$ obtained by flow visualization agree with those obtained by the wind tunnel experiments and the numerical simulation.

Visualized wakes behind the ring model with $d/w = 12$ are shown in Photographs 5.4, 5.10 and 5.13. Regular axisymmetrical vortex ring shedding from the model is also observed as shown in the photographs. The inside and outside vortex rings get close to each other in the wake, similar to the case with $d/w = 6.0$. However, the vortex rings from the ring model with $d/w = 6.0$ get close to each other more quickly in the near wake. The reason for the difference is thought to be that a vortex ring of a smaller diameter has a bigger self-induced velocity (Batchelor 1967). The diameters of vortex rings also slightly increase as they flow downstream. Photo 5.13 shows that velocity fluctuations on the axis of symmetry are very small, as the axis is relatively far from the wake. Therefore, highly regular periodic velocity fluctuations on the axis of symmetry caused by vortex shedding from the ring model of $d/w = 12.0$ cannot be expected.

## 5.3 Flow visualization of wakes behind two flat plates arranged side-by-side

The particle paths of the wakes behind two flat plates in side-by-side arrangements are shown in Photographs 5.14 and 5.15. Regular vortex shedding from the two flat plates with d/w = 4.0 and d/w = 6.0 are observed, whereas vortex shedding from the ring model with d/w = 4.0 is not regular. The patterns of the vortex shedding observed in the present experiment are mainly antiphase, i.e. symmetric about the axis of the gap. Williamson (1985) found that the pattern could be either inphase or antiphase, though the antiphase pattern was predominant. One of the possible reasons is that when there is a disturbance in the flow around the bluff bodies, such as turbulence or a non-uniform velocity profile, it could trigger the main stable pattern switch over to the sub stable pattern for a while. Also, in contrast to the wake behind the ring model with d/w = 6.0, the arrangement of vortices from the two flat plates with d/w = 6.0 keeps an almost constant pattern in the wake and the strengths of the inside and outside vortices seems almost the same level from the length of the particle paths. All the results obtained by flow visualization are in good agreement with those obtained by the wind tunnel experiments and the numerical simulations.

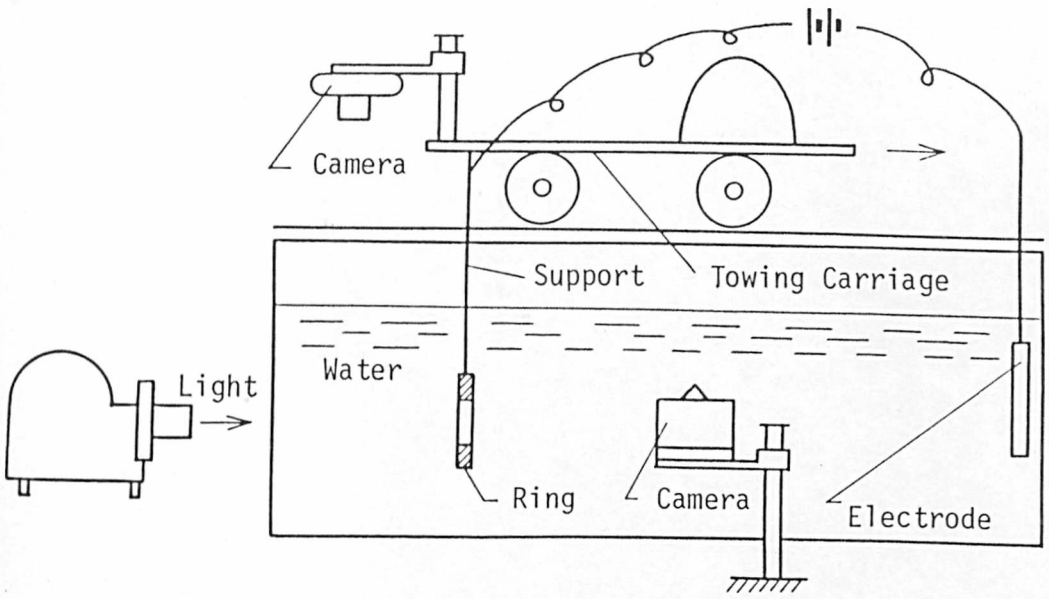



Figure 5.1 Schematic diagram of the apparatus

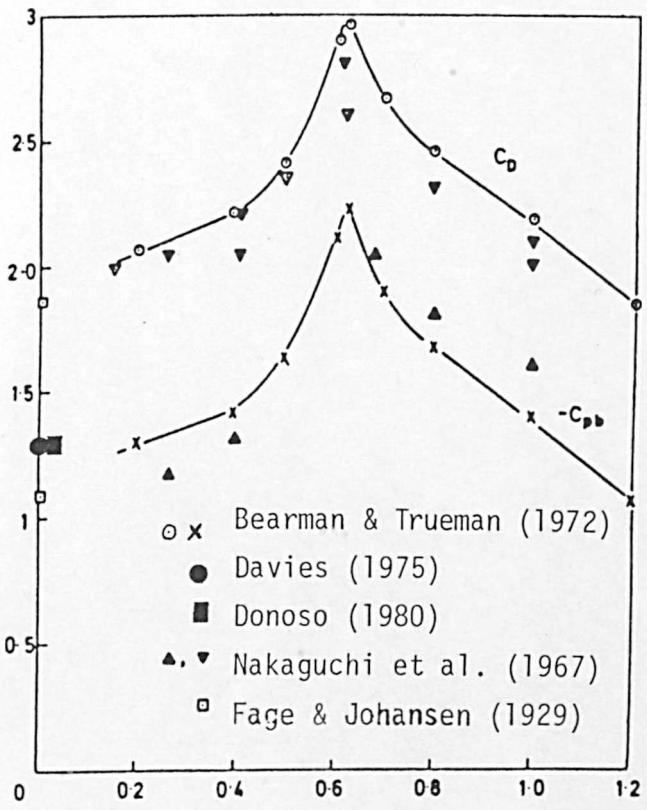



Figure 5.2 Drag coefficient and base pressure coefficient of rectangular cylinders, $R_e = 2 \times 10^4 \sim 7 \times 10^4$. Reproduced from Bearman and Trueman (1972) and Davies (1975).

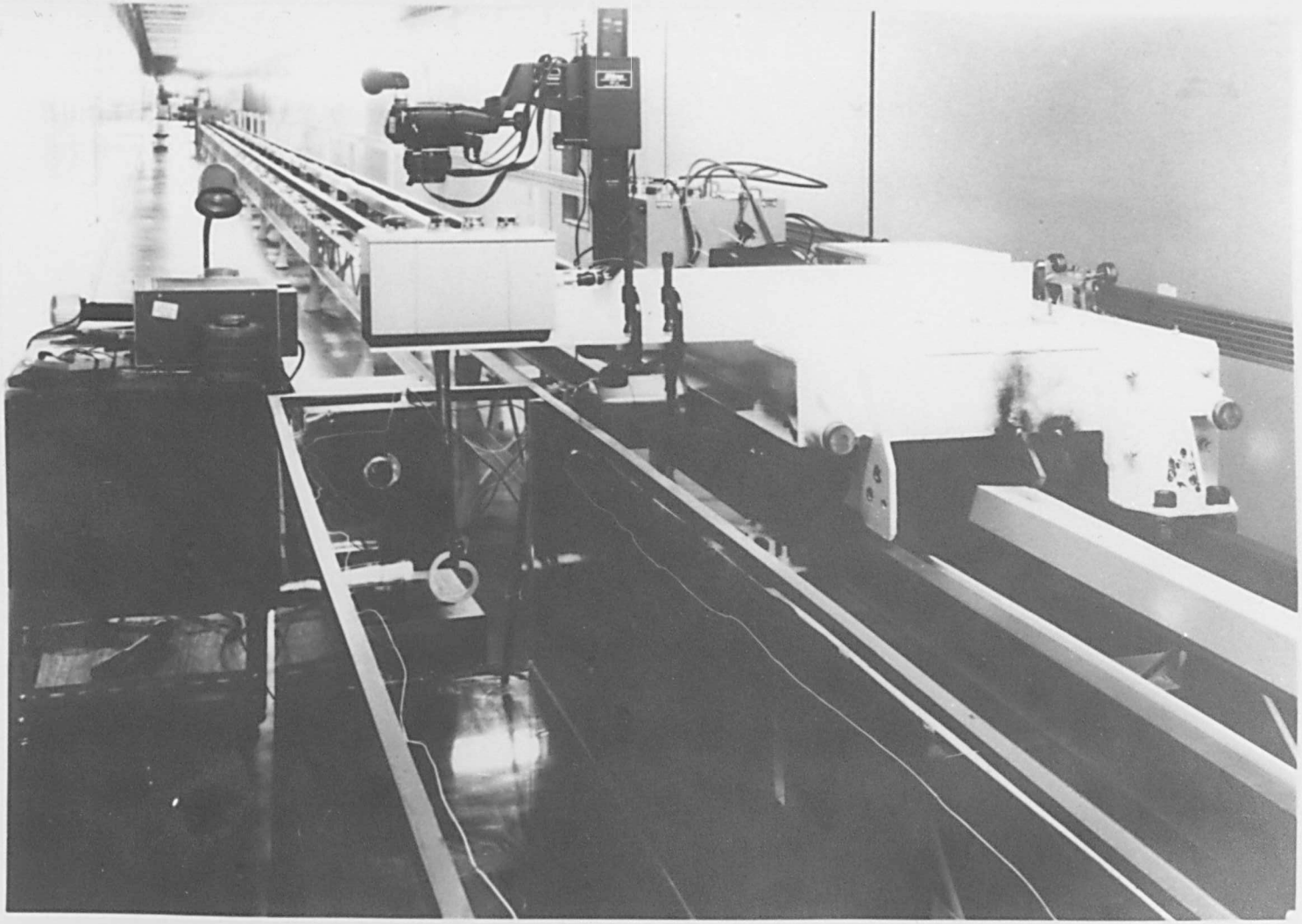


Photo 5.1 The experimental apparatus for flow visualization

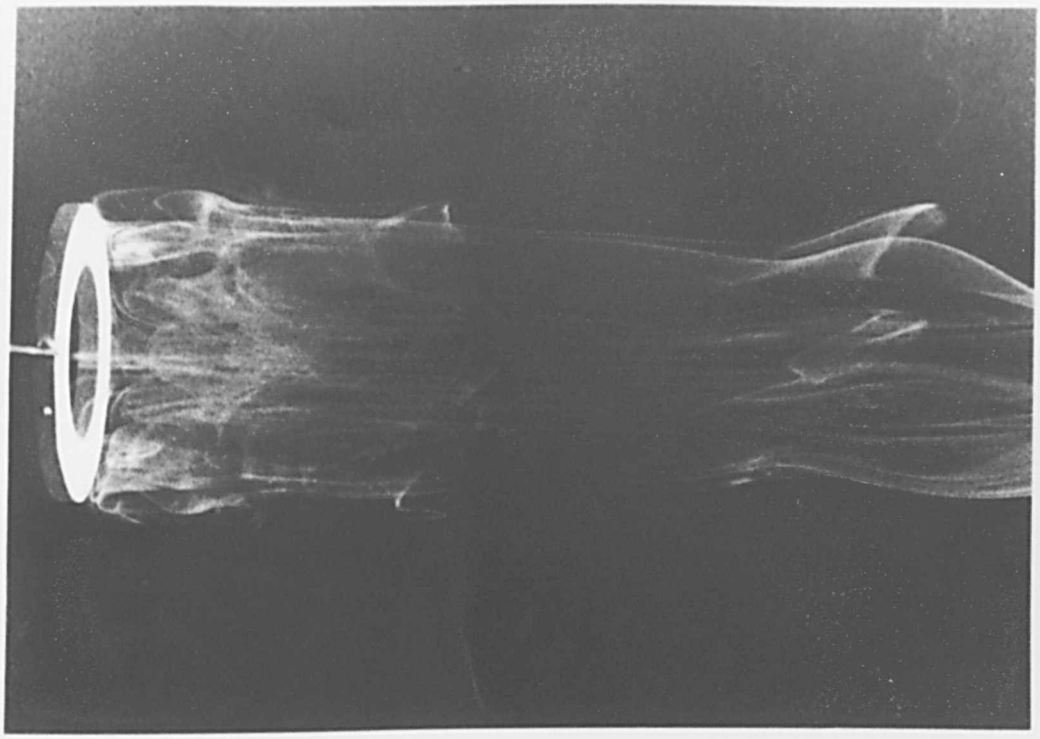


Photo 5.2 Ring, d/w = 4.0, $\delta$/w = 0.3, $R_e$ = 76

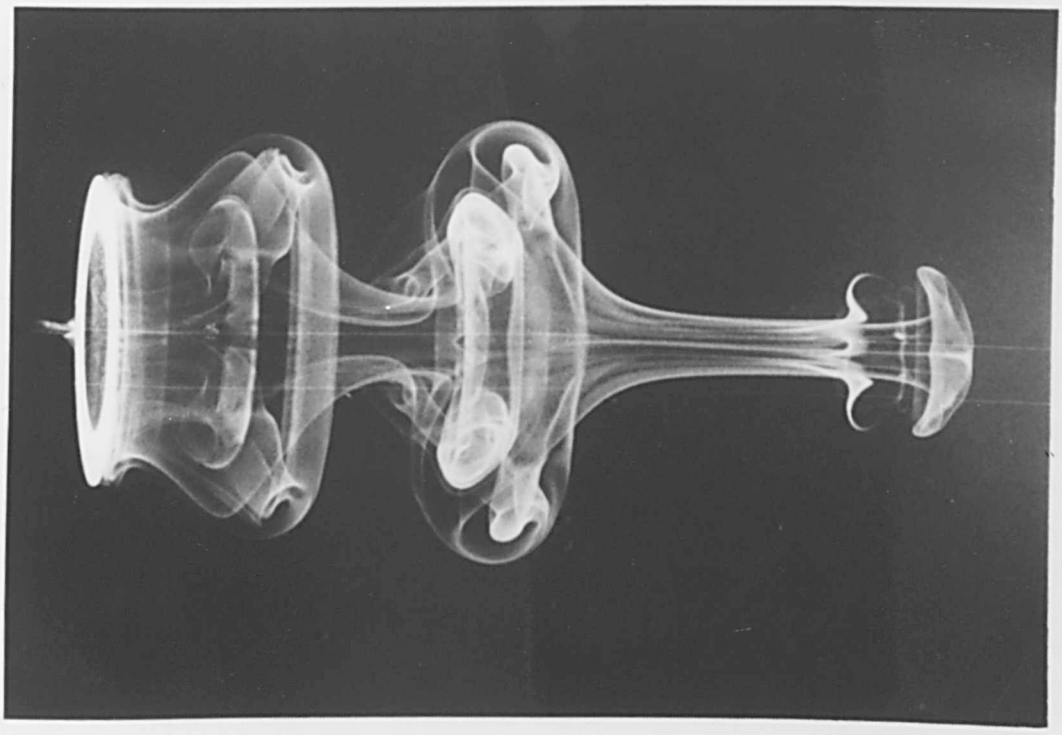


Photo 5.3(a) Ring, d/w = 6.0, $\delta$/w = 0.3, $R_e$ = 76



Photo 5.3(b) Ring, d/w = 6.0, $\delta$/w = 0.3, $R_e$ = 66

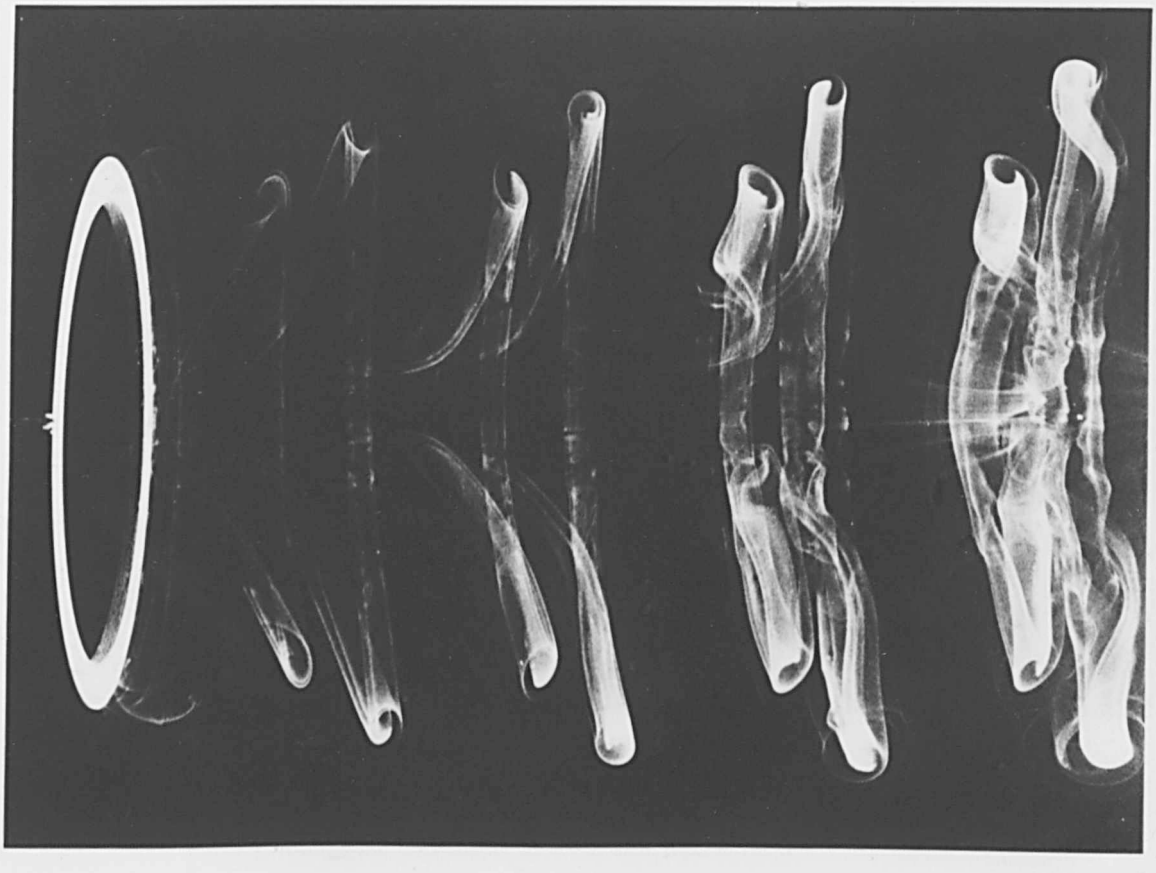


Photo 5.4 Ring, d/w = 12, $\delta$/w = 0.3, $R_e$ = 66



Photo 5.5 Ring, d/w = 4.0, $\delta$/w = 0.3, $R_e$ = 75

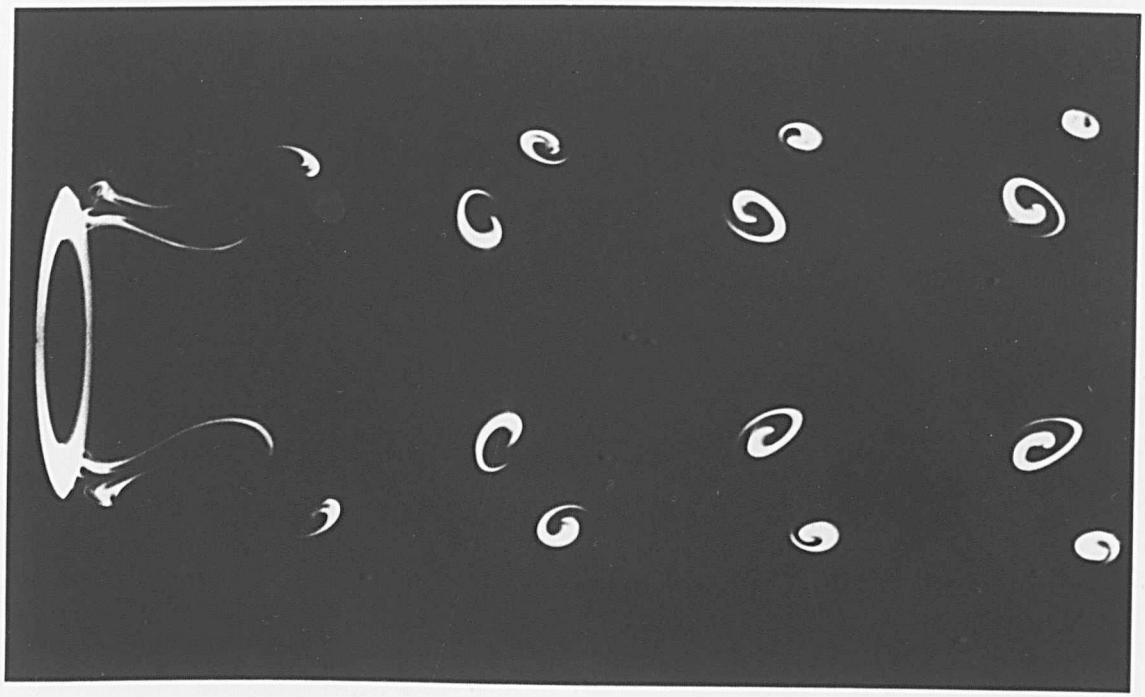
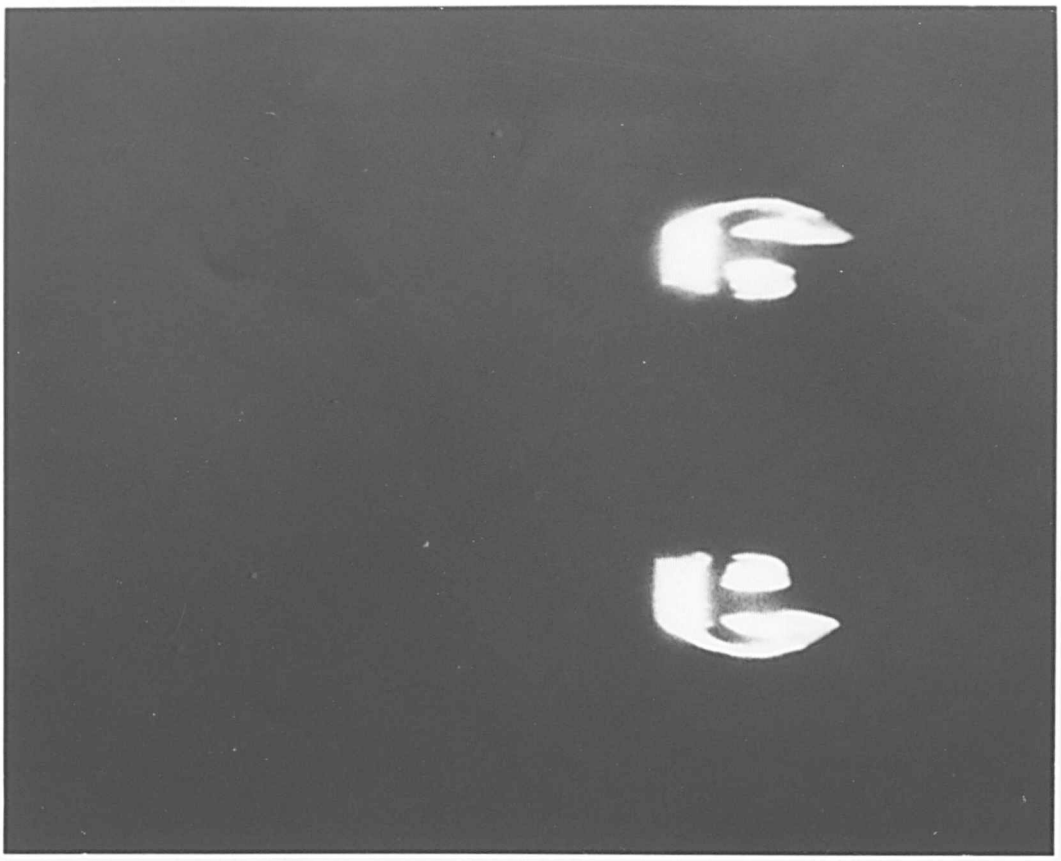


Photo 5.6 Ring, d/w = 6.0, $\delta$/w = 0.3, $R_e$ = 62

(a)



(b)



Photo 5.7 Time sequence of vortex shedding from the sharp-edged ring model of d/w = 6.0, $R_e$ = 95

(c)



(d)

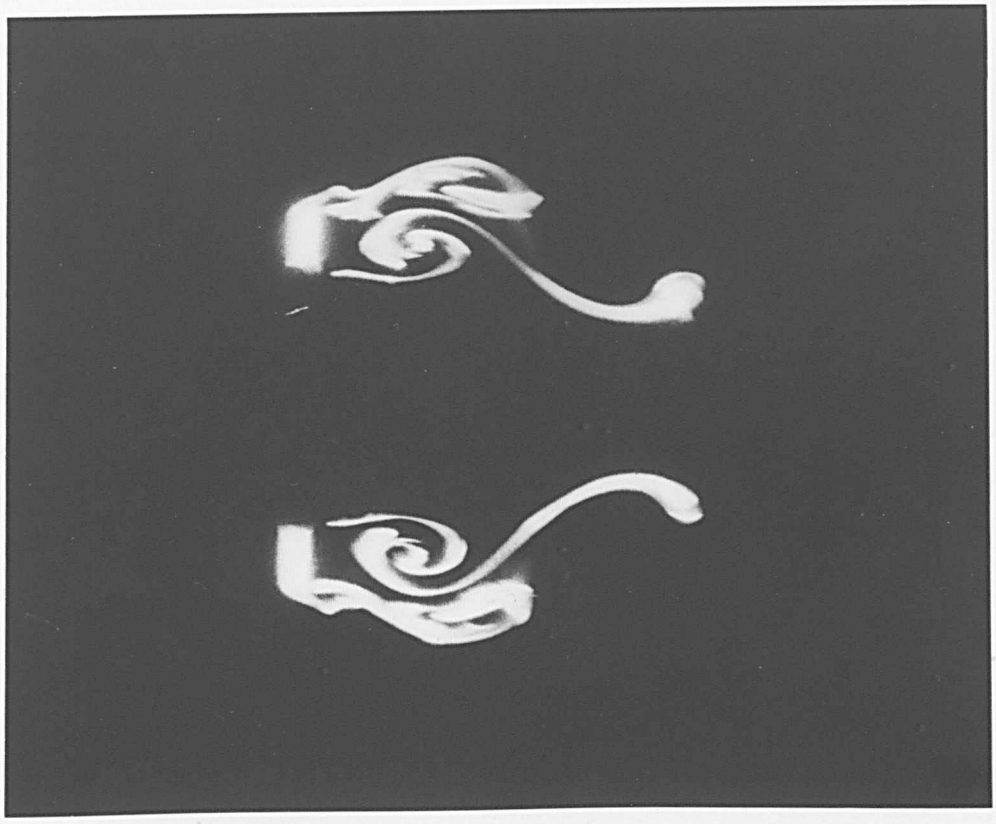
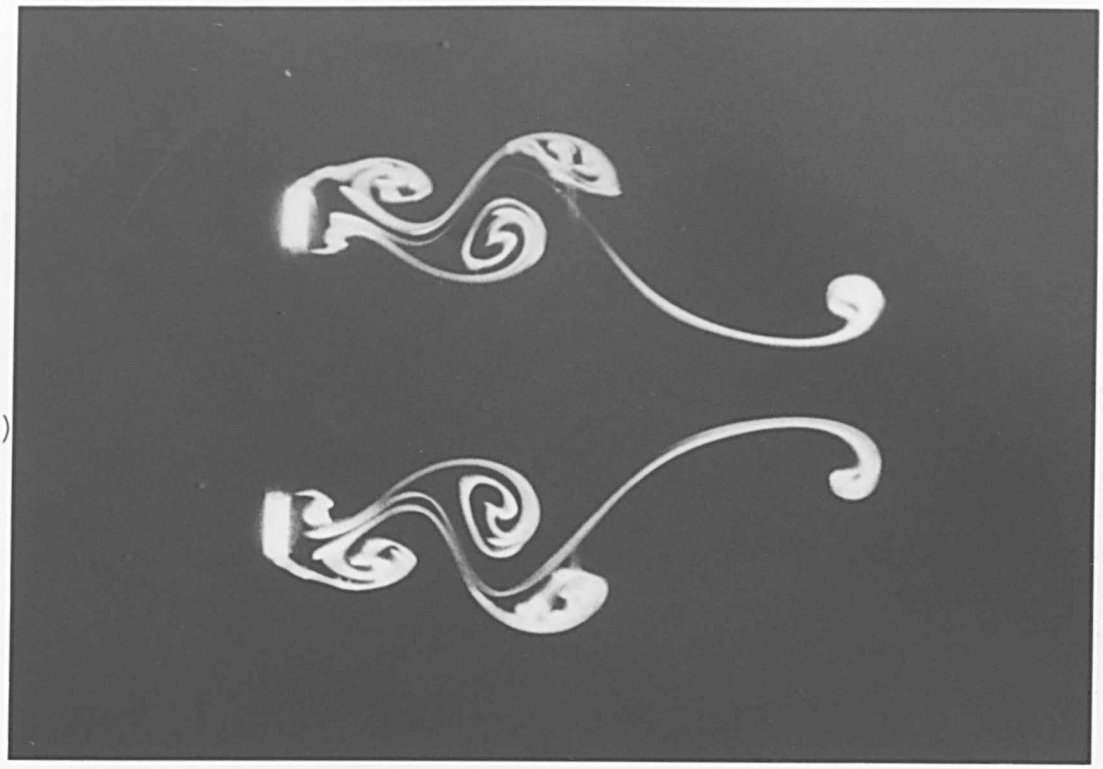


Photo 5.7 Time sequence of vortex shedding from the sharp-edged ring model of d/w = 6.0, $R_e$ = 95

(e)



(f)

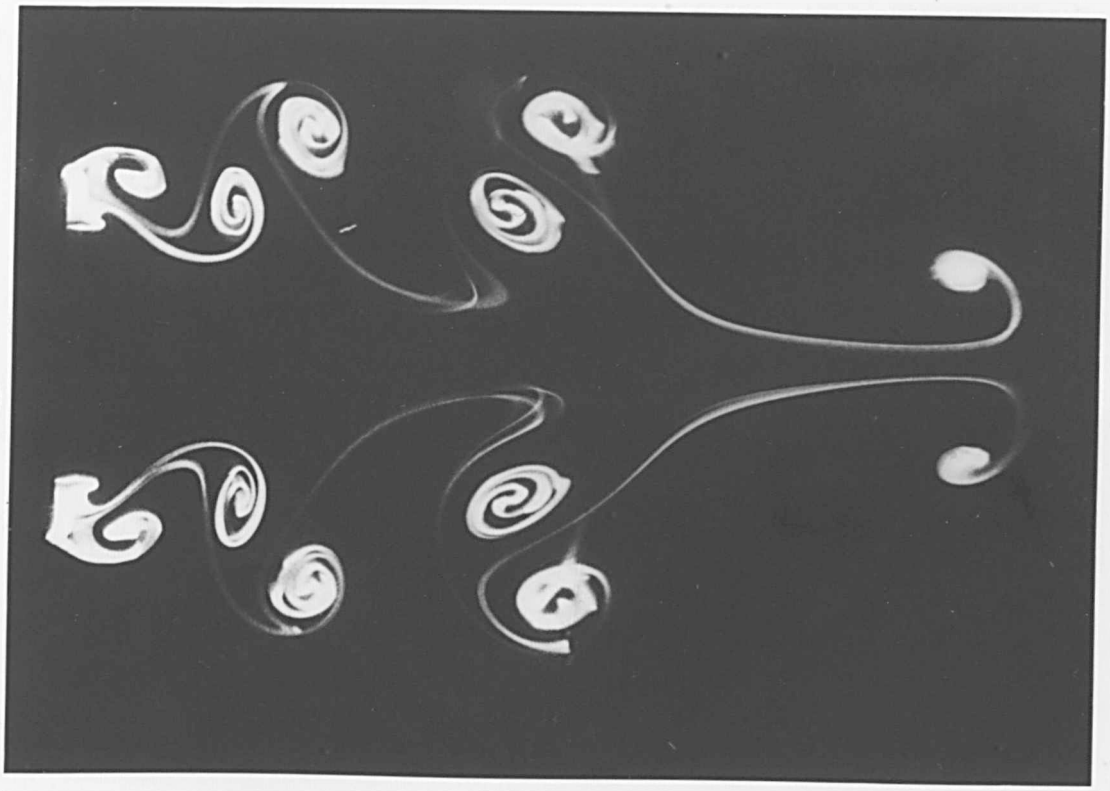


Photo 5.7 Time sequence of vortex shedding from the sharp-edged ring model of d/w = 6.0, $R_e$ = 95

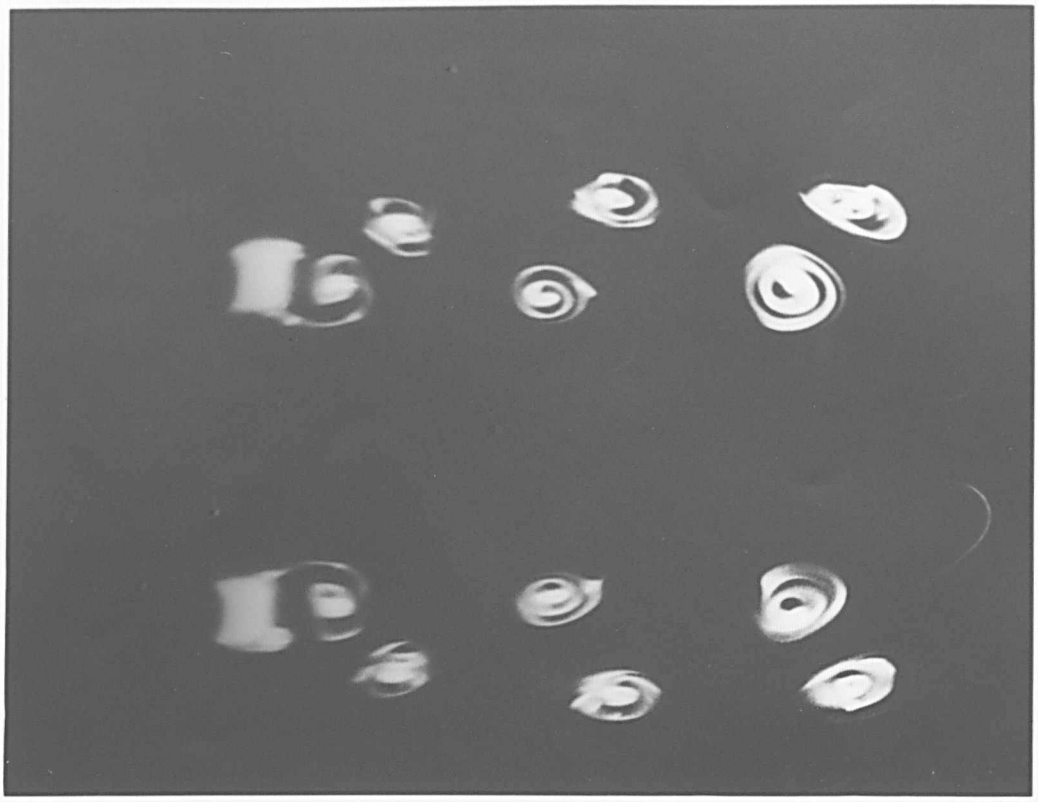


Photo 5.8 Ring with thin sharp-edged cross-section, $d/w = 6.0$, $R_e = 95$

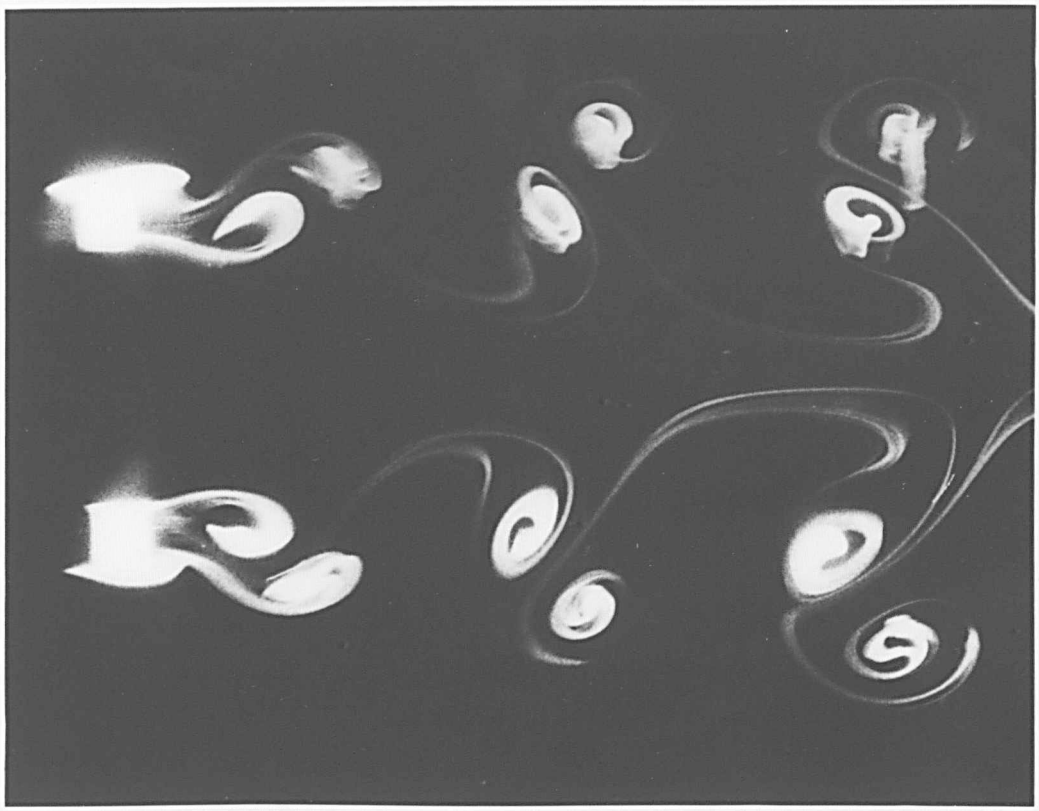


Photo 5.9 Ring with rectangular cross-section of $\delta/w = 0.6$, $d/w = 6.0$, $R_e = 95$

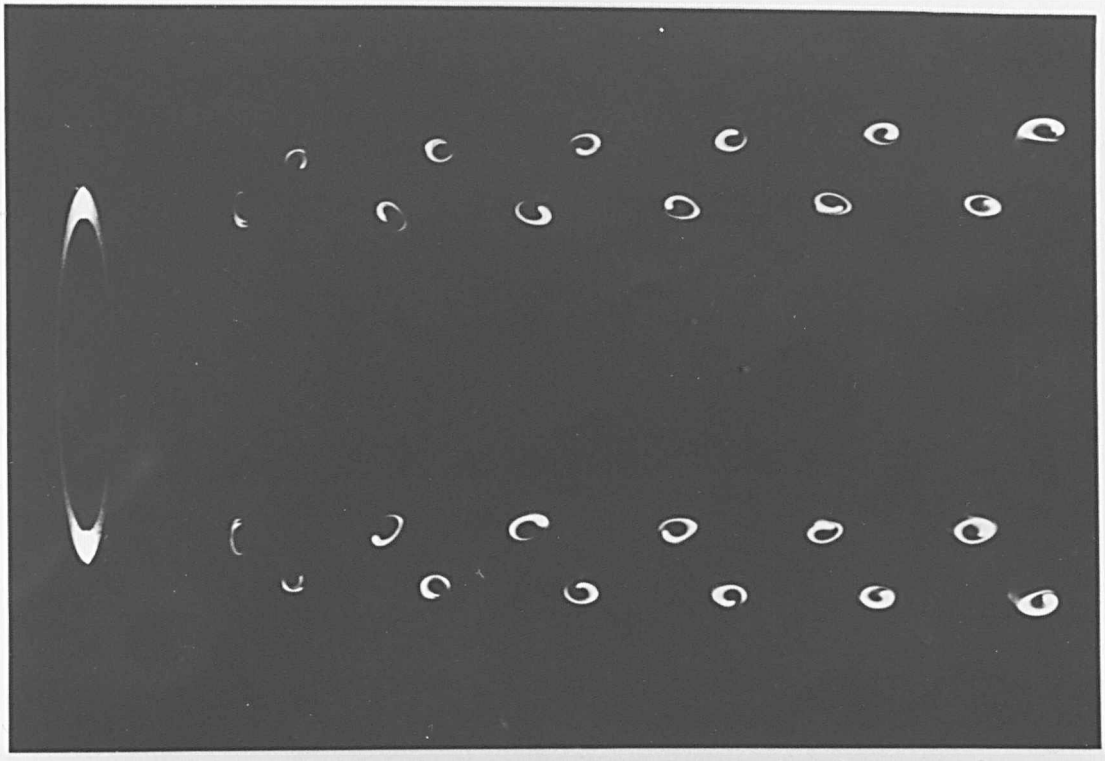


Photo 5.10 Ring, $d/w = 12$, $\delta/w = 0.3$, $R_e = 76$

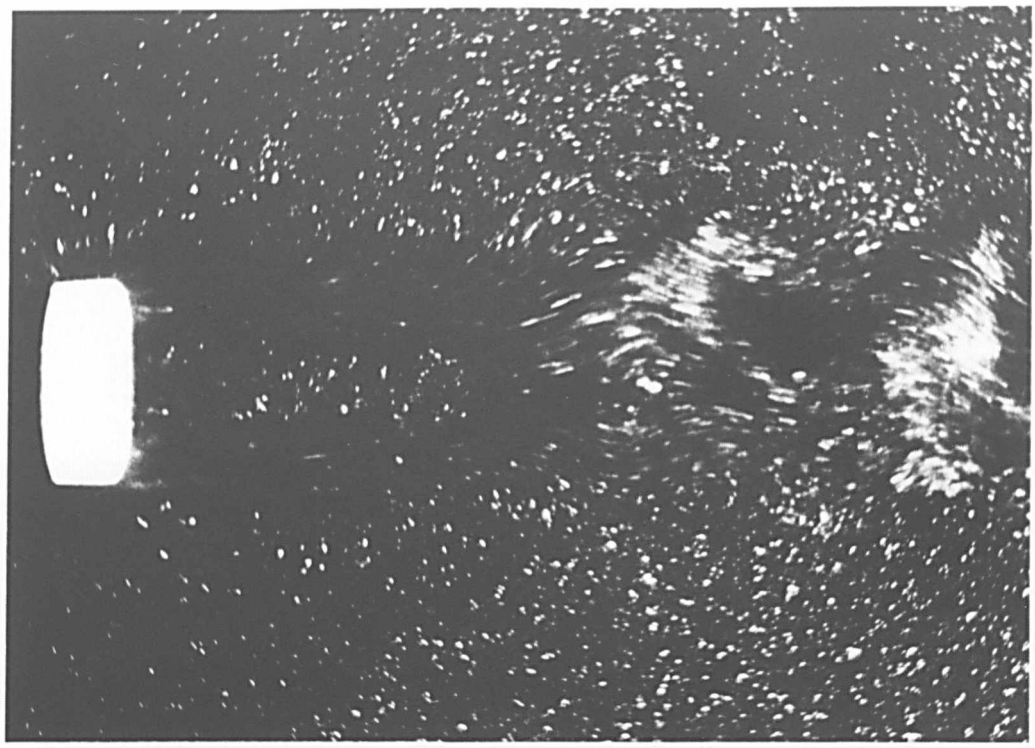


Photo 5.11 Ring, d/w = 4.0, $\delta$/w = 0.3, $R_e$ = 72

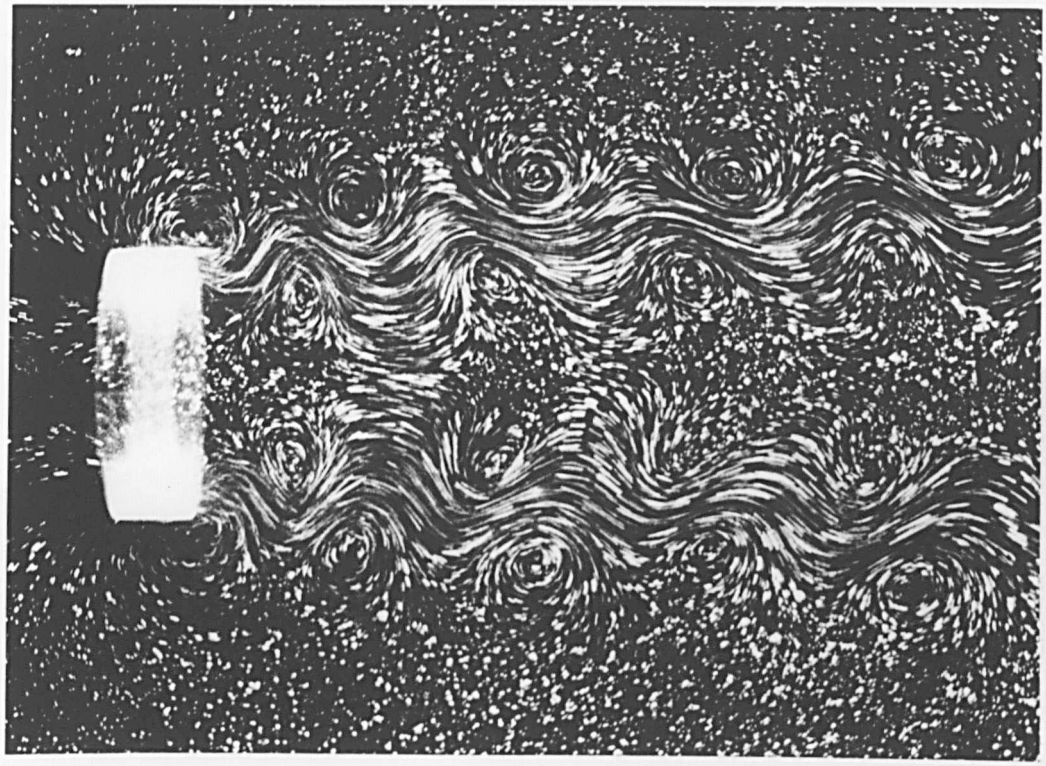


Photo 5.12 Ring, d/w = 6.0, $\delta$/w = 0.3, $R_e$ = 95

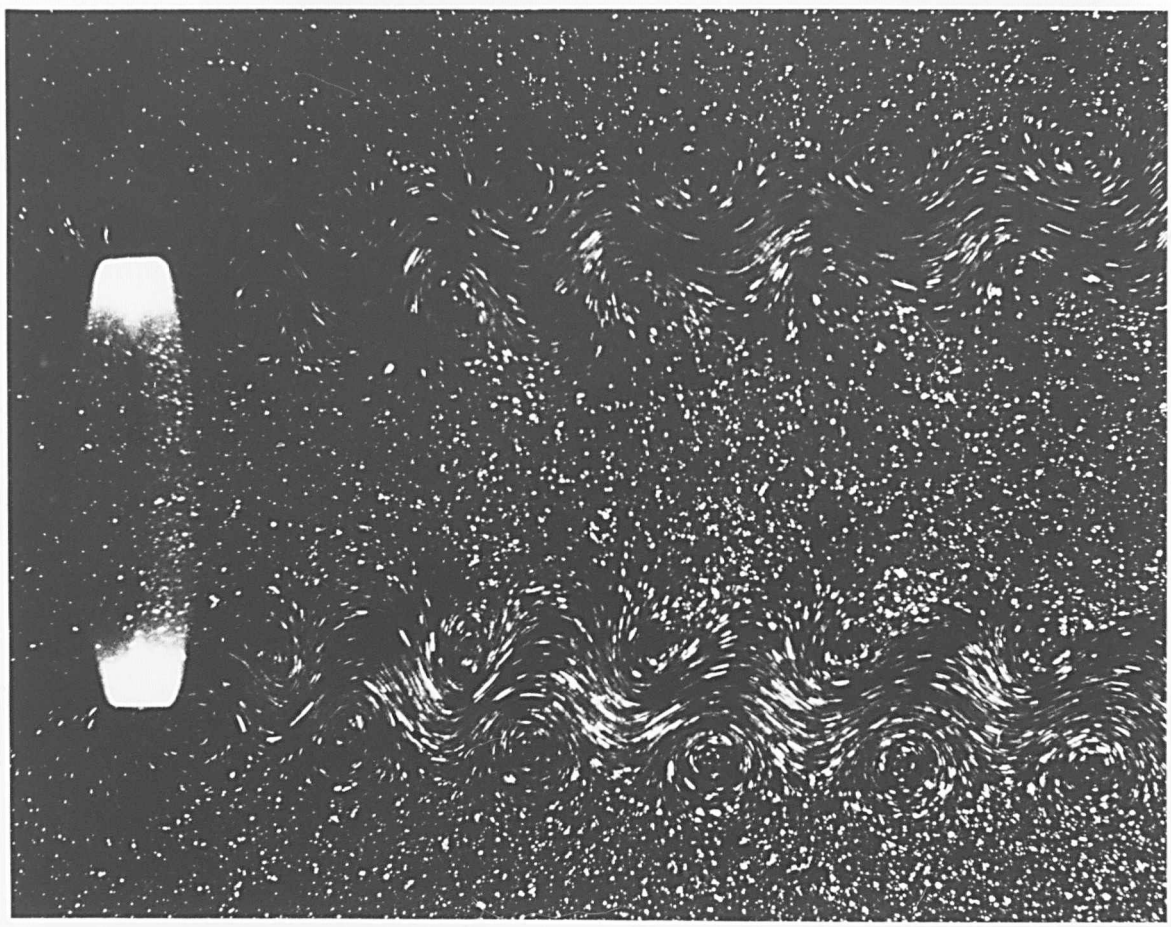


Photo 5.13 Ring, $d/w = 12$, $\delta/w = 0.3$, $R_e = 72$

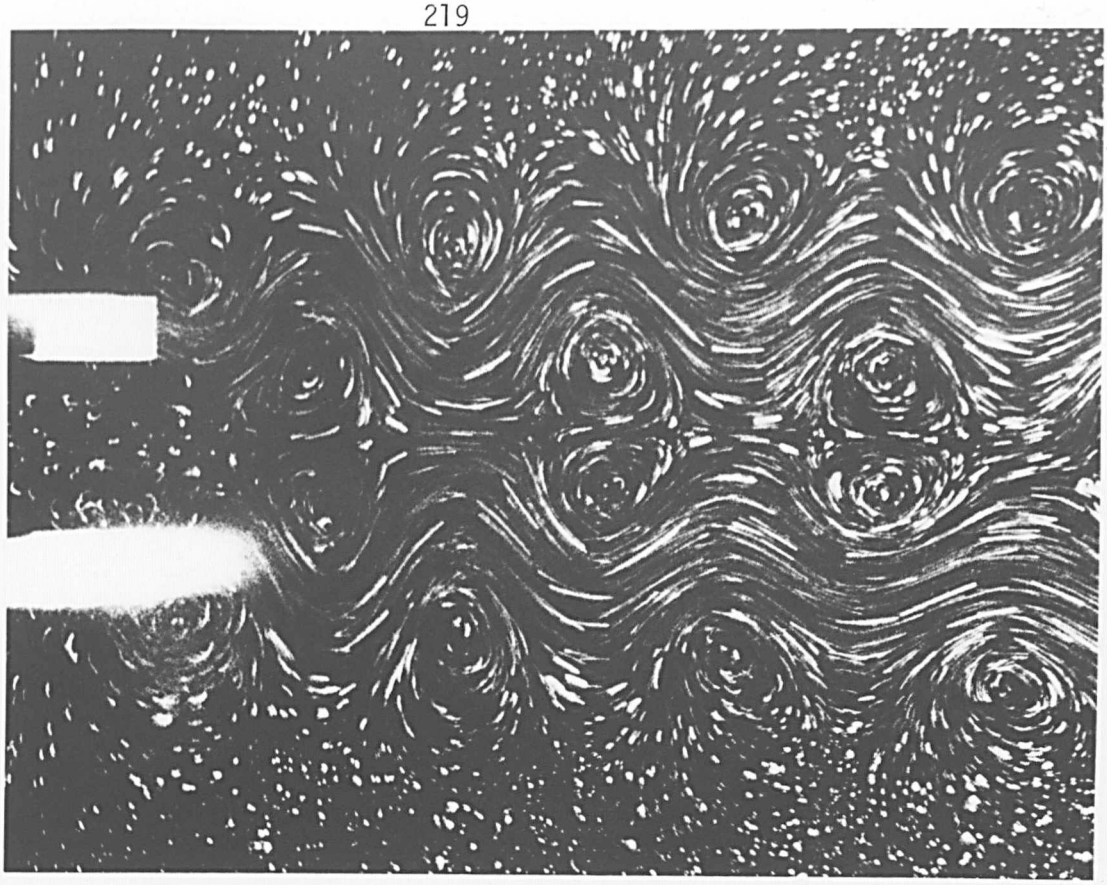


Photo 5.14 Two flat plates, d/w = 4.0, $\delta$/w = 0.3, $R_e$ = 95

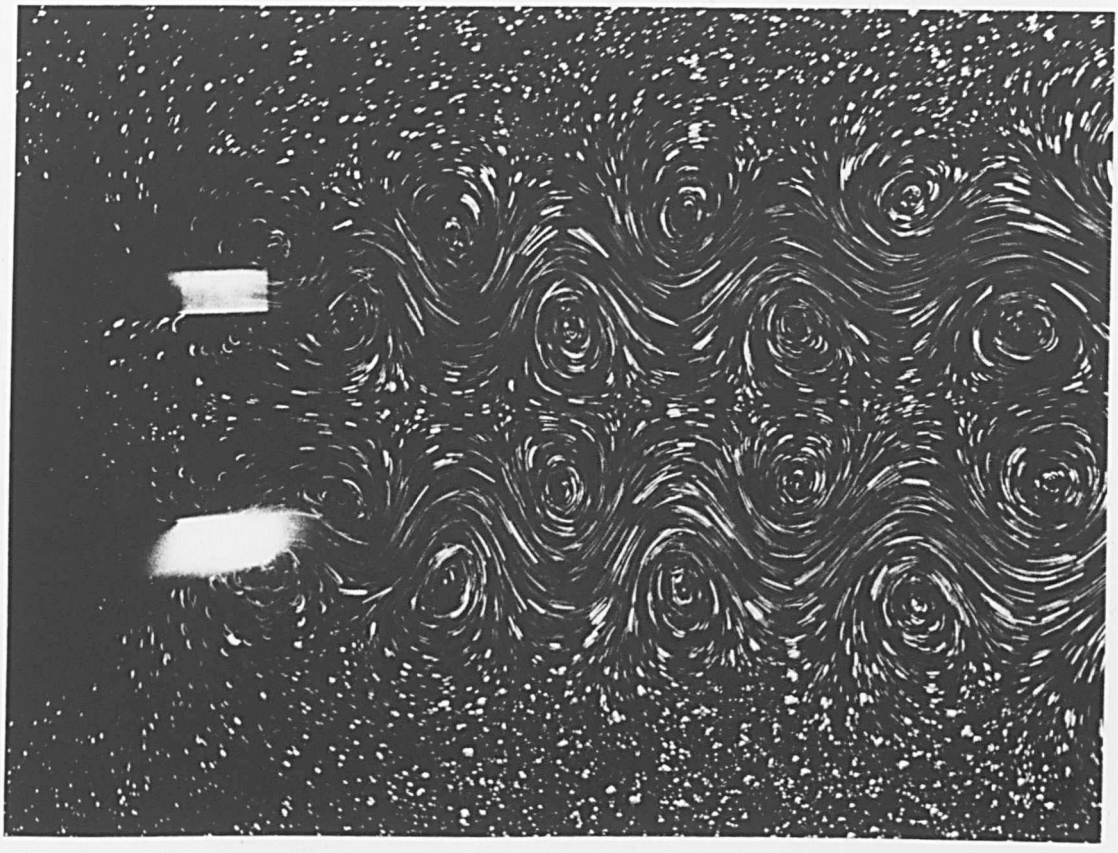


Photo 5.15 Two flat plates, d/w = 6.0, $\delta$/w = 0.3, $R_e$ = 95

# CHAPTER SIX

## CONCLUSIONS

The wake structure of the ring models with various shapes of cross-section has been investigated and compared with the wake of a solid circular disk and the wakes of two flat plates arranged side-by-side. The main results obtained in the present work are summarised as follows:

### (a) Wind tunnel experiments at Reynolds numbers of the order of $10^4$.

1. Axisymmetric vortex rings shed alternately from the inside and outside of thin sharp-edged cross-section ring models with $d/w \geq 5$. The counterrotating inside and outside vortex rings shed from the thin sharp-edged cross-section ring model with $d/w = 6.0$ are nearly $180^{o}$ out of phase with each other at $x = 3.4\ w$. However at further distances downstream they quickly get closer to each other caused by the opposite signed self-induced velocities of both sets of vortex rings.

2. The vorticity distribution in the $(y,t)$ plane in the wake of the solid circular disk at $x = 3.4\ D$ is in nearly

antiphase about the axis of symmetry of the disk. The vorticity distributions in the (y,t) plane (y >0) and (z,t) plane (z >0) conditionally extracted by using the same reference signal in the wake of the disk at x = 3.4 D can be either $90^{o}$ or $-90^{o}$ out of phase with each other. Both modes occur randomly and intermittently and each seem to be equally likely to form.

3. Synchronisation of vortex shedding from two flat plates arranged side-by-side with spacings of d/w = 4.0 and d/w = 6.0 is observed. The vortex shedding is symmetric on the whole about the axis of the gap between the two flat plates, though some irregularities are also observed. In contrast to the wake behind the ring model, the arrangement of vortices from the two flat plates keeps an almost constant pattern in the wake.

4. The strengths of vortex rings from the thin sharp-edged cross-section ring model with d/w = 6.0 and vortices from the two flat plates arranged side-by-side with d/w = 4.0 and d/w = 6.0 are roughly at the same level at the same relative positions in the wake. Nearly two-thirds of the total vorticity discharged from one side of both bluff bodies during one vortex shedding cycle is lost from the concentrated clouds of vorticity by the time they reach x = 8.0 w. The overall decay rate of vortex strength is about 5% per w vortex travel in both wakes at $R_e = 2.0 \times 10^4$, compared with 8% obtained by Cantwell and Coles (1983) who measured in the wake of an isolated circular cylinder at $R_e = 1.4 \times 10^5$.

5. The inside vortices from the two flat plates arranged side-by-side with d/w = 4.0 become weaker than the outside ones. The reason is thought to be that since the two rows of inside vortices have opposite signs then the rows of vortices cancel each other under the mixing action of turbulence when the gap between the two rows is small. Also the inside vortex rings from the ring model are weaker than the outside ones for the same reason.

6. The base pressure coefficients of the thin sharp-edged cross-section ring models with d/w = 4.0 to d/w = 10.0 are lower than that of the solid circular disk and are higher than that of the thin sharp-edged cross-section flat plate. Also, the coefficient rapidly decreases with increasing d/w between d/w = 4.0 and d/w = 6.0.

7. The correlations of velocity fluctuations between two positions located on a plane normal to the axis of symmetry were measured, at the same radial displacement from the axis and at various angular separations, in the wakes of the thin sharp-edged cross-section ring models with d/w = 4.0 to d/w = 10.0. The correlations for d/w = 5.0 and d/w = 6.0 are the highest for all the models at the maximum separation. Also, there exists a sudden change of the correlation curves for rings between d/w = 4.5 and d/w = 5.0, which suggests a structural change of the wake of the models.

8. The Strouhal numbers of the thin sharp-edged cross-section ring models with $d/w = 5.0$ to $d/w = 10.0$ are a little lower than that of the thin sharp-edged cross-section flat plate, and velocity fluctuations in the wakes of the models are correlated in an axisymmetric mode. On the other hand, the Strouhal numbers of the ring models with $d/w = 1.2$ to $d/w = 4.0$ are lower than those for $d/w = 5.0$ to $d/w = 10.0$, but are equal or a little higher than that of the solid circular disk. Velocity fluctuations in the wakes of these models are in the same mode as the disk model. Both modes of velocity fluctuations are observed in the wake of the ring model with $d/w = 4.5$.

9. The spectral density function of velocity fluctuations measured on the axis of symmetry in the wake of the ring model has a narrower peak when the velocity fluctuation is in the axisymmetric mode compared with that measured outside the ring wake.

10. The $C_{pb}$ of the rectangular cross-section ring model is much lower and the $C_{pb}$ of the triangular cross-section ring model is a little lower than that of the thin sharp-edged cross-section ring model. Also, the correlation of velocity fluctuations in the wake of the rectangular cross-section ring model is markedly high.

11. A markedly regular periodic velocity fluctuation is observed on the axis of symmetry in the wake of the rectangular cross-section ring model. The vortex rings shed from this model are stronger, their diameters are larger and they get close to each other more quickly down the wake compared with those from the thin sharp-edged ring model.

**(b) Numerical modelling of vortex wakes**

1. The vortex wakes of the ring and the two flat plates were modelled by using infinite rows of counterrotating coaxial circular line vortices and four rows of infinite two-dimensional point vortices respectively. The trends for both wakes observed in the wind tunnel experiments, i.e. that the inside and outside vortex rings get close to each other and the four rows of the two-dimensional vortices keep almost constant arrangement in the wake, are well predicted by the simple simulations of the temporal development of the wakes.

**(c) Flow visualization experiment at the Reynolds numbers just below $10^2$.**

1. The streakline and particle paths patterns in the wakes of the ring models and the two flat plates arranged side-by-side were visualised in a water tank. Regular axisymmetric vortex ring

shedding from the ring model with $d/w = 6.0$ and $d/w = 12.0$ was clearly recognised. Also, arrangements of vortices from the two flat plates with $d/w = 4.0$ and $d/w = 6.0$ are symmetric about the axis of the gap. The results obtained by flow visualisation agree with those obtained in the wind tunnel experiments.

## REFERENCES

ACHENBACH, E. 1972 Experiments on the flow past spheres at very high Reynolds numbers. J. Fluid Mech. 54, pp 565-595.

ACHENBACH, E. 1974 Vortex shedding from spheres. J. Fluid Mech. 62, pp 209-221.

AMARAKOON, A.M.D. et al 1982 Drag measurements for axisymmetric motion of a torus at low Reynolds number. Phys. of Fluids, 25, pp 1495-1501.

ANDREOPOULOS, J. 1972 Mutual interference between a pair of bluff bodies. M.Sc. project report, Imperial College, London.

BATCHELOR, G.K. 1967 "An Introduction to Fluid Dynamics". Cambridge University Press, Chapter 7.

BEARMAN, P.W. 1967 On vortex street wakes. J. Fluid Mech 28, pp.625-641.

BEARMAN, P.W. and TRUEMAN, D. 1972 An investigation of the flow around rectangular cylinders. The Aero. Quart. 23, pp 229-237.

BEARMAN, P.W. and WADCOCK, A.J. 1973 The interaction between a pair of circular cylinders normal to a stream. J. Fluid Mech. 61, pp 499-511.

BENDAT, J.S. and PIERSOL, A.G. 1971 "Random data analysis and measurement procedures". Wiley Interscience.

BERGER, E 1964 The determination of the hydrodynamic parameters of a Karman vortex street from hot wire measurements at low Reynolds numbers. Z. Flug. 12, pp 41-59.

BIERMANN, D. and HERRNSTEIN, W.H. 1933 The interference between struts in various combinations. NACA TR 468.

BRADBURY, L.J.S. 1976 Measurements with a pulsed-wire and a hot-wire anemometer in the highly turbulent wake of a normal flat plate. J. Fluid Mech. 77, pp 473-497

BRADSHAW, P. 1965 The effect of wind-tunnel screens on nominally two-dimensional boundary layer. J. Fluid Mech. 22, pp 679-687.

BRADSHAW, P. 1975 "An Introduction to Turbulence and Its Measurements". Pergamon Press.

BRADSHAW, P. 1984 High speed analogue to digital magtape conversion system. I.C. Aero TN 84-102.

CALVERT, J.R. 1967a Experiment on the flow past an inclined disk. J. Fluid Mech. 29, pp 691-703.

CALVERT, J.R. 1967b Experiments on the low-speed flow past cones. J. Fluid Mech. 27, pp 273-289.

CALVERT, J.R. 1972 Some experiments on the flow past a sphere. Aero. J. Roy. Soc. 76, pp 248-250.

CANTWELL, B.J. 1976 A flying hot-wire study of the turbulent near wake of a circular cylinder at a Reynolds number of 140.000. Ph.D. Thesis, California Institute of Technology.

CANTWELL, B. and COLES, D. 1983 An experimental study of entrainment and transport in the turbulent near wake of a circular cylinder. J. Fluid Mech. 136, pp 321-374.

CARMODY, T. 1964 Establishment of the wake behind a disk. Trans. ASME, Ser.D. 86, pp 869-883.

CLEMENTS, M.P.M. and UNWIN, G.P. 1973 Calibration of the 3 ft x 3 ft low speed wind tunnel of Imperial College. Third year project report. Dept of Aeronautics, Imperial College, London.

DAVIES, M.E. 1975 Wakes of oscillating bluff bodies. Ph.D. Thesis, University of London.

DAVIES, M.E. 1976 A comparison of the wake structure of a stationary and oscillating bluff body, using a conditional sampling technique. J. Fluid Mech. 75, pp 209-231.

DONOSO, P. 1980 Investigation of wake structure of isolated and intersecting flat plate. M.Phil. Univ. of London.

FAGE, A. 1936 Experiments on a sphere at critical Reynolds numbers. ARC R & M 1766.

FAGE, A. and JOHANSEN, F.C. 1927 On the flow of air behind an inclined flat plate of infinite span. ARC R & M 1104.

FAIL, R., LAWFORD, J.A. and EYRE, R.C.W. 1957 Low-speed experiments on the wake characteristics of flat plates normal to an air stream. ARC R & M 3120.

FRAENKEL, L.E. 1970 On steady vortex rings of small cross section in an ideal fluid. Proc. Roy. Soc. Ser. A, 316, pp 29-62.

FUCHS, H.V. et al. 1979 Large scale coherent structures in the wake of axisymmetric bodies. J. Fluid Mech. 93, pp 185-207.

GERRARD, J.H. 1978 The wakes of cylindrical bluff bodies at low Reynolds number. Proc. Roy. Soc. Ser. A. 288, No. 354, pp 351-382.

GERICH, D. and ECKELMAN, H. 1982 Influence of end plate and free ends on the shedding frequency of circular cylinders. J. Fluid Mech. 122, pp 109-121.

GIBSON C.H. et al. 1968 Measurements of turbulent velocity and temperature fluctuations in the wake of a sphere. AIAA 6, pp 642-649.

GOREN, S.L. and O'NEILL, M.E. 1980 Asymmetric creeping motion of an open torus. J. Fluid Mech. 101, pp 97-110.

HAYASHI, M. et al. 1986 Wake interference of a row of normal flat plates arranged side by side in a uniform flow. J. Fluid Mech. 164, pp 1-15.

HAYWARD, A.T.J. and JELFFS, P.A.M. 1986 The potential of the vortex shedding meter as a custody transfer meter for liquids. Flow measurements in the mid 80's. International Conference, NEL.

HORI, E. 1959 Experiments of flow around a pair of parallel circular cylinders. 9th Japan Nat. Cong. Appl. Mech., pp 231-234.

HWANG, N.H.C. and BALDWIN, L.V. 1966 Decay of turbulence in axisymmetric wakes. Trans. ASME, Ser.D., 88, pp 261-268.

ISHIGAI, S. et al 1971 Experimental study on structure of gas flow in tube banks with tube axis normal to flow. Trans. JSME, 37, pp 2319-2326.

JOHNSON, R.E. and WU, T.Y. 1979 Hydromechanics of low-Reynolds-number flow. J. Fluid Mech. 95, pp 263-277.

KALKHOF, H.G. 1983 Der Wirbel durchflusmesser im Vergleich mit Wirkdruck-Durchflussmessgeraten BTB Berich, Me-47.

KAMEMOTO, K. et al 1986 Numerical simulation of the axisymmetric vortex shedding from a ring by a discrete vortex method combined with the boundary element method. International seminar on Engineering Applications of the Surface and Cloud Vorticity Methods. Wroclaw. Poland.

KAMEMOTO, K. and BEARMAN, P.W. 1980 Numrical modelling of interacting vortex shedding from two flat plates in a side by side arrangement. Trans. JASM, 46, pp 1229-1236.

KARMAN, V. 1911 Uber den Mechanismus des Widerstandes, den ein bewegter Korper in einer Flussigkeit erzeugt. Gottingen. Math.Phys. pp.509-517.

KOHAN, S. and SCHWARZ, W.H. 1973 Low speed calibration formula for vortex shedding from cylinders. Physics of Fluid 16, No.9, pp 1528-1529.

KOVASZNAY, L.S.G. 1949 Hot-wire investigation of the wake behind cylinders at low Reynolds numbers. Proc. Roy. Soc. Ser.A, 198, No. 1053, pp 174-190.

KOVASZNAY, L.S.G. et al. 1970 Large scale motion in the intermittent region of a turbulent boundary layer. J. Fluid Mech. 41, pp 283-325.

LAMB, H. 1945 "Hydrodynamics". Dover Publications. Chapter 7.

LANDWEBER, L. 1942 Flow about a pair of adjacent parallel cylinders normal to a stream. David Taylor Mod. B. Rep. 485. Washington, U.S.A.

MAGARVEY, R.H. and MacLATCHY, C.S. 1965 Vortices in sphere wakes. Can. J. Phys. 43, pp 1649-1656.

MASKELL, E.C. 1963 A theory of the blockage effects on bluff bodies and stalled wings in a closed wind tunnel. R.A.E. Aero Rep 2685.

MAULL, D.J. 1980 The drag of slant-based bodies of revolution. Aero.J. 84, pp 164-166.

MAULL, D.J. and YOUNG, R.A. 1973 Vortex shedding from bluff bodies in a shear flow. J. Fluid Mech. 60, pp 401-409.

MAXWORTHY, T. 1969 Experiments on the flow around a sphere at high Reynolds numbers. Trans. ASME, Ser.E. 36, pp 598-607.

MAXWORTHY, T. 1972 The structure and stability of vortex rings. J. Fluid Mech. 51, pp 15-32.

MAXWORTHY, T. 1977 Some experimental studies of vortex rings. J. Fluid Mech. 81, pp 465-495.

MONSON, D.R. 1983 The effect of transverse curvature on the drag and vortex shedding of elongated bluff bodies at low Reynolds number. Trans ASME Fluid. 105, pp 308-322.

NAKAGUCHI, H. et al. 1968 An experimental study on aerodynamic drag of rectangular cylinders. J. Japan Soc. of Aero & Space Sciences, 16, pp 1-5.

OKUDE, S. and MATSUI, T. 1982 Vorticity profile of a Karman vortex street. Proc. of the 14th Fluid Dynamics Conference, Japan. pp 202-205.

PAO, H.P. and KAO, T.W. 1977 Vortex structure in the wake of a sphere. J. Phys. Fluids, 20, pp 187-191.

RAYLEIGH, J.W.S. 1945 "The Theory of Sound". Vol. II, Dover Publications.

RELTON, F.E. 1931 The steady broadside motion of an anchor ring in an infinite viscous liquid. Proc. Roy. Soc. Ser.A. 134, pp 47-57.

RIDDHAGNI, P.R. et al. 1971 Measurements in the turbulent wake of a sphere. AIAA. 9, No.7, pp 1433-1434.

ROBINSON, E.R. 1985 Simulation studies of pulse interpolation method. Proceedings of international conference on the metering of petroleum and its products. London.

ROBERTS, J.B. 1973 Coherence measurements in an axisymmetric wake. AIAA 11, No. 11, pp 1569-1571.

ROONEY, D.M. and PELTZER, R.D. 1982 The effect of roughness and shear on vortex shedding cell length behind a circular cylinder. Trans. ASME, 104, pp 72-80.

ROSHKO, A. 1954a On the drag and shedding frequency of two-dimensional bluff bodies. NACA TN 3169.

ROSHKO, A. 1954b On the development of turbulent wakes from vortex streets. NACA Report 1191.

ROSHKO, A. 1955 On the wake and drag of bluff bodies. J. Aeronaut. Sci. 22, pp 124-132.

SAFFMAN, P.G. 1970 The velocity of viscous vortex rings. Studies Appl. Math. 49, pp 371-380.

SCHOLZ, D. 1986 Koharente Wirbelstrukturen im Nachlauf einer ruhenden und einer schwingungserregten Kreisscheibe. DFVLR-FB 86-04.

SHIBA, H. 1960 Trans. Japan Soc. Shipbuild 97.

SHIDA, Y. et al. 1984 Numerical study of flow past two circular cylinders. Proc. 2nd Asian Conf. of Fluid Mech., 1983 Beijing, Science Press, China, pp 686-691.

SIMMONS, J.E.L. 1974 Phase measurements between hot-wire signals in the turbulent wake of a two-dimensional bluff body. J. Fluid Mech. 64, pp 599-609.

SLAOUTI, A. and GERRARD, J.H. 1981 An experimental investigation of the end effects on the wake of a circular cylinder towed through water at low Reynolds numbers. J. Fluid Mech. 112, pp 297-314.

SPIVACK, H.M. 1946 Vortex frequency and flow pattern in the wake of two parallel cylinders at varied spacings normal to an airstream. J. Aero. Sci., 13, pp 289-299.

STANSBY, P.K. 1976 The locking-on of vortex shedding due to the cross-stream vibration of circular cylinders in uniform and shear flows. J. Fluid Mech. 74, pp 641-665.

STANSBY, P.K. 1981 A numerical study of vortex shedding from one and two circular cylinders. Aero.Quart. 32, pp 48-71.

STANTON, T.E. and MARSHALL, D. 1930 On the eddy system in the wake of flat circular plates in three dimensional flow. ARC R & M 1358.

STEINER, T.R. 1984 A study of turbulent wakes and the vortex formation process. Ph.D. Thesis, University of Melbourne.

STROUHAL, V. 1878 Uber eine besondere Art der Touerregung. Annalen der Physik und Chemie, Neue Folge, Bd.5, pp.216-251.

SUBRAMANIAN, C.S. and BRADSHAW, P. 1984 Apparatus and programs for digital analysis of fluctuating quantities in turbulent flow. I.C. Aero TN 84-101.

TAKAMOTO, M. and IZUMI, K. 1981 Experimental observation of stable arrangement of vortex rings. Phys of Fluids. 34, pp 1582-1583.

TAKAMOTO, M. and KOMIYA, K. 1979 A study on a ring as a bluff body of a vortex shedding flowmeter. The Proceedings of 18th Japan SICE Conf. pp 625-626.

TAKAMOTO, M. and KOMIYA, K. 1982 Vortex ring shedding flowmeter. ACTA IMEKO '82, pp 87-96.

TANEDA, S. 1952 Studies on wake vortices. Rep. Res. Inst. Appl. Mech. Kyushu Univ. 1, pp 131.

TANEDA, S. et al. 1974 The behaviour of tracer particles in flow visualization by electrolysis of water. J. Phy. Soc. Japan. 37, pp 784.

TANEDA, S. 1978 Visual observations of the flow past a sphere at Reynolds numbers between $10^4$ and $10^6$. J. Fluid Mech. 85, pp 189-198.

TCHEN, C.M. 1954 Motion of small particles in skew shape suspended in a viscous liquid. J. Appl. Phys. 25, pp 463-473.

TSUCHIYA et al 1967 Karman vortex flowmeter. Proc. JSME, No. 169, pp 97.

TYLER, E. 1931 Vortex formation behind obstacles of various sections. Phil. Mag. S.T. 11, No. 72, pp.849-890.

UBEROI, M.S. and FREYMUTH, P. 1970 Turbulent energy balance and spectra of the axisymmetric wake. Phys. Fluid, 13, pp 2205-2211.

WEBSTER, C.A.G. 1964 An experimental study of turbulence in a density-stratified shear flow. J. Fluid Mech. 19, pp 221-245.

WHITE, et al. 1974 The vortex shedding flowmeter. Instrum. Soc. of America, 1, pp 967-974.

WILLIAMSON, C.H.K. 1985 Evolution of a single wake behind a pair of bluff bodies. J. Fluid Mech. 159, pp 1-18.

WILLMARTH, W.W., HAWK, N.E. and HARVEY, R.L. 1964 Steady and unsteady motions and wakes of freely falling disks. Phys. Fluid, 7, pp 197-208.

WINNY, H.F. 1932 The vortex system generated behind a sphere moving through a viscous fluid. ARC R & M 1531.

XIA, X.J. and BEARMAN, P.W. 1983 An experimental investigation of the wake of an axisymmetric body with a slanted base. Aero Quart. XXXIV, pp 24-45.

YAMADA, H. and MATSUI, T. 1978 Preliminary study of mutual slip-through of a pair of vortices. Phys. Fluids. 21, pp 292-294.

YAMASAKI, H. et al. 1967 The vortex flowmeter. 6th Proc. Japan SICE Conf. pp 389-390

ZDRAVKOVICH, M.M. 1977 Review of flow interference between two circular cylinders in various arrangements. Trans. ASME, J. Fluid Eng., pp 618-633.

# APPENDIX A

## Maskell's formulae for corretion of the blockage effects

The corrected base pressure coefficient, $C_{pbc}$, is given by

$$k_c^2 = 1 - C_{pbc} \tag{A1}$$

and $k_c$ is calculated from the following equations.

$$\frac{k_o^2}{k_c^2} = 1 + \frac{C_D}{k_c^2 - 1} \frac{S}{C} \tag{A2}$$

$$k_o^2 = 1 - C_{pb} \tag{A3}$$

where

S : the representative area of the bluff body

C : the cross-sectional area of the wind tunnel

The corrected drag coefficient, $C_{DC}$, and free stream velocity $U_{co}$ are also given by

$$\frac{k_o^2}{k_c^2} = \frac{C_D}{C_{DC}} = \frac{U_{co}^2}{U^2} \tag{A4}$$

Therefore, blockage can be corrected from the measurements of only $C_D$ and $C_{pb}$. When $D_D$ is not available, the following approximation is sometimes used for thin plates.

$$C_D \approx 0.8 - C_{pb} \tag{A5}$$

# APPENDIX B

## Induced velocity of an isolated vortex ring

The stream function (4.1.14) can be written as

$$\psi = \frac{\Gamma}{4\pi} (ar)^{\frac{1}{2}} J(k) \tag{B1}$$

where

$$J(k) = \left( \frac{2}{k} - k \right) K(k) - \frac{2}{k} E(k) \tag{B2}$$

Then, the component of the induced velocity $u$ is given by

$$u = \frac{1}{r} \frac{\partial \psi}{\partial r}$$

$$= \frac{\Gamma}{8\pi r} \left( \frac{a}{r} \right)^{\frac{1}{2}} \left\{ J(k) + 2r \frac{\partial J(k)}{\partial r} \right\} \tag{B3}$$

We can rewrite the differential in (B3) by

$$\frac{\partial J(k)}{\partial r} = \frac{\partial J(k)}{\partial k} \cdot \frac{dk}{dr} \tag{B4}$$

where

$$k^2 = \frac{4ar}{x^2 + (a+r)^2} \tag{B5}$$

$$2 \log k = \log 4ar - \log \{ x^2 + (a+r)^2 \}$$

$$2 \frac{dk}{k} = \frac{dr}{r} - \frac{2(a+r)\, dr}{x^2 + (a+r)^2}$$

$$\therefore \frac{dk}{dr} = \frac{k}{2r} \left( 1 - \frac{1}{2} k^2 - \frac{r}{2a} k^2 \right) \tag{B6}$$

$$\frac{\partial J(k)}{\partial k} = \left( - \frac{2}{k^2} - 1 \right) K(k) + \left( \frac{2}{k} - k \right) \frac{\partial K(k)}{\partial k}$$

$$+ \frac{2}{k^2} E(k) - \frac{2}{k} \frac{\partial E(k)}{\partial k} \tag{B7}$$

Next formulae are available from a mathematical handbook.

$$\frac{\partial K(k)}{\partial k} = \frac{E(k)}{k(1-k^2)} - \frac{K(k)}{k} \tag{B8}$$

$$\frac{\partial E(k)}{\partial k} = \frac{E(k) - K(k)}{k} \tag{B9}$$

From (B8) and (B9), equation (B7) becomes

$$\frac{\partial J(k)}{\partial k} = \frac{2-k^2}{k^2(1-k^2)} E(k) - \frac{2}{k^2} K(k) \tag{B10}$$

Finally we obtain the following equation from (B3), (B4), (B6) and (B10)

$$u = \frac{\Gamma}{8\pi r}\left[\left(\frac{a}{r}\right)^{\frac{1}{2}} \frac{k^3}{1-k^2} E(k) - \left(\frac{r}{a}\right)^{\frac{1}{2}} k\left\{\frac{2-k^2}{1-k^2} E(k) - 2K(k)\right\}\right] \tag{B11}$$

Next the other component of the induced velocity $v$ is given by

$$v = -\frac{1}{r}\frac{\partial \psi}{\partial x}$$

$$= -\frac{\Gamma}{4\pi r}(ar)^{\frac{1}{2}} \frac{\partial J(k)}{\partial k} \cdot \frac{dk}{dx} \tag{B12}$$

where $dk/dx$ is calculated from (B5) and we get

$$\frac{dk}{dx} = -\frac{xk^3}{4ar} \tag{B13}$$

Then we obtain the following equation from (B10), (B12) and (B13)

$$v = \frac{\Gamma}{8\pi r}\left(\frac{a}{r}\right)^{\frac{1}{2}}\left(\frac{x}{a}\right) k\left\{\frac{2-k^2}{1-k^2} E(k) - 2K(k)\right\} \tag{B14}$$

# APPENDIX C

## Induced velocity of the two-dimensional double vortex streets in antiphase

Let us consider the induced velocity of two-dimensional double vortex streets in antiphase, which model vortex shedding from two flat plates in a side-by-side arrangement, when the vortices in each street are staggered exactly in antiphase ($h=0.5\ell$). The velocities of the inside and outside rows are from equations (4.2.2) and (4.2.4)

$$u_a' = \frac{\Gamma_a'}{2\ell'} \coth \frac{2\pi a'}{\ell'} + \frac{\Gamma_b'}{2\ell'} \left[ H(a'+b') + H(b'-a') \right] \tag{C1}$$

$$u_b' = \frac{\Gamma_b'}{2\ell'} \coth \frac{2\pi b'}{\ell'} + \frac{\Gamma_a'}{2\ell'} \left[ H(a'+b') - H(b'-a') \right] \tag{C2}$$

where

$$H(a) = \frac{\sinh \frac{2\pi a}{\ell}}{\cosh \frac{2\pi a}{\ell} - \cos \frac{2\pi h}{\ell}} \tag{C3}$$

When $h = 0.5\ell$, equations (C1) and (C2) become

$$u_a' = \frac{\Gamma_a'}{2\ell'} \coth \frac{2\pi a'}{\ell'} + \frac{\Gamma_b'}{2\ell'} \left\{ \tanh \frac{\pi(a'+b')}{\ell'} + \tanh \frac{\pi(b'-a')}{\ell'} \right\} \quad (C4)$$

$$u_b' = \frac{\Gamma_b'}{2\ell'} \coth \frac{2\pi b'}{\ell'} + \frac{\Gamma_a'}{2\ell'} \left\{ \tanh \frac{\pi(a'+b')}{\ell'} - \tanh \frac{\pi(b'-a')}{\ell'} \right\} \quad (C5)$$

These equations agree with those obtained by Landweber (1952), in which

$$u_a' = u_2 \qquad \Gamma_a' = -\Gamma_2 \quad (C6)$$

$$u_b' = u_1 \qquad \Gamma_b' = \Gamma_1 \quad (C7)$$

$$a' = \frac{k}{2} \quad (C8)$$

$$b' = \frac{k}{2} + h \quad (C9)$$

APPENDIX D

Assumptions used in the calculation of vorticity

The vorticity in the (x,y) plane is defined as

$$\omega = \frac{\partial v}{\partial x} - \frac{\partial u}{\partial y}$$

$\frac{\partial v}{\partial x}$ can be calculated accurately by using two hot-wire probes spaced a small distance $\Delta x$ apart, provided no interference between the probes. However in this research, time dependent measurements were made at one x station and $\frac{\partial v}{\partial x}$ was assumed to be given by the relation

$$\frac{\partial v}{\partial x} = -\frac{\partial v}{\partial t} \cdot \frac{1}{u}$$

where u is the local flow velocity.

The assumptions involved in this transformation are

(i) the mean flow is parallel in the x-direction

(ii) the convection speed of vorticty is equal to the local u-component of the flow velocity

The assumption (i) has been used by Davies (1975) and is the usual one employed by researchers in this field. Strictly, the velocity component used to transfer vorticity from the time plane to the space plane should be the convection velocity of the vortex cores. In the wake of a two-dimensional bluff body, vortices of opposite sign travel with the same convection velocity. Davies (1975) measured the convection velocity separately and used this velocity for his calculation. However, for a ring bluff body or two-dimensional bluff bodies in close

proximity, the convection velocities of the vortic es do not have a common value. Hence, in this research, the local instantaneous velocity component u has been chosen, which will be the velocity of the vorticity at the centres of vortices but will cause some error in the calculation of $\frac{\partial v}{\partial x}$ .

A single viscous vortex model has been used in order to assess the likely size of the error in calculated vorticity due to an incorrect convection velocity. The error $\Delta\omega$ is given by

$$\Delta\omega = -\frac{\partial v}{\partial t}\cdot\frac{1}{u} + \frac{\partial v}{\partial t}\cdot\frac{1}{u_c}$$

$$= \frac{\partial v}{\partial x}\left(\frac{u_c}{u} - 1\right)$$

$$= \frac{\partial v}{\partial x}\cdot\frac{u_\theta \sin\theta}{u_c - u_\theta \sin\theta}$$

(see figure A)

Here,

$$\frac{u_\theta \sin\theta}{u_c - u_\theta \sin\theta} \to 0 \qquad \text{, when } \theta \to 0$$

$$\frac{u_\theta \sin\theta}{u_c - u_\theta \sin\theta} \to \frac{u_\theta}{u_c - u_\theta} \text{ (max), when } \theta \to 90^\circ \text{ or } x \to 0$$

Then,

$$v = \frac{\Gamma x}{2\pi r^2}\left[1 - e^{-1.26\left(\frac{r}{R_0}\right)^2}\right]$$

$$\therefore \frac{\partial v}{\partial x} = \frac{\Gamma}{2\pi}\left\{ \frac{1}{r^2}\left[ 1 - e^{-1.26\left(\frac{r}{R_o}\right)^2} \right] \right.$$

$$\left. - \frac{2x^2}{r^4}\left[ 1 - \left( 1 + \frac{1.26r^2}{R_o^2} \right) e^{-1.26\left(\frac{r}{R_o}\right)^2} \right] \right\}$$

Here,

$$1 \geq \left( 1 + \frac{1.26r^2}{R_o^2} \right) e^{-1.26\left(\frac{r}{R_o}\right)^2}$$

$$\frac{\partial v}{\partial x} \rightarrow \frac{\Gamma}{2\pi r^2}\left[ 1 - e^{-1.26\left(\frac{r}{R_o}\right)^2} \right], \quad \text{when } x \rightarrow 0$$

$$= \frac{u_\theta}{y} \quad (\text{max at a given } r)$$

Therefore, $\Delta\omega = 0$ along the path of the vortex centre and reaches a maximum along the line x = 0. The non-dimensionalized error $\Delta\omega^*$, where $\Delta\omega^* = \frac{\Delta\omega \cdot w}{U}$, is given by

$$\Delta\omega^* = \frac{1}{y^*} \cdot \frac{u_\theta^{*2}}{u_c^* - u_\theta^*}$$

where

$$y^* = \frac{y}{w}$$

$$u_c^* = \frac{u_c}{U}$$

$$u_\theta^* = \frac{u_\theta}{U}$$

Typical values of vortex strength, core radius and convection

speed were taken from the actual measurements shown in figure 4.5 ( page 186 ).

$$u_\theta^* = \frac{0.32}{r^*}\left(1 - e^{-1.15 r^{*2}}\right)$$

$$\omega^* = 0.74\, e^{-1.15 r^{*2}}$$

$$u_c^* = 0.79$$

Calculated values of $\Delta\omega$ and the distorted $\omega$ distribution along the y-axis, where the maximum error occurs, are shown in figures B and C.

There is some distortion but the value of the vorticity at the centre of the vortex is correct. Some cancellation of this error is expected in the calculation of circulation of the vortex since the error is of opposite sign on opposite sides of the centre. There is also an error due to the fact that not all components of v travel at this convection speed. For example, components arising from the potential flow field of other vortices are going at different speeds. Moreover this error is probably also not too large. Davies (1975), who used a measured convection velocity, found that $u_c$ varied by almost 20 % across the wake and hence he used a mean value. Also, the measurement of $u_c$ in the wake of a ring model by using two hot-wires was tried here, but again variations of more than 20 % in $u_c$ were found. Therefore, it is unlikely that the use of a local velocity as the convection velocity gives rise to significantly larger errors

than using a single measured $u_c$ value. The use of the local velocity has the advantage that it provides a means of locating the vortex centres correctly and gives an accurate measurement of the convection speed of the vortex cores. It should be noted that a more accurate estimate of $\frac{\partial v}{\partial x}$ could be obtained by calculating two conditionally-averaged time dependent velocity fields displaced a small distance apart in the x dirction. If the position of the reference wire is unchanged, then v would be known at the same instant at two points a small distance $\Delta x$ apart and $\frac{\partial v}{\partial x}$ could be calculated.

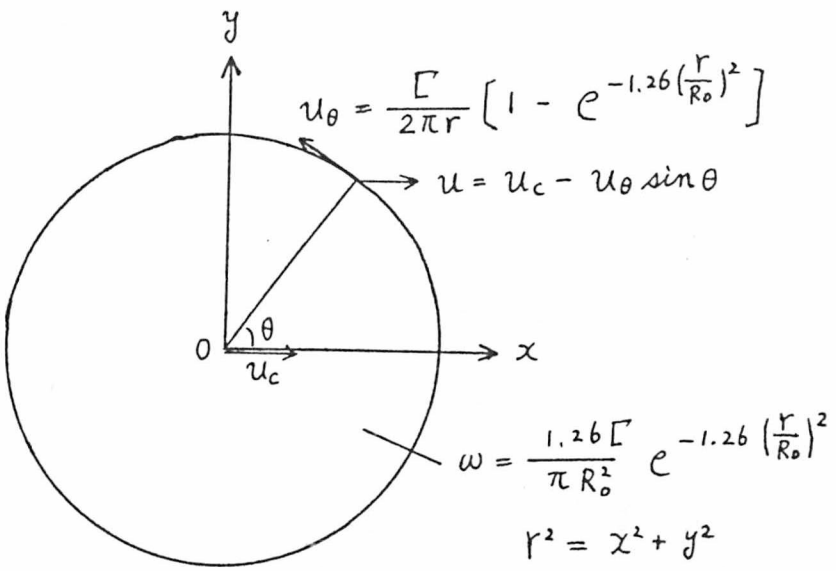



Figure A Isolated viscous vortex model used to assess error.

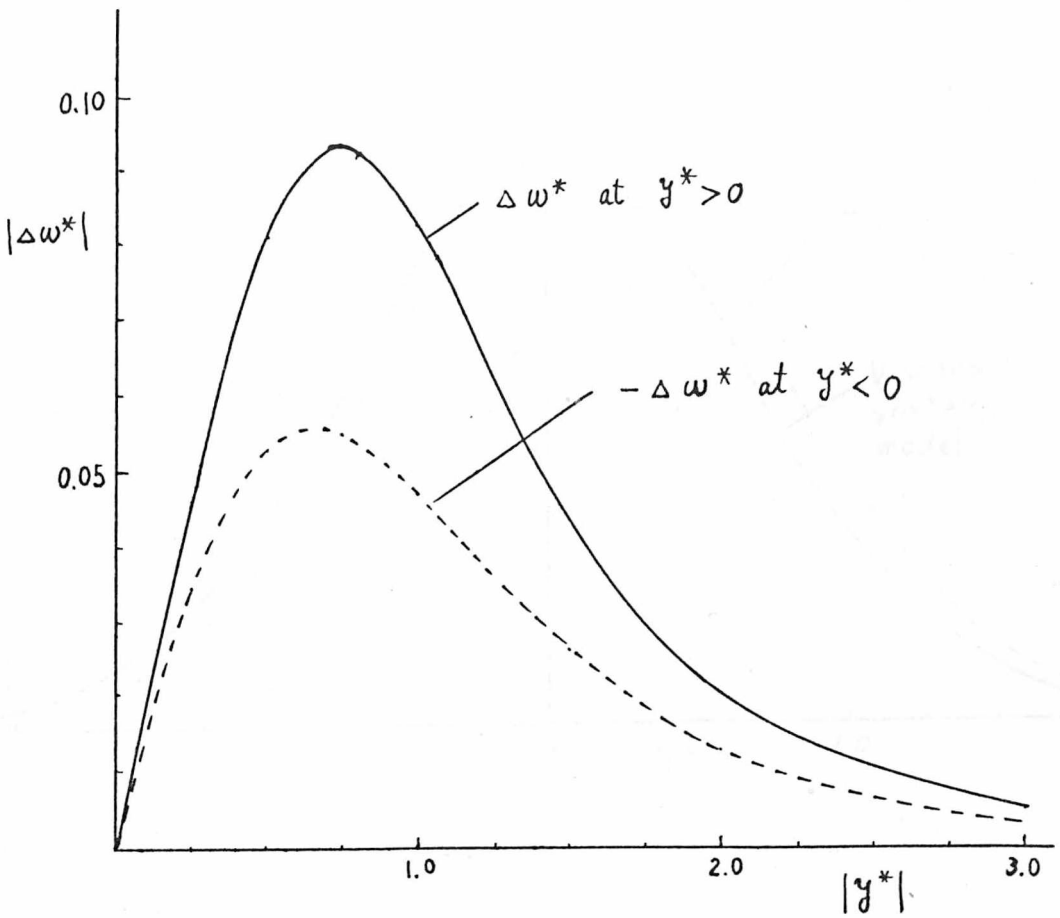



Figure B  Error along the y-axis

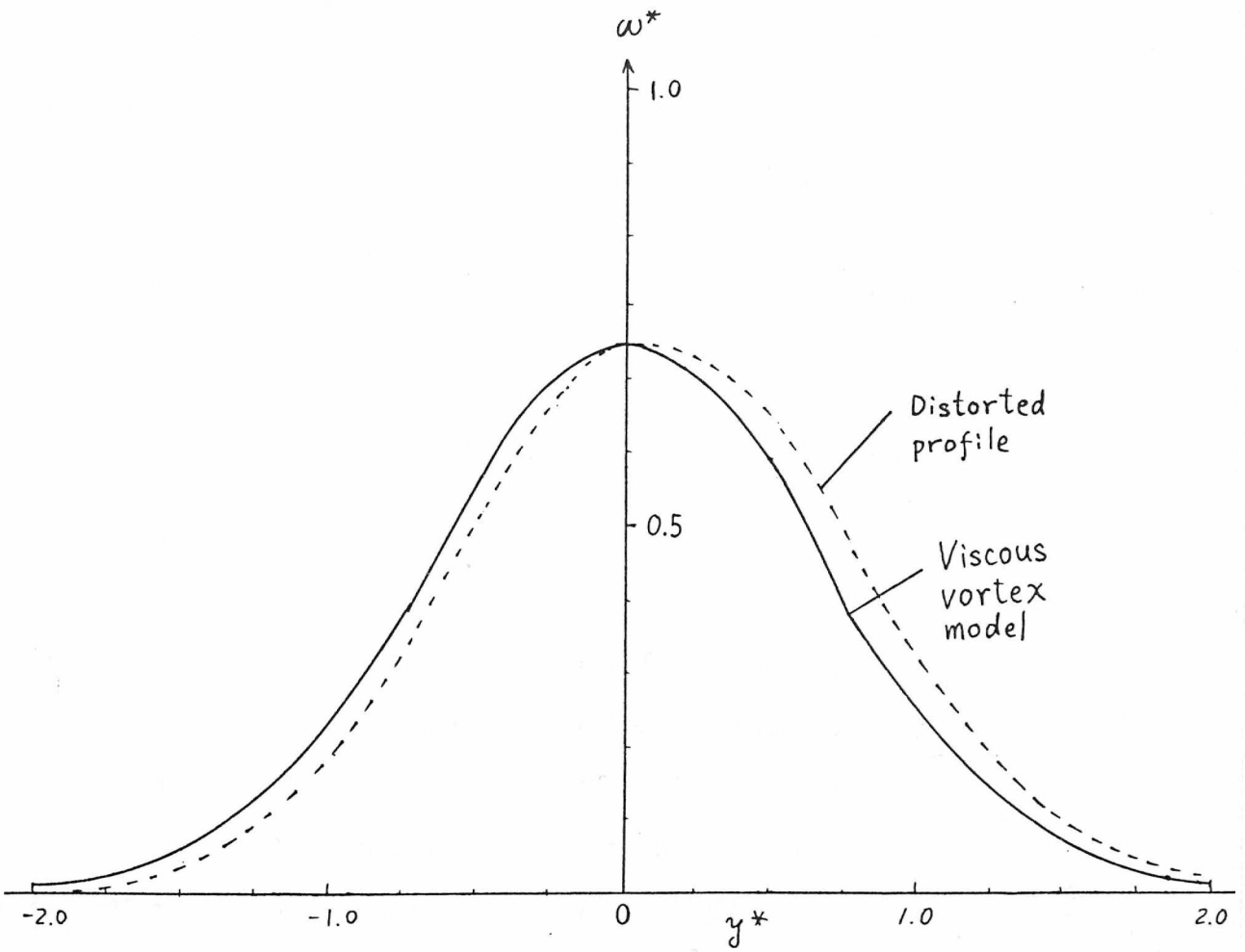



Figure C Distorted vorticity profile along the y-axis